https://www.sciltp.com/journals/mi
Online ISSN: 2982-2394
Volume 2, Issue 2, 2025

Materials and Interfaces

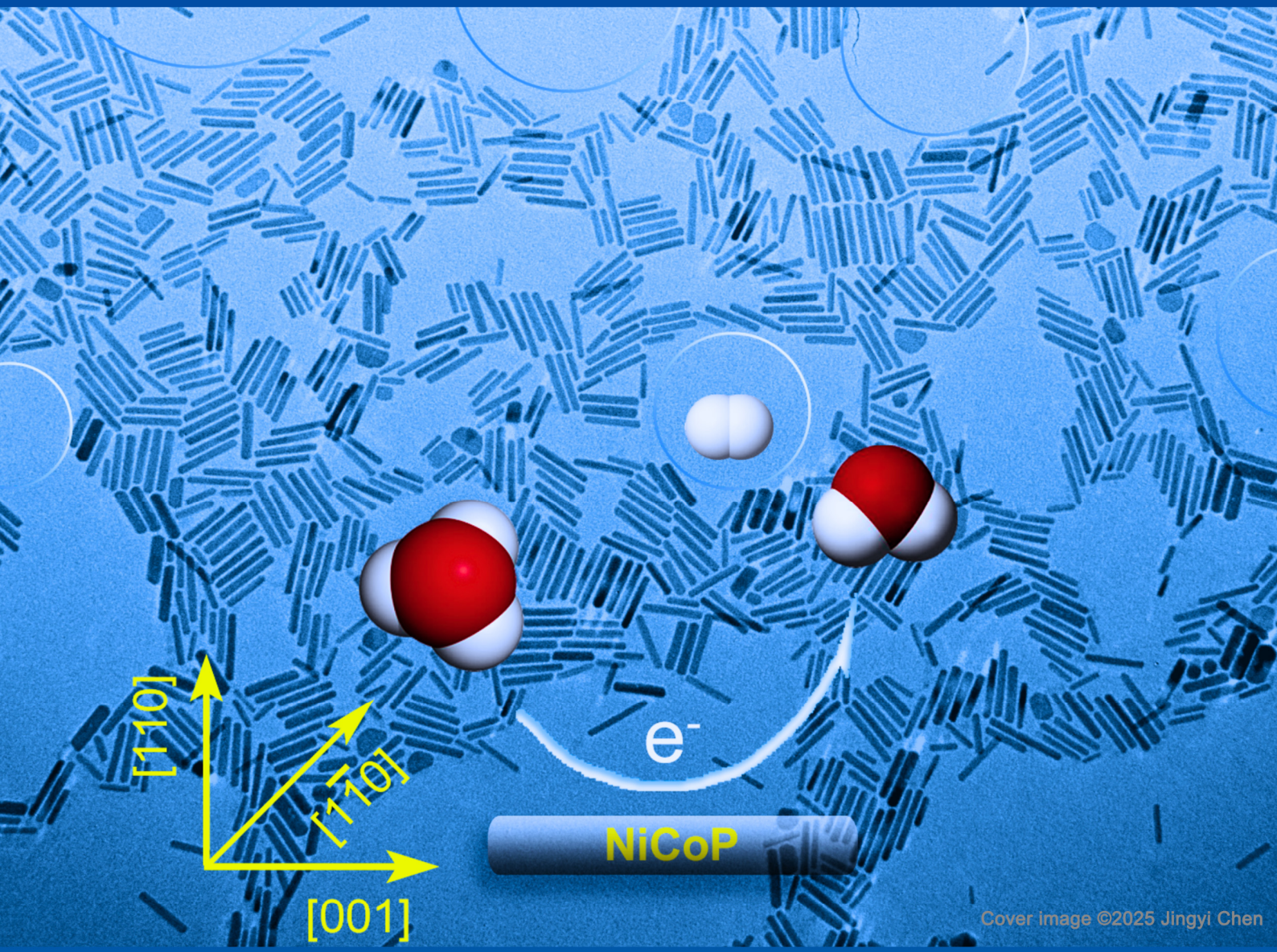

Cover image ©2025 Jingyi Chen

Carbon Monoxide-Assisted Synthesis of Nickel Cobalt Phosphide Nanorods for the Hydrogen Evolution Reaction

Scilight

Contents

Vol. 2 No. 2, June 2025

Article

Photonic Properties of Colloidal Crystal Elastic Sheets Formed by Electrostatic Repulsion and Shear Stress and Their Fundamental Deformation Modes

Hiroshi Fudouzi [1,*], Tsutomu Sawada [1], Satoshi Kawanaka [2], and Fumio Uchida [2]

[1] National Institute for Materials Science, 1-2-1, Sengen, Tsukuba 305-0047, Japan
[2] Fuji Chemical Co., Ltd., 1-35-1, Deyashikinishi-machi, Hirakata-shi 573-0003, Japan
* Correspondence: fudouzi.hiroshi@nims.go.jp
Received: 3 March 2025; Revised: 21 April 2025; Accepted: 23 April 2025; Published: 15 May 2025

Abstract: Recently, mechanochromic soft materials that enable smart sensing functions by visual inspection without the need for special devices have been attracting attention. We have developed a non-close-packed type elastic colloidal crystal sheet through a simple shear-induced process. The colloidal crystal state, in which the (111) plane exhibited significant orientation due to shear stress, was successfully stabilized in the 4-hydroxybutyl acrylate (4-HBA) monomer precursor dispersed with desalted silica colloidal particles through the implementation of UV irradiation radical polymerization. Consequently, a solid colloidal crystal sheet was produced, capable of reversibly modulating its structural color in response to elastic deformation. In this article report will address the stress response functions of this sheet due to elastic deformation of stretching, compressing and bending. In addition, a rapid structural color change at 4.17 ms unit by impacting. By analysis of tensile and strain curve, Young's module was 0.56 MPa, tensile strength 0.73 MPa and elongation brake was 142.9%. In addition, durability repeating elongating the rubber sheet for 100,000 times. Up now 150 cm^2 sheet produced by hand made batch process. This simple process is suitable for scaling up colloidal crystal to mass production and is expected to have a wide range of engineering applications with mechanochromic materials.

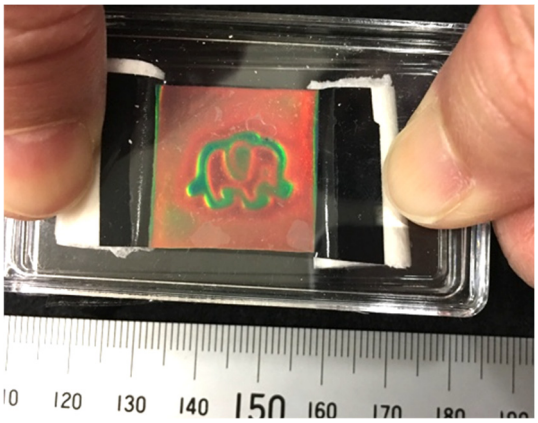

Keywords: silica colloids; poly (4-hydroxybutyl acrylate) elastomer; non-close-packed colloidal crystal; shear stress; elastic deformation; Bragg's diffraction; structural color

1. Introduction

In recent years, the study of mechanochromism, in which the structural color of soft materials changes because of deformation or stress, has become increasingly popular [1–3]. Multilayer films [4], block copolymers [5,6], liquid crystal elastomers [7], and colloidal crystals [8], including opal [9], inverse opal types [10] and core-shelll colloidal powders [11], have been studied and attempted to be applied to smart materials in a wide range of fields, from sports, medical, smart skin, and infrastructure damage detection. For engineering applications, a Role-to-Role coating process, which has been applied to hydroxypropyl cellulose [12] and core-shell colloids [13], has made mass production possible.

Elastic non-close-packed type colloidal crystal is one of important soft materials to produce smart materials with tuning structural color by mechanical deformation. There are two approaches; Core-shell nanospheres were applied thermally shear stress [11,13] and polymerization repulsively charged colloidal crystals embedded in monomer and polymerization. The later approach is traditional approach to form non-close packed colloidal crystal in hydrogel [14]. This method allows colloidal particles to be dispersed in a monomer liquid that does not contain a water-soluble solvent instead of a hydrogel. Recently, non-close packed type of elastic colloidal crystals has been attracting much attention due to their wide range of structural color tuning and rubber-like mechanical

properties. Methods have been reported in which silica particles are dispersed in an acrylic monomer that does not contain aqueous solvent and then polymerized into an elastomer by radical reaction [15–18], and another method in which a high-quality colloidal crystal embedded in hydrogel is formed and then replaced with an acrylic monomer to form an elastomer [19]. Research in this field is expected to have applications in smart skins and other areas and has been actively pursued in recent years. For example, research is progressing on the analysis of the relationship between changes in the microstructure (crystal lattice) of colloidal crystals due to deformation and their optical properties [20]. Additionally, a new type of elastomer that does not change structural color under elastic deformation has been reported [21]. Furthermore, studies are underway to enhance functionality by combining mechanochromic properties with other functionalities, such as electronic-optical [22] and magnetic-optical [23] responses.

Sawada et al., have been investigating colloidal photonic crystals made of soft materials: hydro gels and elastomers [24]. In the previous works, deionized colloidal particles suspension easily form colloidal crystals and furthermore the quality of colloidal crystal improved by adjusted applied shear flow. However, colloidal crystal embedded in hydrogel sheet is too soft and wetted with solvent. From a viewpoint of applications like rubber, solvent free is better. Thus, silica colloids were dispersed in monomer and deionized by ion exchange resin. Deionization causes colloidal particles to form crystals, resulting in a reflection peak. It is believed that removing residual Na^+ ions and other impurities from silica particles during synthesis causes the electric double layer around colloidal particles to expand, leading to electrostatic repulsion and an Alder phase transition, thereby forming colloidal crystal. Highly charged silica formed a repulsion layer and formed multi-crystals colloidal crystal in monomer liquid. It is well known that shear stress is important for forming orientated colloidal crystal [25]. A shear stress method was used as following procedure and finally monomer liquid was changed to solid rubber like elastomer by polymerization of UV radical reaction [26]. Non close packed colloidal crystal with uniform structural color is important for practical mechanochromic applications.

Figure 1 shows the concept image of the process. (A) Preparing UV-curable colloidal dispersion: silica nanosphere are dispersed in UV-curable acrylate monomer liquid, (B) Randomly oriented colloidal crystal grins are formed by deionization originated from electrostatic repulsion layer expanding, (C) Orientation of colloidal crystal planes due to shear stress near the glass plate, and (D) UV-radical polymerization of liquid monomer to solid without broking colloidal crystal, as a result non-close-packed type silica colloidal crystal to fix in solid elastomer. As described later, deionized treatment improves the uniformity of structural color for large size (over 150 cm^2) in colloidal crystal embedded in elastomer sheet. The objective of this study is to provide a comprehensive report on the fundamental photonic functions of an elastic colloidal crystal sheet under typical deformation modes, including stretching, compression, and bending. Furthermore, we have demonstrated a simple and pragmatic photonic functions of elastic colloidal crystal rubber, including strain imaging through the impact of an object and the durability of a large number of cyclic deformations.

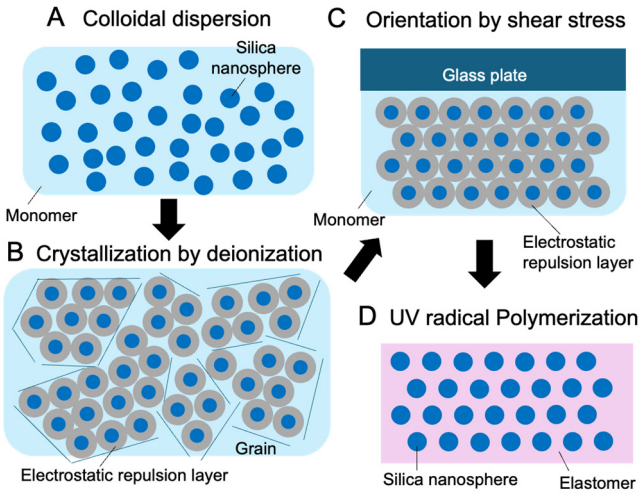

Figure 1. Conceptual diagram of the process for producing colloidal crystal highly-oriented in an elastomer matrix using electrostatic repulsion. (**A**) silica nanospheres are well dispersed in a precursor liquid of monomer, (**B**) ion exchange resin is used to deionize the colloids to form small size grains of colloidal crystal with random orientation planes, (**C**) the colloidal crystals are oriented in one direction by shear stress near the glass plate, and (**D**) the precursor is polymerized by UV irradiation with a radical initiator, and the colloidal crystals are immobilized in the elastomer.

2. Materials and Methods

As a precursor, silica nanospheres were dispersed in UV curable monomer liquid. Monodispersed silica nanosphere (Silbol 150, Fuji Chemical Co., Ltd., Osaka, Japan) was dispersed in 4-Hydroxybutyl Acrylate (4-HBA, Osaka Organic Chemical Industry Ltd., Osaka, Japan). 2-Hydroxy-2-methylpropiophenone (Sigma-Aldrich, St. Louis, MO, USA) is a radical photo-initiator (PI) molecule that was used in the polymerizing 4-HBA monomer by exposure of UV radiation. AG 501-X8 Mixed Bed Resin, biotechnology grade (Bio-Rad Laboratories, Inc., Hercules, CA, USA) was selected as deionized ions from the precursor monomer of 4-HBA and silica colloids.

The concentration of silica in the dispersion was 20 wt% was mixed with 1 wt% PI by tube rotator for 30 min. The de-ionized dispersion indicates a milky bright structural color due to Bragg's diffraction from small grain sized colloidal crystals. Supplemental Figure S1 shows a conceptual flow of making rubber sheet from deionized 4-HBA precursor. This deionized 4-HBA precursor silica suspension was infilled into a between two glass substrates with a 1 mm spaced gap for applying shear stress, as shown in Figure S1B. The lower glass substrate by uniaxial vibration indued a shear stress to 4-HBA precursor. The typical vibration motion was 10 Hz and amplitude length of 1 mm (Vibration shaker (SSV-105) and controller (SVA-ST-30), San-Esu Co. ltd., Tokyo, Japan). As a result, the structural color became more vivid as many small colloidal crystal grains with randomly oriented planes were oriented perpendicular to the glass surface. After stopping the vibration, UV LED light was irradiated through the glass plate as shown in Figure S1C. The 4-HBA liquid changed solid elastomer.

A 365 nm UV LED array (MBRL-CUV7530, 4.3 W LED module and MLEK-A230W2LRDB controller, MORITEX Co., Yokohama, Japan) was used for UV irradiation. As a result, 4-HBA monomer was polymerized to homopolymer with highly (111) plane-oriented colloidal crystal. The glass transition temperature of poly(4-HBA) elastomer is—40 degrees C and shows elastic function like rubber. The LED modules (75 mm × 30 mm) were joined and cover the entire area of the standard sample size, 100 mm × 100 mm. After UV curing, poly (4-HBA) elastomer sheet with uniform structural color was obtained, and a free-standing elastomer sheet of 1 mm thickness was formed by peeling from glass sheet. To support the mechanical strength and improve the structural color, the elastic poly(4-HBA) sheet was bonded to a 1 mm thick black colored chloroprene rubber CR sheet (CB260N, 1 mm thickness, AKITSU Industry Co., Ltd., Hiroshima, Japan).

3. Measurement and Equipment

The reflectance spectra of the poly (4-HBA) elastomer sheets and silica colloid dispersions of monomer were recorded using a miniature fiber optic spectrometer (Ocean Optics, USB2000+, Dunedin, FL, USA). The incident light was perpendicular to the samples (to measure specular reflectance, the probe was oriented at 90° to the sample in a reflectance probe holder) at a local spot (less than 2 mm in diameter) by HL-2000 tungsten halogen light source. The fiber has a core diameter of 200 μm, a numerical aperture of 0.22, and is banded with six illumination fibers around a single read fiber. Using this probe fiber, we measured the reflectance to analyze the shift of the Bragg diffraction peaks due to elastic deformations. In addition, transmittance spectroscopy at different angles of incidence was used to estimate the spacing of the silica array planes. A UV/VIS spectrophotometer with a variable angle specular transmittance accessory (V-570, JASCO Co., Tokyo, Japan) was used. This simple analysis method was reported in our previous paper [27]. In the transmission spectrum, the wavelength position of the valley corresponds to the wavelength of the Bragg diffraction peak. By analyzing the correlation between the angle of incidence and the wavelength of the valley, the interplanar spacing of the particle array plane can be determined. Refractive index of monomer 4-HBA and poly(4-HBA) elastomer was measured with an abbe refractometer at the wavelength of D-Line (NAR-1T SOLID, ATAGO Co., Ltd., Tokyo, Japan).

Reflection photo image and movie were obtained under using a flat high brightness LED white light (LED viewer 5000A, Color temperature: 5000 K, Shinkosha, Co., Tokyo, Japan) irradiation. Digital camera (EXILIM EX-F1, CASIO Computer Co., Ltd., Tokyo, Japan) and with a smart phone camera with 240 fps slow movie mode (iPhone 6 Plus, Apple Inc., Cupertino, CA, US). A part of photo images was taken using a coaxial vertical illumination to obtain uniform structural color image. Stretching and bending of rubber sheets was done by a one-axis manual stage. Compression and impact experiments were conducted using a homemade device shown in the attached figures below.

Stress-strain curves were measured by uniaxial tensile equipment (ZTA-500N+FSA-1KE-500N, IMADA Co., Ltd., Aichi, Japan). The Danbel-shaped test piece with 1.03 mm thickness was punched out using a metal template (JIS K6251 #8). The width of center was 4 mm. Initial length of the test piece was 28 mm between gripping's length. Due to technical reason, the elongation of test piece was measured as the gripping's length. Durability test was performed by desktop model endurance test machine (DMLHP-PP, Yuasa System Co., Ltd.,

Okayama, Japan). The elastomer had a width of 10 mm, an initial length of 40 mm, and an elongated length of 55 mm. The elongation was 55/40 = 137.5%.

4. Results & Discussion

4.1. Deionized Silica Colloidal Crystal in 4-HBA Monomer Liquid

Figure 2 shows the analysis of the Bragg's diffraction of the silica colloidal crystals dispersed in monomer liquid formed by deionization. Figure 2A shows typical reflection spectrum with and without deionization treatment. Silica of 150 nm diameter colloids were dispersed in 4-HBA monomer liquid and deionization using ion-exchange resin. A single diffraction peak appears around 653 nm after deionization. This single peak due to Bragg's diffraction from array of silica colloidal crystal planes. Supplemental Figure S2 compares two cuvettes at 20 wt% silica colloids, the left with de-ionization shows light red color and the right without deionization as shown in the photo A. The left cuvette shows light red color due to the Bragg's diffraction of 653 nm peak. The color of the cuvette is strongly influenced by the direction of the incident light. In the photo C, the light is reflected specularly, and the color appears red. In the photo D, the light is reflected at a 90° angle and the color appears light green or light blue. In the photo B, the light is reflected at a 45° angle and the color of the fiber illumination appears light orange, while the color of the light reflected at a 90° angle appears light green. From these observations, we can conclude that the color is a structural color with angle dependence.

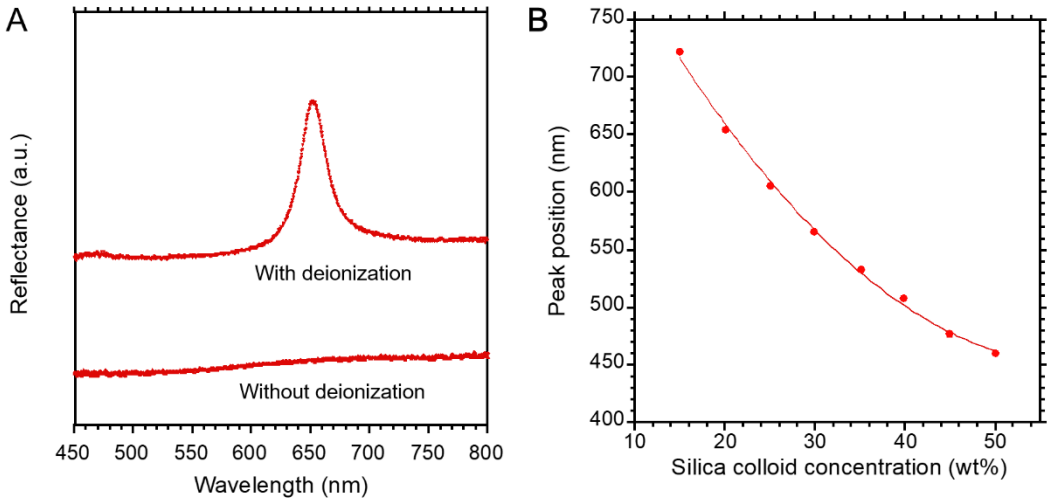

Figure 2. Colloidal crystals formed by silica colloidal particles dispersed in monomer (4-hydroxybutyl acrylate, 4HBA) liquid. (**A**) The effect of deionization treatment using ion exchange resin on crystallization, (**B**) The effect of silica particle concentration on the reflection peak wavelength of the colloidal crystal.

Supplemental Figure S3 shows the silica concentration effect changes the structural color of colloidal crystal in 4-HBA monomer liquid. At low concentration of 15 wt% shows red and high concentration of 50 wt% shows purple. This color change depends on peak shift of the diffraction peak at specular reflection. The diffraction peak position corresponds to the silica particle concentration as shown in Figure 2B. The peak position wide varied from 460 nm to 722 nm, i.e., covering from almost entire visible color region to near NIR region. This means that the lattice distance of colloidal crystal can be tuned by only particle concentration silica colloids in wide visible color range [13,14]. In this paper, we selected initial structural color as red for colloidal crystal rubber sheet for tunable structural color function by mechanical deformations for wide color changeable range.

4.2. Silica Colloidal Crystal in Poly(4-HBA) Elastomer Solid Sheets

Figure 3 shows the uniaxial tensile stress-strain curves of silica colloidal crystals in a poly(4-HBA) elastomer sheet. Photo A shows the elongation of the elastomer sample just before fracture. At the time of fracture, the tensile stress was 3.0 N, and the elongation was 40 mm, as shown in Figure 3B. The tensile strength was calculated to be 0.728 MPa. The elongation at break was 142.9%. The Young's modulus (elastic modulus) can be determined from the slope of the strain-stress curve. Therefore, the Young's modulus was derived from the slope under the low-load conditions (less than 35%) shown in Figure 3C. The correlation coefficient exceeded 0.998, and the Young's modulus was 0.56 MPa.

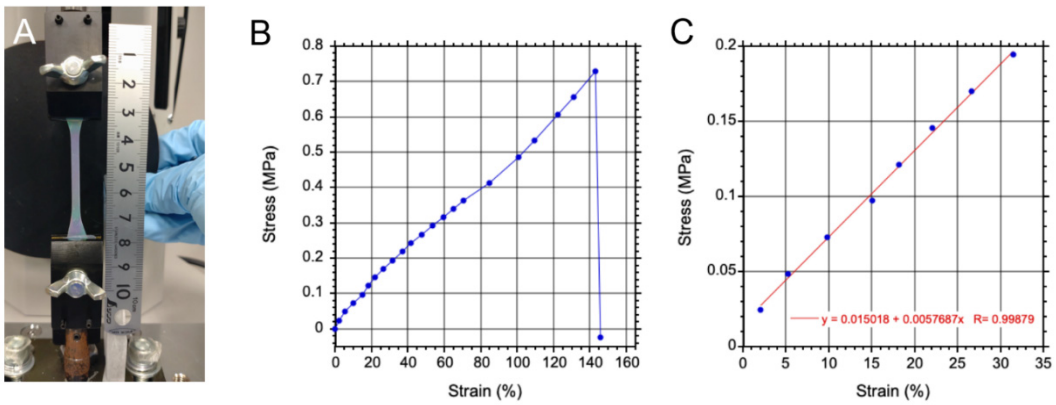

Figure 3. Mechanical property measurement by uniaxial tensile. (**A**) Stretched danbel form specimens, (**B**) Stress-strain curves were plotted up to the point of failure and (**C**) Stress-strain curves at low load conditions.

Figure 4 shows silica colloidal crystals embedded in 4-HBA on a black color supporting CR rubber sheet. Figure 4A shows a uniform structural color over an area of almost 100 mm × 100 mm. The structural color of 4-HBA elastomer is brighter red, peak position around 637 nm. The refractive index of monomer 4-HBA was 1.452, and that of 4-HBA elastomer was 1.493 at 25 °C. On the other hand, the refractive index of the silica colloid is about 1.45, and the refractive index contrast increases as polymerization progresses from monomer to elastomer. This may be one of the reasons why UV radical polymerization contributes to the vividness of the structural color. The photo image was taken using a coaxial vertical illumination. Figure 4B shows a conceptual diagram of the cross-section of the rubber sheet. Colloidal crystal layer was 1 mm and thickness of the black color rubber sheet is also 1 mm. The white light incident at right angles to the colloidal crystal is split into reflected and transmitted light at the alignment planes of the silica particles. The reflected light, due to Bragg's diffraction, depends on the spacing between the alignment planes and causes the red structural color in Figure 4A. Light of other wavelengths transmitted through the colloidal crystal is absorbed by the black supporting rubber sheet. The Bragg's diffraction peak can be expressed by as following equation [27].

$$\lambda = 2d \sqrt{\left(n_p^2 V_p + n_m^2 V_m\right) - \sin^2 \theta} \quad (1)$$

Here, λ is the peak position, d is the interspacing between the particle array planes, n_p is the refractive index of the colloidal particles, V_p is the volume of the colloidal particles, n_m is the refractive index of the matrix, V_m is the volume of the matrix, and θ is the angle of the incident light.

Figure 5 shows the transmittance spectrum at different tilting angles θ and delivered the linear relationship derived from Equation (1). Here due to a simple measurement method, the Bragg's diffraction peaks were corresponding to the dips in the transmission spectrum. From the slope of the line in Figure 5B is 0.4775, the interspacing of silica planes, d was obtained as 229.5 nm. In the case of a colloidal crystal with silica particles arranged in the closest packing of 150 nm silica colloid, the distance between the planes of the silica array can be calculated to be 122.5 nm. Therefore, the difference in interplanar spacing between the non-closest packed and closest packed colloidal crystals is 107 nm, which is a maximum displacement that can change the interplanar spacing. This corresponds to a wavelength of approximately 289 nm when converted to the wavelength of the diffracted peak. The wavelength of the initial state of the non-close-packed colloidal crystal elastomer is 637 nm (red), and it covers a wide range of visible light from 348 nm (ultraviolet region), which means that the range of visible color change is wide due to the advantage of non-close packed colloidal crystal architecture.

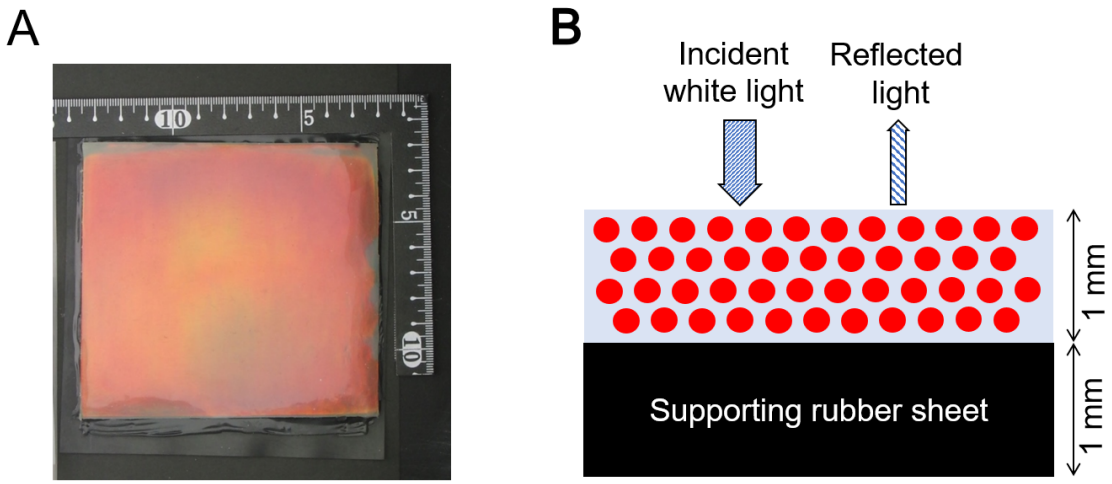

Figure 4. An elastic sheet of colloidal silica crystals arranged in a regular pattern in an elastomeric matrix. (**A**) Digital camera photograph of the surface of the sheet taken under coaxial illumination, showing the nearly red structural color spread over the entire area of the sheet. (**B**) Cross section of the rubber sheet and the concept of structural coloration by selective reflection. Incident white light is selectively reflected only in red by the colloidal crystal sheet. Light of other colors passes through the colloidal crystal layer and is absorbed in the black rubber sheet of the supporting substrate.

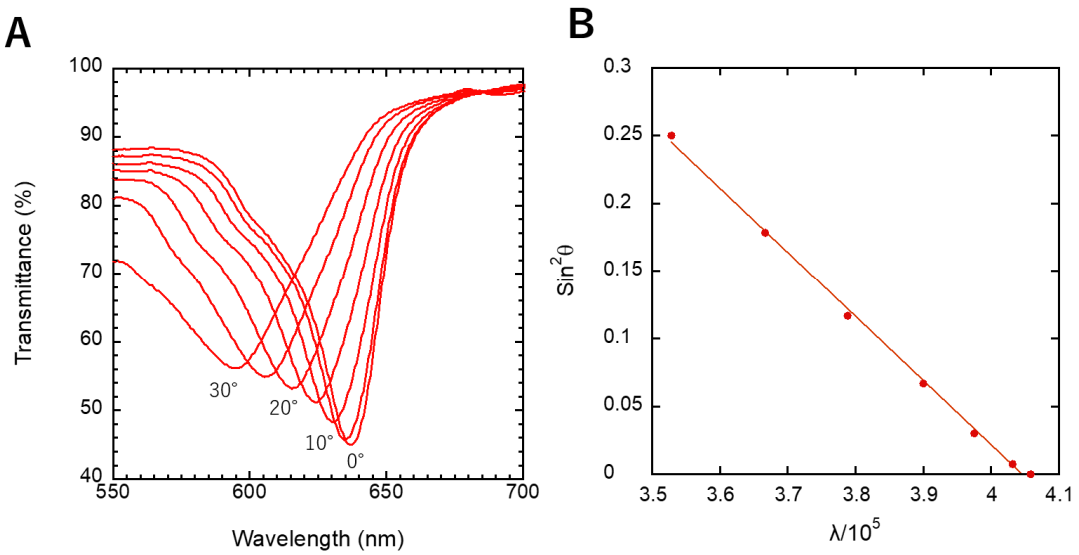

Figure 5. Measurement of the interplanar spacing of colloidal crystals in Poly(4-hydroxybutyl acrylate) using the Bragg-Snell formula. (**A**) Transmittance spectra measured at different angles, from 0° to 30° in 5° steps, (**B**) Measurement data plotted against wavelength and angle of incidence, showing a linear relationship between the two, and the interplanar spacing of the colloidal particles can be calculated from the angle of the straight line.

4.3. Mechnochromic of Silica Colloidal Crystal in Poly(4-HBA) Elastomer

Figure 6 shows the structural color change due to the application of basic mechanical forces; stretching, compressing, and bending. An initial red structural color shown in the photo A was changed to green color by horizontal directional stretching shown in the photo B. A disk-shaped sample sandwiched between two glass plates. The initial sample with no pressure shows a red structural color as shown in the photo C. On the other hand, the disk with pressure applied by the glass plate changed to green color as shown in the photo D. For bending deformation, there are two types, convex and concave, as shown in the photo E and the photo G. The original sheet shown in the photo F is red color. In the photo E, the structural color changed to green color by convex bending. In contrast in the photo G, the structural color changed to deep red color in the middle area by concave bending. The structural color change is available as a Supplementary Video S1.

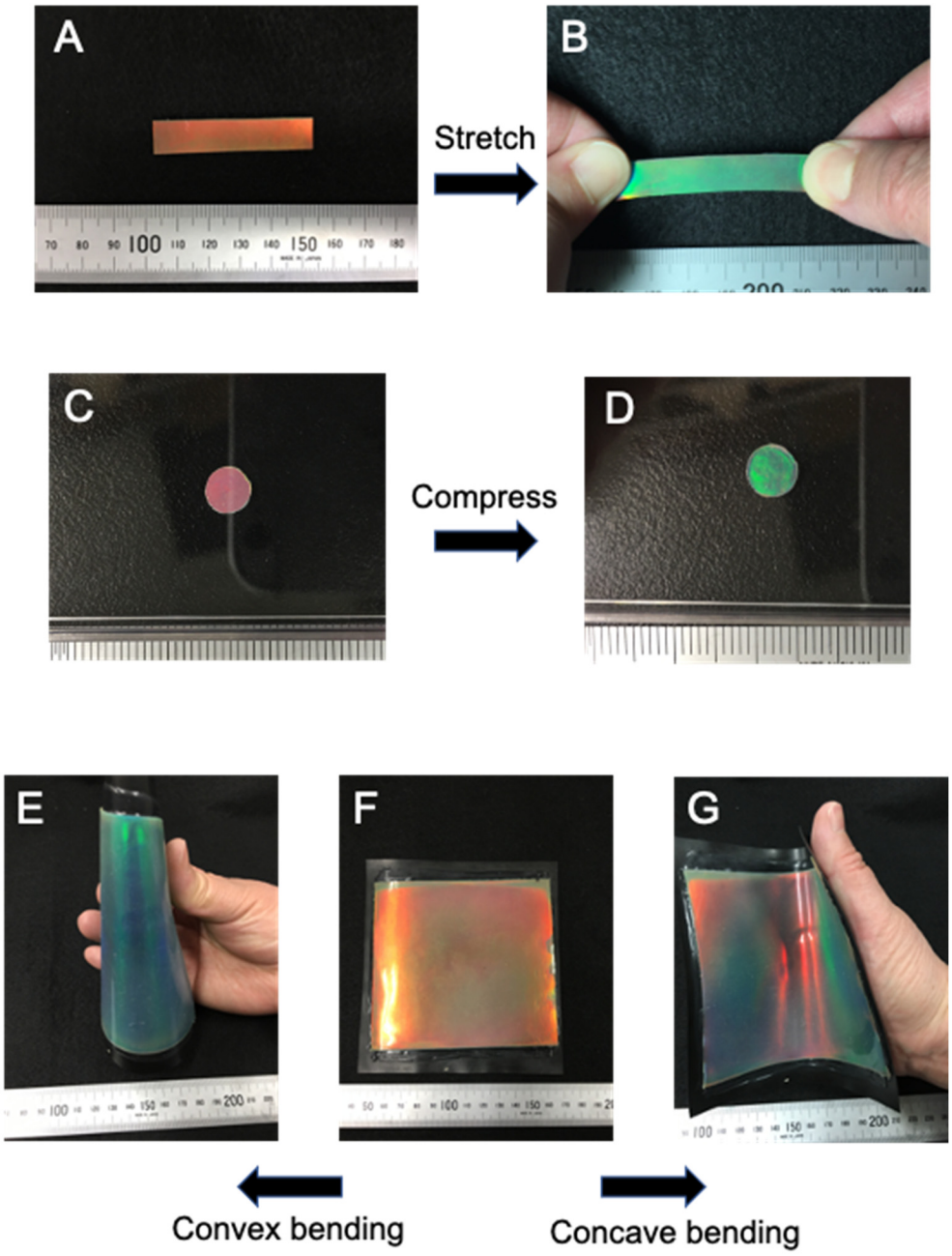

Figure 6. Structural color change due to mechanical-elastic different deformation modes. (**A**) an initial rectangular specimen, (**B**) under stretching, (**C**) an initial disk specimen, (**D**) under applied pressure by pressing a glass plate. (**E**–**G**) show the structural color change by convex and concave bending of a 100 mm square plate.

As the first deformation mode, the colloidal crystal was stretched in one direction using a single-axis stage. The change in structural color due to stretching is shown in the comparison images of coaxial irradiation in Supplementary Figure S4. Before stretching, the red structural color at 0 mm changes to green when stretched to 6 mm. When the stretching is stopped and the stage is returned to its initial state, the structural color returns perfectly to red. Structural color changes are quantitatively analyzed by Bragg diffraction analysis via reflection spectroscopy. Figure 7 show the elastic colloidal crystal was stretched to 8 mm in 1 mm increments and the reflectance spectrum was measured at each strain. Figure 7A shows that the Bragg's diffraction peak shifts to a lower wavelength direction and the reflection intensity decreases due to elongation. Figure 7B shows the relationship between the diffraction peak wavelength and elongation. When comparing the linear approximation and quadratic equation approximation on Figure 7B, the correlation coefficient R^2 is closer to 1 for the latter and expressed as following equation.

$$\lambda = 637.9 - 16.8\Delta L + 0.51\Delta L^2 \quad (2)$$

This result suggests that elastic colloidal crystal can be applied to tension sensor by elongation.

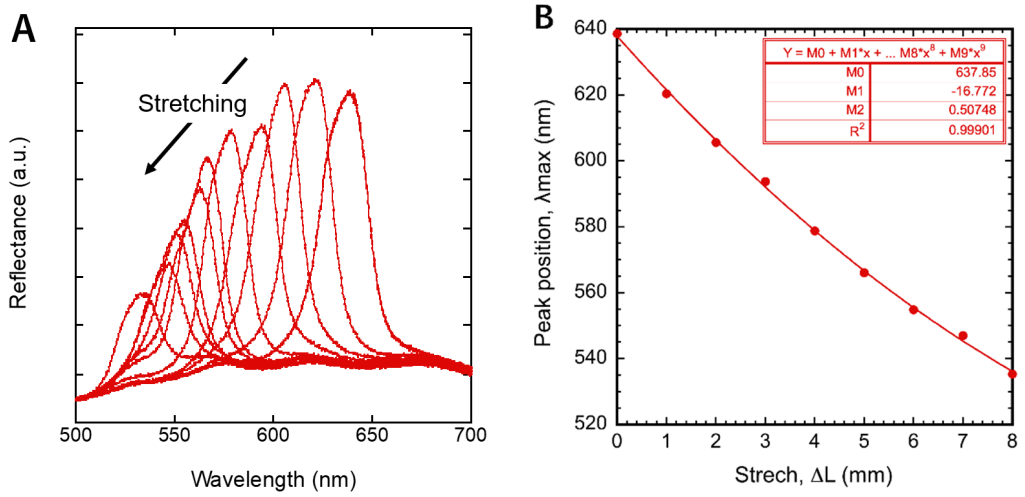

Figure 7. Analysis of structural color changes due to stretching using reflectance spectrometry. (**A**) Change in diffraction peak due to stretching, (**B**) relationship between peak wavelength and stretching length.

Next mechanical mode, we investigated structural color change by compressing deformation. A compression test on elastic colloidal crystals that had been punched out and molded into a disc shape using the equipment and setup described in Supplementary Figure S5. The concept idea of measurement is shown in illustration of Figure S5A. The sensing part of the probe is contacting to the surface of the top table of weigh meter photograph shown in the photo B. The diameter of the disk was 5.5 mm in diameter was mounted on the edge of probe shown in the photo C. The pressure applied to the disk sample came from compressing by vertical moving one dimensional precision stage and as measured by the weight meter. Figure 8 shows change of Bragg's diffraction peaks by increasing pressure on the disk. By increasing pressure, the Bragg diffraction peak shifted to a lower wavelength and its intensity also decreased monotonically (Figure 8A). The relationship between the peak wavelength and pressure is shown in Figure 8B. When comparing the correlation of the two-order approximation fit better than the first-order (linear). In this experiment, the increase in area due to compression was not taken into account. This should affect the approximation of the correlation, but it is currently difficult to measure, so we used the following equation.

$$\lambda = 624.2 - 2.1P + 0.024P^2 \quad (3)$$

By calibrating with the weight scale for each disk, the probe system of colloidal crystal elastomer can be used as a tactile sensor.

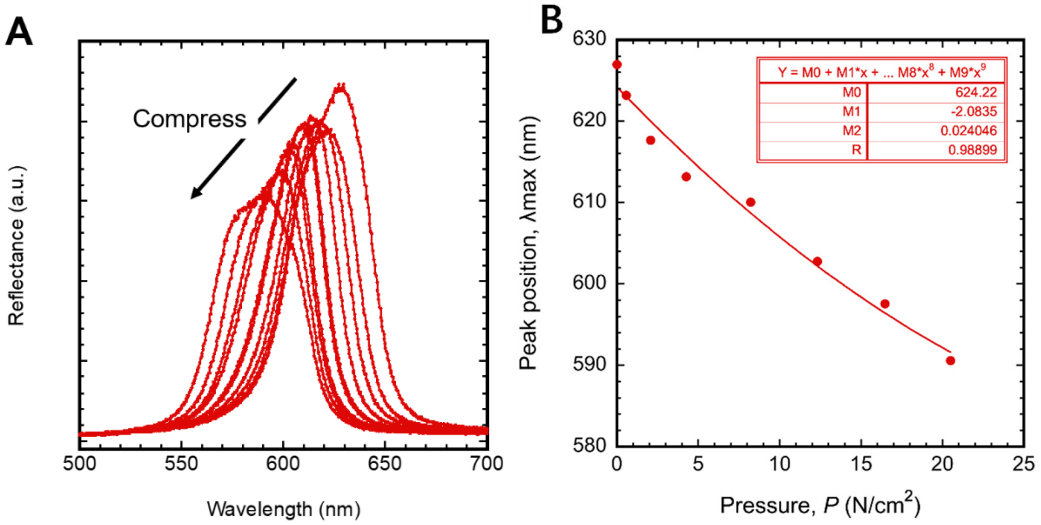

Figure 8. Analysis of structural color changes due to compression using reflectance spectrometry. (**A**) Change in diffraction peak due to compression, (**B**) relationship between peak wavelength and compression force.

Figure 9 shows a bending deformation mode. There are two types of bending, concave and convex, and they have different optical property. The concavity bending show in the photo A and the center indicates red color. In

contrast convexity bending show in the photo B and the center area indicates green color. To investigate the mechanical deformation on both bending, to compare Bragg's diffraction peak shifts shown in Figure 9D,E. In addition, the bending quantity was evaluated by deflection, d as shown in the photo C. As increasing deflection d, Bragg's diffraction peak shift to long wavelength in concavity bending. In contrast, Bragg's diffraction peak shift to short wavelength in convexity bending. The relationship deflection and peak position for both bending modes are shown in Figure 9F. A linear relationship is expressed as following equation.

$$\lambda = 616.4 - 28.28d \quad (4)$$

More detailed information on the mechanism of structural color changes in the two modes were investigated in Supplementary Figure S6. Photographs A, B, and C correspond to concave, flat, and convex curvature, respectively. The flat silica colloidal crystal elastomer shows a uniform red structural color for all area, and its cross-sectional view image is shown in Figure S6E. The elastic colloidal crystal sheet is composed of a 1 mm thick colloidal crystal sheet and a 1 mm thick black rubber sheet. The neutral axis of the bending deformation is the junction layer of the two parts. The plane spacing affects the compression and tension caused by bending. This is mainly the central region of the rubber sheet. In addition, the inclination angle of the plane also affects the structural color change caused by bending deformation. As shown in Figure S6D, the concave center part is subjected to compressive strain. As a result, the center part shows a deeply red color, and the two sides indicated by the white arrows show green and yellow. The color change on both sides is due to the sample tilting due to the concave bending deformation. As shown in Figure S6F, the convex central part is subjected to tensile strain. As a result, the colloidal crystal plane is compressed and the central part changes color to green. On the photo C, both side of the center area also may influence of tilting angle. However, it is not clear structural color change compare with the photo A. The phenomenon of peak shift due to bending deformation shift to longer or shorter wavelength has potential applications in bending sensors. However, bending deformation is dependent on the depth of the sample and produce tilting effect, it is complicated to be applied to sensor applications. Next, we investigated at the characteristics of long period stretching, and impacting phenomena as characteristics related to practical needs.

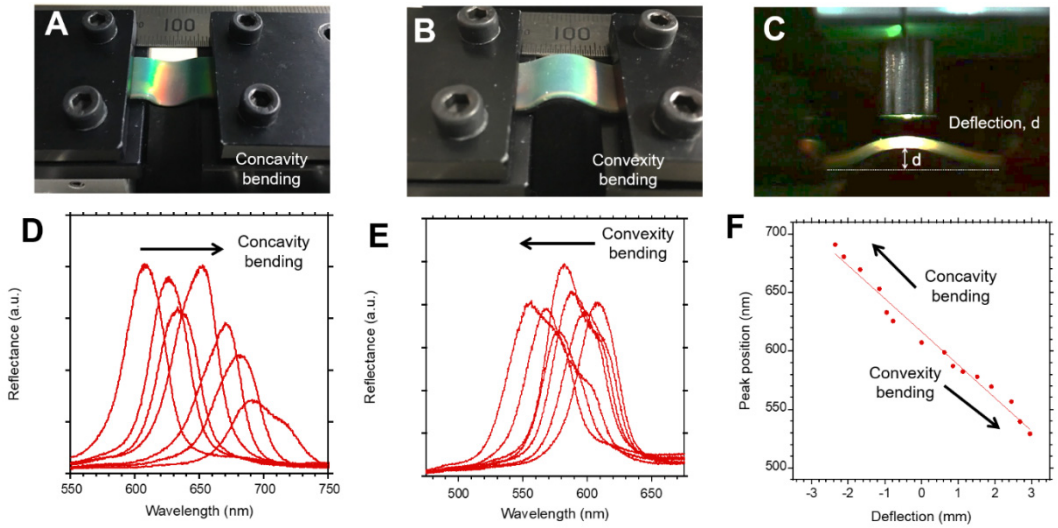

Figure 9. Analysis of structural color changes due to bending in convexity and concavity deformation. (**A**) concavity bending, (**B**) concvexity bending, (**C**) cross section image of the concvexity bending, (**D**) change in diffraction peak due to concavity bending, (**E**) change in diffraction peak due to concvexity bending and (**F**) a relationship deflection of bending and peak position.

4.4. Structural Color Material Properties for Practical Use

For structural color material properties for practical use, we will show two topics: Rapid structural color change by impaction and durability evaluation of repeatable elastic deformation. The former visualizes the change in the impact that the rubber sheet receives when a SUS steel ball falls as structural color. The video movies were shot in slow motion mode (240 frames per second, fps) using an iPhone camera. The details of the video shooting are shown in Supplementary Figure S7. An i-phone was set up below the position of the elastic colloidal crystal sheet. A steel ball was dropped and collided to the back rubber side and pressure was imaging bottom surface of the elastic colloidal crystal sheet. As a result, the structural color change enables to observe from downside. White LED backlighting (color temperature 5000 K) was applied to white diffused glass at an angle of approximately

45 degrees, and the reflected light was applied to the rubber sheet from below side. The pressure distribution image on the rubber sheet was acquired by the camera of the i-phone through the transparent acrylic plate. Figure S7B shows a series of each snap shot images at 240 fps mode. One frame (f) is equivalent to 1/240 of a second, or 0.004167 s. This is equivalent to 4.17 milliseconds. This means the 10th frame image is after 37.6 ms from the 1st frame. We can obtain high speed camera images with 4.17 ms resolution. The video movie can be available in Supplementary Video S2. Another movie was analyzed as shown in Figure 10. The position of the impact was first confirmed in the second frame. In the fifth frame, the color changes to a vivid green. In the seventh frame, the structural color of the second position changes due to the second collision of the rebounding steel ball. In the twentieth frame, the third position changes color. The structural color change caused by compression due to the collision can be visualized as a high-speed phenomenon with a minimum step of 4.17 ms or less. On the other hand, it takes some time for the elastically deformed area to return to its original shape, and the structural color change (from green to red) is slower than the collision. However, it recovered to its original structural color of red within one second. From these results, it is expected that by using a high-resolution high-speed camera, it will be possible to visualize collision phenomena of less than 1 mS as structural color changes, and by using the correlation with compression phenomena shown in Figure 8, it will be possible to analyze the change in stress distribution at high speeds. In this experiment, the slow-motion function of a commercially available general-purpose smartphone was utilized. The employment of a high-resolution high-speed camera will facilitate the capture of high-speed phenomena with enhanced precision, which is anticipated to be instrumental in elucidating collision phenomena.

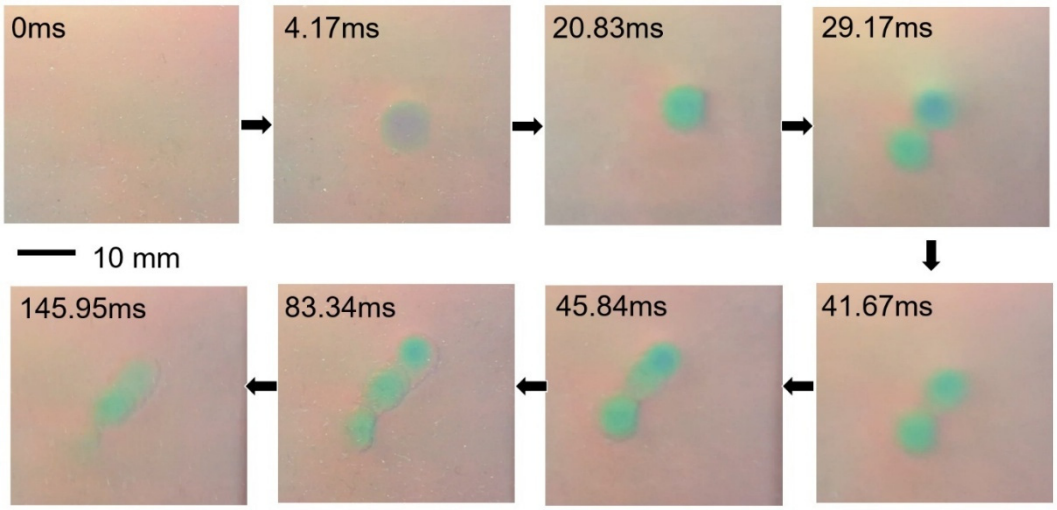

Figure 10. Rapid structural color change by impacting on a steal ball on an elastic colloidal crystal sheet shown in Figure 3A. The images were taken by 240 frames per second (fps) movie mode of iPhone camera. Eight snapshots corresponding to 0 ms to 145.95 ms, respectively.

One of issues on strain sensor issues to be addressed for practical application is the evaluation of durability against repeated elastic deformation. The desktop device (DMLHP-PP, Yuasa System Co., Ltd.) used in the evaluation test is shown in Figure S8. The photo A shows the appearance of the device. The rubber sheet was stretched in one direction by 15 mm at a rate of 15 times per minute (The video movie can be available in Supplementary Video S3). The photo B is a snapshot of the state before stretching, and the photo C is a snapshot of the state after stretching. The former shows a red structural color, and the latter shows a green structural color. As a durability test, we decided to check whether the structural color change function of the elastic colloidal crystal could be maintained after 10,000 or 100,000 cycles of stretching. The evaluation results are shown in Figure 11. The graph A shows the reflectance spectrum of the rubber sheet with initial state (sample length of 40 mm) and stretching (sample length of 50 mm) before durability test. The red line shows the structural color of initial state with a peak wavelength 600.0 nm. In contrast, stretched 10 mm from its unloaded state shows green structural color with a peak wavelength 560.5 nm. Figure 11B shows comparison three state conditions. It was confirmed that the structural color changes with elastic deformation and that this function is maintained even after 100,000 cycle tests. There is no change or damage after durability test. Although there is a little variation in the peak wavelength due to differences in the measurement points, we can conclude that the durability of the material is not a problem.

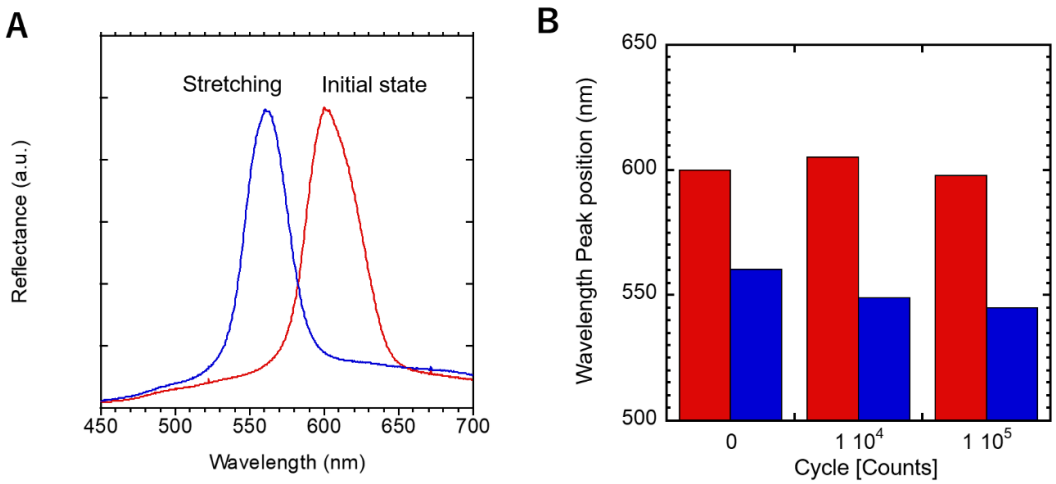

Figure 11. Evaluation of durability by repeated stretching. (**A**) comparing the initial state (length of sample: 40 mm) and after stretched (50 mm), (**B**) Comparison of peak wavelengths after repeated stretching of the sample. Red bar (no stretching) and blue bar (under stretched) after 0, 10,000 and 100,000 cycles elastic deformation.

5. Conclusions

By embedding non-close packed colloidal crystals of silica colloidal particles in polyacrylate elastomer, we fabricate smart material sheet whose structural color changes with elastic deformation.

The formation of this colloidal crystal elasticity was achieved by aligning the silica particle orientation planes through desalination and shear stress using ion exchange resin. In addition, the monomer 4-HBA was polymerized through UV irradiation radical polymerization. The lattice constant of the initial colloidal crystal depended on the particle concentration, and by adjusting it to 20 wt%, the structural color of the colloidal crystal was designed to be red. This elastic sheet was made from 1 mm thick 4-HBA polyacrylate with 150 nm silica particles oriented in one direction at distance of 225 nm between the surfaces. By attaching it to a 1 mm thick black rubber sheet, it becomes a rubber sheet that reversibly changes color with deformation, with a vivid structural color.

In this paper, we investigated three basic mechanical deformation modes (stretching, compression, and bending) as well as impact and durability. In stretching and compression, the peak wavelength of the Bragg diffraction that causes structural color was found to be simple correlated with the amount of stretching, compression stress, and bending (displacement). On bending is two type mode of deformation, concavity and convexity. On concavity bending deformation, peak shift to shorter wavelength. In contrast, concavity deformation, the peak shift to longer wavelength. Bending is also corresponding a simple relationship between peak position and deflection. These three modes suggest that mechanical deformation is applied to smart sensing. In finally, using a high-speed camera, rapid strain changes images on 5 ms order were obtained in the impacting test. The imaging function the strain mapping enables wide applications from sport to industry. Finally, the durability test for elongation suggests that practically application use. 100,000 cycle stretching the rubber has kept the tunable structural color function.

Supplementary Materials: The supporting information can be downloaded at: https://media.sciltp.com/articles/others/2505151015568327/MI-Supplement.zip.

Author Contributions: T.S.: conceptualization, methodology, preparation writing—reviewing and editing; H.F.: data curation, writing—original draft; S.K.: Synthesis silica and prepolymer suspension, investigation; F.U.: Synthesis silica and prepolymer suspension, its supervision. All authors have read and agreed to the published version of the manuscript.

Funding: This research was funded by JSPS KAKENHI Grant Number JP2135017.

Data Availability Statement: The data presented in this study are available upon request from the corresponding author.

Acknowledgments: We thank for Chikako Tsuda and Kaori Terui for their experimental works. Chikako measured photonic functional property and photo pictures. Kaori prepared silica suspensions dispersed in 4-HBA monomer liquid.

Conflicts of Interest: The authors declare no conflict of interest.

References

1. Clough, J.M.; Weder, C.; Schrettl, S. Mechanochromism in structurally colored polymeric materials. *Macromol. Rapid Commun.* **2021**, *42*, 2000528.
2. Xie, M.; Hisano, K.; Zhu, M.; Toyoshi, T.; Pan, M.; Okada, S.; Tsutsumi, O.; Kawamura, S.; Bowen, C. Flexible multifunctional sensors for wearable and robotic applications, *Adv. Mater. Techn.* **2019**, *4*, 1800626.
3. Sandt, J.D.; Moudio, M.; Clark, J.K.; Hardin, J.; Argenti, C.; Carty, M.; Lewis, J.A.; Kolle, M. Stretchable optomechanical fiber sensors for pressure determination in compressive medical textiles, *Adv. Healthcare Mater*. **2018**, *7*, 1800293.
4. Kolle, M.; Zheng, B.; Gibbons, N.; Baumberg, J.J.; Steiner, U. Stretch-tuneable dielectric mirrors and optical microcavities. *Opt. Express* **2010**, *18*, 4356–4364.
5. Chan, E.P.; Walish, J.J.; Thomas, E.L.; Stafford, C.M. Block copolymer photonic gel for mechanochromic sensing, *Adv. Mater.* **2011**, *23*, 4702–4706.
6. Park, T.H.; Yu, S.; Cho, S.H.; Kang, H.S.; Kim, Y.; Kim, M.J.; Eoh, H.; Park, C.; Jeong, B.; Lee, S.W.; et al. Block copolymer structural color strain sensor. *NPG Asia Mater.* **2018**, *10*, 328–339.
7. de Castro, L.D.C.; Engels, T.A.P.; Oliveira, O.N., Jr.; Schenning, A.P.H.J. Sticky multicolor mechanochromic labels. *ACS Appl. Mater. Interfaces* **2024**, *16*, 11, 14144–14151.
8. Li, M.; Lyu, Q.; Peng, B.; Chen, X.; Zhang, L.; Zhu, J. Bioinspired colloidal photonic composites: Fabrications and emerging applications. *Adv. Mater.* **2022**, *34*, 2110488.
9. Fudouzi, H.; Sawada, T.; Photonic rubber sheets with tunable color by elastic deformation. *Langmuir* **2006**, *22*, 1365–1368.
10. Arsenault, A.C.; Clark, T.J.; von Freymann, G.; Cademartiri, L.; Sapienza, R.; Bertolotti, J.; Vekris, E.; Wong, S.; Kitaev, V.; Manners, I.; et al. From colour fingerprinting to the control of photoluminescence in elastic photonic crystals. *Nat. Mater.* **2006**, *5*, 179–184.
11. Finlayson, C.E.; Goddard, C.; Papachristodoulou, E.; Snoswell, D.R.E.; Kontogeorgos, A.; Spahn, P.; Hellmann, G.P.; Hess, O.; Baumberg, J.J. Ordering in stretch-tunable polymeric opal fibers. *Opt. Express* **2011**, *19*, 3144–3154.
12. Liang, H.L.; Bay, M.M.; Vadrucci, R.; Barty-King, C.H.; Peng, J.; Baumberg, J.J.; De Volder, M. F. L.; Vignolini, S.; Roll-to-roll fabrication of touch-responsive cellulose photonic laminates. *Nat. Commun*. **2018**, *9*, 4632.
13. Zhao, Q.; Finlayson, C.; Snoswell, D.; Haines, A.; Schäfer, C.; Spahn, P.; Hellmann, G.P.; Petukhov, A.V.; Herrmann, L.; Burdet, P.; et al. Large-scale ordering of nanoparticles using viscoelastic shear processing. *Nat. Commun.* **2016**, *7*, 11661.
14. Kamenetzky, E.A.; Magliocco, L.G.; Panzer, H.P.; Structure of solidified colloidal array laser filters studied by cryogenic transmission electron microscopy. *Science* **1994**, *263*, 207–210.
15. Lee, G.H.; Choi, T.M.; Kim, B.; Han, S.H.; Lee, J.M.; Kim, S.-H. Chameleon-inspired mechanochromic photonic films composed of non-close-packed colloidal arrays. *ACS Nano* **2017**, *11*, 11350–11357.
16. Miwa, E.; Watanabe, K.; Asai, F.; Seki, T.; Urayama, K.; Odent, J.; Raquez, J.M.; Takeoka, Y.; Composite elastomer exhibiting a stress-dependent color change and high toughness prepared by self-assembly of silica particles in a polymer network. *ACS Appl. Polym. Mater.* **2020**, *2*, 4078.
17. Inci, E.; Topcu, G.; Demir, M.M. Colloidal films of SiO_2 in elastomeric polyacrylates by photopolymerization: A strain sensor application. *Sens. Actuators B* **2020**, *305*, 127452.
18. Kanai, T.; Sawada, T.; Toyotama, A.; Kitamura, K. Air-pulse-drive fabrication of photonic crystal films of colloids with high spectral quality. *Adv. Funct. Mater.* **2005**, *15*, 25–29.
19. Tajima, H.; Amano, A.; Kanai, T. Elastomer-immobilized tunable colloidal photonic crystal films with high optical qualities and high maximum strain. *Mater. Adv.* **2021**, *2*, 3294–3299.
20. An, T.; Jiang, X.; Gao, F.; Schäfer, C.; Qiu, J.; Shi, N.; Song, X.; Zhang, M.; Finlayson, C.E.; Zheng, X.; et al. Strain to shine: Stretching-induced three-dimensional symmetries in nanoparticle-assembled photonic crystals. *Nat. Commun.* **2024**, *15*, 5215.
21. Miyake, D.; He, J.; Asai, F.; Hara, M.; Seki, T.; Nishimura, S.; Tanaka, M.; Takeoka, Y. Optically Transparent and Color-Stable Elastomer with Structural Coloration under Elongation. *Langmuir* **2023**, *39*, 17844–17852.
22. Peng, L.; Hou, L.; Wu, P. Synergetic Lithium and Hydrogen Bonds Endow Liquid-Free Photonic Ionic Elastomer with Mechanical Robustness and Electrical/Optical Dual-Output. *Adv. Mater.* **2023**, *35*, 2211342.
23. Li, X.; Cheng, Y.; Zhou, Y.; Shi, L.; Sun, J.; Ho, G.W.; Wang, R. Programmable Robotic Shape Shifting and Color Morphing Dynamics Through Magneto-Mechano-Chromic Coupling. *Adv. Mater.* **2024**, *36*, 2406714.
24. Fudouzi, H.; Sawada, T. Colloidal photonic crystals made of soft materials: Gels and elastomers. In *Micro and Nanophotonic Technologies*, 1st ed.; Meyrueis, P., Van de Voorde, P.M., Sakoda, K., Eds.; Wiley-VCH: Weinheim, Germany, 2017; pp. 507–526.
25. Ackerson, B.J.; Pusey, P.N. Shear-induced order in suspensions of hard spheres. *Phys. Rev. Lett*. **1988**, *61*, 1033.

26. Kawanaka, S.; Uchida, F.; Sawada, T.; Furumi, S.; Fudoji, H. *Sheet of Colloidal Crystals Immobilized in Resin, Method for Displaying Structural Color Using Same, Method for Detecting Unevenness Distribution or Hardness Distribution of Subject Using Same, and Structural Color Sheet*; International Application Publication: Tokyo, Japan, 2015; 86p.
27. Fudouzi, H. Fabricating high-quality opal films with uniform structure over a large area. *J. Colloid. Interface Sci.* **2004**, *275*, 277–283.

Article

Sn-TiO_2/PTA Nanocomposite Films for High-Contrast Rewritable Media with Visible-Light-Driven Black Coloration

Yao Dou, Dongliang Wei, Yongli Qin, Zhen Zhang, Yun Zhang *, and Wenshou Wang *

School of Chemistry and Chemical Engineering, University of Jinan, Jinan 250022, China
* Correspondence: chm_zhangy2022@ujn.edu.cn (Y.Z.); chm_wangws@ujn.edu.cn (W.W.)
Received: 19 March 2025; Revised: 21 April 2025; Accepted: 23 April 2025; Published: 15 May 2025

Abstract: Photochromic materials are pivotal for rewritable smart media, yet conventional systems suffer from sluggish kinetics, UV dependency, and low optical contrast. Herein, we present a visible-light-responsive Sn-TiO_2/phosphotungstic acid (PTA) nanocomposite film mediated by polyvinylpyrrolidone (PVP) that addresses these challenges through interfacial engineering and bandgap modulation. Sn-doped TiO_2 nanoparticles, synthesized hydrothermally, are covalently linked to phosphotungstic acid (PTA) clusters via PVP-assisted dispersion, enabling efficient charge separation under 450 nm illumination. The Sn-TiO_2/PTA/PVP nanocomposite film achieves ultrafast coloration within 10 s, attributed to the reduction of W^{6+} to W^{5+} in PTA. The colored state exhibits remarkable air stability (48 h) and rapid recovery (<30 min) via H_2O_2 vapor, sustaining >80 reversible cycles without degradation. With a narrowed bandgap (2.23 eV) and broadband intervalence charge transfer (IVCT) absorption (600–800 nm), the film demonstrates high-contrast black-state coloration and 2-day legibility as a rewritable medium. This work overcomes the limitations of organic dyes and UV-dependent systems, offering an inorganic, eco-friendly platform for smart displays, anti-counterfeiting labels, and energy-efficient photochromic technologies.

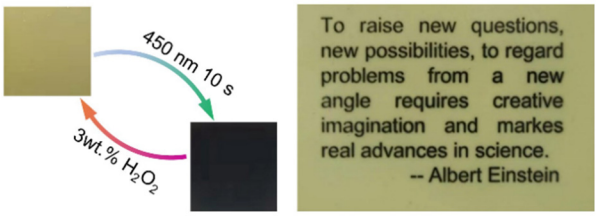

Keywords: photochromic nanocomposites; visible-light response; Sn-doped titanium dioxide; phosphotungstic acid; rewritable smart media

1. Introduction

Photochromic materials, capable of reversible color changes under external stimuli, have emerged as critical components in smart windows [1−5], rewritable media [6−12], and anti-counterfeiting systems [13−18]. Among inorganic photochromic candidates, transition metal oxides (e.g., WO_3, MoO_3, TiO_2) and polyoxometalates (POMs) dominate due to their thermal stability, environmental robustness, and tunable redox properties [19−25]. However, conventional systems face intrinsic limitations: (i) narrow visible-light absorption (typically <450 nm) due to wide bandgaps [26−28], (ii) sluggish coloration/bleaching kinetics caused by inefficient charge separation [29], and (iii) low optical contrast due to their characteristic blue/gray coloration, which reduces readability under ambient lighting [30]. For instance, Zhang et al. [31] reported UV-driven TiO_2/PMoA rewritable paper with a 70-cycle lifespan, yet its reliance on UV light and blue-phase coloration pose safety concerns and visual limitations, such as poor legibility under white-light illumination. These unresolved challenges underscore the need for material systems that simultaneously achieve visible-light activation, rapid switching kinetics, and high-contrast optical states.

Recent advancements focus on enhancing light absorption and charge transfer efficiency through nanostructuring [32,33], heterojunction engineering [34−36], and doping strategies [5,37,38]. Sn-doped TiO_2 (Sn-TiO_2), for example, demonstrates extended visible-light response (up to 450 nm) by introducing intermediate energy levels via Sn^{4+}substitution, which introduces intermediate energy levels to narrow the bandgap [39]. Concurrently, phosphotungstic acid (PTA, $H_3PW_{12}O_{40}$), a Keggin-type POM, exhibits reversible redox activity and structural integrity during coloration [29,40,41]. Xiong et al. [42] developed PTA-polyurethane films with UV-triggered photochromism, yet their reliance on UV light and slow recovery (>5 h) limit scalability. Hybrid systems combining Sn-TiO_2 with organic dyes (e.g., neutral red) partially address visible-light activation [39], but

organic components degrade rapidly under prolonged irradiation and fail to achieve black-state coloration due to narrow absorption bands. Despite these efforts, achieving inorganic composites with integrated fast color switching, black-state optical contrast, and visible-light-driven photochromism remains a formidable challenge.

A critical yet underexplored aspect lies in achieving a high contrast black-state through tailored IVCT absorption. While reduced POMs typically exhibit broad absorption in the near-infrared region (600–800 nm) [43−45], their integration with visible-light-active semiconductors could enable intense black coloration by spanning the entire visible spectrum. However, this requires precise interfacial engineering to maximize electron transfer efficiency and minimize parasitic absorption losses. Recent studies on polyvinyl alcohol-polyethyleneimine-PTA (PVA-PEI-PTA) composites achieved grey mauve [41], but their limited IVCT bandwidth and insufficient electron density prevented true black-state formation. Thus, designing a material system that synergizes visible-light absorption, efficient charge transfer, and broadband IVCT transitions is essential for high-contrast photochromic applications.

In this work, we propose a PVP-mediated Sn-TiO_2/PTA nanocomposite film that synergizes visible-light absorption, efficient charge transfer, and black-state optical contrast. By employing PVP as both a dispersant and interfacial stabilizer, Sn-TiO_2 nanoparticles and PTA clusters are uniformly integrated, enabling enhanced charge separation while suppressing recombination. This architecture enables dual functionality: (i) Sn^{4+} doping narrows the TiO_2 bandgap to 2.23 eV, extending absorption to 450 nm, and (ii) PTA acts as an electron acceptor, triggering broadband IVCT transitions between W^{5+} and W^{6+} species upon reduction. The optimized nanocomposite film achieves ultrafast coloration (10 s) under 450 nm illumination, sustains >80 reversible cycles via H_2O_2 vapor treatment, and delivers intense black coloration through synergistic visible-light absorption and IVCT transitions. As a rewritable medium, the film enables high-resolution patterning with 2-day legibility, surpassing the performance of organic dye-based and UV-dependent systems. This work establishes a sustainable, inorganic platform for smart displays and energy-efficient photochromic technologies, addressing the long-standing trade-offs between speed, contrast, and stability.

2. Experimental Part

2.1. Materials and Methods

2.1.1. Materials

Titanium (IV) ethoxide ($Ti(OC_2H_5)_4$, 33–35%) was purchased from Macklin Biochemical Co. Ltd., (Shanghai, China) Ethylene glycol (EG, 99.0%), tin (II) chloride dihydrate ($SnCl_2·2H_2O$, 98.0%), polyvinylpyrrolidone (PVP, K30), and phosphotungstic acid (PTA, $H_3PW_{12}O_{40}·21H_2O$, 99.9%) were purchased from Sinopharm Chemical Reagent Co. Ltd. (Shanghai, China). Hydrazine hydrate ($N_2H_4·H_2O$, 80%) were purchased from Tianjin Damao Chemical Reagent Factory, (Tianjin, China). Glass substrates (2.5 × 2.5 cm^2) were purchased from Luoyang Nuozhuo Technology Co. Ltd. (Luoyang, China). All chemicals were analytic grade and used without any further purification during the synthesis.

2.1.2. Synthesis of Sn-TiO_2 Nanoparticles

Sn-TiO_2 nanoparticles were synthesized via a hydrothermal method. In a typical procedure, $SnCl_2·2H_2O$ (0.216 g, 0.96 mmol) was dissolved in EG (33 mL) under magnetic stirring (500 rpm, 30 min). $Ti(OC_2H_5)_4$ (1 mL) was added dropwise to the solution, followed by $N_2H_4·H_2O$ (2 mL, 80%) under continuous stirring (30 min). The mixture was transferred into a 50 mL Teflon-lined autoclave (Shanghai Yanzheng Experimental Equipment Co., Ltd., Shanghai, China) and heated at 200 ℃ for 36 h. Light yellow precipitates were obtained by centrifugation, washed 3 times with acetone, and then dried overnight at 60 ℃.

2.1.3. Fabrication of Sn-TiO_2/PTA/PVP Nanocomposite Films

A precisely measured quantity of 14.4 mg Sn-TiO_2 nanoparticles was dispersed in a mixed solvent system containing 100 mg of 20 wt.% PVP aqueous solution, 0.6 mL EG, and 103 mg of PTA solution (5.76 g/mL). The resultant suspension underwent magnetic stirring to ensure uniform colloidal distribution. The optimized coating formulation was then deposited on pre-cleaned glass substrates (2.5 cm × 2.5 cm) followed by drying at 60 °C for 6 h to obtain the typical Sn-TiO_2/PTA/PVP nanocomposite films with Sn-TiO_2:PTA molar ratio of 5:1. Films with varying Sn-TiO_2:PTA molar ratios (3:1, 7:1) were prepared by adjusting precursor quantities. Three independent batches were fabricated for each ratio to ensure reproducibility.

2.1.4. Characterizations

The X-ray powder diffraction (XRD) patterns of the products were performed on a Rigaku SmartLab diffractometer with Cu Kα radiation (λ = 1.54178 Å). Scanning electron microscope (SEM) images were performed on a Hitachi SU8010 microscope. Transmission electron microscopy (TEM) images and elemental mapping results were obtained on Hitachi-7700 and FEI Tecnai G2 F20 microscopes. X-ray photoelectron spectroscopy (XPS) measurement was measured on an Imaging Photoelectron Spectrometer (Escalab 250Xi, Thermo Scientific, Waltham, MA, USA) with a monochromatic Al Ka X-ray source. The Fourier transform infrared (FTIR) spectra were conducted on a Bruker Alpha spectrometer in the range of 500–4000 cm^{-1}. UV-vis absorption spectra were measured using a UV–vis spectrophotometer (UV-2600, Shimadzu Co., Tokyo, Japan) equipped with an integrating sphere unit (ISR-2600, Shimadzu Co., Tokyo, Japan). The Raman spectra were recorded on a micro-Raman LabRAM HR800 spectrometer (Horiba Jobin Yvon Ltd., Tokyo, Japan) with a 633 nm laser. Electron spin resonance (ESR) spectrum was measured with a bruker ESR5000 spectrometer at X-band at 77 K. All photochromic tests were conducted under ambient conditions (temperature: 25 ± 2 °C; relative humidity: 50 ± 5%; atmospheric oxygen content: ~21%). The digital photographs were obtained by a cellphone.

2.2. Results and Discussion

2.2.1. Synthesis and Structural Characterization of Sn-TiO_2/PTA/PVP Nanocomposite Films

The Sn-TiO_2/PTA/PVP nanocomposite films were synthesized through a hierarchical strategy combining hydrothermal synthesis of Sn-TiO_2 nanoparticles and their subsequent integration with PTA clusters via PVP-mediated interfacial engineering. The structural evolution and chemical interactions within the nanocomposite were systematically investigated using XRD, TEM, FT-IR, XPS, and UV-vis spectroscopy.

The crystalline structure of the synthesized components was first evaluated via XRD. As shown in Figure 1a, pristine Sn-TiO_2 nanoparticles exhibited distinct diffraction peaks at 27.4°, 36.1°, and 54.3°, corresponding to the (100), (101), and (211) planes of the rutile TiO_2 phase (JCPDS No. 21-1276) [38]. Notably, the absence of SnO_2-specific peaks (e.g., ~26.5° and ~33.8°) confirmed that Sn^{4+} ions were substitutionally doped into the TiO_2 lattice rather than forming segregated SnO_2 phases [46,47]. This substitutional doping is critical for narrowing the bandgap and enhancing visible-light absorption, as later evidenced by UV-vis analysis. In contrast, the XRD pattern of pristine PTA clusters ($H_3PW_{12}O_{40}$) displayed sharp peaks at 10.2°, 25.6°, and 34.8°, characteristic of the Keggin-type structure (JCPDS No. 50-0655) [48,49]. The XRD peak broadening observed in the Sn-TiO_2/PTA/PVP nanocomposite film is attributed to the dual functionality of PVP as both a steric stabilizer and a hydrogen-bonding mediator. The pyrrolidone groups within PVP coordinate with Sn-TiO_2 and PTA, disrupting long-range crystallinity and simultaneously enhancing interfacial charge transfer. This observation is supported by FT-IR and XPS data (discussed below), which demonstrate weakened intra-component vibrations (Figure 1g) and electron redistribution (Figure 2a–d).

TEM and SEM images provided insights into the morphology and elemental distribution of the Sn-TiO_2/PTA/PVP nanocomposite film. The TEM image (Figure 1b) revealed that the Sn-TiO_2 nanoparticles exhibited an average size of approximately 5 nm. Figure 1c illustrates the uniform dispersion of Sn-TiO_2 nanoparticles and PTA clusters within the PVP matrix. A digital image (Figure 1d) showed the Sn-TiO_2/PTA/PVP nanocomposite film to be transparent with a yellowish-green color, and the UV-vis transmittance spectrum (Figure S1) indicated a transmittance of approximately 80%. Furthermore, a cross-sectional optical microscope image (Figure 1e) confirmed a film thickness of ~270 μm, while low-magnification SEM (Figure 1f) highlighted a smooth surface morphology with minimal porosity. This dense structure is critical for minimizing oxidative degradation during photochromic cycling by impeding oxygen diffusion into the interior of film. The corresponding elemental mapping (Figure 1f) demonstrated uniform distribution of Sn, Ti, W, P, and N (from PVP) across the nanocomposite film, confirming the absence of agglomeration. The homogeneous elemental distribution underscores the effectiveness of PVP as both a dispersant and interfacial linker, ensuring optimal charge transport pathways [50]. The dual functionality of PVP originates from its pyrrolidone ring, where the carbonyl oxygen (C=O) acts as both a hydrogen bond acceptor and a coordination site. The C=O group forms hydrogen bonds with hydroxylated Sn-TiO_2 surfaces and oxygen-rich PTA clusters, as evidenced by FT-IR peak broadening observed at 1665 cm^{-1} (Figure 1g). Furthermore, coordination between C=O and Ti^{4+}/Sn^{4+} stabilizes Sn-TiO_2 nanoparticles, while electrostatic interactions with PTA anions ensure their uniform dispersion, as depicted in Figure 1f. Complementing these interactions, the hydrophobic polymer backbone provides steric hindrance, effectively preventing agglomeration (Figure 1c). These mechanisms work synergistically to enhance interfacial charge transfer without compromising the structural integrity of the composite.

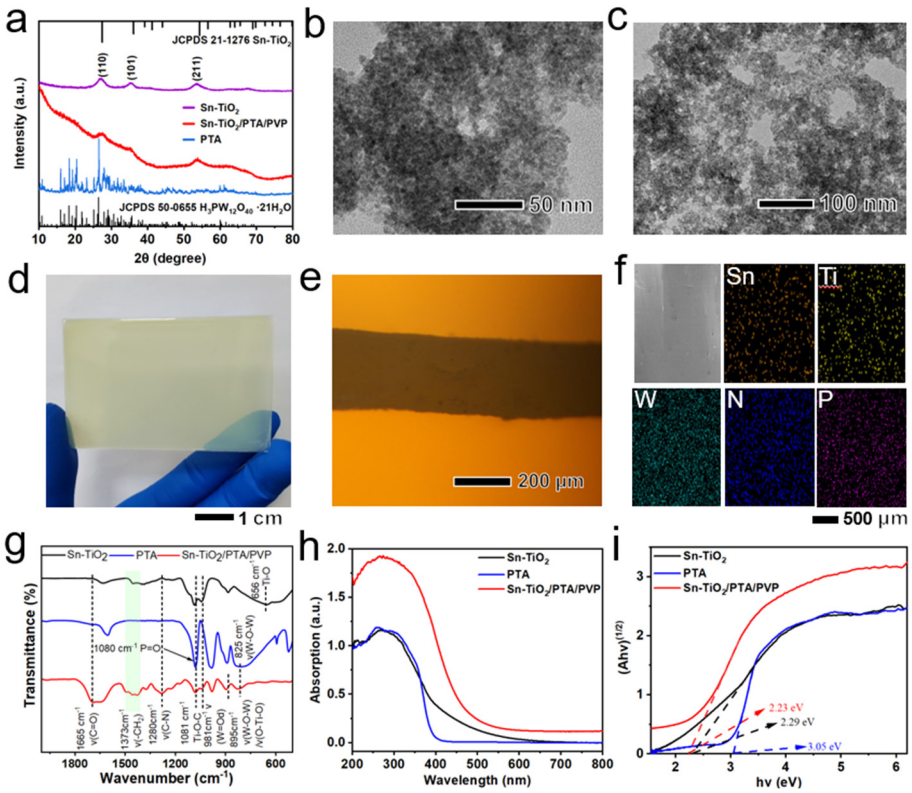

Figure 1. (**a**) XRD patterns of Sn-TiO_2, PTA, and the typical Sn-TiO_2/PTA/PVP nanocomposite film. (**b**,**c**) TEM images of Sn-TiO_2 nanoparticles and the typical Sn-TiO_2/PTA/PVP nanocomposite film. (**d**) Photograph of the typical Sn-TiO_2/PTA/PVP nanocomposite film. (**e**) Optical microscope image of the typical Sn-TiO_2/PTA/PVP nanocomposite film from cross-sectional view. (**f**) SEM images and corresponding elemental mapping of Sn, Ti, W, N, and P of the typical Sn-TiO_2/PTA/PVP nanocomposite film. (**g**–**i**) FT-IR spectra, UV–vis diffuse absorption spectra and the corresponding Tauc ($(Ahv)^{1/2}$ versus hv) plots of Sn-TiO_2, PTA, and the typical Sn-TiO_2/PTA/PVP nanocomposite film, respectively.

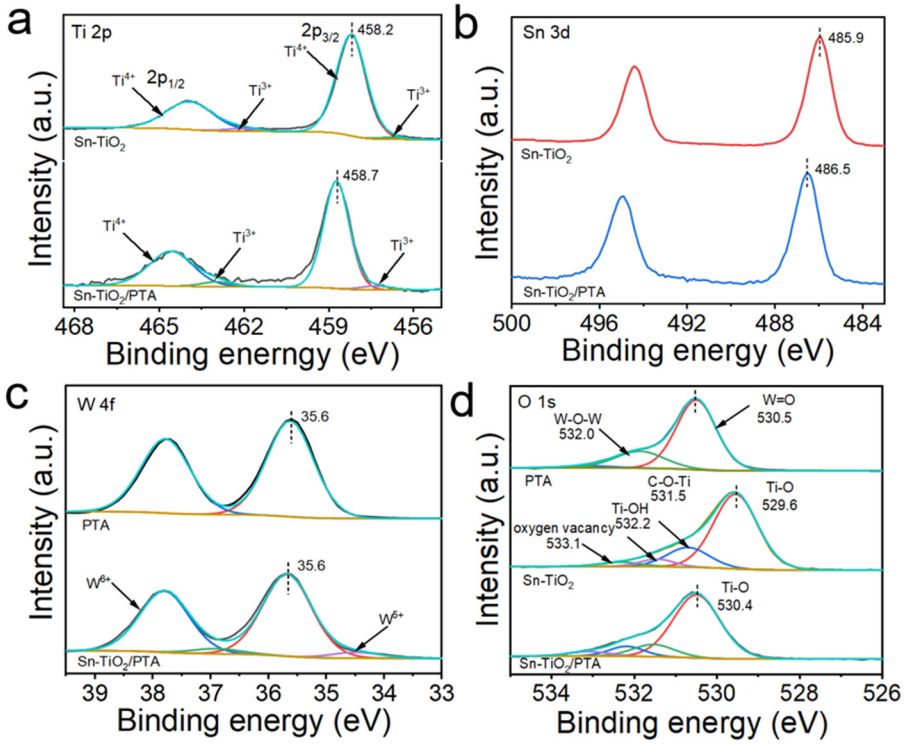

Figure 2. High-resolution XPS spectra of Ti 2p (**a**), Sn 2p (**b**), W 4f (**c**) and O 1s (**d**) of Sn-TiO_2 nanoparticles, PTA, and Sn-TiO_2/PTA nanocomposite.

Figure 1g shows the FT-IR spectra of Sn-TiO_2, PTA, and the typical Sn-TiO_2/PTA/PVP nanocomposite film (Figures 1g and S2). The peaks at 3605–3412 cm^{-1} belong to the stretching vibration of O-H bond on the surface of Sn-TiO_2, PTA, and the typical Sn-TiO_2/PTA/PVP nanocomposite. The characteristic peaks at 2856–2928, 1665, 1373, 1280, 1080, 981, 825 and 656 cm^{-1} arise from the stretching vibration of -CH_2 group, stretching vibration of C=O, wagging vibration of CH_2 group, stretching vibration of the C−N bond, stretching vibration of C-O-Ti or P=O, vibration of W=O, bending vibration of W-O-W, and Ti-O, respectively [39,51,52]. The FT-IR spectra of Sn-TiO_2/PTA/PVP nanocomposite film showed diminished intensity in W–O–W and Ti–O–Ti vibrations (740–525 cm^{-1}), indicative of robust interfacial interactions that suppress nanoparticle aggregation [53,54]. UV-vis diffuse reflectance spectroscopy and Tauc plots (Figure 1h,i) elucidated the optical absorption characteristics and bandgap modulation induced by Sn doping and PVP-mediated integration. The Sn-TiO_2/PTA/PVP nanocomposite exhibited a narrowed bandgap of 2.23 eV, as calculated using Kubelka-Munk function, compared to pristine Sn-TiO_2 (2.29 eV) and PTA (3.05 eV) [55]. Similar bandgap narrowing has been reported for Sn-TiO_2 systems, where Sn^{4+} substitution creates defect states that extend visible-light absorption [39]. The broad absorption of the Sn-TiO_2/PTA/PVP nanocomposite film in the 600–800 nm range (Figure 1h) is attributed to IVCT transitions between W^{5+} and W^{6+} species within the reduced PTA clusters. This IVCT absorption is critical for achieving high-contrast black coloration, as it spans a significant portion of the visible spectrum [56−59]. In contrast, conventional WO_3-based systems exhibit narrower IVCT bands (~600–700 nm), resulting in grayish color [60]. The synergistic effect between the visible-light absorption of Sn-TiO_2 and the broadband IVCT transitions of PTA enables the nanocomposite to achieve enhanced optical contrast.

Due to the shielding effect of the PVP polymer matrix on XPS signals from Sn-TiO_2 and PTA, direct characterization of the photochromic process was performed using Sn-TiO_2/PTA nanocomposites. The survey XPS spectrum (Figure S3) of the Sn-TiO_2/PTA nanocomposite revealed the presence of Ti, Sn, W, P, O, and C signals, originating from the Sn-TiO_2 nanoparticles and PTA components. High-resolution XPS analysis revealed critical insights into interfacial charge transfer dynamics. The Ti $2p_{3/2}$ core-level spectrum (Figure 2a) exhibited a binding energy shift from 458.2 eV (pristine Sn-TiO_2) to 458.7 eV in the nanocomposite, while the Sn $3d_{5/2}$ peak shifted from 485.9 eV to 486.5 eV (Figure 2b). These upward shifts indicate electron depletion at Ti and Sn sites, suggesting electron transfer from Sn-TiO_2 to adjacent species. Conversely, the O 1s peak shifted downward by 0.1 eV (from 530.5 eV in pristine PTA to 530.4 eV in the nanocomposite; Figure 2d), reflecting increased electron density on oxygen atoms, likely due to electron accumulation from Sn-TiO_2 [61,62]. Notably, the W 4f spectra remained unchanged, ruling out direct involvement of W redox states in the interfacial charge transfer process (Figure 2c). The directional electron flow aligns with the observed photochromic kinetics (discussed later), where Sn-TiO_2 acts as an electron donor under visible light, reducing PTA and triggering IVCT transitions. This mechanism is further corroborated by the stability of W 4f signals, which confirms that PTA maintains its structural integrity during charge transfer, serving as a robust electron acceptor. By excluding PVP, this analysis isolates the intrinsic interactions between Sn-TiO_2 and PTA, clarifying their synergistic roles in photochromic behavior.

2.2.2. Photochromic Performance of Sn-TiO_2/PTA/PVP Nanocomposite Films

The photochromic behavior of the Sn-TiO_2/PTA/PVP nanocomposite films was systematically evaluated under 450 nm illumination and H_2O_2 vapor treatment, with a focus on coloration kinetics, bleaching dynamics, cyclic stability, and component ratio effects. For the optimal Sn-TiO_2:PTA molar ratio (5:1), the film exhibited ultrafast coloration within 10 s (Figure 3a), achieving a maximum absorbance at 750 nm (Figure 3b). Illumination with 450 nm light resulted in a pronounced color change in the nanocomposite film, transitioning from an initial light yellow to a black color. This color change is indicative of efficient electron transfer from the Sn-TiO_2 nanoparticles to the PTA component (Figure 3a). Concurrently, the UV−vis diffuse reflectance spectra of the Sn-TiO_2/PTA/PVP nanocomposite film exhibited a time-dependent increase in absorption across the visible region (470–800 nm) upon exposure to 450 nm light for 10 s, with a characteristic absorption peak observed at 750 nm (Figure 3b). This absorption peak is attributed to IVCT transition between W^{5+} and W^{6+} species, providing direct evidence for the reduction of W^{6+} to W^{5+} within the nanocomposite film under 450 nm illumination [31]. The bleaching kinetics of the Sn-TiO_2/PTA/PVP nanocomposite film were initially investigated under ambient atmospheric conditions (Figure 3c). The UV−vis diffuse reflectance spectrum of the photoreduced (darkened) film revealed a gradual decrease in absorption intensity as a function of time, which is attributed to the slow reoxidation kinetics of W^{5+} back to W^{6+} by molecular oxygen present in the ambient air [61]. Beyond 50 h, no further decrease in the UV−vis diffuse reflectance intensity was observed, suggesting that oxygen diffusion from the surface to the interior of the film becomes diffusion-limited due to PVP's oxygen-blocking effect. The prolonged color retention of the photoreduced Sn-TiO_2/PTA/PVP nanocomposite film, lasting for more than 2 days, renders this system a

promising candidate for rewritable paper applications. In order to further manipulate and accelerate the bleaching process for potential applications, the nanocomposite film was subjected to treatment with H_2O_2 vapor. As depicted in Figure 3d, the UV−vis diffuse reflectance spectra of the photoreduced (darkened) film exhibited a gradual shift towards the reverse direction, with complete recovery to the initial state achieved within a period of 22 min upon exposure to H_2O_2 vapor (3 wt. %). This rapid bleaching is attributed to the efficient oxidation of W^{5+} back to W^{6+} within the Sn-TiO_2/PTA/PVP nanocomposite film, where H_2O_2 acts as an effective oxidizing agent [62]. The resulting H_2O_2-treated film demonstrated an enhanced bleaching rate (Figure 3e). The coloration and bleaching process, induced by illumination with 450 nm light and subsequent treatment with 3 wt.% H_2O_2 vapor, respectively, was repeated multiple times to investigate the reversibility and stability of the Sn-TiO_2/PTA/PVP nanocomposite film for potential applications (Figure 3f). The UV-Vis diffuse reflectance spectra were acquired, and the intensity at 750 nm was monitored to quantify the coloration and bleaching efficiency. The nanocomposite film demonstrated exceptional photochromic reversibility and repeatability, retaining over 95% of its initial absorbance after 80 cycles. The performance of the Sn-TiO_2/PTA/PVP nanocomposite film surpasses that of many existing photochromic systems, as detailed in Table S1.

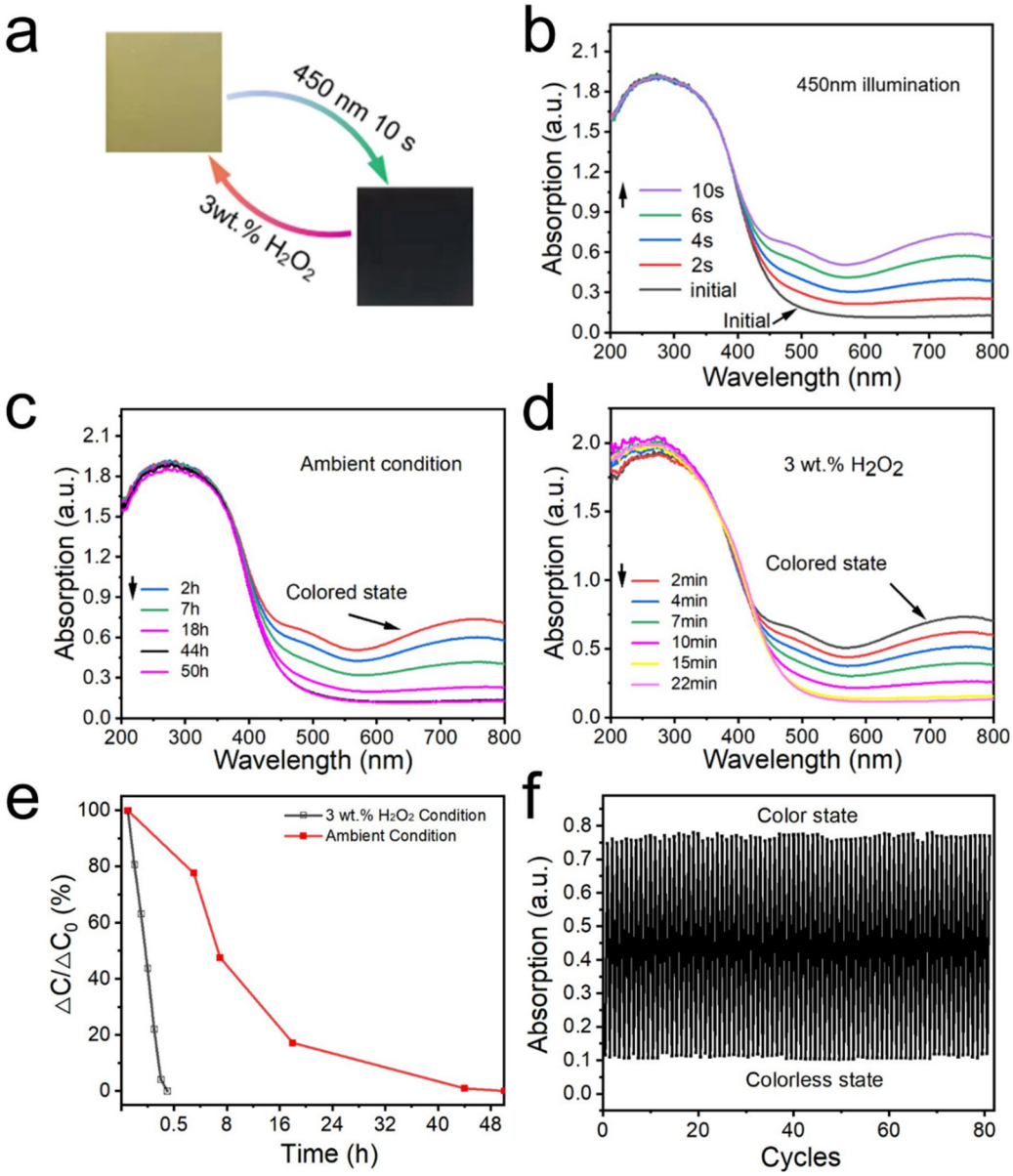

Figure 3. (**a**) Digital photographs showing the color switching process of the typical Sn-TiO_2/PTA/PVP nanocomposite film upon 450 nm illumination and treatment with H_2O_2 vapor. (**b**–**d**) UV-vis diffuse absorption spectra showing the coloration process upon 450 nm illumination (**b**), upon the bleaching process in ambient air (**c**), and in the 3 wt.% H_2O_2 condition (**d**). (**e**) The bleaching rate of the Sn-TiO_2/PTA/PVP nanocomposite film in the ambient condition and treated with H_2O_2 vapor, respectively. (**f**) Absorption intensity at 750 nm of the nanocomposite film in 80 cycles.

To further elucidate the impact of component ratios, the photochromic performance of Sn-TiO_2/PTA/PVP nanocomposite films with Sn-TiO_2:PTA molar ratios of 3:1 and 7:1 was also investigated, respectively. While the 3:1 ratio nanocomposite film exhibited a noticeable color change from light gray to black upon 10 s of illumination with 450 nm light, its cycling stability was limited to only 50 cycles (Figures S4 and S6a). This limited stability at the 3:1 Sn-TiO_2:PTA ratio can be attributed to the lower Sn-TiO_2 content, which restricts the number of photogenerated electrons available for PTA reduction. Consequently, the reduction of W^{6+} to W^{5+} is slowed due to this insufficient electron density, leading to incomplete coloration and accelerated degradation of the partially reduced PTA clusters during cycling. Conversely, the 7:1 ratio resulted in excessive aggregation of Sn-TiO_2 nanoparticles, which hindered film formation. Consequently, the 7:1 ratio nanocomposite film displayed minimal color change after 10 s of illumination at 450 nm (Figures S5 and S6b). These findings highlight the critical importance of maintaining balanced component ratios to achieve optimal photochromic performance.

2.2.3. Mechanistic Insights into Photochromic Behavior

The photochromic mechanism of the Sn-TiO_2/PTA nanocomposite was elucidated through XPS and FTIR analyses. Upon 450 nm illumination, this peak of W $4f_{7/2}$ peak shifted from 35.6 eV to 35.4 eV (Figure 4a), confirming the reduction of W^{6+} to W^{5+} [58]. The intensity ratio of W^{5+}/W^{6+} increased after illumination, indicating efficient electron accumulation at PTA clusters. Concurrently, the Ti $2p_{3/2}$ peak shifted from 458.7 eV to 458.5 eV (Figure 4b), signifying the formation of Ti^{3+} species via electron trapping at oxygen vacancies [31]. These vacancies, introduced by Sn^{4+} substitution into the TiO_2 lattice, act as hole scavengers, prolonging electron lifetimes (>10 ns) and enhancing charge separation efficiency [38]. The O 1s peak shifted downward by 0.2 eV (from 530.5 to 530.3 eV; Figure 4c), reflecting increased electron density at oxygen sites due to interfacial charge transfer. These observations align with prior studies on metal oxide-POM systems, where visible-light excitation drives directional electron flow from the semiconductor to POM clusters [31]. The survey XPS spectra (Figure S7) confirmed the absence of elemental leaching or phase decomposition during cycling, with C 1s and P 2p peaks remaining unchanged, underscoring the structural integrity of the Sn-TiO_2 and PTA clusters.

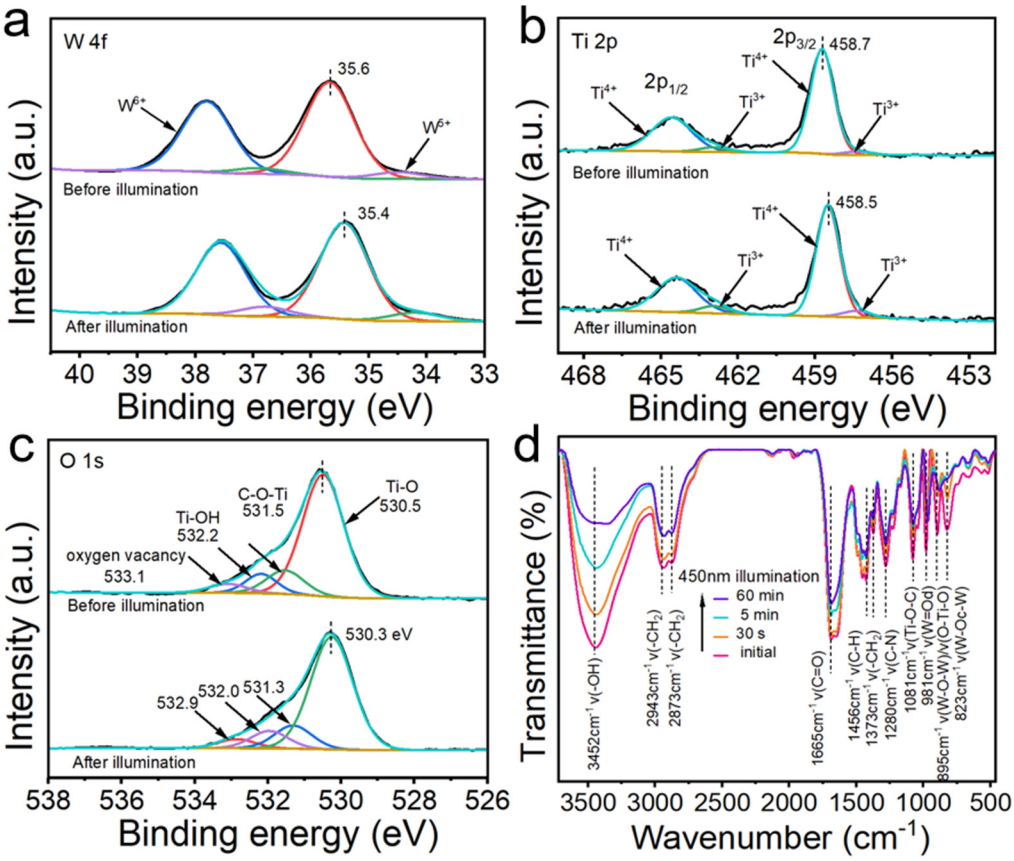

Figure 4. (**a**,**b**) High-resolution XPS spectra of W 4f (**a**), Ti 2p (**b**) and O 1s (**c**) of the Sn-TiO_2/PTA nanocomposite before and after 450 nm illumination. (**d**) FT-IR spectra of the Sn-TiO_2/PTA/PVP nanocomposite film upon 450 nm with different time.

FT-IR spectroscopy (Figure 4d) provided further evidence of dynamic interfacial interactions during photochromic cycling. The W–O–W vibrational peak at 895 cm^{-1} decreased in intensity within 30 s of illumination, indicating electron localization at W sites. Simultaneously, the –OH vibrational peak at 3452 cm^{-1} exhibited a sharp intensity decline with prolonged illumination, attributed to hydroxyl group formation via water oxidation by photogenerated holes. This process stabilizes charge-separated states by suppressing hole recombination [63,64]. The W=O stretching vibration at 981 cm^{-1} also diminished, suggesting partial reduction of terminal oxygen atoms in PTA. These spectral changes correlate with enhanced interfacial electronic coupling between Sn-TiO_2 and PTA, facilitating unidirectional electron transfer under visible light. Notably, the C–N vibrational peak of PVP (1280 cm^{-1}) remained almost unchanged during illumination, confirming its non-redox role as a structural stabilizer. PVP suppresses nanoparticle aggregation and oxidative degradation by forming a protective matrix, ensuring uniform dispersion of Sn-TiO_2 and PTA clusters.

2.2.4. Application of Sn-TiO_2/PTA/PVP Nanocomposite Films as Rewritable Smart Media

The practical utility of the Sn-TiO_2/PTA/PVP nanocomposite film as a high-performance rewritable medium was demonstrated through photopatterning experiments and environmental stability tests, as illustrated in Figure 5. Leveraging its ultrafast visible-light-driven photochromism, high optical contrast, and robust reversibility, the film enables precise, durable, and eco-friendly information recording and erasing, addressing critical limitations of conventional rewritable systems. As shown in Figure 5a, high-definition text patterns were printed onto the nanocomposite film using 450 nm illumination through a photomask (10 s exposure). The printed patterns exhibited sharp edge definition and no pixel bleeding, demonstrating the localized photochromism of the material. This spatial selectivity arises from efficient electron transfer from Sn-TiO_2 to PTA exclusively in illuminated regions, triggering W^{6+}-to-W^{5+} reduction and subsequent broadband IVCT absorption. The environmental stability of printed information was assessed under ambient conditions. As illustrated in Figure 5b, legible text remained discernible for up to 3 days, with complete disappearance observed after 6 days (Figure 5b, panels i–vi). This extended retention time represents a significant improvement compared to organic dye-based systems, such as spiropyran, which typically exhibit a retention period of less than 3 days [65]. This performance characteristic aligns well with the requirements for temporary display applications in logistics, signage, and anti-counterfeiting labels. The slow oxidative fading is attributed to the dense PVP matrix, which impedes oxygen diffusion into the film's interior.

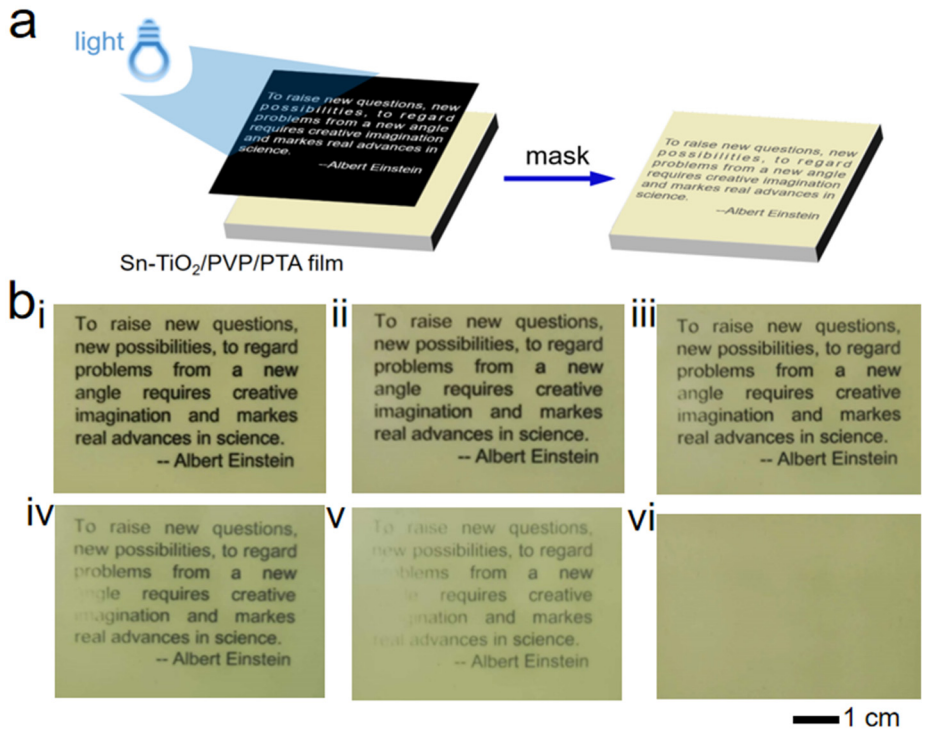

Figure 5. (**a**) Schematic illustration of photoprinting on the Sn-TiO_2/PTA/PVP nanocomposite film under 450 nm illumination in 10 s using a photomask. (**b**) Digital photographs of the original printed rewritable film (**i**) and the printed rewritable film maintained in air for 6 h (**ii**), 12 h (**iii**), 2 days (**iv**), 3 days (**v**), 6 days (**vi**).

3. Conclusions

In summary, we present a visible-light-responsive Sn-TiO_2/PTA/PVP nanocomposite film that synergizes ultrafast photochromic switching, high-contrast black coloration, and exceptional environmental stability for rewritable media applications. By leveraging Sn^{4+} doping to narrow the TiO_2 bandgap (2.23 eV) and PVP-mediated interfacial engineering to integrate PTA clusters, the nanocomposite achieves efficient visible-light absorption (400–500 nm) and broadband IVCT transitions (600–800 nm), enabling full-spectrum black coloration. The material exhibits ultrafast coloration (10 s under 450 nm illumination) and rapid bleaching (<30 min via H_2O_2 vapor), sustaining over 80 reversible cycles with negligible performance decay. This represents a significant improvement over organic dyes and UV-dependent inorganic systems in terms of both speed and durability. The dense PVP matrix further ensures long-term stability by suppressing oxidative degradation, retaining legible patterns for >48 h under ambient conditions. As a rewritable smart medium, the film enables high-resolution, energy-efficient information storage and erasure, showcasing direct applicability in temporary displays, smart packaging, and dynamic signage. From an environmental perspective, the Sn-TiO_2/PTA/PVP nanocomposite offers a sustainable alternative to conventional photochromic systems. The inorganic components (Sn-TiO_2, PTA) are non-toxic and abundant, while the aqueous synthesis process avoids hazardous solvents. The visible-light-driven mechanism reduces energy consumption compared to UV-dependent systems, and the film's long-term stability (>80 cycles) minimizes material waste. These attributes align with global efforts toward green chemistry and energy-efficient technologies. By harmonizing visible-light activation, high optical contrast, and mechanical durability within an eco-friendly inorganic framework, this work establishes a transformative platform for next-generation smart displays, anti-counterfeiting technologies, and energy-efficient rewritable media.

Supplementary Materials: The following supporting information can be downloaded at: https://media.sciltp.com/articles/others/2505151554522574/MI-953-SI-final.pdf, Figure S1: UV-vis transmittance spectrum of the typical Sn-TiO_2/PTA/PVP nanocomposite film; Figure S2: FT-IR spectra of Sn-TiO_2, PTA, and the typical Sn-TiO_2/PTA/PVP nanocomposite film; Figure S3: Survey XPS spectra (a) and high-resolution XPS spectra of C 1s (b) and P 2p (d) of PTA, Sn-TiO_2 nanoparticles and Sn-TiO_2/PTA nanocomposite; Figure S4: (a) Digital photographs showing the color switching process of the Sn-TiO_2/PTA/PVP nanocomposite film (the molar ratio of Sn-TiO_2:PTA is 3:1) upon 450 nm illumination and treatment with H_2O_2 vapor. (b,c) UV-vis diffuse absorption spectra showing the coloration process upon 450 nm illumination (b), upon the bleaching process in the 3 wt.% H_2O_2 condition (c); Figure S5: (a) Digital photographs showing the color switching process of the Sn-TiO_2/PTA/PVP nanocomposite (the molar ratio of Sn-TiO_2:PTA is 7:1) upon 450 nm illumination and treatment with H_2O_2 vapor. (b,c) UV-vis diffuse absorption spectra showing the coloration process upon 450 nm illumination (b), upon the bleaching process in the 3 wt.% H_2O_2 condition (c); Figure S6: (a) The coloration rate and (b) the bleaching rate of Sn-TiO_2/PTA/PVP nanocomposite films with different Sn-TiO_2:PTA molar ratios under 450 nm light illumination in the initial state, treatment with vapor of H_2O_2, respectively. (c) Absorption intensity at 750 nm of films with Sn-TiO_2:PTA molar ratios of 5:1 (80 cycles) and 3:1 (50 cycles) during continuous color switching. Figure S7: Survey XPS spectra (a) and high-resolution XPS spectra of C (b), P (c), N (d) of the Sn-TiO_2/PTA nanocomposite before and after 450 nm illumination. Table S1: Comparison of photochromic performance between Sn-TiO_2/PTA/PVP and existing systems. References [66–69] are cited in the supplementary materials.

Author Contributions: Y.D: conceptualization, methodology, software; D.W: data curation, writing—original draft preparation; Y.Q.: visualization, investigation; Y.Z.: supervision; Z.Z.: software, validation; W.W.: writing—reviewing and editing. All authors have read and agreed to the published version of the manuscript.

Funding: This work was supported by the Natural Science Foundation of Shandong Province (ZR2019JQ15, ZR2024QB097), National Natural Science Foundation of China (22479063), and University of Jinan Postdoctoral Initiation Fund (No.1003880).

Data Availability Statement: The data presented in this study are available upon request from the corresponding author.

Conflicts of Interest: The authors declare no conflict of interest.

References

1. Ke, Y.; Chen, J.; Lin, G.; Wang, S.; Zhou, Y.; Yin, J.; Lee, P.S.; Long, Y. Smart Windows: Electro-, Thermo-, Mechano-, Photochromics, and Beyond. *Adv. Energy Mater.* **2019**, *9*, 1902066.
2. Chun, S.Y.; Park, S.; Lee, S.I.; Nguyen, H.D.; Lee, K.-K.; Hong, S.; Han, C.-H.; Cho, M.; Choi, H.-K.; Kwak, K. Operando Raman and UV-Vis spectrosscopic investigation of the coloring and bleaching mechanism of self-powered photochromic devices for smart windows. *Nano Energy* **2021**, *82*, 105721.
3. Pang, Q.; Bian, L.; Xu, J.; Jia, Y.; Wang, C.; Zhang, Y.; Ju, Q.; Wu, Q.; Fang, Z. Sunlight-Sensitizing Switchable Photochromic Transparent Aesthetic Wood for Smart Windows. *ACS Sustain. Chem. Eng.* **2024**, *12*, 10506–10516.
4. Meng, W.; Kragt, A.J.J.; Gao, Y.; Brembilla, E.; Hu, X.; van der Burgt, J.S.; Schenning, A.; Klein, T.; Zhou, G.; van den Ham, E.R.; et al. Scalable Photochromic Film for Solar Heat and Daylight Management. *Adv. Mater.* **2024**, *36*, e2304910.
5. Ma, T.; Li, B.; Zhu, Y.; Wu, S.; Zhao, X.; Chu, X.; Tian, S. Enhanced photochromic performance of Zn-doped $W_{18}O_{49}$-based films for smart windows. *J. Mater. Chem. C* **2024**, *12*, 10218–10225.

6. Sheng, L.; Li, M.; Zhu, S.; Li, H.; Xi, G.; Li, Y.G.; Wang, Y.; Li, Q.; Liang, S.; Zhong, K.; et al. Hydrochromic molecular switches for water-jet rewritable paper. *Nat. Commun.* **2014**, *5*, 3044.
7. Smith, A.T.; Ding, H.; Gorski, A.; Zhang, M.; Gitman, P.A.; Park, C.; Hao, Z.; Jiang, Y.; Williams, B.L.; Zeng, S.; et al. Multi-color Reversible Photochromisms via Tunable Light-Dependent Responses. *Matter* **2020**, *2*, 680–696.
8. Sarker, S.; Macharia, D.K.; Zhang, Y.; Zhu, Y.; Li, X.; Wen, M.; Meng, R.; Yu, N.; Chen, Z.; Zhu, M. Synthesis of MnO_2-Ag Nanojunctions with Plasmon-Enhanced Photocatalytic and Photothermal Effects for Constructing Rewritable Mono-/Multi-Color Fabrics. *ACS Appl. Mater. Interfaces* **2022**, *14*, 5545–5557.
9. Wang, W.; Yi, L.; Zheng, Y.; Lu, J.; Jiang, A.; Wang, D. Photochromic and mechanochromic cotton fabric for flexible rewritable media based on acrylate latex with spiropyran cross-linker. *Compos. Commun.* **2023**, *37*, 101455.
10. Cui, B.; Guo, C.; Zhang, Z.; Fu, G. Core–shell ZnCo-PBA@$WO_{2.72}$ heterojunctions with enhanced photo-responsive color switching ability for highly efficient rewritable media and information encryption. *Chem. Eng. J.* **2023**, *477*, 147037.
11. Zhang, J.; Guo, M.; Su, Y.; Wu, W.; Wang, S.; Yang, R.; Xu, C.; Yin, H.; Xu, J.; Wang, X. Photochromic ionogel with a wide temperature range and fatigue resistance for high-resolution rewritable information record. *Chem. Eng. J.* **2024**, *495*, 153263.
12. Chen, T.; Xu, B.; Han, J.; Zhu, M.; Zhang, J.; Li, Z. Chelating Coordination Regulated Photochromic Electrospun Nanofibers for Waterproof and Long-Color-Retention Rewritable Wearables. *ACS Appl. Mater. Interfaces* **2024**, *16*, 13305–13315.
13. Li, P.; Zhang, Z.; Gao, X.; Sun, H.; Peng, D.; Zou, H.; Zhang, Q.; Hao, X. Fast self-bleaching Nb_2O_5-based photochromics for high security dynamic anti-counterfeiting and optical storage applications. *Chem. Eng. J.* **2022**, *435*, 134801.
14. Li, X.; Lin, H.; Lin, S.; Li, P.; Wang, P.; Xu, J.; Cheng, Y.; Zhang, Q.; Wang, Y. Rare-Earth-Ion Doped $Bi_{1.5}ZnNb_{1.5}O_7$ Photochromics: A Fast Self-Recoverable Optical Storage Medium for Dynamic Anti-Counterfeiting with High Security. *Laser Photonics Rev.* **2023**, *17*, 2200734.
15. Wan, J.; Xu, J.; Zhu, S.; Li, J.; Chen, K. Multicolor photochromic material with dual protection of anti-counterfeiting and waterproofing. *Chem. Eng. J.* **2023**, *473*, 145500.
16. Sun, L.; Wang, B.; Xing, G.; Liang, C.; Ma, W.; Yang, S. Bi-induced photochromism and photo-stimulated luminescence with fast photochromic response for multi-mode dynamic anti-counterfeiting and optical information storage. *Chem. Eng. J.* **2023**, *455*, 140752.
17. Hu, L.; Gao, Y.; Cai, Q.; Wei, Y.; Zhu, J.; Wu, W.; Yang, Y. Cholesterol-substituted spiropyran: Photochromism, thermochromism, mechanochromism and its application in time-resolved information encryption. *J. Colloid Interface Sci.* **2024**, *665*, 545–553.
18. Wang, L.; Zhong, W.; Gao, W.; Liu, W.; Shang, L. Dynamic multicolor luminescent anti-counterfeiting based on spiropyran-engineered gold nanoclusters. *Chem. Eng. J.* **2024**, *479*, 147490.
19. Song, Y.; Zhao, Y.; Huang, Z.; Zhao, J. Aqueous synthesis of molybdenum trioxide (h-MoO_3, α-$MoO_3 \cdot H_2O$ and h-/α-MoO_3 composites) and their photochromic properties study. *J. Alloys Compd.* **2017**, *693*, 1290–1296.
20. Wang, W.; Ye, Y.; Feng, J.; Chi, M.; Guo, J.; Yin, Y. Enhanced photoreversible color switching of redox dyes catalyzed by barium-doped TiO_2 nanocrystals. *Angew. Chem. Int. Ed.* **2015**, *54*, 1321–1326.
21. Kozlov, D.A.; Shcherbakov, A.B.; Kozlova, T.O.; Angelov, B.; Kopitsa, G.P.; Garshev, A.V.; Baranchikov, A.E.; Ivanova, O.S.; Ivanov, V.K. Photochromic and Photocatalytic Properties of Ultra-Small PVP-Stabilized WO_3 Nanoparticles. *Molecules* **2019**, *25*, 154.
22. Yan, X.; Zhong, W.; Qu, S.; Li, Z.; Shang, L. Photochromic Tungsten Oxide Quantum Dots-based Fluorescent Photoswitches towards Dual-mode Anti-counterfeiting Application. *J. Colloid Interface Sci.* **2023**, *646*, 855–862.
23. Wang, F.; Song, Y.; Xie, R.; Li, J.; Zhang, X.; Xie, H.; Zou, H. TiO_2/PVA Based Composites: Visible Light Activated Rapid Dual-Mode optical Response. *Chem. Eng. J.* **2023**, *475*, 146306.
24. Li, L.; Yu, Y.-T.; Zhang, N.-N.; Li, S.-H.; Zeng, J.-G.; Hua, Y.; Zhang, H. Polyoxometalate (POM)-based crystalline hybrid photochromic materials. *Coord. Chem. Rev.* **2024**, *500*, 215526.
25. Zhang, J.; Chen, T.; Zhu, M.; Lu, J.; Liu, X.; Sun, W.; So, M.Y.; Xu, B. Scalable, Fast Light-Responsive, and Excellent Color-Retention Fiber-Based Photochromic Wearables for Sustainable Photo-Patterning and Information Security Encryption. *Adv. Funct. Mater.* **2024**, *35*, 2415622.
26. Pope, T.R.; Lassig, M.N.; Neher, G.; Weimar Iii, R.D.; Salguero, T.T. Chromism of Bi_2WO_6 in single crystal and nanosheet forms. *J. Mater. Chem. C* **2014**, *2*, 3223–3230.
27. Kayani, A.B.A.; Kuriakose, S.; Monshipouri, M.; Khalid, F.A.; Walia, S.; Sriram, S.; Bhaskaran, M. UV Photochromism in Transition Metal Oxides and Hybrid Materials. *Small* **2021**, *17*, e2100621.
28. Yang, Y.; Li, J.; Li, X.; Guan, L.; Gao, Z.; Duan, L.; Jia, F.; Gao, G. Easily Prepared and Reusable Films for Fast-Response Rewritable Light Printing. *ACS Appl. Mater. Interfaces* **2019**, *11*, 14322–14328.
29. Wu, W.; Ni, M.; Feng, Q.; Zhou, Y.; Cui, Y.; Zhang, Y.; Xu, S.; Lin, L.; Zhou, M.; Li, Z. A wet bacterial cellulose film self-anchored by phosphotungstic acid: Flexible, quick-response and stable cycling performance for photochromic

application. *Mater. Des.* **2024**, *238*, 112613.
30. Hussain, M.; Ahmad, Z.; Ejeromedoghene, O.; Shehzad, K.; Akhtar, M.; Fu, G. Hybrid polysaccharide film infused with polyoxometalates for inkless printing and solar ultraviolet sensing. *Int. J. Biol. Macromol.* **2025**, *293*, 139308.
31. Zhang, Y.; Gao, Z.; Liu, F.; Liu, L.; Yan, M.; Wang, W. Electrostatic Assembly of Photochromic TiO_2/Phosphomolybdic Acid Composite Nanoparticles for Light-Responsive Rewritable Papers. *ACS Appl. Nano Mater.* **2022**, *5*, 13218–13226.
32. Tian, Y.; Liu, W.; Hu, J.; Li, Z.; Xin, X.; Fu, G. Synthesis of highly transparent and fast-responding photochromic coating by template method with space-limited domains. *Chem. Eng. J.* **2024**, *500*, 156961.
33. Hutomo, F.A.; Pramata, A.D.; Saputra, F.; Pratama, P.R.; De Yonarosa, T.G.; Rasyida, A.; Widyastuti; Sutarsis; Hamidah, N.L. Visible light-driven Synergetic antimicrobial activity of Cu_2O quantum dots and electrospun PAN/PCL nanofiber matrix. *J. Sci.:Adv. Mater. Devices* **2024**, *9*, 100779.
34. Nazari, S.; Asgari, E.; Sheikhmohammadi, A.; Mokhtari, S.A.; Alamgholiloo, H. Visible-light-driven photocatalytic activity of WO_3/ZIF-67 S-scheme heterojunction for upgrading degradation of oxytetracycline. *J. Environ. Chem. Eng.* **2023**, *11*, 110393.
35. Jia, L.; Ma, N.; Shao, P.; Ge, Y.; Liu, J.; Dong, W.; Song, H.; Lu, C.; Zhou, Y.; Xu, X. Incorporating ReS_2 Nanosheet into $ZnIn_2S_4$ Nanoflower as Synergistic Z-Scheme Photocatalyst for Highly Effective and Stable Visible-Light-Driven Photocatalytic Hydrogen Evolution and Degradation. *Small* **2024**, *20*, e2404622.
36. Zhang, J.; Lei, Y.; Jiang, J.; Zhao, S.; Yi, H.; Tang, X.; Huang, X.; Zhou, Y.; Gao, F. $ZnIn_2S_4$/g-C_3N_4 binary heterojunction nanostructure for enhancing visible light CO_2 reduction at the reaction interface. *Renew. Energy* **2025**, *242*, 122380.
37. Chen, P.; Wang, X.; Liu, B.; Yan, L.; Du, X.; Zhang, J.; Zhao, J. Cu-doped KTN crystal with controllable, reversible, and fast photochromic properties: A superior electro-optical material for improving beam deflection performance. *Ceram. Int.* **2024**, *50*, 32645–32654.
38. Wang, B.; Guo, Y.; Li, Q.; Xin, C.; Tian, Y.; Zhang, W.; Yu, X. Design of porous ZrO_2 with well-tuned band structures and strong visible-light harvesting via Zn doping for enhanced visible-light photocatalysis. *Chem. Eng. J.* **2024**, *481*, 148489.
39. Zhang, Y.; Dou, Y.; Ye, Z.; Xue, W.; Liu, F.; Yan, M.; Wang, W.; Yin, Y. Visible-Light-Responsive Photoreversible Multi-Color Switching for Rewritable Light-Printing and Information Display. *Small* **2024**, *20*, e2310962.
40. Ma, Y.; Li, A.; Wang, C.; Ge, X. Preparation of HPW@UiO-66 catalyst with defects and its application in oxidative desulfurization. *Chem. Eng. J.* **2021**, *404*, 127062.
41. Sun, A.; Nan, F.; Wei, Q.; Wang, L.; Yu, W.W. Color-tunable, multifunctional photochromic composites for wearable UV monitoring and biomechanical energy harvesting. *Nano Energy* **2024**, *126*, 109679.
42. Xiong, T.; Yong, W.; Chen, N.; Fu, G. Transparent insulating photochromic PU/PTA films for Wide-Spectrum modulated smart windows. *J. Photochem. Photobiol. A* **2024**, *456*, 115853.
43. Gu, H.; Guo, C.; Zhang, S.; Bi, L.; Li, T.; Sun, T.; Liu, S. Highly Efficient, Near-Infrared and Visible Light Modulated Electrochromic Devices Based on Polyoxometalates and $W_{18}O_{49}$ Nanowires. *ACS Nano* **2018**, *12*, 559–567.
44. Chen, L.; Chen, W.L.; Wang, X.L.; Li, Y.G.; Su, Z.M.; Wang, E.B. Polyoxometalates in dye-sensitized solar cells. *Chem. Soc. Rev.* **2019**, *48*, 260–284.
45. Chen, X.; Zhang, G.; Li, B.; Wu, L. An integrated giant polyoxometalate complex for photothermally enhanced catalytic oxidation. *Sci. Adv.* **2021**, *7*, eabf8413.
46. Ganeshraja, A.S.; Thirumurugan, S.; Rajkumar, K.; Zhu, K.; Wang, Y.; Anbalagan, K.; Wang, J. Effects of structural, optical and ferromagnetic states on the photocatalytic activities of Sn–TiO_2 nanocrystals. *RSC Adv.* **2016**, *6*, 409–421.
47. Xiang, H.; Luo, T.; Ji, Y.; Xiong, T.; Qian, L.; Yang, S.; Wang, H. Photocatalytic degradation of low-concentration gaseous benzene in air via bifunctional tin-doped titanium dioxide catalyst. *Environ. Technol. Innov.* **2024**, *36*, 103804.
48. Cui, Y.; Xing, Z.; Guo, M.; Qiu, Y.; Fang, B.; Li, Z.; Wang, Y.; Chen, P.; Zhou, W. Core–shell carbon colloid sphere@phosphotungstic acid/CdS as a Z-scheme heterojunction with synergistic adsorption, photothermal and photocatalytic performance. *Catal. Sci. Technol.* **2021**, *11*, 6080–6088.
49. Cai, S.; Wu, H.; Gao, X.; Chen, X.; Cheng, C.; Yang, X.; Sun, R. Phosphotungstic acid decorated free-standing electrode accelerates polysulfides conversion for high-performance flexible Li-S batteries. *J. Energy Storage* **2024**, *89*, 111663.
50. Li, R.; Zhou, Y.; Shao, Z.; Zhao, S.; Chang, T.; Huang, A.; Li, N.; Ji, S.; Jin, P. Enhanced Coloration/Bleaching Photochromic Performance of WO_3 Based on PVP/PU Composite Matrix. *Chem. Select* **2019**, *4*, 9817–9821.
51. Yang, Z.; Wang, D.; Zhang, Y.; Feng, Z.; Liu, L.; Wang, W. Photoreductive BiOCl ultrathin nanosheets for highly efficient photocatalytic color switching. *ACS Appl. Mater. Interfaces* **2020**, *12*, 8604–8613.
52. Gao, Z.; Zhou, Z.; Wang, M.; Shang, N.; Gao, W.; Cheng, X.; Gao, S.; Gao, Y.; Wang, C. Highly dispersed Pd anchored on heteropolyacid modified ZrO_2 for high efficient hydrodeoxygenation of lignin-derivatives. *Fuel* **2023**, *334*, 126768.
53. Boga, B.; Székely, I.; Pap, Z.; Baia, L.; Baia, M. Detailed Spectroscopic and Structural Analysis of TiO_2/WO_3 Composite Semiconductors. *J. Spectro.* **2018**, *2018*, 6260458.
54. Khan, H.; Rigamonti, M.G.; Boffito, D.C. Enhanced photocatalytic activity of Pt-TiO_2/WO_3 hybrid material with energy storage ability. *Appl. Catal. B* **2019**, *252*, 77–85.

55. Wei, D.; Zhang, Y.; Xue, W.; Dou, Y.; Liu, F.; Yan, M.; Wang, W. Visible-Light-Responsive Photoreversible Color Switching of Oxygen-Deficient WO_{3-x} Hierarchical Nanostructures for Long-Legible Rewritable Paper. *ACS Sustain. Chem. Eng.* **2024**, *12*, 6310–6319.
56. Hua, C.; Doheny, P.W.; Ding, B.; Chan, B.; Yu, M.; Kepert, C.J.; D'Alessandro, D.M. Through-space intervalence charge transfer as a mechanism for charge delocalization in metal–organic frameworks. *J. Am. Chem. Soc.* **2018**, *140*, 6622–6630.
57. Ramírez-Wierzbicki, I.; Cotic, A.; Cadranel, A. Photoinduced intervalence charge transfers: spectroscopic tools to study fundamental phenomena and applications. *ChemPhysChem* **2022**, *23*, e202200384.
58. Yang, C.; Guo, N.; Qu, S.; Ma, Q.; Liu, J.; Chen, S.; Ouyang, R. Design of anti-thermal quenching Pr^{3+}-doped niobate phosphors based on a charge transfer and intervalence charge transfer band excitation-driven strategy. *Inorg. Chem. Front.* **2023**, *10*, 4808–4818.
59. Kong, L.; Jing, Z.; Mamoor, M.; Jiang, Y.; Zhai, Y.; Qu, G.; Wang, L.; Wang, B.; Xu, L. Enhancing the Reversibility and Kinetics of Heterovalent Ion-Substituted Mn-Based Prussian Blue Analogue Cathodes via Intervalence Charge Transfer. *Angew. Chem. Int. Ed.* **2025**, e202500254.
60. Chang, X.; Dong, X.; Liu, X.; Tong, Y.; Li, K.; Li, Z.; Lu, Y. Constructing a hexagonal/orthorhombic WO_3 phase junction for enhanced photochromism. *Opt. Mater.* **2023**, *142*, 114131.
61. Wang, Q.; Zhang, W.; Hu, X.; Xu, L.; Chen, G.; Li, X. Hollow spherical WO_3/TiO_2 heterojunction for enhancing photocatalytic performance in visible-light. *J. Water Process Eng.* **2021**, *40*, 101943.
62. Zhao, J.; Liu, L.; Zhang, Y.; Feng, Z.; Zhao, F.; Wang, W. Light-responsive color switching of self-doped $TiO_{2-x}/WO_3 \cdot 0.33H_2O$ hetero-nanoparticles for highly efficient rewritable paper. *Nano Res.* **2020**, *14*, 165–171.
63. Zhang, Y.; Cheng, C.; Zhou, Z.; Long, R.; Fang, W.H. Surface Hydroxylation during Water Splitting Promotes the Photoactivity of $BiVO_4$(010) Surface by Suppressing Polaron-Mediated Charge Recombination. *J. Phys. Chem. Lett.* **2023**, *14*, 9096–9102.
64. Deng, H.; Qin, C.; Pei, K.; Wu, G.; Wang, M.; Ni, H.; Ye, P. TiO_2/reduced hydroxylated graphene nanocomposite photocatalysts: Improved electron–hole separation and migration. *Mater. Chem. Phys.* **2021**, *270*, 124796.
65. Yang, Y.; Chen, Y.; Li, Y.; Wang, Z.; Zhao, H. Acid-, mechano- and photochromic molecular switches based on a spiropyran derivative for rewritable papers. *Mater. Chem. Front.* **2022**, *6*, 916–923.
66. Zhang, Y.; Wang, Q., Acceleration photochromic performance in tungsten oxide. *Opt. Mater.* **2024**, 157, 116365.
67. Zhu, Y.; Li, B.; Li, C.; Tian, S., Transparent photochromic Fe-doped $W_{18}O_{49}$ films with ultrahigh solar energy modulation for smart windows. *J. Mater. Chem. C* **2025**, 13, 6115–6122.
68. Oderinde, O.; Ejeromedoghene, O.; Fu, G., Synthesis and properties of low-cost, photochromic transparent hydrogel based on ethaline-assisted binary tungsten oxide-molybdenum oxide nanocomposite for optical memory applications. *Polym. Adv. Technol.* **2022**, 33, 687–699.
69. Liu, T.; Li, J. L.; Xie, Z.; Huang, C.; Wang, J.; Zhang, C.; Sha, C.; Wang, L., Naphthalene-embedded spiropyran derivative-A type of conjugated expanded material with solid-state photochromic properties and tunable color switching range. *J. Mol. Struct.* **2024**, 1318, 139404.

Review

Additive Manufacturing of Bioinspired Structural-Color Materials

Zhilong Cao [1], Yanzhao Yang [1,*], Yuanhao Chen [1], Wei Feng [1,*], and Ling Wang [1,2,*]

[1] School of Materials Science and Engineering, Tianjin University, Tianjin 300350, China
[2] Binhai Industrial Research Institute, Tianjin University, Tianjin 300452, China
* Correspondence: yangyanzhao@tju.edu.cn (Y.Y.); weifeng@tju.edu.cn (W.F.); lwang17@tju.edu.cn (L.W.)
Received: 8 January 2025; Revised: 2 April 2025; Accepted: 6 April 2025; Published: 19 May 2025

Abstract: Structural color is ubiquitous in nature and biological systems, and synthetic structural-color materials have been considered as a more durable substitute for traditional pigments. Recent advancements in the additive manufacturing of exquisite photonic objects have enabled the preparation of structurally colored materials with customized properties. Herein, an up-to-date review about additive manufacturing of bioinspired structural-color materials is presented. This review begins with an overview of the direct ink writing of colloidal crystals, chiral liquid crystals, cellulose nanocrystals, and block copolymers. Then, significant advances in inkjet printing strategy are showcased, including inkjet printing of colloidal crystals and cellulose nanocrystals, inkjet printing inks on photonic polymer coatings, and inkjet printing based on total internal reflections. The third section focuses on the recent advances in other additive manufacturing methods, including digital light processing, two-photon lithography, and fused deposition modeling. This review summarizes a perspective on potential opportunities, challenges, and future prospects encountered by advanced printing technology and functional structural-color materials.

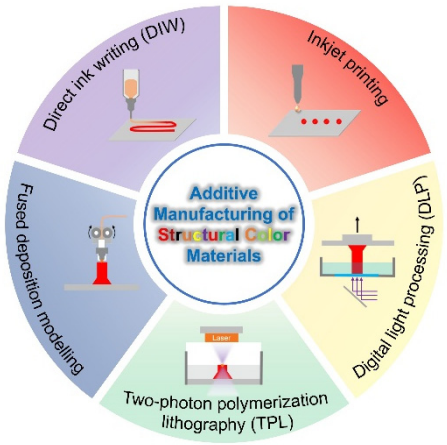

Keywords: additive manufacturing; structural color; direct ink writing; inkjet printing; colloidal crystals; chiral liquid crystals

1. Introduction

Structural-color materials possess periodic dielectric nanostructures that reflect light at visible wavelengths, exhibiting vivid colors [1–5]. Nature has evolved different types of periodic nanostructures over millions of years of evolution to develop structural colors that intensify or weaken the visibility of biological organisms for purposes of camouflage, communication, and predator warning [6–8]. For instance, chameleons may camouflage by changing their skin colors to blend them with the background colors [9]. The spectacular iridescent colors of certain insects, opals, butterflies, plants, and peacocks are created due to periodic nanostructures on their surfaces that reflect light in specific spectral ranges [10–14]. Inspired by nature, investigators have proposed synthetic periodic nanostructures which offer nonfading, tunable, nontoxic, and iridescent structural colors [15–17]. In recent decades, structural-color materials have attracted substantial attention because of their fundamental importance and technological applications. The exploitation of exquisite structural-color patterns capacitates the manufacture of customized color images that are crucial for several emerging applications like sensors [18], decoration [19], bioanalysis [20], displays [21], anticounterfeiting [22], and optical communication [23]. Furthermore, three-dimensional (3D) structural-color materials enable the manipulation of optical properties and light paths, such as amplitude regulation, phase, and polarization, and generate new or enhanced optical properties [24]. In this context, functional structural color patterns and 3D structural color objects have been developed based on diverse fabrication strategies, including swelling [25], stamping [26], regioselective etching [27], mask-assisted photography [28], and die making [29]. However, these methods require expensive tooling, lithographic masks, and time-consuming multi-step processes.

Additive manufacturing, which involves ink-based printing techniques that allow the digital design and manufacturing of exquisite patterns or 3D objects, is upgrading the science and engineering of advanced structural-color materials. In contrast to traditional manufacturing techniques, additive manufacturing enables the conversion of computer-aided designs into intricate objects as needed [30–36]. Additive manufacturing facilitates the on-demand production of customized products, characterized by specific shapes and sizes, while ensuring high production efficiency. This capability presents a significant economic actuation for its adoption across a range of industrial sectors, such as robotics, biomedicine, automotive, and aerospace [37–40]. Recently, additive manufacturing has emerged as a versatile method for fabricating structurally colored materials using micro- and nanoscale building blocks as printable inks. Several additive manufacturing approaches, including direct ink writing (DIW), inkjet printing, digital light processing (DLP), two-photon lithography (TPL), and fused deposition modeling (FDM), have been proposed for the manufacture of structural-color materials from diverse building block systems such as colloidal particles, chiral liquid crystals (CLCs), cellulose nanocrystals (CNCs), and block copolymers (BCPs). These printing platforms use building blocks in the following forms: polymer solution, photocurable resin, or thermoplastic monofilament. Additive manufacturing of structural-color materials currently stands in the limelight of research on account of the unparalleled advantages including remarkable universality, diversity, and stability. By carefully choosing the appropriate additive manufacturing parameters and techniques, it is possible to achieve sophisticated and customized patterns or 3D geometries of structural colors while attaining desirable optical properties.

Several reviews have focused on printable structural colors or the design of structural-color patterns [41–43]. To the best of our knowledge, there is no specific classification for the additive manufacturing of structural-color materials. Herein, an up-to-date account of the advancements in high-throughput printing methods capable of fabricating structural-color materials is showcased (Scheme 1). This review focuses on the following three aspects: In the first section, the DIW of colloidal crystals, CLCs, CNCs, and BCPs is introduced. The second section introduces recent significant progress in inkjet printing strategies, including inkjet printing of colloidal crystals, inkjet printing of CNCs, inkjet printing inks on photonic polymer coatings, and inkjet printing based upon total internal reflections. The third section summarizes the recent advances in other additive manufacturing methods, including DLP, TPL, and FDM. Finally, this review summarizes with perspectives on the opportunities and challenges in the future exploitation of additive manufacturing for structural-color materials.

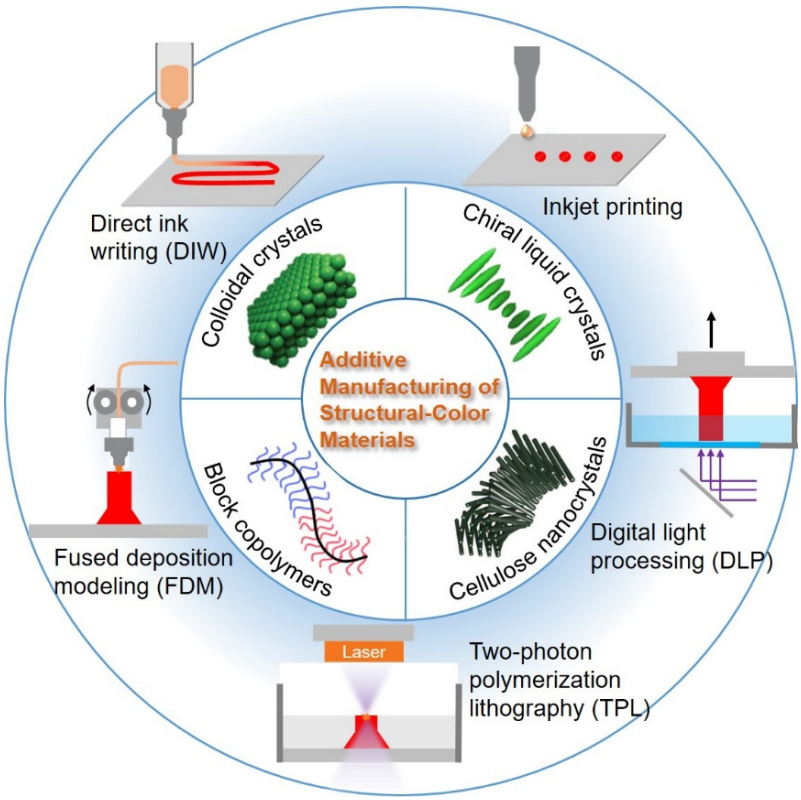

Scheme 1. Schematic of additive manufacturing of structural-color materials. The additive manufacturing approaches include DIW, inkjet printing, DLP, TPL, and FDM. The building block systems used for printable inks include colloidal particles, CLCs, CNCs, and BCPs.

2. Bioinspired Structural-Color Materials and Additive Manufacturing Technologies

2.1. Principles of Bioinspired Structural-Color Materials

In nature, the brilliant iridescent colors of some opals, fruits, and butterflies are induced by the periodic nanostructures on their surface that reflect light in specific ranges of the spectrum. Taking lessons from nature, bioinspired structural color materials derive their colors from periodical micro-nanoscale structures that interact with light, which has been recommended as a more environmentally friendly and long-term stable alternative to traditional pigments and dyes. The photonic crystal structure is featured with long-range order. The characteristics of amorphous structure are short-range order. They all follow Bragg's law of light interference, diffraction, and reflection. These properties of structural colors hinge on the design of the structure-function relationship to a great degree [42].

According to the structural principles and fabrication techniques, structural-color materials can be categorized into colloidal crystals, chiral liquid crystals, cellulose nanocrystals, block copolymers, etc. As a few to name, opals have been known since ancient times (Figure 1a) [12]. The unusual gemstones are impressed by their gorgeous coloration that results from a highly ordered, densely packed arrangement of silica spheres with several microns in diameter indicated by scanning electron microscopy (SEM) (Figure 1b) [44]. Following suit, colloidal crystals can be formed by the self-assembly of monodisperse micro/nanoparticles in a facile and cost-effective manner like face-centered cubic packing, which possess long-range order to manipulate light and display vibrant colors with strong iridescence (Figure 1c). For practical coloration, it is essential to pattern colloidal arrays with a manipulated arrangement and robust mechanical stability in a reproducible and reliable way [45]. *Pollia condensate* is an African forest understory spherical species exhibiting bright metallic blue arising from Bragg reflection of helicoidally stacked cellulose microfibrils shown by transmission electron microscopy (TEM) (Figure 1d,e) [46]. CLCs have hierarchical architecture consisting of superimposing planar layers of parallel-aligned rod-like molecules/nanostructures with a certain twisting angle. This chiral morphology reflects circularly polarized light of the same handedness as the helicoid structure and transmits circularly polarized light with the opposite handedness (Figure 1f) [47]. The helical pitch of CLCs is proportional to the peak wavelength of the selective reflection. Thus, the reflection spectrum and the rendered structural color can be dynamically controlled via applying the physical stimuli to tune the helical pitch. The resulting helicoidal organization have been extensively studied to exploit structural colors which are iridescent, circularly polarized, tunable, and non-fading. Moreover, the inherent long-range order self-assembly of liquid crystals (LCs) can be a perfect characteristic for the manufacturing of structural-color materials on a large scale [48–50]. Especially, if LC molecular suffers a process of double-twist arrangement and self-organizes into a three dimensional (3D) periodic cubic lattices, blue-phase liquid crystals (BPLCs) are formed and treated as 3D photonic materials, whose name derives from the brilliant blue color when it was first discovered. [51–54]. BPLCs are widely utilized in flexible displays, tunable photonic devices, and biomimetic materials for the properties of the three-dimensional photonic bandgap and tunable structural coloration. CNCs are the crystalline regions of cellulose nanofibers, which consist of parallel linear cellulose chains bound by van der Waals forces and hydrogen bonding. The excellent amphiphilic character owing to different surface chemistries at varying crystal planes facilitates the heterogeneous interaction with other amphiphilic nanocomponents used in assembling hierarchical nanostructures similar to CLCs. The addition of water-soluble polymers can manipulate the mechanical stability and the pitch length of the chiral structures to fabricate brilliant structural-color patterns via evaporation-driven self-assembly [55]. *Morpho* butterflies' rainbow-like, shimmering iridescence can maintain bluish even over an extensive range of viewing angle, which is resulted from the light interference within the multilayered, periodic ridges on the scales covering the surface of their wings (Figure 1g,h) [56]. BCPs comprising a corporate backbone attached to grafted side chains are a promising substitute for linear block copolymers to fabricate the analogous one-dimension periodic structure and realize structural colors in the visible range [57]. The spatial repulsion among dense side chains generates more extensive cylindrical conformations and restrains chain entanglement, accelerating self-assembly into large ordered-region-size nanostructures (Figure 1i) [58]. The facile preparation of photonic crystals with BCPs holds promise for various potential applications containing the production of 3D-printed photonic structures, photonic pigments, photonic resins, and stress-responsive photonic structures [59,60]. In addition, woodpile photonic crystals (WPCs) as a specific structural-color material are fabricated through stacking plentiful parallel square columnar units in the vertical direction. The photonic band gaps of WPCs can be simultaneously and independently engineered in three dimensions to display structural colors with ultrahigh resolution due to the effective regulation of the nanometer-scale lattice constant, which are one of the most versatile platforms among the micro/nanodevices for the stability and scalability [61].

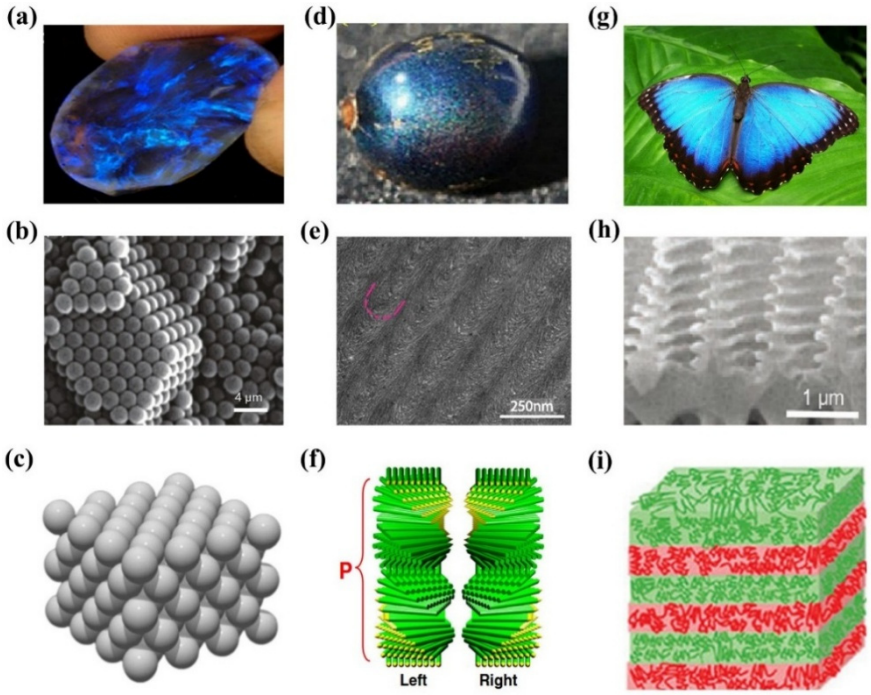

Figure 1. Photonic nanostructures in nature. (**a**) Photograph of black opal. Reproduced with permission [44]. Copyright 2011, Elsevier Ltd. (**b**) SEM image of the opal nanostructure. Reproduced with permission [12]. Copyright 2009, Wiley-VCH. (**c**) Schematic illustration of 3D self-assembly of colloidal crystals. (**d**,**e**) Photograph and TEM image of singe Pollia condensata fruit collected in Ghana. Reproduced with permission [46]. Copyright 2012, National Academy of Sciences. (**f**) A schematic representation of the cholesteric helix for both handedness. Reproduced with permission [47]. Copyright 2014, Elsevier Ltd. (**g**,**h**) Photograph and cross-sectional SEM image of a *Morpho didius* butterfly. Reproduced with permission [56]. Copyright 2012, Wiley-VCH. (**i**) Schematic illustration of 1D BPCs prepared by hierarchical thermal self-assembly. Reproduced with permission [58]. Copyright 2020, American Chemical Society.

2.2. Additive Manufacturing Technologies

The remarkable advancement in additive manufacturing technologies has revolutionized the realm of the intelligent manufacturing system and offered remarkable universality, diversity, and stability for the preparation of structural-color materials. In accordance with the difference of logical sequence in operation, fabrication methods of additive manufacturing technologies for structural colors can be categorized into two types: top-down and bottom-up approaches. The former is to utilize multilayer deposition or lithography techniques to transform bulk materials into the desired micro-nano structures, such as DIW, inkjet printing and DLP. The latter relies on the self-assembly of basic building blocks through physical and chemical interactions to achieve ordered nanostructures, which includes TPL and FDM [62].

In DIW printing, nanoparticle clusters in liquid media with highly stable dispersibility and viscosity, which serves as the ink, are extruded directly onto a substrate for manufacturing materials with designed architectures and components, while a computer-controlled translation stage simultaneously moves the nozzle to realize an automated injection molding process [63]. Similar to DIW, inkjet printing has been more previously but commonly utilized in the patterned printing of structural-color materials. In inkjet printing, inks are ejected from a micrometer-sized printing nozzle as droplets and subsequently deposited onto the target substrates [64]. For DLP, particles dispersing in precursor solution polymerize under the irradiation of projected light to create a customized structure. A DLP machine can project 2D images sliced from target 3D objects, and the exposed parts are selectively polymerized. Once a layer was cured, the platform moved vertically for a certain distance and project the next image. Until the entire 3D object was constructed, this process needed repeat layer by layer [65]. In TPL processing, bulk materials produce localized photochemical reactions by utilizing high-energy pulsed lasers [66]. This technique enables the precise orientation and manipulation of chemical reactions in stereoscopic space, realizing the construction of high-precision structures on the micro-nano scale with a high-resolution [67]. Thermoplastic ingredients incorporated suitable building blocks can be melted into filamentous individuals and stacked layer-by-layer via FDM. These wires are self-assembled rapidly during the extrusion at high temperature. Desired products with centimeter-size 3D geometric shapes can be printed quickly and conveniently through this

process [68,69]. The selection of additive manufacturing technologies plays a pivotal role in determining the scalability, speed, and resolution of the process, meanwhile the choice of materials significantly influences the resulting color, durability, and performance of the structures. Thus, the properties of printable structural colors heavily hinge on the precision of structure construction fabricated by the printing technique employed and the options of materials.

3. Direct Ink Writing of Structural-Color Materials

For DIW of structural-color materials, the ink must be formulated for microscopic self-assembly properties and macroscopic printing rheology [70]. During the DIW printing, the parameters (e.g., the printing speed, pressure, and substrate temperature) could also make influences on the result of deposition and further control the quality of colors.

3.1. Direct Ink Writing of Colloidal Crystals

The DIW of colloidal crystals can be used to print photonic patterns according to the type of target substrate, color combination, and design. Colloidal crystal inks must be designed to provide a satisfactory printing rheology and conspicuous coloration after deposition.

Kim et al. reported the use of DIW with colloidal photonic inks in the preparation of customizable structural color graphics (Figure 2a) [71]. To eliminate the prolonged evaporation process, colloidal particles were designed with an exclusive interparticle potential lacking volatile components that induced particles to order spontaneously (Figure 2b,c). The lines were written directly through a dispenser using these inks, and the line width could be regulated by controlling the speed of writing. Faces were obtained through merging lines. The colloidal arrangement within the lines and the faces was scheduled to construct an amorphous array for relatively matte coloration or a crystalline array for strongly iridescent coloration in accordance with the viscosity of resins (Figure 2d,e). In addition, the structural-color patterns could be detached from the substrates for forming free-standing films or transferred onto other surfaces. Later, Kim et al. prepared elastic photonic microbeads via variable-size bulk emulsification and formulated photonic inks including microbeads for DIW [72]. The photonic inks retained the excellent color saturation of microbeads and provided reinforced capacity of printing. These printed graphics exhibited robust mechanical durability because of the elastic microbeads imbedded into the polyurethane matrix. Additionally, the resultant colors showed an extensive viewing angle with weak angle dependency by reason of light refraction at the interface of the air matrix and the optical isotropy of the single microbead. Color graphics can be determined by customers and printed on apparel and accessories for fashions. Besides, twinkling and iridescent colors and unique shape of the reflectance spectrum featured by a sharp single peak enable to function as anticounterfeiting patterns for top-secret documents and art masterpieces.

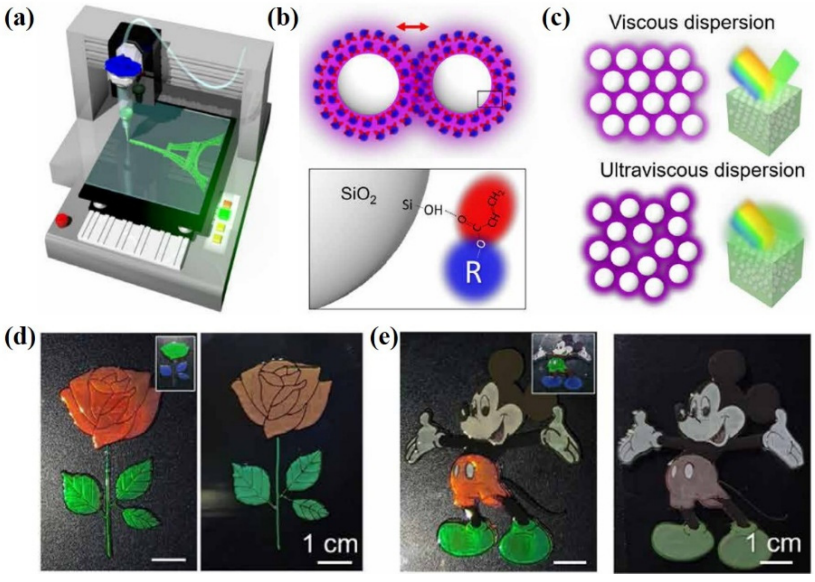

Figure 2. DIW of colloidal crystals. (**a**) Scheme of DIW of colloidal crystals. (**b**) Construction of a solvation layer on the silica surface with hydrogen bond assistance. (**c**) Crystalline and glassy packing in viscous ethoxylate acrylate (EA) and ultra-viscous urethane acrylate (UA). (**d**) Pattern of a rose and leaves printed directly with UA and EA inks. (**e**) Mickey Mouse written with UA and EA inks. Reproduced with permission [71]. Copyright 2021, AAAS.

3.2. Direct Ink Writing of Chiral Liquid Crystals (CLCs)

Currently, the fabrication techniques for CLC-based materials are often complicated owing to the inevitable employment of alignment procedures for uniform LC orientation and high-quality structural colors. Particularly for DIW, CLC inks must be formulated with satisfactory printing rheology for DIW [73–75].

In 2021, Sol et al. synthesized a CLC oligomer ink for DIW (Figure 3a) [76]. The ink was squeezed out of the nozzle and organized into a visually impactful cholesteric arrangement via a shear-induced alignment. Controlling the speed and writing direction generated a programmed construction of cholesteric liquid crystal elastomers (CLCEs) that exhibited polarization selectivity and atypical iridescence. This chiroptical photonic ink paves the way for design of specialized polymeric optical elements with disparate optical effects. The attractive and uniquely iridescent appearance of materials can be utilized in high-end decorative elements. Later, they synthesized a humidity-sensitive CLC oligomer ink for printing hydrochromic coatings that could be activated with aqueous hydrochloric acid solvent, inducing an obvious redshift in the reflectance spectrum when exposed to water (Figure 3b,c) [77]. No apparent negative impact had happened on the optical qualities of the material during the extended exposure to the acidic environment even up to 17 weeks, while resulting in swelling and changes in the reflectance spectrum due to the protonation. This stimuli-responsive ink can be integrated with information technologies and function as 3D-printed optical sensors and actuators.

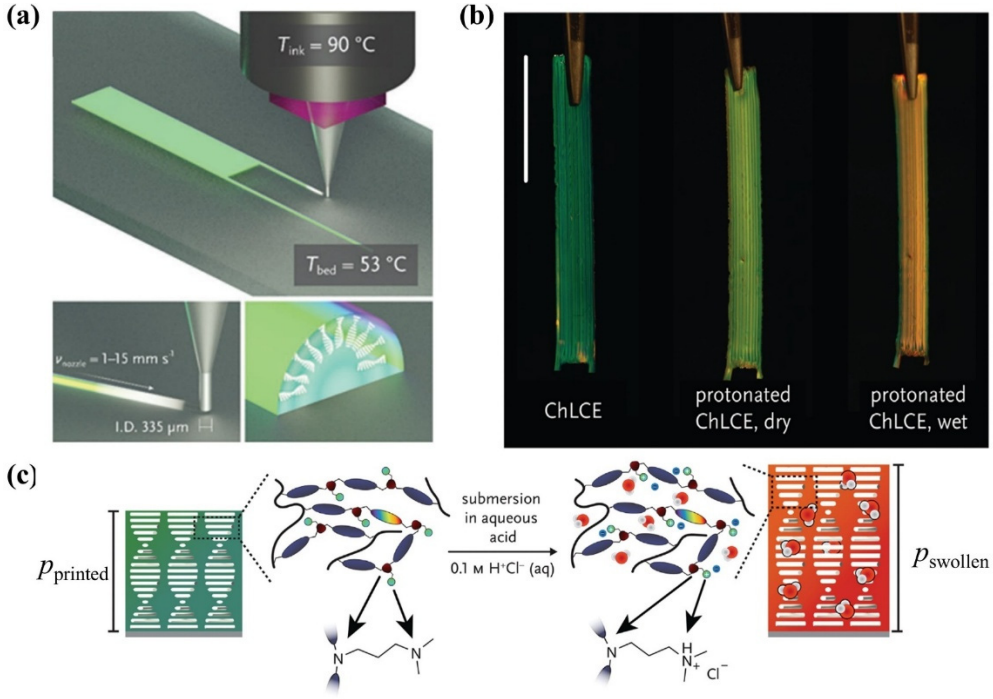

Figure 3. DIW of CLC oligomer inks. (**a**) Schematic of the DIW of the cholesteric liquid crystal elastomers (CLCEs) (**top**), mesophase transitions of the CLCEs (**bottom-left**), and the eventually proposed molecular structure for a perfect planar aligned CLCE (**bottom-right**). Reproduced with permission [76]. Copyright 2021, Wiley-VCH. (**b**) Free-standing CLCE films presenting visible color changes after protonating and pursuant exposure to water. Scale bar: 1 cm. (**c**) Schematic of the transition of CLCE undergoing acidic treatment, highlighting the occurrence of chemical modification with the synchronous change in the length of the cholesteric pitch. Reproduced with permission [77]. Copyright 2022, Wiley-VCH.

To create spatially controlled CLCE geometries, Choi et al. proposed DIW for CLCEs with a programmable mechanochromic response [78]. After deposition, the helical axis was tilted by approximately 32° relative to the printing direction for the combined effects of shear-induced alignment and the generated elongational force upon deposition onto the substrate. The printed CLC elastomers exhibited anisotropic mechanochromism when stretching owing to stretching-direction-dependent differences in the slant angle of the helical axis.

Because CLC oligomer inks are viscous, it is challenging to prepare well-defined helical nanostructures with outstanding color reflection [79–86]. The DIW of solution-processable and low-viscosity CLC inks for dynamic molecular self-assembly allows the preparation of structural-color graphics with vivid colors. Recently, our research group proposed solution-processable CLC inks for DIW of chiral structural-color patterns characterized

by bright colors and mechanochromic responses (Figure 4a) [87]. The solution-processable CLC inks were formulated optimally to enable microscopic self-assembly and macroscopic printing. After deposition onto target surfaces in line with preprogrammed trajectories, the monomers in CLC inks quickly self-organize into helical nanostructures through the evaporation-induced self-assembly process, in which Michael addition reaction enables to proceed in situ on the substrate for several hours at room temperature. The printed LCs are consequently polymerized by UV light for approximately 10 min to cure the microscopic helical arrangement. Multicolored, circularly polarized photonic patterns were fabricated on diverse substrates (Figure 4b). A concept of the circular-polarization cinefilm was proved by printing CLC inks which possess inverse chirality (Figure 4c,d). In addition, mechanochromic, circularly polarized photonic graphics were fabricated by printing CLC inks directly onto highly stretchable elastomeric films (Figure 4e). The as-proposed CLC inks were further printed on a wireless somatosensory electronic glove that can output synchronous visual and electrical signals. Upon bending the human fingers, the glove fingers accordingly stretch, resulting in immediate and simultaneous changes in the structural color and capacitance which can be converted into distinctive electrical signals. The interactively stretchable electronics possessing brilliant colors and antifading characteristics can be extensively utilized in numerous applications like entertainment, home healthcare, medical industry, and robotic control.

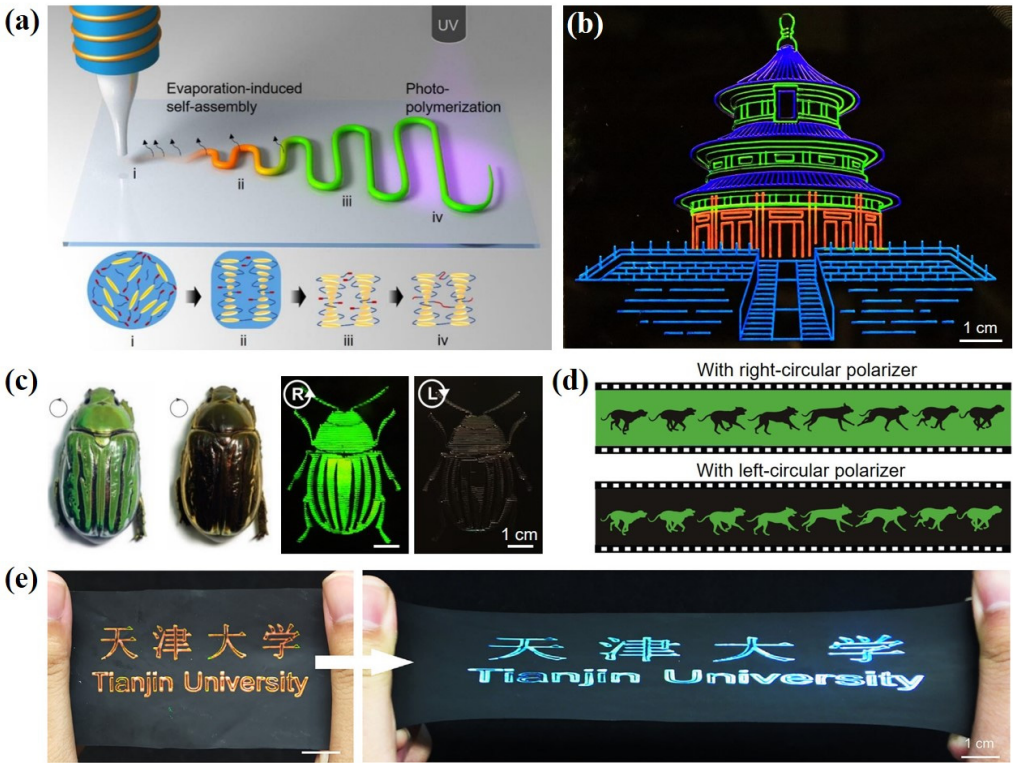

Figure 4. DIW of CLC molecular inks. (**a**) Schematic of DIW of CLC inks on glasses. (**b**) Temple of Heaven pattern printed by utilizing four kinds of CLC inks. (**c**) Beetle *C. gloriosa* (**left**) and the printed beetle patterns (**right**). Green iridescent color was observed with a right-circular polarizer and disappeared with a left-circular polarizer. (**d**) Circular polarization cinefilm via observation under right-circular polarizer (**top**) and left-circular polarizer (**bottom**). (**e**) CLC pattern changed colors from red to blue upon stretching. Reproduced with permission [87]. Copyright 2024, Elsevier Ltd.

3.3. Direct Ink Writing of Cellulose Nanocrystals (CNCs)

The range of wavelengths reflected by the CNCs films can be extended via introducing additives like polyethylene glycol (PEG) or hydroxypropyl cellulose (HPC) to enlarge the length of the cholesteric pitch. Cellulose-based materials can form photonic nanostructures and provide an opportunity to develop eco-friendly structural-color materials and coatings. HPC is an inexpensive, biocompatible cellulose capable of exhibiting lyotropic LC properties. At low concentrations (<40 wt.%), HPC aqueous solutions exhibit a disordered, isotropic structure and are extensively applied as thickening agents and binders in the food and pharmaceutical industries. At high concentrations (50–70 wt.%), polymer chains in a photonic chiral nematic phase constructed using HPC solutions self-assembled into helicoidal nanostructures similar to those found in scarab beetles.

Zhang et al. proposed a CNC ink for fabricating 3D structural-colored objects (Figure 5a) [88]. Two other elements, poly(acrylamide-co-acrylic acid) (PACA) and gelatin, were incorporated into the HPC solutions to produce printable HPC-gelatin-PACA ink. PACA could maintain the shape after printing by in-situ UV crosslinking, and gelatin afforded appropriate rheological properties during printing. This ink can be designed into 3D customized objects on substrates to exhibit angle-independent and vivid structural colors (Figure 5b–d). The resultant macroscopic 3D objects exhibited color adjustability under the control of the ambient temperature owing to the synergic thermoresponsiveness of PACA and HPC. Thus, this CNC ink system can be extended to daily-life commodities including colorant-free decorations in wearable biosensors, cosmetics, and drugs, as well as food industry or customized bionic skins.

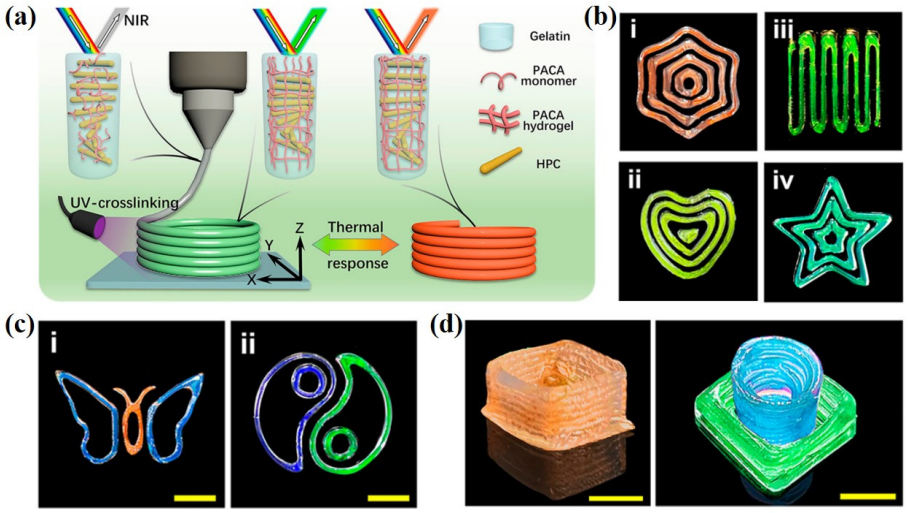

Figure 5. DIW of CNCs. (**a**) DIW of CNC inks for 3D structural coloration. (**b**) Single-colored graphics. (**c**) Multicolored graphics. (**d**) 3D objects. Scale bars: 4 mm. Reproduced with permission [88]. Copyright 2022, National Academy of Sciences.

Similarly, George et al. incorporated PEG into anisotropic HPC solutions to establish printable CNC inks for the DIW of CNCs [89]. At higher shearing rates (97 s^{-1}), the alignment along print paths at an approximately 20° could be attained, generating the coloration with high angle dependence. Materials with unique chiroptical properties displaying an optical response to mechanical deformation were fabricated due to the plasticizing effect of PEG in conjunction high-shear-rate extrusion. The utilization of path-dependent cholesteric domains to be an additional parameter expanded the design space further and allowed the response pattern to be modified by changing the infilling path of objects. The aesthetics of the materials acquired by HPC-based inks during high- or low-shear extrusion afford a sustainable source of structural colors capable of being utilized in optical sensing and coating applications.

Despite the capability of DIW to accomplish the printing of some complex-shaped 3D structural-colored materials, it is limited by inherent defects, leading to pervasive challenges such as coarse surface texture, constraints in material versatility, and reduced printing precision. In DIW, the ink is extruded through a nozzle, which means that the printing resolution is limited by the nozzle diameter. In addition, to achieve a bright structural color, a lengthy post-treatment is necessary, which may cause material cracking. These limitations restrict the application of DIW in printing high-precision structural-colored materials.

3.4. Direct Ink Writing of Block Copolymers (BCPs)

For high-production volume printing of BCPs, Patel et al. reported customizable DIW for BCP deposition to achieve functional, spatial, and microstructural patterning of structural colors (Figure 6a) [90]. Well-designed poly(dimethylsiloxane)-block-poly(lactic acid) (PDMS-b-PLA) bottlebrush BCPs were used as ink. The structural colors of bottlebrush photonic crystals could be modulated via controlling the bed temperature and printing speed during DIW printing (Figure 6b). After the comparison of printed samples, a pronounced blueshift in reflected wavelength is observed as printing speed increases, while increasing temperature results in a marked redshift. The intricate spatial and functional control for depositing more versatile patterns like the chameleon pattern comprising diverse colors printed as sequential layers via nonequilibrium assembly techniques with the integration of hardware and software approach.

Jeon et al. achieved the dynamic tunability of structural colors during printing by integrating polystyrene-block-polylactide (PS-b-PLA) cross-linkable BCPs with a UV-supported 3D printer (Figure 6c) [91]. By employing a single ink material, multiple colors were achieved within a single printing process by UV-crosslinking-driven kinetic trapping of the evaporative assembly. The technique realized the preparation of structural colors from dark blue (392 nm) to orange (582 nm) in the visible wavelength spectrum through reducing UV light irradiance from 411 to 0 μW/cm^2. A mimic of Van Gogh's "The Starry Night" with yellow-to-green-to-blue village, yellow-to-green moonlight, and blue-to-green night sky through programming the temporal profile of UV light irradiance to create patterns with color gradients merely adopting a single ink material. (Figure 5d). It can be predicted that this approach would shine light on anticounterfeiting patterns for art masterpieces and decorations in luxurious furniture.

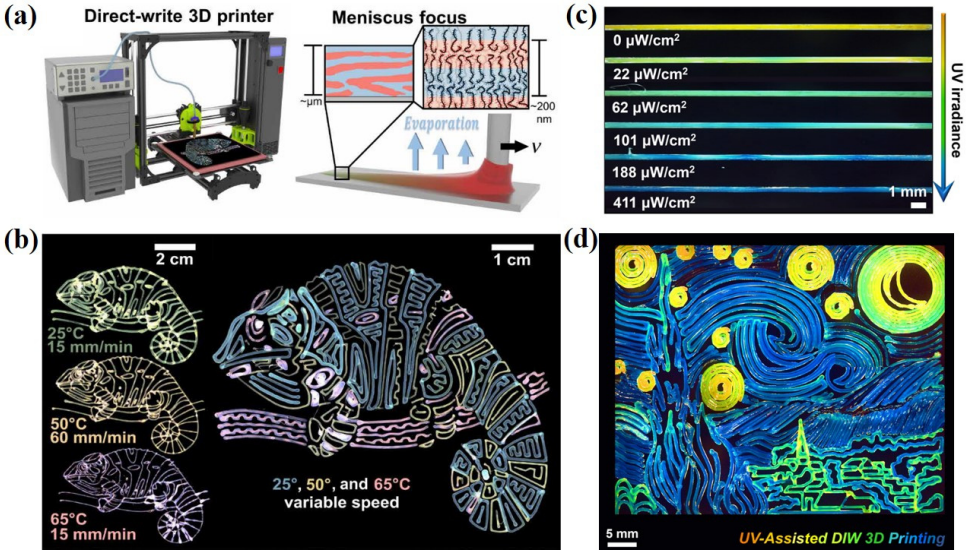

Figure 6. DIW of BCPs. (**a**) Scheme of molecular self-assembly and DIW of BCPs during the solution-casting process. (**b**) Chameleon patterns created under stationary printing conditions (bed temperature, pressure, and printing speed) as successive prints. Reproduced with permission [90]. Copyright 2020, AAAS. (**c**) Printed lines under various standards of irradiance of UV light when printing. (**d**) Starry Night pattern fabricated via dynamic UV-assisted DIW printing. Reproduced with permission [91]. Copyright 2024, National Academy of Sciences.

4. Inkjet Printing of Structural-Color Materials

Inkjet-printed structural-color materials could be categorized into two types according to the mechanism of generation of structural-color patterns: drop-on-demand inkjet-printed inks on substrates and continuous inkjet-printed inks on photonic polymer films. In drop-on-demand inkjet printing, droplets are merely created and ejected when needed, allowing for minimal material usage, smaller drop size generation, higher placement accuracy, and low cost. Typically, drop-on-demand inkjet printing is a functional technique for preparing structural-color patterns by integrating direct writing with particle self-assembly in droplets [92–94]. The inkjet-printing quality of structural-color patterns is subject to elements such as ambient temperature, humidity, substrate wettability, ink composition, and inkjet printing parameter settings. Continuous inkjet printing of inks on photonic polymer films is an emerging strategy for printing multicolor patterns [95,96]. The advantage of this strategy is that the pattern can be erased by removing the ink and reprinting.

4.1. Inkjet Printing of Colloidal Crystals

Song et al. achieved significant results and made tremendous contributions to the preparation of patterned colloidal crystals for practical applications [97–99]. In their researches, structural-color patterns containing dots, lines, and surface shapes were fabricated successfully by the self-assembly of colloidal nanoparticles via adjusting the preparation conditions of inkjet printing. For the dot-like structural-color patterns, inkjet printing was applied to deposit latex droplets onto an octadecyltrichlorosilane-treated substrate which afforded a high receding contact angle and enabled free sliding of the three-phase contact line (TCL). All the particles within each droplet were driven inwardly during the drying process for the effect of the free-sliding TCL and assembled into structural-color domes spontaneously, realizing a great height-to-diameter (H/D) ratio (Figure 7a) [100]. The printed structural-color domes had a uniform shape and size with the particles assembled into a densely-packed face-

centered cubic structure. Interestingly, structural-color domes with H/D ratios exceeding 3/8 exhibited angle independence (Figure 7b). This convenient printing approach affords an efficient method for exploiting displays with extensive viewing angles. The facile printing approach could offer a high-efficiency strategy for creating advanced displays and other optical devices. DIW-printed advanced displays based on structural-color materials through this method can control the phase, amplitude, and polarization of light at subwavelength scales as beam deflectors and optical encryption devices. Structural-color optical sensors capable of making adjustment to their reflection wavelength in response to environmental stimuli can be extensively applied in environmental monitoring, biosensing, and wearable health diagnostics.

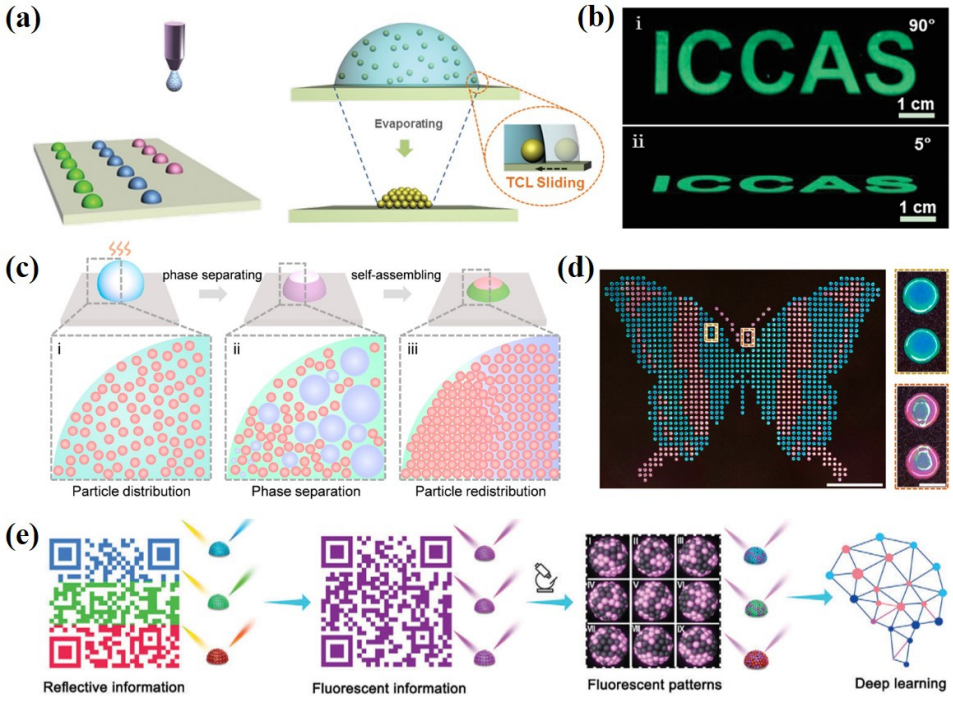

Figure 7. Inkjet printing of colloidal crystals. (**a**) Inkjet printing patterned PC domes onto hydrophobic surfaces through adjusting the sliding TCL. (**b**) Fluorescent structural-color domes' angle-independence of the fluorescence images. Reproduced with permission [100]. Copyright 2014, Wiley-VCH. (**c**) Schematic of the fabrication of dual-color domes on a basis of phase separation. Reproduced with permission [101]. Copyright 2022, American Chemical Society. (**d**) A butterfly-like pattern printed via heterogeneously self-assembling on a PDMS substrate. 180 nm and 220 nm silica nanoparticles were utilized to construct green-blue and red-green depositions, respectively. Scale bar: 1 cm; zoom in 0.5 mm. Reproduced with permission [102]. Copyright 2023, American Chemical Society. (**e**) Inkjet-printed pattern combined with the structural colors and fluorescence for multiplex encryption and anticounterfeiting. Reproduced with permission [103]. Copyright 2024, Wiley-VCH.

Dual-color spots are significant identity labels that deliver warnings and mating information. Li et al. developed a one-pot method on a basis of the phase-separation-associated non-uniform self-assembly of silica nanoparticles to fabricate dual structural-color domes (Figure 7c) [101]. In the drying droplets, individual nanoparticles were nonuniformly distributed into two compartments owing to the varying compatibility of nanoparticles between the two phases and the droplet inner flows. The colors of the domes resulted from nanoparticles' self-assembly are capable of being programmed via modulating the assembly conditions. A tremendous volume of content in encrypted patterns was designed using dual-color domes, presenting promising applications for information transfer. Later, Li et al. utilized the spatial restriction induced owing to the skin layer packaging of a drying colloid PEG droplet to enable the heterogeneous self-assembly of individual nanoparticles (Figure 7d) [102]. Colloidal crystals with homogeneous or heterogeneous plane orientations were fabricated by modulating the concentration of PEG within the droplets. This heterogeneous self-assembly approach enables the extensive utilization of various colloidal nanoparticles, different droplet shapes, and diverse substrates. Coatings fabricated by this strategy have the advantages of tunable colors, unfadeness, and low-energy consumption, which can be extensively used in anti-counterfeiting for economic security and human health.

The combination of fluorescence and structural color is a good strategy for fabricating multiplex encryption systems. Gao et al. proposed a robust multiple encryption system with integration of structural color and

fluorescence via programmable inkjet printing using colloidal photonic inks (Figure 7e) [103]. Colloidal photonic crystals exhibit structural-color patterns under sunlight. Under UV light, those exhibiting fluorescence in the same region display different fluorescence patterns. Microscopic fluorescence patterns which are unclonable physically can be observed in specific regions with fluorescence microscopy, the resulting macroscopic dual-mode encryption offered strong identifiable encrypted information. Moreover, evaporation process-induced fluorescence patterns exhibit unparalleled, uniform, and irrelevant random properties with high complexity and sufficient encoding capacity and further deep learning could be employed to construct a database and certify its credibility. It is expected that this system will provide a promising technique to combat counterfeiting and reinforce the practical application of fluorescent and structural colors for anticounterfeiting in high value products.

4.2. Inkjet Printing of Cellulose Nanocrystals (CNCs)

CNCs are ideal candidates for use as cost-effective and sustainable inks to print bespoke patterns and scalable photonic coatings. Whereas, the small volume and large surface area of sessile CNC droplets typically generate rapid evaporation, producing microfilms with a coffee-stain-like morphology and pretty vague coloration. Williams et al. proved that inkjet printing of CNC droplets directly via an immiscible oil layer enables instantly inhibit water loss, realizing a reduced internal mass flow and more sufficient time used for cholesteric self-assembly [104]. The color of individual microfilm depended on the initial composition of the droplet, which was capable of being adjusted as required through leveraging the overprinting and coalescence of numerous smaller droplets of various inks. The approach realizes the fabrication of multicolored patterns with intricate optical behaviors, like polarization-selective reflection and angle-dependent color. Finally, the array could be achieved responsive to stimulations (e.g., polar solvents and UV light) by the inclusion of degradable additives. These advantageous properties make inkjet-printed photonic CNC arrays suitable for optical anticounterfeiting and smart colorimetric labeling applications. It can be envisaged that high-quality, full-color photonic patterns could be highly compatible with the stringent processability demands of commercial printing including packaging labels.

4.3. Inkjet Printing Inks on Photonic Polymer Coatings

In 2018, Schenning and coworkers proposed inkjet printing of CLC inks on photonic polymer coatings for the first time (Figure 8a) [105]. They first prepared CLC polymer coatings containing nonpolymerizable LCs. Elimination of the non-polymerizable cyanobiphenyl LC derivative (5CB) resulted in the collapse of the polymer network, achieving to reduce the helical pitch length and impart a violet color to the coatings. This process also made the network highly flexible and optical response to stimuli enhanced. Moreover, this flexible network can be swollen using nematic-phase LC inks E7, which could be readily filled in an inkjet printer cartridge and precisely introduced at the desired areas in a controlled method. The wavelength of the reflected light is in direct proportion to the helical pitch length. Therefore, full-color images can be patterned on polymer coatings through inkjet printing with different amounts of LC ink on demand. Importantly, the printed patterns exhibited stability and durability under ambient conditions and could be entirely erased to allow for printing another new pattern. The fully rewritable and printable photonic coating from a CLC polymer network paves the avenue for rewritable photonic papers and arbitrary polymer patterns responsive to external stimulus.

For universal patterning of program dual-mode images, Liu et al. designed fluorescent LC polymer coatings to create geminate patterns using two-chromatic inkjet printing technique (Figure 8b) [106]. Nanocomposites as a novel paradigm of fluorescent LC materials integrate colloidal quantum dots with CLC polymer networks for producing extensive color palettes of photoluminescence and Bragg reflection. Based on two-chromatic inkjet printing technology, geminate, high-resolution, and full-color patterns with two colors of different mechanisms have been inkjet printed, for example, fluorescent dragon and reflective Phoenix.

BPLCs can be used as photonic polymer coatings for inkjet printing. Yang et al. fabricated a printable photonic polymer coating was on a basis of a monodomain BPLC network (Figure 8c) [107]. BPLC polymer coatings were covalently bonded to a glass substrate that was patterned with LC ink to swell the polymer network. The degree of swelling was determined by the amount of LC ink printed, which could be manipulated via regulating the voltage of the inkjet printer. Random multicolor patterns spanning the visible light wavelength from 451 to 618 nm could be printed and erased multiple times, rendering these BPLC polymer coatings shine light on responsive photonic materials and rewritable photonic papers. Meng et al. reported a high-resolution “live” pattern was resulted from the well-scheduled diffusion of LC ink on BPLC polymer networks with modified wettability (Figure 8d) [108]. This hydrophobic substrate significantly suppressed random spreading and diffusion of the ink, generating high-resolution patterns. BPLC materials featured with the intrinsic properties like ultrafast electro-

optical switching and wide viewing angle generate field-sequential color displays in the millisecond range, which function as advanced optical communication and adaptive photonic devices.

In addition to LC inks, water can also be used as an ink for inkjet printing. Yang et al. fabricated humidity-responsive, color-changing photonic polymer coatings on a basis of hydrogen-bonded BPLC networks [109]. The polymer coatings exhibited humidity-responsive reversible color changes in the visible spectrum of light, which were driven by breaking the hydrogen bonds and subsequently converted into hygroscopic polymer coatings. Rewritable photonic patterns were obtained by inkjet printing water onto the dried hygroscopic BPLC polymer coatings. This work shines light on applications in diverse civil and military fields containing adaptive camouflage, information encryption, sensors, and beyond.

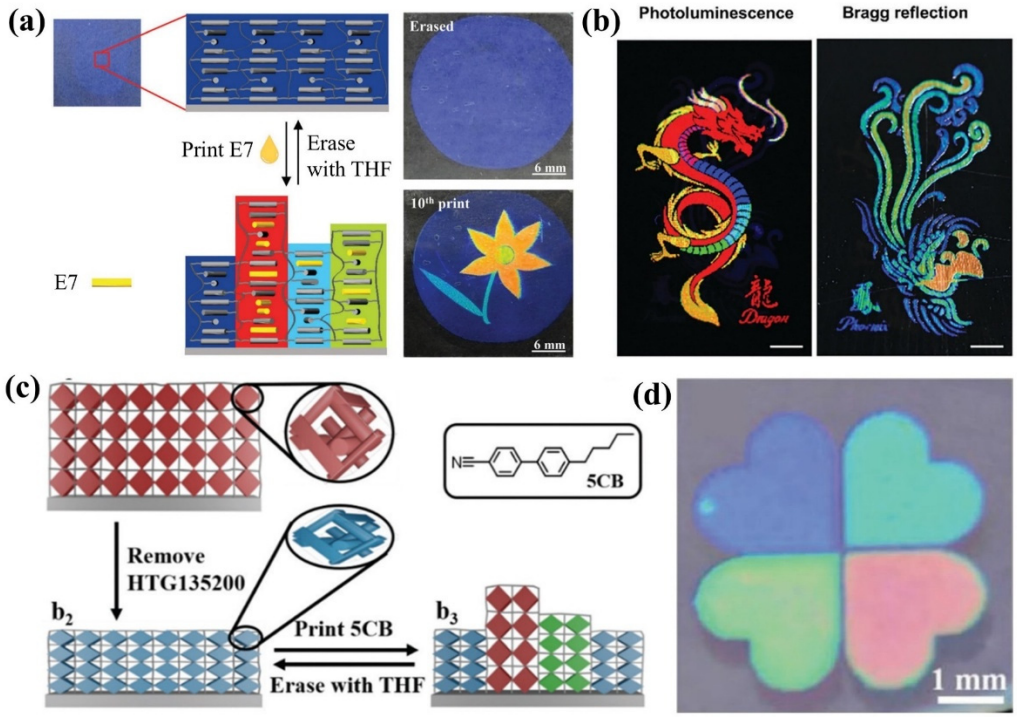

Figure 8. Inkjet printing of LCs on photonic polymer coatings. (**a**) Working mechanism of patterning in the CLC polymer coating. Reproduced with permission [105]. Copyright 2018, The Royal Society of Chemistry. (**b**) Photographs of a full-color pattern achieved by two-chromatic printing technique to display the images of fluorescent Dragon and reflective Phoenix upon UV excitation and white light irradiation, respectively. Scale bars: 5 mm. Reproduced with permission [106]. Copyright 2024, Wiley-VCH. (**c**) Working mechanism of patterning in the BPLC polymer coating. Reproduced with permission [107]. Copyright 2019, The Royal Society of Chemistry. (**d**) Four-leaf flower pattern created through well-designed multilayer printing on a BPLC polymer coating. Reproduced with permission [108]. Copyright 2022, Wiley-VCH.

4.4. Inkjet Printing Based on Total Internal Reflections

In 2020, Goodling and Zarzar illustrated brilliant structural colors could be created at microscale concave interfaces and proved the coloration principle of interference due to total internal reflections systematically, thereby establishing the feasibility of manipulating the structural colors using low-index materials [110]. The structural colors of total internal reflections could be directly achieved using single microstructure without applying complex particle self-assembly or polymer phase-separation structures [111–113].

Based on the total internal reflection effect, Li et al. developed a facile structural-color printing technique were capable of realizing the full-color fabrication of highly photorealistic images with an individual transparent ink by the commercial inkjet printing approach (Figure 9a) [114]. Transparent inks can be produced in a large quantity from monomer or polymer solutions. When ink droplets are printed on a transparent and hydrophobic substrate, they retract into the ideal microdomes with large curvature angles for the effect of surface tension. These inverted microdomes can generate an interference color from total internal reflections and function as independent pixels for constructing the color images. The color of each microdome which was controlled by the optical path is adjusted across the whole visible region by modulating the physical morphology (Figure 9b). Thus, we can facilely gain full-color pixels using one transparent ink and one printing nozzle. Every pixel was decoded into the

corresponding printing parameters, and a digital programmable printer was utilized to prepare the full-color structural-color images. The lightness, grayscale, gamut, and saturation of the image can be systematically manipulated using single-pixel precision (Figure 9c). Additionally, this color-printing approach is entirely compatible with the commercial printing technique and is suitable for large-scale industrial production. Therefore, it is greatly anticipated that the optical Janus property of coloration and transparency gained from different sides will facilitate structural colors for the practical applications in colorimetric sensor, anticounterfeiting technology, dynamic display, and smart window. For instance, the facile flipping can realize the fully reversible switching between radiative cooling and heating due to the asymmetrical optical effect.

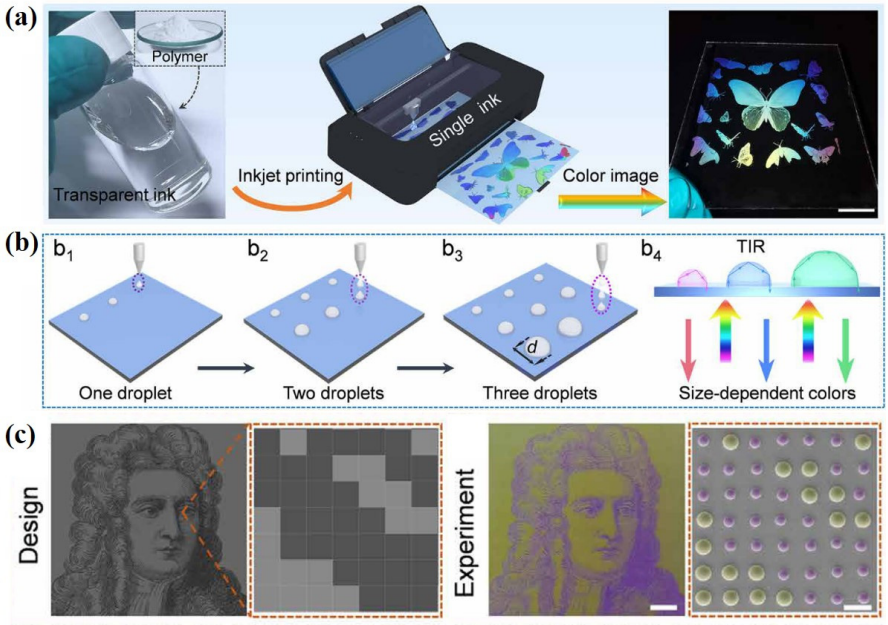

Figure 9. Full-color printing based on total internal reflections. (**a**) Process of structural-color printing with an individual transparent polymer ink. Polymer ink can be directly created by dissolving the polyacrylic acid into the mixture of ethylene glycol and water. Scale bar: 2 cm. (**b**) Schematic of the D-B-D printing (b_1 to b_3) to fabricate and integrate the different microdomes through which the microdome diameter can be controlled precisely. Viewing from the bare-glass (blank) side (b_4), the microdomes can display size-dependent colors for diverse optical paths of total internal reflection. (**c**) Designed grayscale and experimental colorful patterns of Isaac Newton's portrait. Scale bars: 40 μm. Reproduced with permission [114]. Copyright 2021, AAAS.

5. Other Additive Manufacturing Methods for Preparing Structural-Color Materials

5.1. Digital Light Processing (DLP)

The formulation of precursor solutions for DLP printing is critical for the successful printing of 3D structures with ideal performance. Specifically, the precursor solutions used in DLP printing consist of monomers, cross-linking agents, and photosensitizers, which can be cured by the phase transition from liquid to solid during exposure to UV or blue light. Because precursor solutions containing colloidal particles have been extensively utilized in the fabrication of patterned photonic crystal films, they can also be cured layer-by-layer to theoretically establish a 3D structure through integration with DLP [115]. DLP enables the fabrication of complex, high-resolution aesthetic patterns with durable structural colors. DLP-printed structural-color materials can be precisely engineered to manipulate light for sensing, display, and counterfeiting technologies [116].

Liao et al. were the first to report a combination of DLP and precursor solutions containing colloidal particles [117]. They reported a printable colloidal photonic crystal ink consisting of highly charged elastic nanoparticles (HENPs) achieved dispersion in a precursor solution. They fabricated 3D colloidal photonic crystal hydrogels with macroscopic geometries and the corresponding structural colors using DLP (Figure 10a,b). The key to this approach is to preserve the ordered arrangement of the HENPs in the precursor solution through electrostatic interactions before printing. During the printing process, the precursor solution polymerizes under the projected pattern, which locks the arrangement of the HENPs into the printed structure. Consequently, a 3D customized object with a stable structural color is formed. This approach allows the production of 3D colloidal photonic crystal hydrogels with the desired functions by tuning the ink composition or printing parameters. For

instance, using an ink containing a thermoresponsive monomer, such as N-isopropylacrylamide (PNIPAm), they prepared bioinspired structures that exhibit color variations corresponding to temperature changes. The tunable and reversible structural-color performance reinforces the practical applications like color-morphing soft robots for surveillance, reconnaissance, and wildlife observation without disturbing natural habitats.

However, the printing process in this method is non-continuous, as each consequent layer cannot be printed until the previous layer is complete. This limitation results in a layered structure with a rough surface and poor fidelity. To solve this problem, continuous DLP has been proposed, and a similar method has been successfully employed for the fabrication of structural-colored materials.

Zhang et al. utilized a hydrogen-bond-assisted colloidal resin to print 3D structural-colored materials which have been self-assembled well through a previously developed one-droplet 3D printing strategy (Figure 10c–f) [118]. During the printing process, the resin was refilled while the supporting platform was simultaneously elevated. Figure 9d,e shows the ink composition and the final printed structures. In the UV-curable system, polystyrene latex particles as the structural color provider, carbon black designed to decrease incoherent scattering, and photocurable monomers were stabilized by hydrogen bonds between them during printing. Meanwhile, using the continuous curing method, the pressure difference between the newly filled resin and the already cured layer creates a suction force that ensures the inward filling of the resin and tight self-assembly of the colloidal particles within the cured layer. Just-printed objects exhibit minimal structural colors. After the removal of water via evaporating, the printed objects can construct a densely arranged hexagonal colloidal particle structure to generate a brighter structural color. Moreover, the structural color could be fine-tuned through controlling the printing speed and particle diameter [119–123].

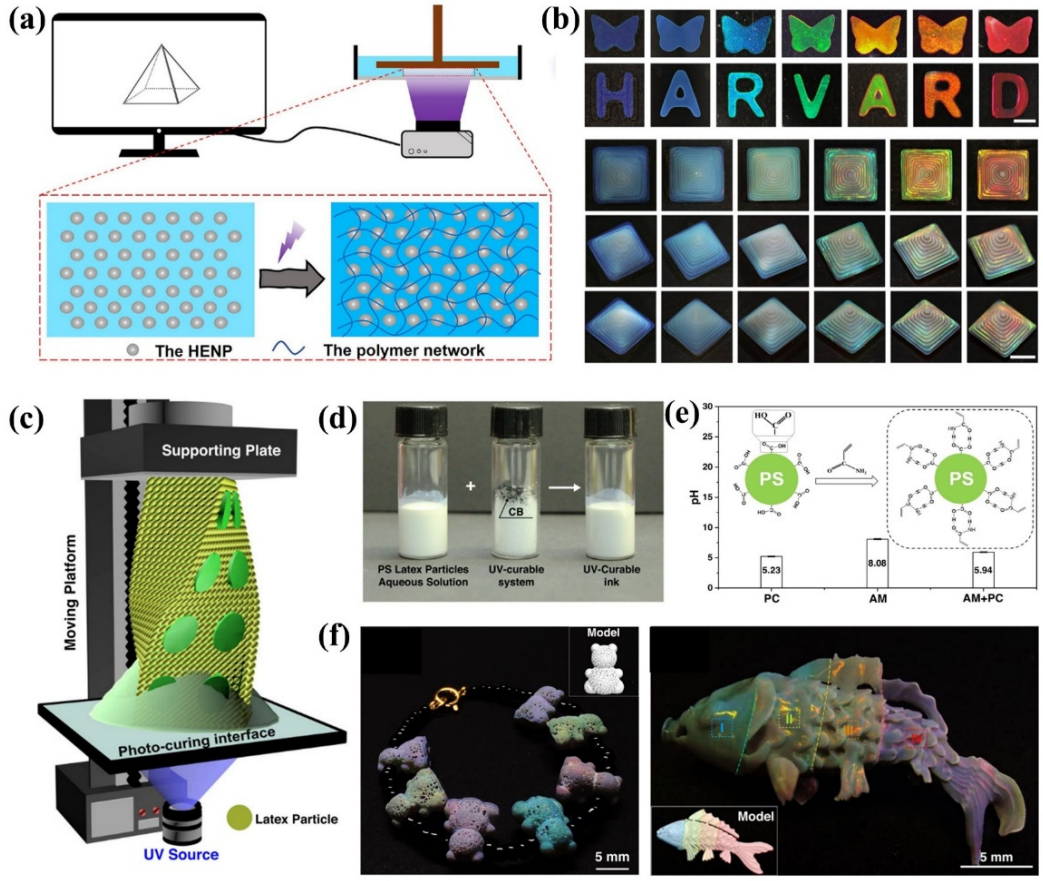

Figure 10. Structural-color materials via DLP. (**a**) Schematic of the DLP 3D printing of colloidal photonic crystals. (**b**) Printed 2D and 3D non-close-packed colloidal photonic crystals with different colors. Scale bars: 2 mm. Reproduced with permission [117]. Copyright 2024, Elsevier Ltd. (**c**) Scheme showing the process of consecutive resin refilling and hydrogen bond-assisted synergistically DLP 3D printing apparatus. (**d**) UV-curable structural-color ink formation. (**e**) pH characterization of pure aqueous dispersion solution of PS latex particles, pure aqueous solution of monomer acrylamide (AM), and aqueous mixture of PS latex particles with AM. (**f**) Optical images of the multiple structural-color models printed using various PS latex particle diameters. Reproduced with permission [118]. Copyright 2022, Nature Publishing Group.

5.2. Two-Photon Polymerization Lithography (TPL)

TPL relies primarily on a process known as two-photon polymerization. During this process, the photoinitiator at the laser focus simultaneously absorbs two photons and generates radicals that trigger polymerization in the photoresist. TPL has been extensively investigated for the manufacture of various 3D micro/nanodevices with high resolutions, which can be utilized in fluidic devices, optical materials, metamaterials, and cell cultures [124].

Using TPL technology, freely designed structural-color materials with highly ordered 3D nanostructures could be prepared using photoresists. However, creating forbidden gaps in the visible light wavelength desires a high resolution that exceeds that of the regular TPL system. The laser-writing process disturbs the stable microenvironment in the photoresist and results in unwanted polymerization within the surrounding regions. To overcome this challenge, Liu et al. proposed a heat-shrinking technique was leveraged to fabricate 3D-printed photonic crystals which possessed a 5× reduction in the lattice constants, realizing sub-100-nm features with a full spectrum of colors (Figure 11a,b) [125]. The lattice structures as 3D color volumetric elements facilitated the printing of the 3D microscopic scale objects, such as the first multicolor microscopic model of the Eiffel Tower, which measured just 39 μm in height and a color pixel size of 1.45 μm. This method for printing colorful 3D structures at the microscopic scale offers significant potential for direct patterning and the integration of spectrally selective devices, including photonic crystal-based color filters, onto curved surfaces and freeform optical elements. This ability to precisely produce structural color within complex 3D objects could be extended to developments in integrated 3D photonic circuitry and compact optical components, achieving position tracking and full-color wide angle panoramic views.

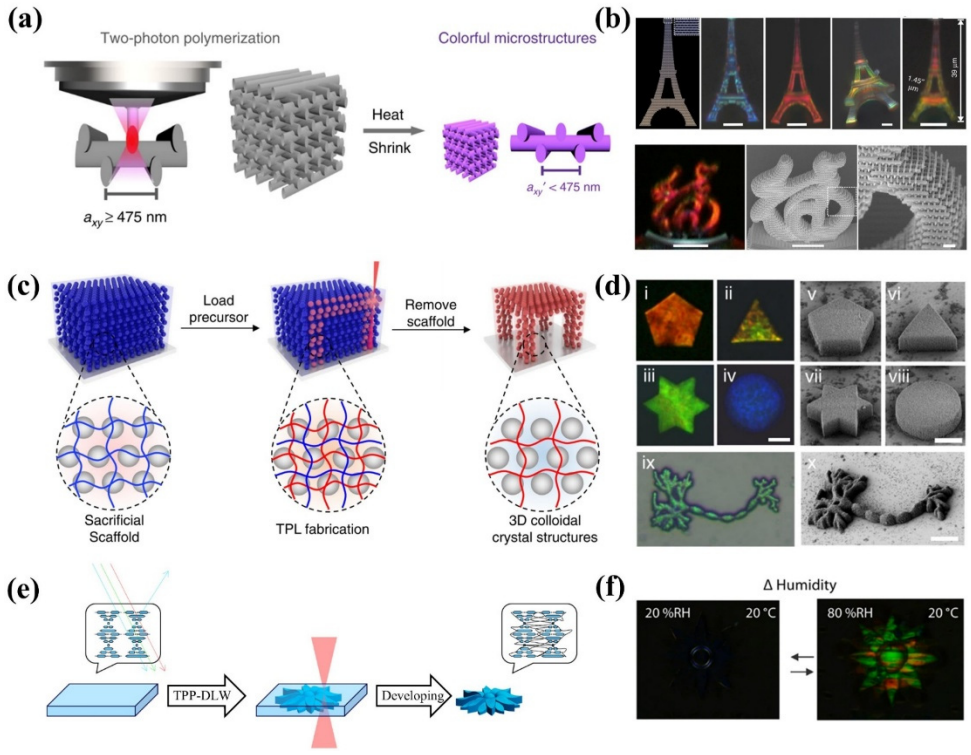

Figure 11. Structural-color materials via TPL. (**a**) Schematic of 3D-printed structural-color materials via heat-induced shrinking. (**b**) 3D color prints. Scale bars: 10 μm. Reproduced with permission [125]. Copyright 2019, Nature Publishing Group. (**c**) Schematic of the sacrificial-scaffold-mediated TPL process. (**d**) Colloidal crystal microstructures manufactured via the sacrificial-scaffold-mediated TPL. Scare bars: 20 μm. Reproduced with permission [126]. Copyright 2022, Nature Publishing Group. (**e**) Fabrication of 4D photonic microactuators via TPL. (**f**) Polarized optical micrographs of the flower presenting the color changes driven by humidity. Reproduced with permission [127]. Copyright 2020, American Chemical Society.

Endowing structural-color materials with highly precise 3D microarchitectures will open exciting prospects for novel applications. Liu et al. reported a sacrificial scaffold-mediated TPL method to enable the preparation of intricate 3D colloidal crystal microstructures possessing ordered nanoparticles inside (Figure 11c,d) [126]. Utilizing a degradable hydrogel scaffold, the disturbance effect of the femtosecond laser on the self-assembly of

nanoparticles can be solved. Thus, colloidal crystal microstructures in hydrogel and solid state with variable structural colors, free-designed geometries, and diverse compositions can be facilely manufactured.

Stimuli-responsive photoresists can also be used to construct four-dimensional (4D) microstructures. Pozo et al. reported a photonic photoresist on a basis of supramolecular CLC was developed for fabricating stimuli-responsive photonic microactuators using two-photon polymerization direct laser writing, during which hydrogen bonds as supramolecular cross-linkers formed and cleaved after base treatment. This reversible process contributed to a stimuli responsive network (Figure 11e,f) [127]. Photonic 4D microactuators, including butterflies, flowers, and pillars with submicron resolution, have been created according to the advanced method. In addition, these structures exhibited dual responses to changes in humidity (directly) and temperature (indirectly). The hygroscopic character of the polymer network induced a shape change of up to 42% at 75% RH. The controlled expansion of the microactuators under conditions of various humidity and temperatures generates a corresponding color change for the adjustment of the nanoscale CLC pitch within the ordered network. This dual-mode responsive material can construct microrobots, which can release drugs and operate tissue repair within the physical environment in a directional manner.

5.3. Fused Deposition Modeling (FDM)

A FDM machine comprises a movable platform and a mechanical arm that controls the extrusion nozzle. Customized 3D structures can be created by controlling the movements of the nozzle and platform in the X, Y, and Z directions. The main difference between the FDM and DIW is the printing material. In DIW, the printing materials are in a liquid or paste state that can be directly extruded. In contrast, FDM requires the material to melt into filaments before printing. Similar to the previously mentioned DIW, FDM can also print structurally colored materials by incorporating suitable "building blocks" into the extruded material [128]. FDM enables to facilitate the practical applications including new passive color mixing [129], biocompatible scaffold [130] and biomimetic soft robots [131].

Boyle et al. designed a structural-colored material using a ring-opening polymerization method and used it as a building block in FDM to create 3D objects exhibiting structural color [132]. As depicted in Figure 12a, such a material is composed of dendritic BCPs that can self-assemble into various kinds of 1D, 2D, and 3D periodic structures. More specifically, BCPs can self-assemble into a layered structure with a scale similar to the wavelength of light, thus resulting in a structural color. By directly controlling the molecular weight of the block copolymers, the domain size of the nanostructure in the printed parts could be adjusted to tune the reflection peak across the visible light spectrum. Therefore, printed objects with diverse structural colors can be manufactured by altering the molecular weights of the BCPs (Figure 12b). This FDW 3D printing approach has the advantages of ease of use, reliability, and low cost; however, each object is merely available in an individual color. Thus, intricate parts of diffractive optical elements with customized optical properties can be fabricated without any pigments or dyes. The printed photonic objects with high precision enable to manipulate the wavefront in line with different wavelengths and generate the desired pattern or structural beams for filtering light or even guiding specified light frequencies around a curved geometry.

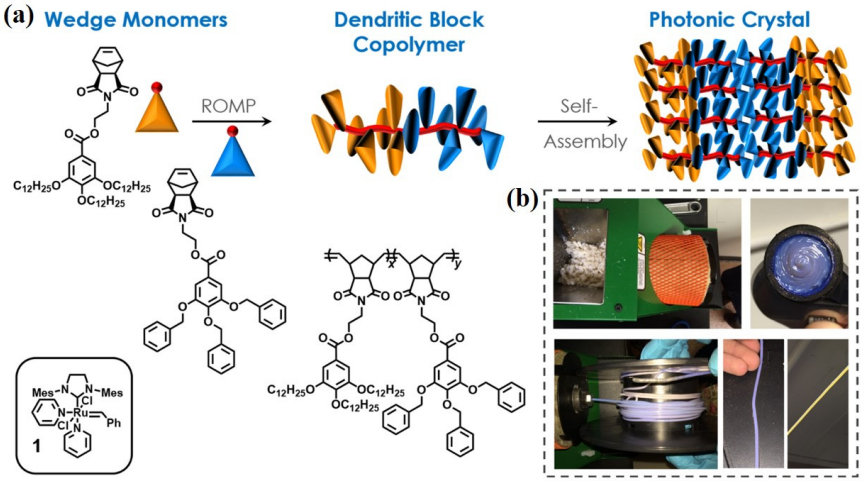

Figure 12. Structural-color materials via FDM. (**a**) Synthesis of the rigid-rod dendritic block copolymers and their self-assembly process. (**b**) Colorless block copolymers self-assemble into a colored filament during extrusion in the extruder nozzle. Reproduced with permission [132]. Copyright 2017, American Chemical Society.

Similar to DIW, FDM presents challenges such as surface roughness, restricted printing resolution, and limited material selection, as it also involves the controlled extrusion of certain materials from a nozzle. Moreover, to ensure the homogeneous dispersion of the nanoscale building blocks in the raw materials, a prolonged agitation and blending process is required, which is essential for achieving consistent color and optical properties throughout the printed objects. However, these extended processes require long-term stirring at high temperatures, which inhibits the incorporation of molecules with low thermal stability, such as bioactive molecules, into the raw materials.

6. Conclusions

In this work, we deliver a state-of-the-art review of the additive manufacturing of structural-color materials. A comprehensive overview of each manufacturing method, printable ink, properties, and limitations is presented in Table 1. For the DIW of structural-color materials, several printable inks, such as colloidal crystal inks, CLC inks, CNC inks, and BCP inks, have been formulated with both macroscopic printing rheology and microscopic self-assembly properties. For inkjet printing of structural-color materials, four strategies have been showcased: inkjet printing of colloidal crystals, inkjet printing of cellulose nanocrystals, inkjet printing inks on photonic polymer coatings, and inkjet printing based on total internal reflections. For the DLP of structural-color materials, the printable inks are cured from the liquid state to the solid state when exposed to UV or blue light; this process is repeated layer-by-layer until the entire 3D object has been constructed. For TPL of structural-color materials, high-energy pulse lasers are utilized to induce localized photochemical reactions within the material and produce high-resolution photonic nanostructures. In the FDM of structural-color materials, the printable build blocks self-assemble into filaments, and 3D structural-color objects are formed via filament extrusion.

Despite significant progress, additive manufacturing of structural-color materials for practical applications is still in the early phases of development. There are numerous challenges and opportunities to accelerate the development of this exciting field. On the one hand, the structural designability of additive manufacturing approaches is limited. Extrusion-based printing methods, like DIW, inkjet printing, and FDM, are characterized by rough surfaces and limited ink options because the printing materials and resolution are strictly constrained by the extrusion process. Structurally colored materials generated using DLP methods also exhibit notable layered structures and have limited design freedom. TPL can achieve high printing resolutions but faces challenges in efficiently printing large-scale structures. Therefore, novel additive manufacturing strategies that facilitate rapid and efficient material processing on a large scale are necessary to address these issues [133,134]. On the other hand, the capabilities of structure-color materials need to reinforce and extend its practical applications. The following key respects of printed structure-color materials should be considered to achieve this goal: (1) Printable structural-color inks: currently, the printable structural-color inks mainly involve colloidal particles, CLCs, CNCs, and BCPs. The limited material selection is a prevalent barrier for additive manufacturing manners, considering the compatibility of ink properties with additive manufacturing methods. Structural-color inks with high printability and stable periodic arrangements are urgently desired. Under the support of machine learning, the relevant abundant samples can be assembled and managed to predict ink formulations that optimize printability and color vibrancy. (2) High quality structural color: the color quality is often unsatisfied owing to the inevitable impact of the additive manufacturing process on the self-assembly. Considerable efforts are still required to obtain fine color resolution, broad color gamut, high color reflectivity, and improved color stability. Achieving this goal entails novel materials and self-assembly mechanism that can mitigate the undesired influence caused by the printing process [135]. Specifically, it can be solved via leveraging microfluidic droplet-based methods to precisely deposit self-assembling colloidal particles in a controlled manner either or applying programmable electric, magnetic, or acoustic fields to guide nanoparticles positioning for defect-free photonic structures. (3) Functionality: the long-term development goal of structure-color materials is to reinforce its functionality for practical applications. Key solutions for achieving this goal include using functional inks [136], printing combinatorial materials [137], and expansion of functional substrates capable of supporting structural colors [138,139], such as flexible substrates, textiles, and three-dimensional objects. The functionalization of materials with versatile and robust properties should be highlighted in the future, which aims at reinforcing resistance to environmental factors and exploiting extensive opportunities of environmentally conscious manufacturing practices. In the last decade, the additive manufacturing of structural-color materials has shown a feasible path for programming and manipulating photonic crystal objects in customized geometries. With the development of additive manufacturing technology and a deepening understanding of artificial structural-color materials, we believe that structural colors with free-designed structures and unprecedented properties will be developed in the near future. It is anticipated that the exploitation of additive manufacturing of bioinspired structural-color materials would yield vast opportunities and significant challenges, and joint collaboration from scientific researchers in the fields of multi-disciplinary specialties will expedite the

development of advanced manufacturing techniques, which mainly contains portable medical devices [140,141], biomedical imaging [142,143], personal wearable devices [144,145], etc.

Table 1. The manufacturing methods, printable inks, properties and limitations of structural colors.

Manufacturing Methods	Refs.	Printable Inks	Properties	Limitations
DIW	[71]	Silica particles/carbon black nanoparticles in acrylate resin	Customized structural-color graphics (absolute reflectivity > 80%)	High viscosity (>1.6 × 106 mPa·s); Immiscibility of distinct inks for limited material selection
	[76]	CLC oligomer inks	Tunable chiroptical properties; Polarization independence of reflected light (−60° < θ < 60°)	Low saturation; Low pattern resolution
	[77]	CLC oligomer inks	Humidity-sensitive "hinge" driving actuation with reflected color shift	Low saturation Low pattern resolution
	[87]	CLC oligomer inks	Mechanochromic structural-color graphics; Sensitivity ≈1.64 nm% $^{-1}$	Limited material selection
	[88]	HPC-gelatin-PACA inks	3D customized objects on arbitrary substrates; Environmental friendliness; Color tunability via temperature (from green to red in the range of 20–40 °C)	Low pattern resolution
	[89]	HPC-PEG inks	Optical response to mechanical deformation; Path-dependent tilt of the cholesteric domains	Low saturation; Low pattern resolution
	[90]	PDMS-b-PLA BBCP inks	Spatial patterning of structural colors; Exquisite modulation of microstructural (>70 nm)	Limited material selection; high cost
	[91]	PS-b-PLA cross-linkable BBCP inks	Multiple-color adjustment (from deep blue to orange via UV light irradiance from 411 to 0 μW/cm^2)	Limited material selection; high cost
Inkjet printing	[100]	PS particles in mixture of deionized water and ethylene glycol with fluorescence	Angle independent structural colors; Enhanced brightness (>40 times); Wide viewing-angle (from 0° to 180°)	2D patterns only
	[101]	Silica nanoparticles in ATPS of PEG and DEX	Dual-color domes for nonuniform self-assembly	2D pattern only
	[103]	PS nanoparticles in a binary solvent (ethylene glycol and formamide) with fluorescence	Unclonable multiplex encryption pattern; Rapid (≈2 s) and accurate (0 false alarm rate) authentication	2D pattern only
	[104]	Aqueous CNC suspension	Angle-dependent color and polarization-selective reflection; Ability to be printed in full-color dot-matrix patterns and bespoke images	2D pattern only
	[106]	colloidal quantum dots/CLC networks inks	Fluorescent LC polymer coatings; Full-color, high-resolution geminate patterns	Limited material selection
	[108]	BPLC inks	Erasable high-resolution "live" pattern	Limited material selection
	[110]	Fluorinated monomer in 1 wt% Pluronic F-127 in water	Full-color printing using only one transparent ink	Complex preparation process
DLP	[117]	NCPC composed of HENPs dispersed in a crosslinkable pre-gel solution	Tunable multicolor NCPC patterns and mechanical properties	Low Resolution; Rough surfaces;
	[118]	aqueous solution of PS latex particles mixing with CB, AM, PEGDA and TPO-H	Excellent shape fidelity; High precision; Angle dependence	Low Resolution; Rough surfaces;

Table 1. *Cont.*

Manufacturing Methods	Refs.	Printable Inks	Properties	Limitations
TPL	[125]	Silica polymeric woodpile microstructures	Multicolor microscopic 3D objects; The smallest achievable color voxel size: xy-directions: 1.45 μm z-direction: 2.63 μm	Limited size (μm level); Low efficiency
	[126]	Silica particles with hydrogel as sacrificial scaffold	Complex 3D colloidal crystal microstructures: minimum feature size down to 3 μm	Limited size; Low efficiency
	[127]	Supramolecular CLCs	Response to variations in humidity and temperature through modulation of their shape and color	Limited size; Low efficiency
FDM	[132]	Rigid-rod dendritic BCPs	Filter light or even guide specified light frequencies around a curved geometry	Low saturation; Low resolution

Author Contributions: L.W. and Y.Y. conceptualized the project. L.W. and W.F. supervised the project. Z.C. and Y.Y. drafted the manuscript and all authors contributed to revising it. All authors have read and agreed to the published version of manuscript.

Funding: The authors acknowledge the support from the Joint Fund for Regional Innovation and Development of National Natural Science Foundation China (No. U24A2078), the National Key R&D Program of China (2023YFB3812800), the National Natural Science Foundation of China (No. 52173181, 52203143 and 52327802), the Tianjin Science Fund for Distinguished Young Scholars (22JCJQJC00060), Young Elite Scientists Sponsorship Program by CAST (No. 2022QNRC001).

Data Availability Statement: The data that support the findings of this study are available from the corresponding authors upon reasonable request.

Conflicts of Interest: The authors declare no conflict of financial interest.

References

1. Cai, Z.; Li, Z.; Ravaine, S.; He, M.; Song, Y.; Yin, Y.; Zheng, H.; Teng, J.; Zhang, A. From colloidal particles to photonic crystals: Advances in self-assembly and their emerging applications. *Chem. Soc. Rev.* **2021**, *50*, 5898–5951. https://doi.org/10.1039/D0CS00706D.
2. Foelen, Y.; Schenning, A.P.H.J. Optical indicators based on structural colored polymers. *Adv. Sci.* **2022**, *9*, 2200399. https://doi.org/10.1002/advs.202200399.
3. Yang, J.; Zhang, X.; Zhang, X.; Wang, L.; Feng, W.; Li, Q. Beyond the visible: Bioinspired infrared adaptive materials. *Adv. Mater.* **2021**, *33*, 2004754. https://doi.org/10.1002/adma.202004754.
4. Li, Z.; Fan, Q.; Yin, Y. Colloidal Self-Assembly Approaches to Smart Nanostructured Materials. *Chem. Rev.* **2022**, *122*, 4976–5067. https://doi.org/10.1021/acs.chemrev.1c00482.
5. Xuan, Z.; Li, J.; Liu, Q.; Yi, F.; Wang, S.; Lu, W. Artificial Structural Colors and Applications. *Innovation* **2021**, *2*, 100081. https://doi.org/10.1016/j.xinn.2021.100081.
6. Lopez-Garcia, M.; Masters, N.; O'Brien, H.E.; Lennon, J.; Atkinson, G.; Cryan, M.J.; Oulton, R.; Whitney, H.M. Light-induced dynamic structural color by intracellular 3D photonic crystals in brown algae. *Sci. Adv.* **2018**, *4*, eaan8917. https://doi.org/10.1126/sciadv.aan8917.
7. Whitney, H.M.; Kolle, M.; Andrew, P.; Chittka, L.; Steiner, U.; Glover, B.J. Floral Iridescence, Produced by Diffractive Optics, Acts as a Cue for Animal Pollinators. *Science* **2009**, *323*, 130–133. https://doi.org/10.1126/science.1166256.
8. Parker, A.R.; Welch, V.L.; Driver, D.; Martini, N. Opal analogue discovered in a weevil. *Nature* **2003**, *426*, 786–787. https://doi.org/10.1038/426786a.
9. Teyssier, J.; Saenko, S.V.; van der Marel, D.; Milinkovitch, M.C. Photonic crystals cause active colour change in chameleons. *Nat. Commun.* **2015**, *6*, 6368. https://doi.org/10.1038/ncomms7368.
10. Yoshioka, S.; Fujita, H.; Kinoshita, S.; Matsuhana, B. Alignment of crystal orientations of the multi-domain photonic crystals in Parides sesostris wing scales. *J. R. Soc. Interface* **2014**, *11*, 20131029. https://doi.org/10.1098/rsif.2013.1029.
11. Saranathan, V.; Osuji, C.O.; Mochrie, S.; Noh, H.; Narayanan, S.; Sandy, A.; Dufresne, E.R.; Prum, R.O. Structure, function, and self-assembly of single network gyroid ($I4_132$) photonic crystals in butterfly wing scales. *Proc. Natl. Acad. Sci. USA* **2010**, *107*, 11676–11681. https://doi.org/10.1073/pnas.0909616107.
12. Marlow, F.; Sharifi, P.; Brinkmann, R.; Mendive, C. Opals: Status and Prospects. *Angew. Chem. Int. Ed.* **2009**, *48*, 6212–6233. https://doi.org/10.1002/anie.200900210.
13. Welch, V.; Lousse, V.; Deparis, O.; Parker, A.; Vigneron, J.P. Orange reflection from a three-dimensional photonic crystal in the scales of the weevil *Pachyrrhynchus congestus pavonius* (Curculionidae). *Phys. Rev. E* **2007**, *75*, 041919. https://doi.org/10.1103/PhysRevE.75.041919.

14. Sharma, V.; Crne, M.; Park, J.O.; Srinivasarao, M. Structural Origin of Circularly Polarized Iridescence in Jeweled Beetles. *Science* **2009**, *325*, 449–451. https://doi.org/10.1126/science.1172051.
15. Zhang, X.; Li, L.; Chen, Y.; Valenzuela, C.; Liu, Y.; Yang, Y.; Feng, Y.; Wang, L.; Feng, W. Mechanically Tunable Circularly Polarized Luminescence of Liquid Crystal-Templated Chiral Perovskite Quantum Dots. *Angew. Chem. Int. Ed*. **2024**, *63*, e202404202. https://doi.org/10.1002/ange.202404202.
16. Lin, X.; Shi, D.; Yi, G.; Yu, D. Structural color-based physical unclonable function. *Responsive Mater.* **2024**, *2*, e20230031. https://doi.org/10.1002/rpm.20230031.
17. Wang, F.; Lyu, R.; Xu, H.; Gong, R.; Ding, B. Tunable colors from responsive 2D materials. *Responsive Mater.* **2024**, *2*, e20240007. https://doi.org/10.1002/rpm.20240007.
18. Lyu, Q.; Li, M.; Zhang, L.; Zhu, J. Structurally-colored adhesives for sensitive, high-resolution, and non-invasive adhesion self-monitoring. *Nat. Commun.* **2024**, *15*, 8419. https://doi.org/10.1038/s41467-024-52794-5.
19. Li, H.; Zhao, G.; Zhu, M.; Guo, J.; Wang, C. Robust Large-Sized Photochromic Photonic Crystal Film for Smart Decoration and Anti-Counterfeiting. *ACS Appl. Mater. Interfaces* **2022**, *14*, 14618–14629. https://doi.org/10.1021/acsami.2c01211.
20. Fu, F.; Shang, L.; Chen, Z.; Yu, Y.; Zhao, Y. Bioinspired living structural color hydrogels. *Sci. Robot.* **2018**, *3*, eaar8580. https://doi.org/10.1126/scirobotics.aar8580.
21. Liu, C.; Fan, Z.; Tan, Y.; Fan, F.; Xu, H. Tunable Structural Color Patterns Based on the Visible-Light-Responsive Dynamic Diselenide Metathesis. *Adv. Mater.* **2020**, *32*, 1907569. https://doi.org/10.1002/adma.201907569.
22. Hong, W.; Yuan, Z.; Chen, X. Structural Color Materials for Optical Anticounterfeiting. *Small* **2020**, *16*, 1907626. https://doi.org/10.1002/smll.201907626.
23. Kim, I.; Jang, J.; Kim, G.; Lee, J.; Badloe, T.; Mun, J.; Rho, J. Pixelated bifunctional metasurface-driven dynamic vectorial holographic color prints for photonic security platform. *Nat. Commun.* **2021**, *12*, 3614. https://doi.org/10.1038/s41467-021-23814-5.
24. Zhu, C.; Jin, J.; Wang, Z.; Xu, Z.; Folgueras, M.C.; Jiang, Y.; Uzundal, C.B.; Le, H.K.D.; Wang, F.; Zheng, X.; et al. Supramolecular assembly of blue and green halide perovskites with near-unity photoluminescence. *Science* **2024**, *383*, 86–93. https://doi.org/10.1126/science.adi4196.
25. Yang, W.; Zheng, C.; Sun, L.; Bie, Z.; Yue, Y.; Li, X.; Sun, W.; Ikeda, T.; Wang, J.; Jiang, L. Spatiotemporal Programmability of 3D Chiral Color Units Driven by Ink Spontaneous Diffusion toward Customized Printing. *Adv. Mater.* **2024**, *36*, 2411988. https://doi.org/10.1002/adma.202411988.
26. Fang, Y.; Ni, Y.; Leo, S.-Y.; Taylor, C.; Basile, V.; Jiang, P. Reconfigurable photonic crystals enabled by pressure-responsive shape-memory polymers. *Nat. Commun.* **2015**, *6*, 7416. https://doi.org/10.1038/ncomms8416.
27. Lee, J.-S.; Je, K.; Kim, S.-H. Designing Multicolored Photonic Micropatterns through the Regioselective Thermal Compression of Inverse Opals. *Adv. Funct. Mater.* **2016**, *26*, 4587–4594. https://doi.org/10.1002/adfm.201601095.
28. Qin, L.; Gu, W.; Wei, J.; Yu, Y. Piecewise Phototuning of Self-Organized Helical Superstructures. *Adv. Mater.* **2018**, *30*, 1704941. https://doi.org/10.1002/adma.201704941.
29. Wang, Y.; Aurelio, D.; Li, W.; Tseng, P.; Zheng, Z.; Li, M.; Kaplan, D.L.; Liscidini, M.; Omenetto, F.G. Modulation of Multiscale 3D Lattices through Conformational Control: Painting Silk Inverse Opals with Water and Light. *Adv. Mater.* **2017**, *29*, 1702769. https://doi.org/10.1002/adma.201702769.
30. Truby, R.L.; Lewis, J.A. Printing soft matter in three dimensions. *Nature* **2016**, *540*, 371–378. https://doi.org/10.1038/nature21003.
31. del Pozo, M.; Sol, J.A.H.P.; Schenning, A.P.H.J.; Debije, M.G. 4D Printing of Liquid Crystals: What's Right for Me? *Adv. Mater.* **2021**, *33*, 2104390. https://doi.org/10.1002/adma.202104390.
32. Zhao, S.; Siqueira, G.; Drdova, S.; Norris, D.; Ubert, C.; Bonnin, A.; Galmarini, S.; Ganobjak, M.; Pan, Z.; Brunner, S.; et al. Additive manufacturing of silica aerogels. *Nature* **2020**, *584*, 387–392. https://doi.org/10.1038/s41586-020-2594-0.
33. Walker, D.A.; Hedrick, J.L.; Mirkin, C.A. Rapid, large-volume, thermally controlled 3D printing using a mobile liquid interface. *Science* **2019**, *366*, 360–364. https://doi.org/10.1126/science.aax1562.
34. Wang, L.; Dong, H.; Li, Y.; Liu, R.; Wang, Y.; Bisoyi, H.K.; Sun, L.; Yan, C.; Li, Q. Luminescence-driven reversible handedness inversion of self-organized helical superstructures enabled by a novel near-infrared light nanotransducer. *Adv. Mater.* **2015**, *27*, 2065–2069. https://doi.org/10.1002/adma.201405690.
35. Wang, L.; Dong, H.; Li, Y.; Xue, C.; Sun, L.; Yan, C.; Li, Q. Reversible Near-Infrared Light Directed Reflection in a Self-Organized Helical Superstructure Loaded with Upconversion Nanoparticles. *J. Am. Chem. Soc.* **2014**, *136*, 4480–4483. https://doi.org/10.1021/ja500933h.
36. Zeng, M.; King, D.; Huang, D.; Do, C.; Wang, L.; Chen, M.; Lei, S.; Lin, P.; Chen, Y.; Cheng, Z. Iridescence in nematics: Photonic liquid crystals of nanoplates in absence of long-range periodicity. *Proc. Natl. Acad. Sci. USA* **2019**, *116*, 18322–18327. https://doi.org/10.1073/pnas.1906511116.
37. Bauer, J.; Crook, C.; Baldacchini, T. A sinterless, low-temperature route to 3D print nanoscale optical-grade glass. *Science* **2023**, *380*, 960–966. https://doi.org/10.1126/science.abq3037.

38. Kuang, X.; Wu, J.; Chen, K.; Zhao, Z.; Ding, Z.; Hu, F.; Fang, D.; Qi, H.J. Grayscale digital light processing 3D printing for highly functionally graded materials. *Sci. Adv.* **2019**, *5*, eaav5790. https://doi.org/10.1126/sciadv.aav5790.
39. Hinton, T.J.; Jallerat, Q.; Palchesko, R.N.; Park, J.H.; Grodzicki, M.S.; Shue, H.-J.; Ramadan, M.H.; Hudson, A.R.; Feinberg, A.W. Three-dimensional printing of complex biological structures by freeform reversible embedding of suspended hydrogels. *Sci. Adv.* **2015**, *1*, e1500758. https://doi.org/10.1126/sciadv.1500758.
40. Yuk, H.; Lu, B.; Lin, S.; Qu, K.; Xu, J.; Luo, J.; Zhao, X. 3D printing of conducting polymers. *Nat. Commun.* **2020**, *11*, 1604. https://doi.org/10.1038/s41467-020-15316-7.
41. Kang, Y.; Zhao, J.; Zeng, Y.; Du, X.; Gu, Z. 3D Printing Photonic Crystals: A Review. *Small* **2024**, *20*, 2403525. https://doi.org/10.1002/smll.202403525.
42. Li, G.; Leng, M.; Wang, S.; Ke, Y.; Luo, W. Printable structural colors and their emerging applications. *Mater. Today* **2023**, *69*, 133–159. https://doi.org/10.1016/j.mattod.2023.08.022.
43. Zhao, C.; Wang, J.; Zhang, Z.; Chi, C. Research Progress on the Design of Structural Color Materials Based on 3D Printing. *Adv. Mater. Technol.* **2023**, *8*, 2200257. https://doi.org/10.1002/admt.202200257.
44. Withnall, R.; Silver, J.; Ireland, T.G.; Zhang, S.; Fern, G.R. Achieving structured colour in inorganic systems: Learning from the natural world. *Opt. Laser Technol.* **2011**, *43*, 401–409. https://doi.org/10.1016/j.optlastec.2009.06.016.
45. Meng, Z.; Wu, S.; Tang, B.; Ma, W.; Zhang, S. Structurally colored polymer films with narrow stop band, high angle-dependence and good mechanical robustness for trademark anti-counterfeiting. *Nanoscale* **2018**, *10*, 14755–14762. https://doi.org/10.1039/C8NR04058C.
46. Vignolini, S.; Rudall, P.J.; Rowland, A.V.; Reed, A.; Moyroud, E.; Faden, R.B.; Baumberg, J.J.; Glover, B.J.; Steiner, U. Pointillist structural color in *Pollia* fruit. *Proc. Natl. Acad. Sci. USA* **2012**, *109*, 15712–15715. https://doi.org/10.1073/pnas.1210105109.
47. Sharma, V.; Crne, V.; Park, J.O.; Srinivasarao, M. Bouligand Structures Underlie Circularly Polarized Iridescence of Scarab Beetles: A Closer View. *Mater. Today Proc.* **2014**, *1*, 161–171. https://doi.org/10.1016/j.matpr.2014.09.019.
48. Ma, J.; Yang, Y.; Valenzuela, C.; Zhang, X.; Wang, L.; Feng, W. Mechanochromic, Shape-Programmable and Self-Healable Cholesteric Liquid Crystal Elastomers Enabled by Dynamic Covalent Boronic Ester Bonds. *Angew. Chem. Int. Ed.* **2022**, *61*, e202116219. https://doi.org/10.1002/anie.202116219.
49. Liu, Y.; Ma, J.; Yang, Y.; Valenzuela, C.; Zhang, X.; Wang, L.; Feng, W. Smart chiral liquid crystal elastomers: Design, properties and application. *Smart Mol.* **2024**, *2*, e20230025. https://doi.org/10.1002/smo.20230025.
50. Li, X.; Yang, Y.; Valenzuela, C.; Zhang, X.; Xue, P.; Liu, Y.; Liu, C.; Wang, L. Mechanochromic and Conductive Chiral Nematic Nanostructured Film for Bioinspired Ionic Skins. *ACS Nano* **2023**, *17*, 12829–12841. https://doi.org/10.1021/acsnano.3c04199.
51. Yang, J.; Zhao, W.; He, W.; Yang, Z.; Wang, D.; Cao, H. Liquid crystalline blue phase materials with three-dimensional nanostructures. *J. Mater. Chem. C* **2019**, *7*, 13352–13366. https://doi.org/10.1039/C9TC04380B.
52. Yang, Y.; Wang, L.; Yang, H.; Li, Q. 3D Chiral Photonic Nanostructures Based on Blue-Phase Liquid Crystals. *Small Sci*. **2021**, *1*, 2100007. https://doi.org/10.1002/smsc.202100007.
53. Yang, J.; Zhao, W.; Yang, Z.; He, W.; Wang, J.; Ikeda, T.; Jiang, L. Photonic Shape Memory Polymer Based on Liquid Crystalline Blue Phase Films. *ACS Appl. Mater. Interfaces* **2019**, *11*, 46124–46131. https://doi.org/10.1021/acsami.9b14202.
54. Valenzuela, C.; Ma, S.; Yang, Y.; Chen, Y.; Zhang, X.; Wang, L.; Feng, W. Direct Ink Writing of 3D Chiral Soft Photonic Crystals. *Adv. Funct. Mater.* **2025**, 2421280. https://doi.org/10.1002/adfm.202421280.
55. Sun, C.; Zhu, D.; Jia, H.; Yang, C.; Zheng, Z.; Wang, X. Bio-based visual optical pressure-responsive sensor. *Carbohydr. Polym.* **2021**, *260*, 117823. https://doi.org/10.1016/j.carbpol.2021.117823.
56. Chung, K.; Yu, S.; Heo, C.-J.; Shim, J.W.; Yang, S.-M.; Han, M.G.; Lee, H.-S.; Jin, Y.; Lee, S.Y.; Park, N.; et al. Flexible, Angle-Independent, Structural Color Reflectors Inspired by Morpho Butterfly Wings. *Adv. Mater*. **2012**, *24*, 2375–2379. https://doi.org/10.1002/adma.201200521.
57. Sveinbjörnsson, B.R.; Weitekamp, R.A.; Miyake, G.M.; Xia, Y.; Atwater, H.A.; Grubbs, R.H. Rapid self-assembly of brush block copolymers to photonic crystals. *Proc. Natl. Acad. Sci*. *USA* **2012**, *109*, 14332–14336. https://doi.org/10.1073/pnas.1213055109.
58. Guo, T.; Yu, X.; Zhao, Y.; Yuan, X.; Li, J.; Ren, L. Structure Memory Photonic Crystals Prepared by Hierarchical Self-Assembly of Semicrystalline Bottlebrush Block Copolymers. *Macromolecules* **2020**, *53*, 3602–3610. https://doi.org/10.1021/acs.macromol.0c00274.
59. Verduzco, R.; Li, X.; Pesek, S.L.; Stein, G.E. Structure, function, self-assembly, and applications of bottlebrush copolymers. *Chem. Soc. Rev.* **2015**, *44*, 2405–2420. https://doi.org/10.1039/C4CS00329B.
60. Dalsin, S.J.; Rions-Maehren, T.G.; Beam, M.D.; Bates, F.S.; Hillmyer, M.A.; Matsen, M.W. Bottlebrush Block Polymers: Quantitative Theory and Experiments. *ACS Nano* **2015**, *9*, 12233–12245. https://doi.org/10.1021/acsnano.5b05473.
61. Liu, H.; Wang, H.; Wang, H.; Deng, J.; Ruan, Q.; Zhang, W.; Abdelraouf, O.A.M.; Ang, N.S.S.; Dong, Z.; Yang, J.K.W.; et al. High-Order Photonic Cavity Modes Enabled 3D Structural Colors. *ACS Nano* **2022**, *16*, 8244–8252.

https://doi.org/10.1021/acsnano.2c01999.

62. Yadav, A.; Yadav, N.; Agrawal, V.; Polyutov, S.P.; Tsipotan, A.S.; Karpov, S.V.; Slabko, V.V.; Yadav, V.S.; Wu, Y.; Zheng, H.; et al. State-of-art plasmonic photonic crystals based on self-assembled nanostructures. *J. Mater. Chem. C* **2021**, *9*, 3368–3383. https://doi.org/10.1039/D0TC05254J.
63. Kim, J.B.; Lee, H.-Y.; Chae, C.; Lee, S.Y.; Kim, S.-H. Advanced Additive Manufacturing of Structurally-Colored Architectures. *Adv. Mater.* **2024**, *36*, 2307917. https://doi.org/10.1002/adma.202307917.
64. Hou, X.; Li, F.; Song, Y.; Li, M. Recent Progress in Responsive Structural Color. *J. Phys. Chem. Lett.* **2022**, *13*, 2885–2900. https://doi.org/10.1021/acs.jpclett.1c04219.
65. Xing, Y.; Fei, X.; Ma, J. Ultra-Fast Fabrication of Mechanical-Water-Responsive Color-Changing Photonic Crystals Elastomers and 3D Complex Devices. *Small* **2024**, *20*, 2405426. https://doi.org/10.1002/smll.202405426.
66. Bellis, I.D.; Martella, D.; Parmeggiani, C.; Wiersma, D.S.; Nocentini, S. Temperature Tunable 4D Polymeric Photonic Crystals. *Adv. Funct. Mater.* **2023**, *33*, 2213162. https://doi.org/10.1002/adfm.202213162.
67. Wang, H.; Ruan, Q.; Wang, H.; Rezaei, S.D.; Lim, K.T.P.; Liu, H.; Zhang, W.; Trisno, J.; Chan, J.Y.E.; Yang, J.K.W. Full Color and Grayscale Painting with 3D Printed Low-Index Nanopillars. *Nano Lett.* **2021**, *21*, 4721–4729. https://doi.org/10.1021/acs.nanolett.1c00979.
68. Kim, J.B.; Nam, S.K.; Park, S.; Amstad, E.; Kim, S.-H. Void-Free Photonic Surfaces Created by Adaptive Dense Packing of Emulsion Droplets. *Chem. Mater.* **2023**, *35*, 261–270. https://doi.org/10.1021/acs.chemmater.2c03124.
69. Zhu, Y.; Tang, T.; Zhao, S.; Joralmon, D.; Poit, Z.; Ahire, B.; Keshav, S.; Raje, A.R.; Blair, J.; Zhang, Z.; et al. Recent advancements and applications in 3D printing of functional optics. *Addit. Manuf.* **2022**, *25*, 102682. https://doi.org/10.1016/j.addma.2022.102682.
70. Tan, A.T.L.; Beroz, J.; Kolle, M.; Hart, A.J. Direct-Write Freeform Colloidal Assembly. *Adv. Mater.* **2018**, *30*, 1803620. https://doi.org/10.1002/adma.201803620.
71. Kim, J.B.; Chae, C.; Han, S.H.; Lee, S.Y.; Kim, S.-H. Direct writing of customized structural-color graphics with colloidal photonic inks. *Sci. Adv.* **2021**, *7*, eabj8780. https://doi.org/10.1126/sciadv.abj8780.
72. Kim, J.H.; Kim, J.B.; Kim, S.-H. Structural Color Inks Containing Photonic Microbeads for Direct Writing. *ACS Appl. Mater. Interfaces* **2024**, *16*, 21098–21108. https://doi.org/10.1021/acsami.4c01224.
73. Geng, Y.; Kizhakidathazhath, R.; Lagerwall, J.P.F. Robust cholesteric liquid crystal elastomer fibres for mechanochromic textiles. *Nat. Mater.* **2022**, *21*, 1441–1447. https://doi.org/10.1038/s41563-022-01355-6.
74. Li, X.; Chen, Y.; Du, C.; Liao, X.; Yang, Y.; Feng, W. Direct Ink Writing of Cephalopod Skin-Like Core-Shell Fibers from Cholesteric Liquid Crystal Elastomers and Dyed Solutions. *Adv. Funct. Mater.* **2024**, *34*, 2413965. https://doi.org/10.1002/adfm.202413965.
75. Bi, R.; Li, X.; Ou, X.; Huang, J.; Huang, D.; Chen, G.; Sheng, Y.; Hong, W.; Wang, Y.; Hu, W.; et al. 3D-Printed Biomimetic Structural Colors. *Small* **2024**, *19*, 2306646. https://doi.org/10.1002/smll.202306646.
76. Sol, J.A.H.P.; Sentjens, H.; Yang, L.; Grossiord, N.; Schenning, A.P.H.J.; Debije, M.G. Anisotropic Iridescence and Polarization Patterns in a Direct Ink Written Chiral Photonic Polymer. *Adv. Mater.* **2021**, *33*, 2103309. https://doi.org/10.1002/adma.202103309.
77. Sol, J.A.H.P.; Smits, L.G.; Schenning, A.P.H.J.; Debije, M.G. Direct Ink Writing of 4D Structural Colors. *Adv. Funct. Mater.* **2022**, *32*, 2201766. https://doi.org/10.1002/adfm.202201766.
78. Choi, J.; Choi, Y.; Lee, J.-H.; Kim, M.C.; Park, S.; Hyun, K.; Lee, K.M.; Yoon, T.-H.; Ahn, S.-k. Direct-Ink-Written Cholesteric Liquid Crystal Elastomer with Programmable Mechanochromic Response. *Adv. Funct. Mater.* **2024**, *33*, 2310658. https://doi.org/10.1002/adfm.202310658.
79. Chen, Y.; Valenzuela, C.; Liu, Y.; Yang, X.; Yang, Y.; Zhang, X.; Ma, S.; Bi, R.; Wang, L.; Feng, W. Biomimetic artificial neuromuscular fiber bundles with built-in adaptive feedback. *Matter* **2025**, *8*, 101904. https://doi.org/10.1016/j.matt.2024.10.022.
80. Yang, X.; Valenzuela, C.; Zhang, X.; Chen, Y.; Yang, Y.; Wang, L.; Feng, W. Robust integration of polymerizable perovskite quantum dots with responsive polymers enables 4D-printed self-deployable information display. *Matter* **2023**, *6*, 1278–1294. https://doi.org/10.1016/j.matt.2023.02.003.
81. Xue, P.; Chen, Y.; Xu, Y.; Valenzuela, C.; Zhang, X.; Bisoyi, H.K.; Yang, X.; Wang, L.; Xu, X.; Li, Q. Bioinspired MXene-Based Soft Actuators Exhibiting Angle-Independent Structural Color. *Nano-Micro Letters* **2023**, *15*, 1. https://doi.org/10.1007/s40820-022-00977-4.
82. Guan, Z.; Wang, L.; Bae, J. Advances in 4D printing of liquid crystalline elastomers: Materials, techniques, and applications. *Mater. Horiz.* **2022**, *9*, 1825–1849. https://doi.org/10.1039/D2MH00232A.
83. Ma, S.; Xue, P.; Tang, Y.; Bi, R.; Xu, X.; Wang, L.; Li, Q. Responsive soft actuators with MXene nanomaterials. *Responsive Mater.* **2024**, *2*, e20230026. https://doi.org/10.1002/rpm.20230026.
84. Lu, W.; Wang, R.; Si, M.; Zhang, Y.; Wu, S.; Zhu, N.; Wang, W.; Chen, T. Synergistic fluorescent hydrogel actuators with selective spatial shape/color-changing behaviors via interfacial supramolecular assembly. *SmartMat* **2024**, *5*, e1190.

https://doi.org/10.1002/smm2.1190.

85. Ma, J.; Yang, Y.; Zhang, X.; Xue, P.; Valenzuela, C.; Liu, Y.; Wang, L.; Feng, W. Mechanochromic and ionic conductive cholesteric liquid crystal elastomers for biomechanical monitoring and human–machine interaction. *Mater. Horiz.* **2024**, *11*, 217–226. https://doi.org/10.1039/D3MH01386C.
86. Lv, P.; Lu, X.; Wang, L.; Feng, W. Nanocellulose-Based Functional Materials: From Chiral Photonics to Soft Actuator and Energy Storage. *Adv. Funct. Mater.* **2021**, *31*, 2104991. https://doi.org/10.1002/adfm.202104991.
87. Yang, Y.; Zhang, X.; Valenzuela, C.; Bi, R.; Chen, Y.; Liu, Y.; Zhang, C.; Li, W.; Wang, L.; Feng, W. High-throughput printing of customized structural-color graphics with circularly polarized reflection and mechanochromic response. *Matter* **2024**, *7*, 2091–2107. https://doi.org/10.1016/j.matt.2024.03.011.
88. Zhang, Z.; Wang, C.; Wang, Q.; Zhao, Y.; Shang, L. Cholesteric cellulose liquid crystal ink for three-dimensional structural coloration. *Proc. Natl. Acad. Sci. USA* **2022**, *119*, e2204113119. https://doi.org/10.1073/pnas.2204113119.
89. Georgea, K.; Esmaeilia, M.; Wang, J.; Taheri-Qazvini, N.; Abbaspourrad, A.; Sadatia, M. 3D printing of responsive chiral photonic nanostructures. *Proc. Natl. Acad. Sci. USA* **2023**, *120*, e2220032120. https://doi.org/10.1073/pnas.2220032120.
90. Patel, B.B.; Walsh, D.J.; Kim, D.H.; Kwok, J.; Lee, B.; Guironnet, D.; Diao, Y. Tunable structural color of bottlebrush block copolymers through direct-write 3D printing from solution. *Sci. Adv.* **2020**, *6*, eaaz7202. https://doi.org/10.1126/sciadv.aaz7202.
91. Jeona, S.; Kamble, Y.L.; Kang, H.; Shi, J.; Wade, M.A.; Patel, B.B.; Pan, T.; Rogers, S.A.; Sing, C.E.; Guironnet, D.; et al. Direct-ink-write cross-linkable bottlebrush block copolymers for on-the-fly control of structural color. *Proc. Natl. Acad. Sci. USA* **2024**, *121*, e2313617121. https://doi.org/10.1073/pnas.2313617121.
92. Shanker, R.; Sardar, S.; Chen, S.; Gamage, S.; Rossi, S.; Jonsson, M.P. Noniridescent Biomimetic Photonic Microdomes by Inkjet Printing. *Nano Lett.* **2020**, *20*, 7243–7250. https://doi.org/10.1021/acs.nanolett.0c02604.
93. Hu, Z.; Bradshaw, N.P.; Vanthournout, B.; Forman, C.; Gnanasekaran, K.; Thompson, M.P.; Smeets, P.; Dhinojwala, A.; Shawkey, M.D.; Hersam, M.C.; et al. Non-Iridescent Structural Color Control via Inkjet Printing of Self-Assembled Synthetic Melanin Nanoparticles. *Chem. Mater.* **2021**, *33*, 6433–6442. https://doi.org/10.1021/acs.chemmater.1c01719.
94. Bai, L.; Xie, Z.; Wang, W.; Yuan, C.; Zhao, Y.; Mu, Z.; Zhong, Q.; Gu, Z. Bio-Inspired Vapor-Responsive Colloidal Photonic Crystal Patterns by Inkjet Printing. *ACS Nano* **2014**, *8*, 11094–11100. https://doi.org/10.1021/nn504659p.
95. Li, W.; Wang, Y.; Li, M.; Garbarini, L.P.; Omenetto, F.G. Inkjet Printing of Patterned, Multispectral, and Biocompatible Photonic Crystals. *Adv. Mater.* **2019**, *31*, 1901036. https://doi.org/10.1002/adma.201901036.
96. Moirangthem, M.; Schenning, A.P.H.J. Full Color Camouflage in a Printable Photonic Blue-Colored Polymer. *ACS Appl. Mater. Interfaces* **2018**, *10*, 4168–4172. https://doi.org/10.1021/acsami.7b17892.
97. Kuang, M.; Wang, L.; Song, Y. Controllable Printing Droplets for High-Resolution Patterns. *Adv. Mater.* **2014**, *26*, 6950–6958. https://doi.org/10.1002/adma.201305416.
98. Liu, M.; Wang, J.; He, M.; Wang, L.; Li, F.; Jiang, L.; Song, Y. Inkjet Printing Controllable Footprint Lines by Regulating the Dynamic Wettability of Coalescing Ink Droplets. *ACS Appl. Mater. Interfaces* **2014**, *6*, 13344–13348. https://doi.org/10.1021/am5042548.
99. Wu, L.; Dong, Z.; Kuang, M.; Li, Y.; Li, F.; Jiang, L.; Song, Y. Printing Patterned Fine 3D Structures by Manipulating the Three Phase Contact Line. *Adv. Funct. Mater.* **2015**, *25*, 2237–2242. https://doi.org/10.1002/adfm.201404559.
100. Kuang, M.; Wang, J.; Bao, B.; Li, F.; Wang, L.; Jiang, L.; Song, Y. Inkjet Printing Patterned Photonic Crystal Domes for Wide Viewing-Angle Displays by Controlling the Sliding Three Phase Contact Line. *Adv. Opt. Mater.* **2014**, *2*, 34–38. https://doi.org/10.1002/adom.201300369.
101. Li, C.; Yu, Y.; Li, H.; Tian, J.; Guo, W.; Shen, Y.; Cui, H.; Pan, Y.; Song, Y.; Shum, H.C. One-Pot Self-Assembly of Dual-Color Domes Using Mono-Sized Silica Nanoparticles. *Nano Lett.* **2022**, *22*, 5236–5243. https://doi.org/10.1021/acs.nanolett.2c01090.
102. Li, C.; Yu, Y.; Li, H.; Lin, H.; Cui, H.; Pan, Y.; Zhang, R.; Song, Y.; Shum, H.C. Heterogeneous Self-Assembly of a Single Type of Nanoparticle Modulated by Skin Formation. *ACS Nano* **2023**, *17*, 11645–11654. https://doi.org/10.1021/acsnano.3c02082.
103. Gao, Y.; Ge, K.; Zhang, Z.; Li, Z.; Hu, S.; Ji, H.; Li, M.; Feng, H. Fine Optimization of Colloidal Photonic Crystal Structural Color for Physically Unclonable Multiplex Encryption and Anti-Counterfeiting. *Adv. Sci.* **2024**, *11*, 2305876. https://doi.org/10.1002/advs.202305876.
104. Williams, C.A.; Parker, R.M.; Kyriacou, A.; Murace, M.; Vignolini, S. Inkjet Printed Photonic Cellulose Nanocrystal Patterns. *Adv. Mater.* **2024**, *36*, 2307563. https://doi.org/10.1002/adma.202307563.
105. Moirangthem, M.; Scheers, A.F.; Schenning, A.P.H.J. A full color photonic polymer, rewritable with a liquid crystal ink. *Chem. Commun.* **2018**, *54*, 4425–4428. https://doi.org/10.1039/C8CC02188K.
106. Liu, X.; Cui, S.; Qin, L.; Yu, Y. Two-Chromatic Printing Creates Skin-Inspired Geminate Patterns Featuring Crosstalk-Free Chemical and Physical Colors. *Adv. Opt. Mater.* **2024**, *12*, 2302573. https://doi.org/10.1002/adom.202302573.
107. Yang, J.; Zhao, W.; Yang, Z.; He, W.; Wang, J.; Ikeda, T.; Jiang, L. Printable photonic polymer coating based on a

monodomain blue phase liquid crystal network. *J. Mater. Chem. C* **2019**, *7*, 13764–13769. https://doi.org/10.1039/C9TC05052C.

108. Meng, F.; Zheng, C.; Yang, W.; Guan, B.; Wang, J.; Ikeda, T.; Jiang, L. High-Resolution Erasable "Live" Patterns Based on Controllable Ink Diffusion on the 3D Blue-Phase Liquid Crystal Networks. *Adv. Funct. Mater.* **2022**, *32*, 2110985. https://doi.org/10.1002/adfm.202110985.
109. Yang, Y.; Zhang, X.; Chen, Y.; Yang, X.; Ma, J.; Wang, J.; Wang, L.; Feng, W. Bioinspired Color-Changing Photonic Polymer Coatings Based on Three-Dimensional Blue Phase Liquid Crystal Networks. *ACS Appl. Mater. Interfaces* **2021**, *13*, 41102–41111. https://doi.org/10.1021/acsami.1c11711.
110. Goodling, A.E.; Nagelberg, S.; Kaehr, B.; Meredith, C.H.; Cheon, S.I.; Saunders, A.P.; Kolle, M.; Zarzar, L.D. Colouration by total internal reflection and interference at microscale concave interfaces. *Nature* **2019**, *566*, 523–527. https://doi.org/10.1038/s41586-019-0946-4.
111. Wang, L.; Urbas, A.M.; Li, Q. Nature-Inspired Emerging Chiral Liquid Crystal Nanostructures: From Molecular Self-Assembly to DNA Mesophase and Nanocolloids. *Adv. Mater.* **2020**, *32*, 1801335. https://doi.org/10.1002/adma.201801335.
112. Zhang, X.; Xu, Y.; Valenzuela, C.; Zhang, X.; Wang, L.; Feng, W.; Li, Q. Liquid crystal-templated chiral nanomaterials: From chiral plasmonics to circularly polarized luminescence. *Light Sci. Appl.* **2022**, *11*, 223. https://doi.org/10.1038/s41377-022-00913-6.
113. Yang, Y.; Liu, Y.; Chen, Y.; Wang, L.; Feng, W. Bioinspired Stretchable Polymers for Dynamic Optical and Thermal Regulation. *Adv. Energy Sustain. Res.* **2024**, *5*, 2300289. https://doi.org/10.1002/aesr.202300289.
114. Li, K.; Li, T.; Zhang, T.; Li, H.; Li, A.; Li, Z.; Lai, X.; Hou, X.; Wang, Y.; Shi, L.; et al. Facile full-color printing with a single transparent ink. *Sci. Adv.* **2021**, *7*, eabh1992. https://doi.org/10.1126/sciadv.abh1992.
115. Zhang, Y.; Dong, Z.; Li, C.; Du, H.; Fang, N.X.; Wu, L.; Song, Y. Continuous 3D printing from one single droplet. *Nat. Commun.* **2020**, *11*, 4685. https://doi.org/10.1038/s41467-020-18518-1.
116. Llorens, J.S.; Barbera, L.; Demirörs, A.F.; Studar, A.R. Light-Based 3D Printing of Complex-Shaped Photonic Colloidal Glasses. *Adv. Mater.* **2023**, *35*, 2302868. https://doi.org/10.1002/adma.202302868.
117. Liao, J.; Ye, C.; Guo, J.; Garciamendez-Mijares, C.E.; Agrawal, P.; Kuang, X.; Japo, J.O.; Wang, Z.; Mu, X.; Li, W.; et al. 3D-printable colloidal photonic crystals. *Mater. Today* **2022**, *56*, 29–41. https://doi.org/10.1016/j.mattod.2022.02.014.
118. Zhang, Y.; Zhang, L.; Zhang, C.; Wang, J.; Liu, J.; Ye, C.; Dong, Z.; Wu, L.; Song, Y. Continuous resin refilling and hydrogen bond synergistically assisted 3D structural color printing. *Nat. Commun.* **2022**, *13*, 7095. https://doi.org/10.1038/s41467-022-34866-6.
119. Zhang, X.; Yang, Y.; Xue, P.; Valenzuela, C.; Chen, Y.; Yang, X.; Wang, L.; Feng, W. Three-Dimensional Electrochromic Soft Photonic Crystals Based on MXene-Integrated Blue Phase Liquid Crystals for Bioinspired Visible and Infrared Camouflage. *Angew. Chem. Int. Ed.* **2022**, *61*, e202211030. https://doi.org/10.1002/anie.202211030.
120. Yang, H.; Fang, H.; Wang, C.; Wang, Y.; Qi, C.; Zhang, Y.; Zhou, Q.; Huang, M.; Wang, M.; Wu, M. 3D printing of customized functional devices for smart biomedical systems. *SmartMat* **2024**, *5*, e1244. https://doi.org/10.1002/smm2.1244.
121. Hou, I.C.-Y.; Li, L.; Zhang, H.; Naumov, P. Smart molecular crystal switches. *Smart Mol.* **2024**, *2*, e20230031. https://doi.org/10.1002/smo.20230031.
122. Qi, Y.; Zhang, S. Recent progress in low-swellable polymer-based smart photonic crystal sensors. *Smart Mol.* **2023**, *1*, e20230018. https://doi.org/10.1002/smo.20230018.
123. Liu, Y.; Bi, R.; Zhang, X.; Chen, Y.; Valenzuela, C.; Yang, Y.; Liu, H.; Yang, L.; Wang, L.; Feng, W. Cephalopod-Inspired MXene-Integrated Mechanochromic Cholesteric Liquid Crystal Elastomers for Visible-Infrared-Radar Multispectral Camouflage. *Angew. Chem. Int. Ed.* **2024**, *137*, e202422636. https://doi.org/10.1002/ange.202422636.
124. Wang, H.; Zhang, W.; Ladika, D.; Yu, H.; Gailevičius, D.; Wang, H.; Pan, C.-F.; Nair, P.N.S.; Ke, Y.; Mori, T.; et al. Two-Photon Polymerization Lithography for Optics and Photonics: Fundamentals, Materials, Technologies, and Applications. *Adv. Funct. Mater.* **2023**, *33*, 2214211. https://doi.org/10.1002/adfm.202214211.
125. Liu, Y.; Wang, H.; Ho, J.; Ng, R.C.; Ng, R.J.H.; Hall-Chen, V.H.; Koay, E.H.H.; Dong, Z.; Liu, H.; Qiu, C.-W.; et al. Structural color three-dimensional printing by shrinking photonic crystals. *Nat. Commun.* **2019**, *10*, 4340. https://doi.org/10.1038/s41467-019-12360-w.
126. Liu, K.; Ding, H.; Li, S.; Niu, Y.; Zeng, Y.; Zhang, J.; Du, X.; Gu, Z. 3D printing colloidal crystal microstructures via sacrificial-scaffold-mediated two-photon lithography. *Nat. Commun.* **2022**, *13*, 4563. https://doi.org/10.1038/s41467-022-32317-w.
127. del Pozo, M.; Delaney, C.; Bastiaansen, C.W.M.; Diamond, D.; Schenning, A.P.H.J.; Florea, L. Direct Laser Writing of Four-Dimensional Structural Color Microactuators Using a Photonic Photoresist. *ACS Nano* **2020**, *14*, 9832–9839. https://doi.org/10.1021/acsnano.0c02481.
128. Cano-Vicent, A.; Tambuwala, M.M.; Hassan, S.S.; Barh, D.; Aljabali, A.A.A.; Birkett, M.; Arjunan, A.; Serrano-Aroca, A. Fused deposition modelling: Current status, methodology, applications and future prospects. *Addit. Manuf.* **2021**, *47*, 102378. https://doi.org/10.1016/j.addma.2021.102378.

129. Reiner, T.; Carr, N.; Měch, R.; Šťava, O.; Dachsbacher, C.; Miller, G. Dual-color mixing for fused deposition modeling printers. *Com. Gra. For.* **2014**, *33*, 479–486. https://doi.org/10.1111/cgf.12319.
130. Korpela, J.; Kokkari, A.; Korhonen, H.; Malin, M.; Närhi, T.; Seppälä, J. Biodegradable and bioactive porous scaffold structures prepared using fused deposition modeling. *J Biomed. Mater. Res. Part B* **2013**, *101B*, 610–619. https://doi.org/10.1002/jbm.b.32863.
131. Wang, J.; Wang, Z.; Song, Z.; Ren, L.; Liu, Q.; Ren, L. Biomimetic Shape–Color Double-Responsive 4D Printing. *Adv. Mater. Technol*. **2019**, *4*, 1900293. https://doi.org/10.1002/admt.201900293.
132. Boyle, B.M.; French, T.A.; Pearson, R.M.; McCarthy, B.G.; Miyake, G.M. Structural Color for Additive Manufacturing: 3D-Printed Photonic Crystals from Block Copolymers. *ACS Nano* **2017**, *11*, 3052–3058. https://doi.org/10.1021/acsnano.7b00032.
133. Zhang, W.; Wang, H.; Wang, H.; Chan, J.Y.E.; Liu, H.; Zhang, B.; Zhang, Y.-F.; Agarwal, K.; Yang, X.; Ranganath, A.S.; et al. Structural multi-colour invisible inks with submicron 4D printing of shape memory polymers. *Nat. Commun.* **2021**, *12*, 112. https://doi.org/10.1038/s41467-020-20300-2.
134. Rorem, B.A.; Cho, T.H.; Farjam, N.; Lenef, J.D.; Barton, K.; Dasgupta, N.P.; Guo, L.J. Integrating Structural Colors with Additive Manufacturing Using Atomic Layer Deposition. *ACS Appl. Mater. Interfaces* **2022**, *14*, 31099–31108. https://doi.org/10.1021/acsami.2c05940.
135. Xiao, X.; Chen, Z.-J.; Varley, R.J.; Li, C.-H. Smart bistable coordination complexes. *Smart Mol.* **2024**, *2*, e20230028. https://doi.org/10.1002/smo.20230028.
136. Demirörs, A.F.; Poloni, E.; Chiesa, M.; Bargardi, F.L.; Binelli, M.R.; Woigk, W.; de Castro, L.D.C.; Kleger, N.; Coulter, F.B.; Sicher, A.; et al. Three-dimensional printing of photonic colloidal glasses into objects with isotropic structural color. *Nat. Commun.* **2022**, *13*, 4397. https://doi.org/10.1038/s41467-022-32060-2.
137. Zeng, M.; Du, Y.; Jiang, Q.; Kempf, N.; Wei, C.; Bimrose, M.V.; Tanvir, A.N.M.; Xu, H.; Chen, J.; Kirsch, D.J.; et al. High-throughput printing of combinatorial materials from aerosols. *Nature* **2023**, *617*, 292–298. https://doi.org/10.1038/s41586-023-05898-9.
138. Bai, L.; Mai, V.C.; Lim, Y.; Hou, S.; Möhwald, H.; Duan, H. Large-Scale Noniridescent Structural Color Printing Enabled by Infiltration-Driven Nonequilibrium Colloidal Assembly. *Adv. Mater.* **2018**, *30*, 1705667. https://doi.org/10.1002/adma.201705667.
139. Jiang, H.; Kaminska, B. Scalable Inkjet-Based Structural Color Printing by Molding Transparent Gratings on Multilayer Nanostructured Surfaces. *ACS Nano* **2018**, *12*, 3112–3125. https://doi.org/10.1021/acsnano.7b08580.
140. Zhang, X.; Zhou, K.; Zhao, Z.; Lin, Y. Printable Photonic Materials and Devices for Smart Healthcare. *Adv. Mater.* **2025**, 2418729. https://doi.org/10.1002/adma.202418729.
141. Chen, H.; Bian, F.; Luo, Z.; Zhao, Y. Biomimetic Anticoagulated Porous Particles with Self-Reporting Structural Colors. *Adv. Sci.* **2024**, *11*, 2400189. https://doi.org/10.1002/advs.202400189.
142. Middleton, R.; Tunstad, S.A..; Knapp, A.; Winters, S.; McCallum, S.; Whitney, H. Self-assembled, disordered structural color from fruit wax bloom. *Sci. Adv.* **2024**, *10*, eadk4219. https://doi.org/10.1126/sciadv.adk4219.
143. Kang, X.; Du, Z.; Yang, S.; Liang, M.; Liu, Q.; Qi, J. Smart molecular probes with controllable photophysical property for smart medicine. *Smart Mol.* **2024**, *2*, e20240033. https://doi.org/10.1002/smo.20240033.
144. Kim, T.; Park, T.H.; Lee, J.W.; Lee, D.; Mun, S.; Kim, G.; Kim, Y.; Kim, G.; Park, J.W.; Lee, K.; et al. Self-Powered Sweat-Responsive Structural Color Display. *Adv. Funct. Mater.* **2024**, *34*, 2314721. https://doi.org/10.1002/adfm.202314721.
145. Liao, Z.-H.; Wang, F. Light-controlled smart materials: Supramolecular regulation and applications. *Smart Mol*. **2024**, *2*, e20240036. https://doi.org/10.1002/smo.20240036.

Article

Stimuli-Responsive Naphthalene Diimide-Based Charge-Transfer Liquid Materials Showing Thermal Response to Tune Photoluminescent Properties

Takumi Omura [1,2], Shogo Morisako [1], and Kyosuke Isoda [1,*]

[1] Organic Materials Chemistry Group, Sagami Chemical Research Institute, 2743-1, Hayakawa, Ayase 252-1193, Kanagawa, Japan
[2] Division of Molecular Sciences, Graduate School of Science, Kitasato University, 1-15-1 Kitasato Minami-ku, Sagamihara 252-0373, Kanagawa, Japan
* Correspondence: k-isoda@sagami.or.jp; Tel.: +81-467-76-9264

Received: 16 April 2025; Revised: 26 May 2025; Accepted: 29 May 2025; Published: 3 June 2025

Abstract: Stimuli-responsive luminescent liquid materials have recently attracted considerable attention due to their potential to address the limitations of solid-state materials, such as the necessity of organic solvents and the difficulty in fabricating composite systems. Liquid-state materials offer superior processability and enable facile modulation of photophysical properties by simply selecting appropriate solutes. In particular, molecular designs incorporating electron-donating or electron-accepting properties into liquid materials allow to form charge-transfer (CT) complexes upon dissolving solutes with their opposite electronic properties, altering both solution color and photoluminescence (PL) behavior. In this study, we developed a room-temperature supercooled liquid material based on an electron-accepting naphthalene diimide (NADI) derivative, **BR-Val-NADI**. Upon dissolving electron-rich naphthalene-based derivatives (**NA-##s**) into **BR-Val-NADI**, **NA-##/BR-Val-NADI** with CT character were readily obtained as solutions, exhibiting various colors and PL properties. **NA-##/BR-Val-NADI** also functioned as printable PL inks that could be applied onto various substrates such as glass and paper. Notably, the PL properties of **NA-##/BR-Val-NADI** were responsive to thermal stimuli, with temperature-induced changes in PL color and PL off/on switching. These results highlight the potential of **NA-##/BR-Val-NADI** as a new class of stimuli-responsive soft materials for applications in printable photonic devices and smart sensing platforms.

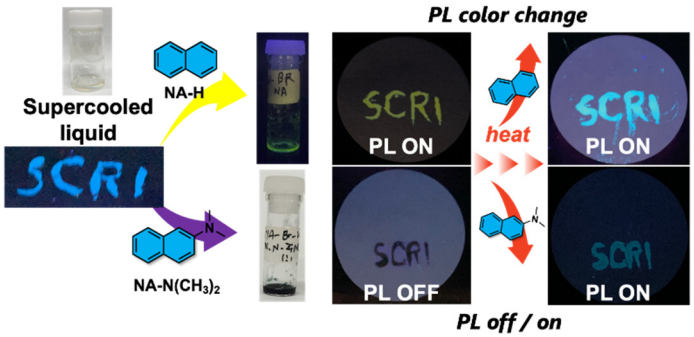

Keywords: naphthalene diimide; stimuli response; liquid material; stimuli-responsive liquid; photoluminescence

1. Introduction

Stimuli-responsive luminescent solid-state materials have been extensively reported and have emerged as a major research focus in materials science over the past two decades [1–10]. Molecular design strategies based on π-conjugated frameworks have been established for such materials, and research is underway not only on the development of novel compounds but also on their response to external stimuli and potential practical applications. However, these solid-state materials often require the use of volatile organic solvents during thin-film fabrication and precise molecular engineering techniques to avoid crystal polymorphism [11–13], which result in variations in luminescence colors in thin films. To address these challenges, the development of liquid-state materials has recently attracted growing attention, as they offer promising soft materials to overcome the limitations associated with solid-state systems [14–18].

Solvent-free liquid materials composed of π-conjugated frameworks are promising candidates for environmental-friendly soft materials [19–29]. Because these materials can be used under a wide range of conditions

without harmful volatile organic solvents, they present a sustainable alternative to conventional solid-state materials, of which applications align with some of the Sustainable Development Goals (SDGs) [30–32]. One of the key advantages of liquid materials lies in their ability to dissolve/disperse a wide variety of compounds such as organic and inorganic materials, enabling the facile preparation of composite materials [20,21,23,33–35]. For example, π-conjugated liquid materials with electron-accepting properties can readily dissolve electron-donating π-conjugated compounds, allowing for the straightforward preparation of charge-transfer (CT) solutions [20,36,37]. In contrast, the fabrication of composite solid-state materials typically requires complicated procedures such as co-crystallization or co-evaporation, which are both technically demanding and time-consuming. In this study, for the development of novel liquid materials in response to external stimuli, we focus on the liquification of 1,4,5,8-naphthalene diimide (NADI) framework.

NADI, a well-known rylene-based aromatic planar molecule, has attracted considerable attention due to its high thermal and photochemical stability, along with its intrinsic electronic and optical properties [38–40]. In particular, NADI exhibits high electron affinity and has been widely studied as an electron acceptor in CT complexes, both in the bulk state and in the dilute solution state in the field of supramolecular chemistry [38,39]. Recent studies have explored the incorporation of the NADI framework into macrocyclic molecules with host–guest interactions [41–45], covalent organic frameworks (COFs) [46–49], and n-type organic semiconductors [50–53]. Among these applications, the use of NADI-based materials for solid-state photoluminescence has drawn growing interest [39,54,55], however, their photoluminescent (PL) properties are often quenched due to strong molecular aggregation (aggregate-caused quenching (ACQ)) in the bulk state [56], which poses a significant challenge. To overcome this problem, various molecular design strategies have been reported, including the introduction of bulky substituents to suppress intermolecular interactions [57], the utilization of aggregation-induced enhanced emission (AIEE) properties [58–60], and the precise control of molecular packing. Despite the wide applicability of NADI derivatives, to the best of our knowledge, no reports have been reported on the liquefaction of NADI showing PL properties, except for one report on the preparation of the CT liquid composed of a supercooled-liquid NADI derivative [36].

In this study, we aimed to suppress the aggregation of the NADI core by introducing valine, a bulky amino acid with isopropyl side chains, during the imidization step, as well as by incorporating branched alkyl chains with large excluded volumes (Schemes 1 and 2). As a result, we obtained compound **BR-Val-NADI** exhibiting a supercooled liquid state at room temperature upon heating and subsequent cooling. Also, we found that **BR-Val-NADI** exhibits clear photoluminescence in its supercooled liquid state, whereas its luminescence is significantly reduced in the solid state. Notably, the emission color could be tuned by dissolving various π-conjugated naphthalene derivatives (**NA-##s**) via CT/exciplex formation. Also, their thermal stimuli enabled modulation of the PL properties. To the best of our knowledge, this represents the first report on the development of a PL NADI-based liquid material.

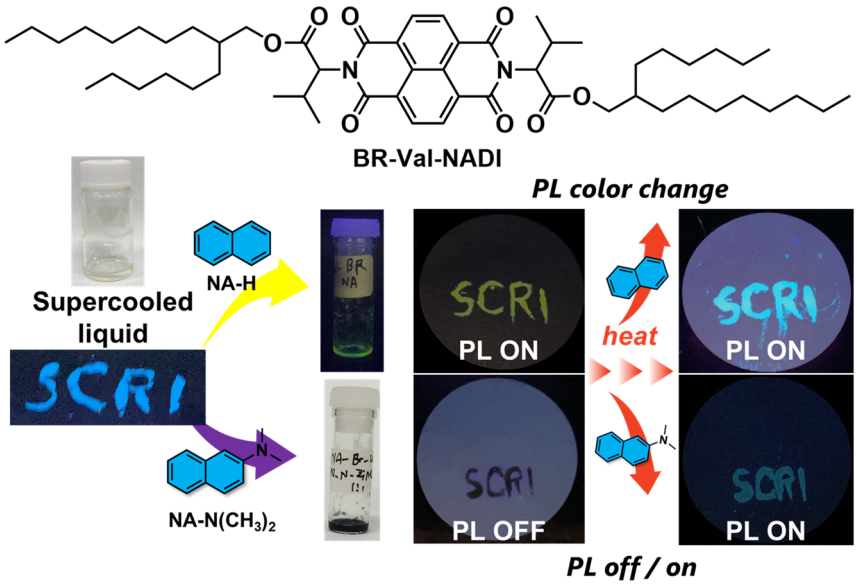

Scheme 1. Molecular structure of **BR-Val-NADI**, its photographs under room light and coated onto glass substrate under black light (365 nm), and photographs of thermal-responsive behaviors for **NA-H**/**BR-Val-NADI** and **NA-NMe$_2$**/**BR-Val-NADI** solutions under light and black light (365 nm).

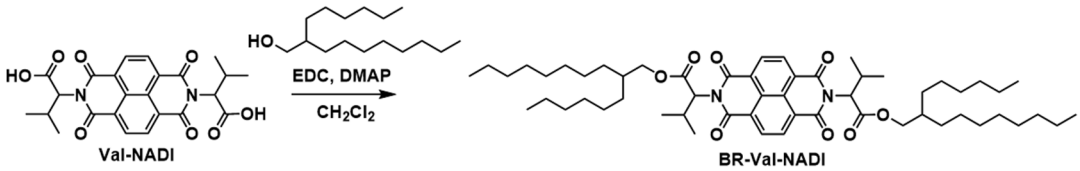

Scheme 2. Synthesis of **BR-Val-NADI.**

2. Materials and Methods

2.1. General Methods

The ^{1}H and ^{13}C NMR spectra were recorded on a Bruker AscendTM Avance III HD 400 MHz or UltraShield Plus 400 MHz NMR spectrometers (^{1}H: 400 MHz, ^{13}C: 101 MHz). All the spectroscopic measurements were carried out at room temperature. The chemical shifts of the ^{1}H and ^{13}C NMR signals are quoted relative to tetramethylsilane ($\delta = 0.00$) as internal standards. High-resolution atmospheric-pressure-chemical-ionization time-of-flight (HR-APCI-TOF-MS) mass spectra were collected on a Bruker compact QTOF spectrometer. UV-vis absorption spectra were recorded on a JASCO V-770 UV-vis spectrometer and the fluorescence spectra were recorded on a JASCO FP-8500 luminescence spectrophotometer. UV-vis and PL spectra were measured in thin films coated onto quartz glass substrates. DSC and TG-DTA measurements were performed on a Hitachi High-Tech EXSTAR6000 DSA6220 and Hitachi High-Tech EXSTAR6000 TG/DTA6200 at a scan rate of 10 °C min^{-1}. A OLYMPUS BX53M optical and polarizing optical microscope equipped with a Mettler FP90/82HT hot stage was used for visual observations of the optical textures. All reagents, all naphthalene derivatives, and solvents were purchased from FUJIFILM Wako Pure Chemical Co. (Osaka, Japan), Tokyo Chemical Industry Co., Ltd. (Tokyo, Japan), Kanto Chemical Co., Inc. (Tokyo, Japan), or Sigma Aldrich (St. Louis, MO, USA), and were used as received. **Val-NADI** was prepared according to previous reports [61].

2.2. Synthesis of **BR-Val-NADI**

To the CH_2Cl_2 (50 mL) solution of **Val-NADI** (3.50 g, 7.5 mmol), 2-hexyl-1-decanol (4.00 g, 16.5 mmol), 1-ethyl-3-(3-dimethylaminopropyl)carbodiimide hydrochloride (EDC, 3.16 g, 16.5 mmol), and 4-dimethylaminopyridine (DMAP, 4.58 g, 37.5 mmol) were added and stirred at room temperature for 2 days. After the addition of deionized water, the resulting mixture was extracted with $CHCl_3$ three times and the combined organic layer was dried over Na_2SO_4, filtered, and evaporated. The residual oil was purified by column chromatography (silica gel) with EtOAc/hexane (1/19) as the eluent to afford **BR-Val-NADI** (1.63 g, 23.8%) as a colorless waxy solid.

BR-Val-NADI: ^{1}H NMR (400 MHz, $CDCl_3$) δ 8.78 (s, 4H), 5.35 (d, J = 9.2 Hz, 2H), 4.10–3.97 (m, 4H), 2.93–2.82 (m, 2H), 1.59–1.49 (m, 2H), 1.33 (d, J = 7.1 Hz, 6H), 1.31–0.93 (m, 48H), 0.87 (t, J = 7.1 Hz, 6H), 0.80 (t, J = 7.4 Hz, 12H); $^{13}C\{^{1}H\}$ NMR (101 MHz, $CDCl_3$) δ 169.3, 162.5, 131.4, 126.8, 126.3, 68.1, 59.3, 37.1, 31.8, 31.7, 31.6, 31.3, 31.3, 29.9, 29.9, 29.5, 29.5, 29.4, 29.4, 29.3, 27.6, 26.6, 26.6, 26.5, 26.5, 22.6, 22.6, 22.1, 19.2, 14.1, 14.0; HRMS (APCI/TOF), m/z: Found: 915.6461 ([M+H]+), Calcd. for $C_{56}H_{86}N_2O_8$ ([M+H]+): 915.6457.

2.3. Computational Details

To obtain details of the electronic structure of **NA-#/BR-Val-NADI** complexes, computational studies were carried out by using the model compound **Val-NADI** instead of **BR-Val-NADI**. All calculations were performed in the gas phase using the Gaussian 16 program package (Rev. C.01) [62]. The ground-state geometry optimization of **NA-#/Val-NADI** was carried out with a B3LYP-D3(BJ) functional using 6-311+G(d,p) basis set [63]. After each geometry optimization, a frequency calculation at the same level was performed to verify that all the stationary points had no imaginary frequency. The time-dependent density functional theory (TD-DFT) [64,65] calculation was performed with a CAM-B3LYP-D3(BJ) functional using 6-311+G(d,p) basis set [66]. The results for TD-DFT calculations are summarized in Table S1. HOMO and LUMO levels for **NA-##s** and **Val-NADI** were calculated with a B3LYP-D3(BJ) functional using 6-31G (d,p) basis set.

2.4. Arrhenius Plot

TG diagrams obtained using the heating method can be analyzed by reaction kinetics theory [67]. The sublimation rate *v* follows an Arrhenius trend as

$$\frac{dm}{dt} = v = A\exp\left(-\frac{\Delta E}{RT}\right) f(m) \tag{5}$$

where m, A, ΔE, R, and T are mass loss rate, a pre-exponential factor, the activation energy, the universal real gas constant, and absolute temperature, respectively. $f(m)$ denotes $(1–m)^n$, and the parameter n is 1.0 when the sample is a supercooled liquid for **BR-Val-NADI** and a liquid for **BR-Val-PMDI**. Equation (1) can be rewritten as

$$\ln v - n\ln(1-m) = -\left(\frac{\Delta E}{R}\right)\frac{1}{T} + \ln A \tag{6}$$

The ΔE can be calculated from the slope of plots of $\ln v – n\ln(1–m)$ and $1/T$. Arrhenius plots of TG diagrams in Figure 1c was illustrated in Figure 1d by using the temperature range of vaporization for **BR-Val-NADI** and **BR-Val-PMDI**, where the values of ΔE were determined, respectively.

3. Results and Discussion

We investigated the fluidic behavior of **BR-Val-NADI** using differential scanning calorimetry (DSC) (Figure 1a). During the 1st heating, **BR-Val-NADI** exhibited a distinct endothermic peak derived from the melting. Upon the 1st cooling, no exothermic peak indicative of crystallization was observed corresponding to the endothermic peak observed on the 1st heating, whereas a glass transition (T_g) was observed at approximately −21 °C. Furthermore, the 2nd heating showed T_g similar to that upon the 1st cooling, however, the peak due to the post crystallization did not appear. Then, we conducted optical microscopy (OM) and polarized optical microscopy (POM) observations of **BR-Val-NADI** before and after melting by thermal treatment at 100 °C in Figure 1b. Before heating, **BR-Val-NADI** at room temperature showed a crystalline state with birefringence, whereas, after melting and subsequent cooling back to room temperature, no birefringence or crystalline features were observed. In addition, **BR-Val-NADI** could be used as an ink to be coated onto glass substrates and papers at room temperature, indicating that **BR-Val-NADI** adopts a room-temperature supercooled liquid state under ambient conditions.

It should be noted that T_g of **BR-Val-NADI** at −21 °C is higher than that of PMDI-based liquid material (**BR-Val-PMDI**) at −50 °C reported previously, which is composed of pyromellitic diimide core smaller p-conjugated framework than of **BR-Val-NADI** [20]. This increase in T_g suggests that **BR-Val-NADI** shows stronger intermolecular interactions, likely due to the expansion of the π-conjugated core as well as the influence on increase in the molecular weight compared to **BR-Val-PMDI**. It should be noted that the cold crystallization process was not observed during heating. Oguni et al. have reported that the supercooled liquid may have the crystal nucleation processes much lower than the glass transition temperature [68]. For **BR-Val-NADI**, the glass transition occurred prior to crystallization by branched alkyl chains suppressing the molecular ordering during the cooling. As a result, during heating, it presumably speculated that the phase transition from glass state to liquid state happened through no cold crystallization due to the molecular ordering. To evaluate the thermal stability of **BR-Val-NADI**, we performed the thermogravimetry-differential thermal analysis (TG-DTA) in Figure 1c. The TG trace of **BR-Val-NADI** showed a clearly single-step weight loss, indicating that **BR-Val-NADI** undergoes thermal evaporation without decomposition, which is an almost similar feature to **BR-Val-PMDI** [20]. Both of temperatures corresponding to 5 wt% and 100 wt% weight loss for **BR-Val-NADI** (365 °C and 433 °C) were higher than those of **BR-Val-PMDI** (318 °C and 416 °C), suggesting that the thermal durability of **BR-Val-NADI** should be improved. Furthermore, we estimated the activation energies ΔE due to the evaporation of both **BR-Val-NADI** and **BR-Val-PMDI** in Figure 1d from results of TG traces, of which values were calculated to be 171.1 kJ/mol for **BR-Val-NADI** and 113.4 kJ/mol for **BR-Val-PMDI**, respectively. These results are consistent with the observed T_g trends and suggest that the expanded π-conjugated core and the increase in molecular weight in **BR-Val-NADI** should enhance intermolecular interactions, contributing to its improved thermal and phase behavior.

To investigate the photophysical properties of **BR-Val-NADI** and its CT complexes, we measured the UV–vis absorption and PL spectra of **BR-Val-NADI** solutions containing various naphthalene derivatives as solutes in Figure 2. The solutions (**NA-##/BR-Val-NADI**) were prepared by dissolving **NA-##**s into **BR-Val-NADI** at a 1:1 molar ratio under heating, respectively. The UV–vis absorption spectrum of pure **BR-Val-NADI** exhibited a no characteristic peak in the long-wavelength range (Figure S1), whereas the **NA-##/BR-Val-NADI** showed new absorption bands at different wavelengths, distinct from that of **BR-Val-NADI** alone, indicating the formation of new electronic transitions (Figure 2a). In particular, **NA-NMe$_2$/BR-Val-NADI**, dissolving **NA-NMe$_2$** with the strongest electron-donating substituent, showed a new absorption peak at 620 nm, of which solution color is deep blue. To investigate the nature of this longer-wavelength peak observed in **NA-NMe$_2$/BR-Val-NADI**, time-dependent density functional theory (TD-DFT) calculations were performed using Gaussian 16 at the TD-CAM-

B3LYP-D3(BJ)/6-311+G(d,p) level of theory. For the calculation, a 1:1 complex of **NA-NMe$_2$** and **Val-NADI** instead of **BR-Val-NADI** was used (Figure 2). The TD-CAM-B3LYP functional was selected due to its long-range correction, making it suitable for modeling CT transitions. The TD-DFT results of 1:1 complex (**NA-NMe$_2$/Val-NADI**) revealed a low-energy absorption peak at 580 nm, which is almost consistent with the experimentally observed peak in the **NA-NMe$_2$/BR-Val-NADI** solution. The frontier molecular orbital analysis revealed that this transition is indicative of the electron transfer from the HOMO localized on **NA-NMe$_2$** as electron donor to the LUMO localized on **Val-NADI** as electron acceptor (Figure 2a). These results strongly support the assignment of the observed band as a CT transition from **NA-NMe$_2$** to **BR-Val-NADI**. In addition, TD-DFT calculations were performed for **NA-H/Val-NADI** and **NA-CN/Val-NADI**, which shows weaker electron-donating abilities compared to **NA-NMe$_2$**. In both cases, the calculations indicated the presence of CT transitions corresponding to HOMO–LUMO electron transfer, of which predicted CT bands appeared at shorter wavelengths than that of **NA-NMe$_2$**, consistent with their deeper HOMO levels. In the UV–vis absorption spectrum, **NA-H/BR-Val-NADI** showed a weak CT band. It is noteworthy that the position of the CT band was dependent on the HOMO levels of **NA-##**s. Peaks arising from the CT transition tend to undergo a bathochromically red-shift as the HOMO level of **NA-##**s becomes shallower, which correlates with a reduction in the energy gap between the HOMO level of **NA-##s** and the LUMO level of **BR-Val-NADI** (Figure S2). In contrast, solutions containing **NA-CN** and other electron-deficient derivatives (**NA-HCO** and **NA-COMe**) exhibit less CT bands than those with electron-donating **NA-##**s (Figure S3). This absence might be due to the weak donor ability of these compounds with electron-deficient substitutes and/or overlap between the expected CT bands and intrinsic absorption peaks of either **BR-Val-NADI** or **NA-##**s itself.

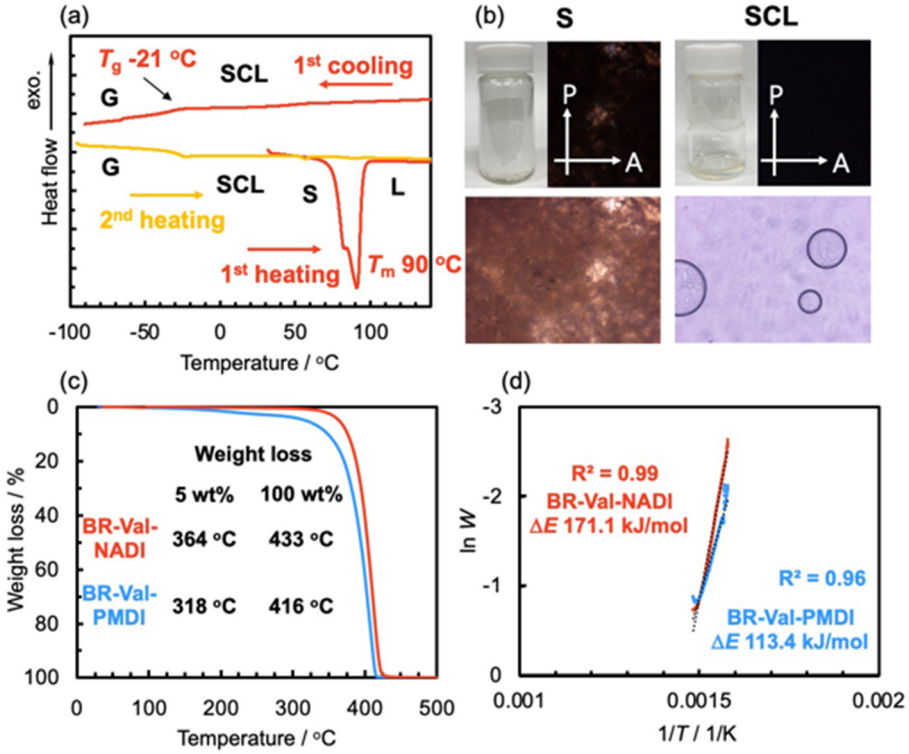

Figure 1. (**a**) DSC thermograms of **BR-Val-NADI** (red-colored lines: 1st heating and 1st cooling; orange-colored line: 2nd heating) at 10 K min^{-1}. S: solid state; L: liquid state; SCL: supercooled-liquid state; G: glassy state. (**b**) Photographs, polarized optical photomicrographs (POM) and optical photomicrographs (OM) of **BR-Val-NADI** in solid state (**left**) and supercooled-liquid state (**right**) at room temperature. S: solid state; SCL: supercooled-liquid state. Arrows indicate the directions of polarizer (P) and analyzer (A) axes. **BR-Val-NADI** in the solid state was obtained after purification through column chromatography, evaporation from hexane/ethyl acetate, and drying under vacuum. (**c**) TG analysis of **BR-Val-NADI** and **BR-Val-PMDI** over the temperature range from 25 to 500 °C under N_2 atmosphere with their temperatures at 5 wt% and 100 wt% weight loss. (**d**) Temperature dependence for weight loss due to vaporization process of **BR-Val-NADI** and **BR-Val-PMDI** (ln$W$ vs. T^{-1}) at 10 K min^{-1} heating rate under static N_2 atmosphere. These plots correspond to the range of weight loss of **BR-Val-NADI** and **BR-Val-PMDI** in TG traces. The values shown in the figure indicate activation energies of **BR-Val-NADI** and **BR-Val-PMDI**, respectively.

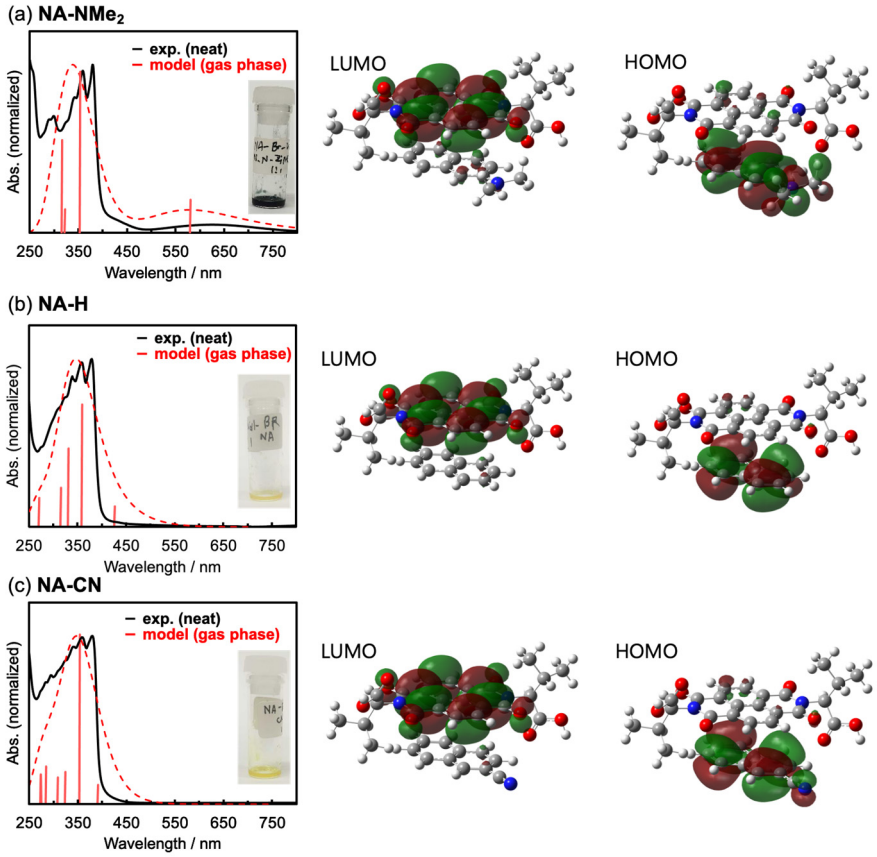

Figure 2. Experimental (neat) and simulated (gas) UV-vis absorption spectra and frontier orbitals based on TD-DFT calculations (TD-CAM-B3LYP-D3(BJ)/6-311+G(d,p)) for (**a**) NA-NMe_2/BR-Val-NADI and **NA-NMe_2/Val-NADI**, (**b**) **NA-H/BR-Val-NADI** and **NA-H/Val-NADI**, and (**c**) **NA-CN/BR-Val-NADI** and **NA-CN/Val-NADI**.

Next, we investigated the PL properties of the **BR-Val-NADI**-based solutions in Figures 3a,b, S2 and S3. In its supercooled-liquid state, **BR-Val-NADI** exhibited sky-blue emission with a peak at 481 nm, which is distinctly different from its solid state showing less emission (Figures 3b and S1). Upon dissolving **NA-H** into **BR-Val-NADI**, the resulting solution **NA-H/BR-Val-NADI** exhibited yellow emission with a PL peak at 550 nm. Furthermore, varying the substituents introduced into **NA-##**s could tune the emission colors. For instance, **NA-##**s (**NA-CN**, **NA-HCO** and **NA-COMe**) bearing electron-withdrawing groups exhibited blue-shifted PL peaks compared to **NA-H**, while those (**NA-Me**) with electron-donating substituents showed red-shifted emissions, with the appearance of peaks at longer wavelengths than **NA-H**. To understand these trends, we examined the correlation between the observed PL emission peaks and the HOMO levels of **NA-##**s by DFT calculations (Figure 3c). The results revealed a clear trend: as the HOMO level becomes shallower (i.e., higher in energy), the emission peaks shifts toward the bathochromic region, indicating a stronger CT interaction.

Finally, we investigated the thermal responsiveness of **NA-##/BR-Val-NADI** (Figure 4). Given that **NA-##**s are known to volatilize upon heating [69,70], we hypothesized that selective evaporation of the **NA-##** component from **NA-##/BR-Val-NADI** could modulate the emission properties. When a filter paper coated with **NA-H/BR-Val-NADI** was observed under UV light (365 nm), it emitted yellow fluorescence similar to the original solution (Figure 4). After heating the coated paper at 150 °C for 5 min, the emission color changed from yellow to sky-blue. This change indicates the evaporation of **NA-H**, leaving behind **BR-Val-NADI**, which emits sky-blue fluorescence. In contrast, **NA-NMe_2/BR-Val-NADI**, which initially exhibited no emission, could emit sky-blue fluorescence after heating at 150 °C for 5 min by the evaporation of **NA-NMe_2** only. These findings suggest that **NA-##/BR-Val-NADI** systems can function as thermal-responsive liquid materials, enabling tunable PL color changes or PL OFF/ON switching of emission through thermal stimuli.

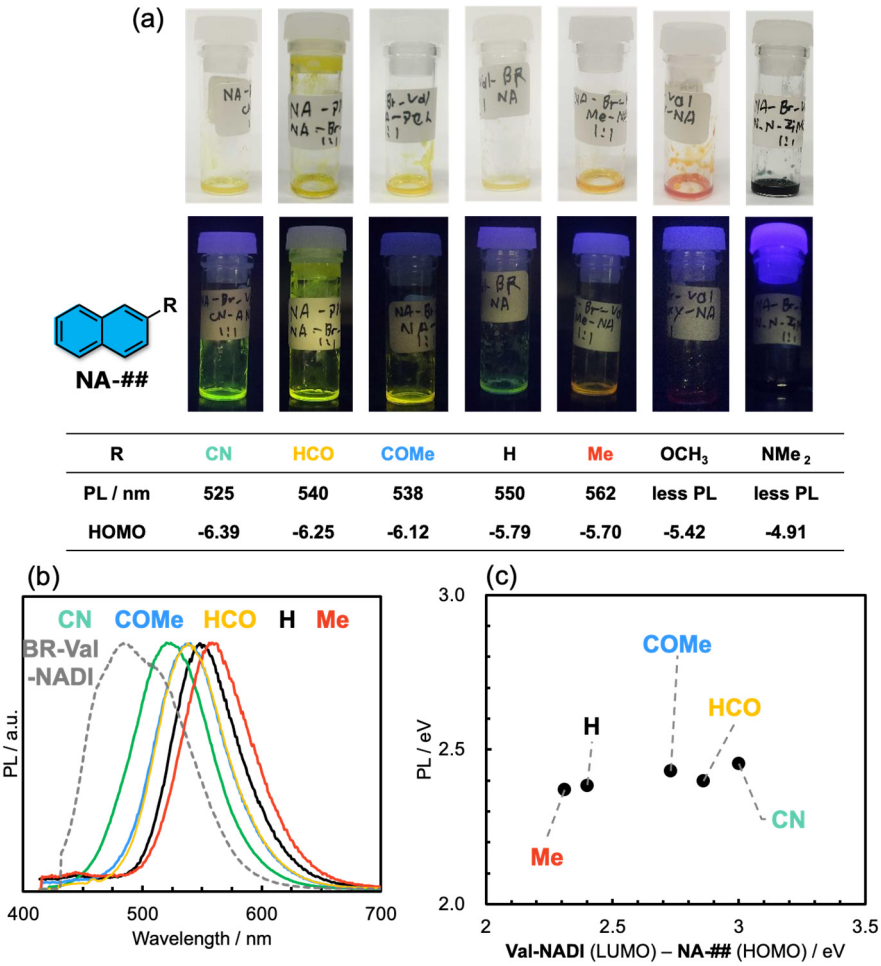

R	CN	HCO	COMe	H	Me	OCH_3	NMe_2
PL / nm	525	540	538	550	562	less PL	less PL
HOMO	-6.39	-6.25	-6.12	-5.79	-5.70	-5.42	-4.91

Figure 3. (**a**) Photographs of **NA-##/BR-Val-NADI** under 365 nm light. (**b**) PL spectra of **NA-##/BR-Val-NADI** in a neat state. (**c**) The relationship between peaks in PL spectra and HOMO-LUMO gap estimated by DFT calculations with a B3LYP-D3(BJ) functional using 6-31G (d,p) basis set.

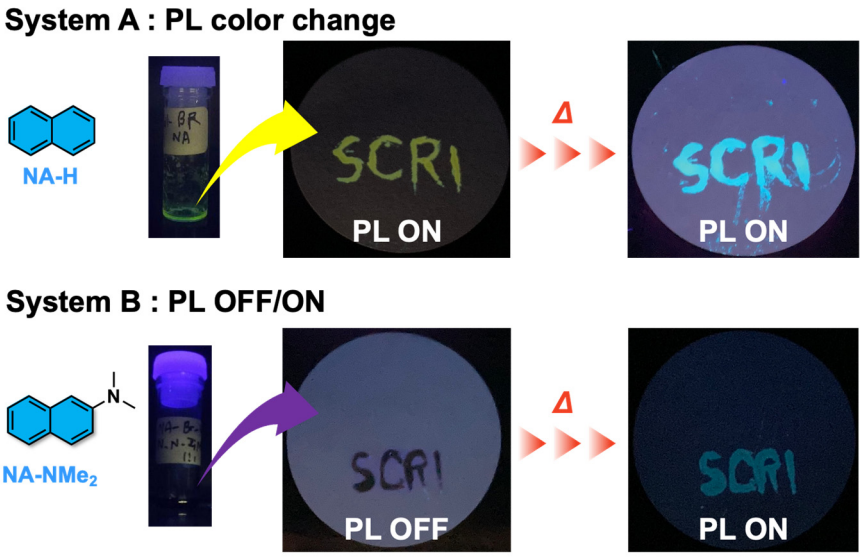

Figure 4. Thermal-responsive behaviors of **NA-H/BR-Val-NADI** in PL color change for system A and **NA-NMe_2/BR-Val-NADI** in PL color change for system B.

4. Conclusions

We successfully synthesized a room-temperature supercooled liquid material based on an electron-accepting naphthalene diimide derivative, **BR-Val-NADI**. By dissolving **NA-##**s, **NA-##/BR-Val-NADI** can be readily

obtained as CT-type liquid solutions, that exhibited tunable colors and distinct PL properties. **NA-##/BR-Val-NADI** also demonstrated excellent printability, enabling their application as PL inks on various substrates such as glass and paper. Also, the PL characteristics of **NA-##/BR-Val-NADI** were highly responsive to thermal stimuli, including temperature-dependent color change and PL off/on switching. These findings underscore the promise of **NA-##/BR-Val-NADI** systems as a new class of thermos-responsive soft materials with potential for use in printable photonic devices and smart sensing technologies.

Supplementary Materials: The following supporting information can be downloaded at: https://media.sciltp.com/articles/others/250604170835175 8/MI-1043-SI-final.pdf, Figure S1: Photographs of **BR-Val-NADI** under room light and under 365 nm light. SCL: supercooled liquid; S: solid. The UV-vis absorption and PL spectra of **BR-Val-NADI** in supercooled-liquid state; Figure S2. The UV-vis absorption (left) and PL (right) spectra of **NA-H/BR-Val-NADI**, **NA-Me/BR-Val-NADI**, **NA-OMe/BR-Val-NADI**, and **NA-NMe$_2$/BR-Val-NADI** in solution states. Photographs of solutions under room light and under 365 nm light. Arrows indicate CT peaks; Figure S3. The UV-vis absorption (left) and PL (right) spectra of **NA-CN/BR-Val-NADI**, **NA-HCO/BR-Val-NADI**, and **NA-COMe/BR-Val-NADI**, in solution states. Photographs of solutions under room light and under 365 nm light; Table S1. Calculated wavelengths for the absorption spectrum of (a) **NA-NMe$_2$/Val-NADI**, (b) **NA-H/Val-NADI**, and (c) **NA-CN/Val-NADI** complexes, their oscillator strengths (>0.02), and the associated transitions with |CI coefficient| > 0.2.

Author Contributions: T.O. synthesized **BR-Val-NADI** and carries out experiments. S.M. carried out the DFT calculation and experiments. K.I. de-signed and supervised this project and wrote the manuscript. All authors have read and agreed to the published version of the manuscript.

Funding: This work was supported by the Japan Society for the Promotion of Science (JSPS) KAKENHI Grant Numbers 22K05257 (K.I.), 25K08603 (K.I.), 23K13727 (S.M.), and 25K08617 (S.M.) and Iketani Science and Technology Foundation (K.I.), Kato Foundation for Promotion of Science (K.I.), and Tokyo Ohka Foundation for The Promotion of Science and Technology (K.I.).

Data Availability Statement: The data that support the findings of this study are available from the corresponding author upon reasonable request.

Conflicts of Interest: The authors declare no conflict of interest.

References

1. Yerushalmi, R.; Scherz, A.; van der Boom, M.E.; Kraatz, H.-B. Stimuli responsive materials: New avenues toward smart organic devices. *J. Mater. Chem.* **2005**, *15*, 4480–4487. https://doi.org/10.1039/B505212B.
2. Huang, Y.; Ning, L.; Zhang, X.; Zhou, Q.; Gong, Q.; Zhang, Q. Stimuli-fluorochromic smart organic materials. *Chem. Soc. Rev.* **2024**, *53*, 1090–1166. https://doi.org/10.1039/D2CS00976E.
3. Yan, D.; Wang, Z.; Zhang, Z. Stimuli-Responsive Crystalline Smart Materials: From Rational Design and Fabrication to Applications. *Acc. Chem. Res.* **2022**, *55*, 1047–1058. https://doi.org/10.1021/acs.accounts.2c00027.
4. Sun, H.; Shen, S.; Li, C.; Yu, W.; Xie, Q.; Wu, D.; Zhu, L. Stimuli-Responsive Dual-Emission Property of Single-Luminophore-Based Materials. *Adv. Funct. Mater.* **2025**, *35*, 2415400. https://doi.org/10.1002/adfm.202415400.
5. Wu, W.; Chen, K.; Wang, T.; Wang, N.; Huang, X.; Zhou, L.; Wang, Z.; Hao, H. Stimuli-responsive flexible organic crystals. *J. Mater. Chem. C* **2023**, *11*, 2026–2052. https://doi.org/10.1039/D2TC04642C.
6. Huang, L.; Qian, C.; Ma, Z. Stimuli-Responsive Purely Organic Room-Temperature Phosphorescence Materials. *Chem.-Eur. J.* **2020**, *26*, 11914–11930. https://doi.org/10.1002/chem.202000526.
7. Karunakar, K.K.; Cheriyan, B.V.; Anandakumar, R.; Murugathirumal, A.; Kataria, K.; Yabase, L. Stimuli-Responsive Smart Materials: Bridging the Gap Between Biotechnology and Regenerative Medicine. *Bioprinting* **2025**, *48*, e00415. https://doi.org/10.1016/j.bprint.2025.e00415.
8. Zhao, J.; Du, J.; Qin, T.; Zhang, S.X.-A.; Sheng, L. "Confined Eutectic" Strategy for Visual Refrigeration Responsive Fluorescent Materials with Easy Preparation and Multi-Color Tunability. *Adv. Sci.* **2025**, 2503779. https://doi.org/10.1002/advs.202503779.
9. Du, J.; Sheng, L.; Xu, Y.; Chen, Q.; Gu, C.; Li, M.; Zhang, S.X.-A. Printable Off-On Thermoswitchable Fluorescent Materials for Programmable Thermally Controlled Full-Color Displays and Multiple Encryption. *Adv. Mater.* **2021**, *33*, 2008055. https://doi.org/10.1002/adma.202008055.
10. Du, J.; Sheng, L.; Chen, Q.; Xu, Y.; Li, W.; Wang, X.; Li, M.; Zhang, S.X.-A. Simple and general platform for highly adjustable thermochromic fluorescent materials and multi-feasible applications. *Mater. Horiz.* **2019**, *6*, 1654–1662. https://doi.org/10.1039/C9MH00253G.
11. Davey, R.J.; Schroeder, S.L.M.; ter Horst, J.H. Nucleation of Organic Crystals—A Molecular Perspective. *Angew. Chem. Int. Ed.* **2013**, *52*, 2166–2179. https://doi.org/10.1002/anie.201204824.
12. Liang, C. Organic Polymorphs Based on AIE-Active Molecules: Preparation, Characterization, and Application. *Cryst. Growth Des.* **2024**, *24*, 7322–7341. https://doi.org/10.1021/acs.cgd.4c00499.
13. Chung, H.; Diao, Y. Polymorphism as an emerging design strategy for high performance organic electronics. *J. Mater. Chem. C* **2016**, *4*, 3915–3933. https://doi.org/10.1039/C5TC04390E.

14. Nakanishi, T. (Ed.) *Functional Organic Liquids*; John Wiley & Sons: Hoboken, NJ, USA, 2019; pp. i–xii.
15. Ghosh, A.; Nakanishi, T. Frontiers of solvent-free functional molecular liquids. *Chem. Commum.* **2017**, *53*, 10344–10357. https://doi.org/10.1039/C7CC05883G.
16. Tateyama, A.; Nakanishi, T. Responsive molecular liquid materials. *Responsive Mater.* **2023**, *1*, e20230001. https://doi.org/10.1002/rpm.20230001.
17. Lu, F.; Nakanishi, T. Solvent-Free Luminous Molecular Liquids. *Adv. Opt. Mater.* **2019**, *7*, 1900176. https://doi.org/10.1002/adom.201900176.
18. Wakchaure, V.C.; Channareddy, G.; Babu, S.S. Solvent-Free Organic Liquids: An Efficient Fluid Matrix for Unexplored Functional Hybrid Materials. *Acc. Chem. Res.* **2024**, *57*, 670–684. https://doi.org/10.1021/acs.accounts.3c00670.
19. Tateyama, A.; Nagura, K.; Yamanaka, M.; Nakanishi, T. Alkyl–π Functional Molecular Gels: Control of Elastic Modulus and Improvement of Electret Performance. *Angew. Chem. Int. Ed.* **2024**, *63*, e202402874. https://doi.org/10.1002/anie.202402874.
20. Omura, T.; Morisako, S.; Isoda, K. Amino acid-appended pyromellitic diimide liquid materials, their photoluminescence, and thermal response turning photoluminescence off. *Chem. Commum.* **2024**, *60*, 9352–9355. https://doi.org/10.1039/D4CC02229G.
21. Ogoshi, T.; Azuma, S.; Wada, K.; Tamura, Y.; Kato, K.; Ohtani, S.; Kakuta, T.; Yamagishi, T.-A. Exciplex Formation by Complexation of an Electron-Accepting Guest in an Electron-Donating Pillar [5] arene Host Liquid. *J. Am. Chem. Soc.* **2024**, *146*, 9828–9835. https://doi.org/10.1021/jacs.3c14582.
22. Xu, Z.; Wang, Z.; Yao, W.; Gao, Y.; Li, Y.; Shi, H.; Huang, W.; An, Z. Supercooled Liquids with Dynamic Room Temperature Phosphorescence Using Terminal Hydroxyl Engineering. *Angew. Chem. Int. Ed.* **2023**, *62*, e202301564. https://doi.org/10.1002/anie.202301564.
23. Tanabe, Y.; Tsutsui, H.; Matsuda, S.; Shikita, S.; Yasuda, T.; Isoda, K. Pyromellitic-Diimide-Based Liquid Material Forming an Exciplex with Naphthalene. *ChemPhotoChem* **2023**, *7*, e202200287. https://doi.org/10.1002/cptc.202200287.
24. Sato, Y.; Mutoh, Y.; Morishita, S.; Tsurumachi, N.; Isoda, K. Stimulus-Responsive Supercooled π-Conjugated Liquid and Its Application in Rewritable Media. *J. Phys. Chem. Lett.* **2021**, *12*, 3014–3018. https://doi.org/10.1021/acs.jpclett.1c00247.
25. Ikenaga, A.; Akiyama, Y.; Ishiyama, T.; Gon, M.; Tanaka, K.; Chujo, Y.; Isoda, K. Stimuli-Responsive Self-Assembly of π-Conjugated Liquids Triggers Circularly Polarized Luminescence. *ACS Appl. Mater. Interfaces* **2021**, *13*, 47127–47133. https://doi.org/10.1021/acsami.1c13119.
26. Isoda, K.; Matsubara, M.; Ikenaga, A.; Akiyama, Y.; Mutoh, Y. Reversibly/irreversibly stimuli-responsive inks based on N-heteroacene liquids. *J. Mater. Chem. C* **2019**, *7*, 14075–14079. https://doi.org/10.1039/C9TC05195C.
27. Isoda, K.; Ishiyama, T.; Mutoh, Y.; Matsukuma, D. Stimuli-Responsive Room-Temperature N-Heteroacene Liquid: In Situ Observation of the Self-Assembling Process and Its Multiple Properties. *ACS Appl. Mater. Interfaces* **2019**, *11*, 12053–12062. https://doi.org/10.1021/acsami.8b21695.
28. Giri, N.; Del Pópolo, M.G.; Melaugh, G.; Greenaway, R.L.; Rätzke, K.; Koschine, T.; Pison, L.; Gomes, M.F.C.; Cooper, A.I.; James, S.L. Liquids with permanent porosity. *Nature* **2015**, *527*, 216–220. https://doi.org/10.1038/nature16072.
29. Chung, K.; Kwon, M.S.; Leung, B.M.; Wong-Foy, A.G.; Kim, M.S.; Kim, J.; Takayama, S.; Gierschner, J.; Matzger, A.J.; Kim, J. Shear-Triggered Crystallization and Light Emission of a Thermally Stable Organic Supercooled Liquid. *ACS Cent. Sci.* **2015**, *1*, 94–102. https://doi.org/10.1021/acscentsci.5b00091.
30. Clarke, C.J.; Tu, W.-C.; Levers, O.; Bröhl, A.; Hallett, J.P. Green and Sustainable Solvents in Chemical Processes. *Chem. Rev.* **2018**, *118*, 747–800. https://doi.org/10.1021/acs.chemrev.7b00571.
31. Horváth, I.T. Introduction: Sustainable Chemistry. *Chem. Rev.* **2018**, *118*, 369–371. https://doi.org/10.1021/acs.chemrev.7b00721.
32. Ghosh, A.; Yoshida, M.; Suemori, K.; Isago, H.; Kobayashi, N.; Mizutani, Y.; Kurashige, Y.; Kawamura, I.; Nirei, M.; Yamamuro, O.; et al. Soft chromophore featured liquid porphyrins and their utilization toward liquid electret applications. *Nat. Commun.* **2019**, *10*, 4210. https://doi.org/10.1038/s41467-019-12249-8.
33. Goudappagouda; Manthanath, A.; Wakchaure, V.C.; Ranjeesh, K.C.; Das, T.; Vanka, K.; Nakanishi, T.; Babu, S.S. Paintable Room-Temperature Phosphorescent Liquid Formulations of Alkylated Bromonaphthalimide. *Angew. Chem. Int. Ed.* **2019**, *58*, 2284–2288. https://doi.org/10.1002/anie.201811834.
34. Santhosh Babu, S.; Aimi, J.; Ozawa, H.; Shirahata, N.; Saeki, A.; Seki, S.; Ajayaghosh, A.; Möhwald, H.; Nakanishi, T. Solvent-Free Luminescent Organic Liquids. *Angew. Chem. Int. Ed.* **2012**, *51*, 3391–3395. https://doi.org/10.1002/anie.201108853.
35. Babu, S.S.; Hollamby, M.J.; Aimi, J.; Ozawa, H.; Saeki, A.; Seki, S.; Kobayashi, K.; Hagiwara, K.; Yoshizawa, M.; Möhwald, H.; et al. Nonvolatile liquid anthracenes for facile full-colour luminescence tuning at single blue-light excitation. *Nat. Commun.* **2013**, *4*, 1969. https://doi.org/10.1038/ncomms2969.

36. Wakchaure, V.C.; Pillai, L.V.; Goudappagouda; Ranjeesh, K.C.; Chakrabarty, S.; Ravindranathan, S.; Rajamohanan, P.R.; Babu, S.S. Charge transfer liquid: A stable donor–acceptor interaction in the solvent-free liquid state. *Chem. Commum.* **2019**, *55*, 9371–9374. https://doi.org/10.1039/C9CC03671G.
37. Iguchi, H.; Furutani, H.; Kimizuka, N. Ionic Charge-Transfer Liquid Crystals Formed by Alternating Supramolecular Copolymerization of Liquid π-Donors and TCNQ. *Front. Chem.* **2021**, *9*, 657246. https://doi.org/10.3389/fchem.2021.657246.
38. Al Kobaisi, M.; Bhosale, S.V.; Latham, K.; Raynor, A.M.; Bhosale, S.V. Functional Naphthalene Diimides: Synthesis, Properties, and Applications. *Chem. Rev.* **2016**, *116*, 11685–11796. https://doi.org/10.1021/acs.chemrev.6b00160.
39. Bhosale, S.V.; Jani, C.H.; Langford, S.J. Chemistry of naphthalene diimides. *Chem. Soc. Rev.* **2008**, *37*, 331–342. https://doi.org/10.1039/B615857A.
40. Langford, S.J.; Latter, M.J.; Woodward, C.P. Progress in Charge Transfer Systems Utilizing Porphyrin Donors and Simple Aromatic Diimide Acceptor Units. *Photochem. Photobiol.* **2006**, *82*, 1530–1540. https://doi.org/10.1111/j.1751-1097.2006.tb09808.x.
41. Wang, Y.; Wu, H.; Stoddart, J.F. Molecular Triangles: A New Class of Macrocycles. *Acc. Chem. Res.* **2021**, *54*, 2027–2039. https://doi.org/10.1021/acs.accounts.1c00108.
42. Hartmann, D.; Penty, S.E.; Zwijnenburg, M.A.; Pal, R.; Barendt, T.A. A Bis-Perylene Diimide Macrocycle Chiroptical Switch. *Angew. Chem. Int. Ed.* **2025**, *64*, e202501122. https://doi.org/10.1002/anie.202501122.
43. Tominaga, M.; Kawahata, M.; Itoh, T.; Yamaguchi, K. Spherical Aggregates and Crystal Structure of Naphthalenediimide-Based Macrocycle and Complexation with Perylene. *Cryst. Growth Des.* **2018**, *18*, 37–41. https://doi.org/10.1021/acs.cgd.7b01361.
44. Beldjoudi, Y.; Narayanan, A.; Roy, I.; Pearson, T.J.; Cetin, M.M.; Nguyen, M.T.; Krzyaniak, M.D.; Alsubaie, F.M.; Wasielewski, M.R.; Stupp, S.I.; et al. Supramolecular Tessellations by a Rigid Naphthalene Diimide Triangle. *J. Am. Chem. Soc.* **2019**, *141*, 17783–17795. https://doi.org/10.1021/jacs.9b08758.
45. Ling, Q.-H.; Zhu, J.-L.; Qin, Y.; Xu, L. Naphthalene diimide- and perylene diimide-based supramolecular cages. *Mater. Chem. Front.* **2020**, *4*, 3176–3189. https://doi.org/10.1039/D0QM00540A.
46. Jhulki, S.; Feriante, C.H.; Mysyk, R.; Evans, A.M.; Magasinski, A.; Raman, A.S.; Turcheniuk, K.; Barlow, S.; Dichtel, W.R.; Yushin, G.; et al. A Naphthalene Diimide Covalent Organic Framework: Comparison of Cathode Performance in Lithium-Ion Batteries with Amorphous Cross-linked and Linear Analogues, and Its Use in Aqueous Lithium-Ion Batteries. *ACS Appl. Energy Mater.* **2021**, *4*, 350–356. https://doi.org/10.1021/acsaem.0c02281.
47. van der Jagt, R.; Vasileiadis, A.; Veldhuizen, H.; Shao, P.; Feng, X.; Ganapathy, S.; Habisreutinger, N.C.; van der Veen, M.A.; Wang, C.; Wagemaker, M.; et al. Synthesis and Structure–Property Relationships of Polyimide Covalent Organic Frameworks for Carbon Dioxide Capture and (Aqueous) Sodium-Ion Batteries. *Chem. Mater.* **2021**, *33*, 818–833. https://doi.org/10.1021/acs.chemmater.0c03218.
48. Wang, L.-L.; Ni, X.-Q.; Han, Y.-J.; Zhang, J.; Luo, H.-B.; Qiao, Q.; Wu, Y.-P.; Ren, X.-M. Acidified naphthalene diimide covalent organic frameworks with superior proton conduction for solid-state proton batteries. *J. Mater. Chem. C* **2025**, *13*, 4398–4404. https://doi.org/10.1039/D4TC04322G.
49. Huang, Z.; Zhang, Y.; Zhao, S.; Xu, Y.; Qi, X.; Zhang, L.; Zhao, Y. Two-dimensional covalent organic frameworks with spatial-distribution defined D-A structures for efficient near-infrared photothermal conversion. *Microporous Mesoporous Mater.* **2022**, *343*, 112191. https://doi.org/10.1016/j.micromeso.2022.112191.
50. Katz, H.E.; Johnson, J.; Lovinger, A.J.; Li, W. Naphthalenetetracarboxylic Diimide-Based n-Channel Transistor Semiconductors: Structural Variation and Thiol-Enhanced Gold Contacts. *J. Am. Chem. Soc.* **2000**, *122*, 7787–7792. https://doi.org/10.1021/ja000870g.
51. Katz, H.E.; Lovinger, A.J.; Johnson, J.; Kloc, C.; Siegrist, T.; Li, W.; Lin, Y.Y.; Dodabalapur, A. A soluble and air-stable organic semiconductor with high electron mobility. *Nature* **2000**, *404*, 478–481. https://doi.org/10.1038/35006603.
52. He, T.; Stolte, M.; Burschka, C.; Hansen, N.H.; Musiol, T.; Kälblein, D.; Pflaum, J.; Tao, X.; Brill, J.; Würthner, F. Single-crystal field-effect transistors of new Cl_2-NDI polymorph processed by sublimation in air. *Nat. Commun.* **2015**, *6*, 5954. https://doi.org/10.1038/ncomms6954.
53. Kao, C.-C.; Lin, P.; Shen, Y.-Y.; Yan, J.-Y.; Ho, J.-C.; Lee, C.-C.; Chan, L.-H. Solid-state structure of the naphthalene-based n-type semiconductor, and performance improved with Mo-based source/drain electrodes. *Synth. Met.* **2008**, *158*, 299–305. https://doi.org/10.1016/j.synthmet.2008.01.019.
54. Basak, S.; Nandi, N.; Paul, S.; Banerjee, A. Luminescent Naphthalene Diimide-Based Peptide in Aqueous Medium and in Solid State: Rewritable Fluorescent Color Code. *ACS Omega* **2018**, *3*, 2174–2182. https://doi.org/10.1021/acsomega.7b01813.
55. Sakai, N.; Mareda, J.; Vauthey, E.; Matile, S. Core-substituted naphthalenediimides. *Chem. Commum.* **2010**, *46*, 4225–4237. https://doi.org/10.1039/C0CC00078G.

56. Yuan, W.Z.; Lu, P.; Chen, S.; Lam, J.W.Y.; Wang, Z.; Liu, Y.; Kwok, H.S.; Ma, Y.; Tang, B.Z. Changing the Behavior of Chromophores from Aggregation-Caused Quenching to Aggregation-Induced Emission: Development of Highly Efficient Light Emitters in the Solid State. *Adv. Mater.* **2010**, *22*, 2159–2163. https://doi.org/10.1002/adma.200904056.
57. Pervin, R.; Manian, A.; Chen, Z.; Christofferson, A.J.; Owyong, T.C.; Bradley, S.J.; White, J.M.; Ghiggino, K.P.; Russo, S.P.; Wong, W.W.H. Medium effects on the fluorescence of Imide-substituted naphthalene diimides. *J. Photochem. Photobiol. A* **2023**, *436*, 114364. https://doi.org/10.1016/j.jphotochem.2022.114364.
58. Hong, Y.; Lam, J.W.Y.; Tang, B.Z. Aggregation-induced emission. *Chem. Soc. Rev.* **2011**, *40*, 5361–5388. https://doi.org/10.1039/C1CS15113D.
59. Molla, M.R.; Ghosh, S. Aqueous self-assembly of chromophore-conjugated amphiphiles. *Phys. Chem. Chem. Phys.* **2014**, *16*, 26672–26683. https://doi.org/10.1039/C4CP03791J.
60. Lasitha, P.; Prasad, E. Orange red emitting naphthalene diimide derivative containing dendritic wedges: Aggregation induced emission (AIE) and detection of picric acid (PA). *RSC Adv.* **2015**, *5*, 41420–41427. https://doi.org/10.1039/C5RA04857E.
61. Mollick, S.; Mukherjee, S.; Kim, D.; Qiao, Z.; Desai, A.V.; Saha, R.; More, Y.D.; Jiang, J.; Lah, M.S.; Ghosh, S.K. Hydrophobic Shielding of Outer Surface: Enhancing the Chemical Stability of Metal–Organic Polyhedra. *Angew. Chem. Int. Ed.* **2019**, *58*, 1041–1045. https://doi.org/10.1002/anie.201811037.
62. Frisch, M.J.; Trucks, G.W.; Schlegel, H.B.; Scuseria, G.E.; Robb, M.A.; Cheeseman, J.R.; Scalmani, G.; Barone, V.; Petersson, G.A.; et al. *Gaussian 16, Revision C.01*; Gaussian, Inc.: Wallingford, CT, USA, 2019.
63. Grimme, S.; Ehrlich, S.; Goerigk, L. Effect of the damping function in dispersion corrected density functional theory. *J. Comput. Chem.* **2011**, *32*, 1456–1465. https://doi.org/10.1002/jcc.21759.
64. Bauernschmitt, R.; Ahlrichs, R. Treatment of electronic excitations within the adiabatic approximation of time dependent density functional theory. *Chem. Phys. Lett.* **1996**, *256*, 454–464. https://doi.org/10.1016/0009-2614(96)00440-X.
65. Casida, M.E.; Jamorski, C.; Casida, K.C.; Salahub, D.R. Molecular excitation energies to high-lying bound states from time-dependent density-functional response theory: Characterization and correction of the time-dependent local density approximation ionization threshold. *J. Chem. Phys.* **1998**, *108*, 4439–4449. https://doi.org/10.1063/1.475855.
66. Yanai, T.; Tew, D.P.; Handy, N.C. A new hybrid exchange–correlation functional using the Coulomb-attenuating method (CAM-B3LYP). *Chem. Phys. Lett.* **2004**, *393*, 51–57. https://doi.org/10.1016/j.cplett.2004.06.011.
67. Chirico, R.D.; Knipmeyer, S.E.; Nguyen, A.; Steele, W.V. The thermodynamic properties to the temperature 700 K of naphthalene and of 2,7-dimethylnaphthalene. *J. Chem. Thermodyn.* **1993**, *25*, 1461–1494. https://doi.org/10.1006/jcht.1993.1148.
68. Okamoto, N.; Oguni, M. Discovery of crystal nucleation proceeding much below the glass transition temperature in a supercooled liquid. *Solid State Commun.* **1996**, *99*, 53–56. https://doi.org/10.1016/0038-1098(96)00139-1.
69. Dai, J.; McKee, M.L.; Samokhvalov, A. Adsorption of naphthalene and indole on F300 MOF in liquid phase by the complementary spectroscopic, kinetic and DFT studies. *J. Porous Mater.* **2014**, *21*, 709–727. https://doi.org/10.1007/s10934-014-9818-3.
70. Berlman, I.B.; Weinreb, A. On the fluorescence spectrum and decay time of naphthalene. *Mol. Phys.* **1962**, *5*, 313–319. https://doi.org/10.1080/00268976200100351.

Article

Self-Assembly of Hydrogen-Bonded Fibrous Fe^{II} Triazole Complexes and Their Spin Crossover Characteristics in Organic Media

Keita Kuroiwa *,†, Yukari Jo, and Nobuo Kimizuka

Department of Chemistry and Biochemistry, Graduate School of Engineering, Kyushu University, 744 Moto-oka, Nishi-ku, Fukuoka 819-0395, Japan

* Correspondence: keitak@nano.sojo-u.ac.jp

† Current address: Department of Nanoscience, Faculty of Engineering, Sojo University, 4-22-1 Ikeda, Nishi-ku, Kumamoto 860-0082, Japan.

Received: 20 February 2025; Revised: 30 May 2025; Accepted: 3 June 2025; Published: 6 June 2025

Abstract: The lipophilic linear Fe^{II} triazole complexes $[Fe^{II}(\mathbf{L})_3]Cl_2$ (**L** = **1**–**5**) were synthesized using ligands **1**–**5** containing amide bonds between alkyl chains and 1,2,4-triazole ligands with various spacer methylene length. When the amido and ether linkages are introduced in the alkyl chain moiety, the iron complexes are dissolved in chloroform, $[Fe^{II}(\mathbf{1})_3]Cl_2$ forms a pale purple jelly-like phase. The purple color is accompanied by a structured absorption around 540 nm, characteristic of iron (II) in the low spin (LS) state. Atomic force microscopy (AFM) and transmission electron microscopy (TEM) of the jelly-like phase confirm the formation of networks of fibrous nano assemblies with widths of 10–30 nm. The observed widths are larger than the molecular lengths of the triazole ligands. The pale purple jelly-like phase turned into a pale-yellow solution by heating above ca 310 K, indicating the formation of high spin (HS) state complexes. The complexes show irreversible spin crossover in the solid state, characterized by SQUID. Interestingly, an abrupt spin crossover is observed in solution reversibly with some thermal hysteresis. UV-vis spectra also showed reversible spin crossover phenomena dependent on the spacer length between the amide group and the Fe(II) triazole complexes. IR spectra of these complexes in chloroform show the formation of hydrogen bonding from amide groups, which enhanced alkyl-chain packing in the coordination polymers. The freeze-dried iron triazole complexes form lamellar structures, which indicates the alkyl chains extending radially from the octahedral triazole complex moiety are oriented in a lamellar packing due to the presence of flexible ether linkages in alkyl chains, which allowed decoupling the alignment of the dodecyloxy alkyl chains from the spacer methylenes connected to the Fe(II) triazole complexes. Introducing amide bondages to the lipophilic one-dimensional coordination systems stabilizes the low-spin state by hydrogen bond networks. It provides hysteresis in the spin crossover in solution, ascribed to the recombination of hydrogen bonds during the temperature change between the heating and cooling sides. Combining hydrogen bonds and lipophilic one-dimensional complexes provides a valuable means to enhance their stability and control physical properties in solution.

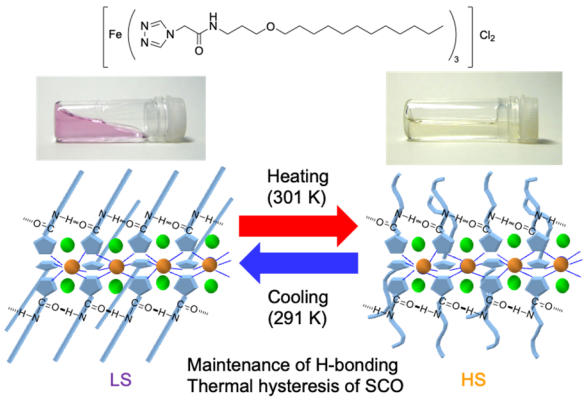

Keywords: spin crossover; thermal hysteresis; nano metal complex; coordination polymer; self-assembly

1. Introduction

The concept of spin crossover (SCO) was first introduced by Cambi and colleagues in the 1930s [1]. Since then, a significant number of SCO compounds have been reported, particularly those in solid-state materials. The phenomenon of spin crossover with hysteresis, realized by strong cooperative effects, has attracted much attention due to its potential applications in magnetic devices and information storage materials [2,3]. Cooperativity, a crucial phenomenon, facilitates the propagation of spin state information from a metal complex to neighboring

complexes, resulting in collective spin state transitions throughout the system. In crystalline solids, the degree of cooperativity is determined by the interactions between neighboring metal complexes, which are influenced by the molecular structure of metal complexes, intermolecular interactions, and molecular arrangement in crystals. Achieving enhanced cooperativity in spin-crossover systems with long-range interactions between metal ion units is essential. Realizing such cooperativity in one-dimensional (1D), two-dimensional (2D), or three-dimensional (3D) networks, along with the rational control of the spin crossover behavior is essential to develop next-generation materials with quantum spin functions [4–12].

In particular, the spin crossover properties of 1D iron(II) triazole complexes have been studied extensively by both chemists and physicists. For instance, Kahn and his collaborators reported that mixed-ligand iron(II) triazole complexes exhibit abrupt spin crossover with sizeable thermal hysteresis near room temperature [3,13]. After this seminal work, iron(II) triazole complexes were recognized as promising candidates for magnetic devices. These complexes have been studied in bulk crystalline forms and other matrices, including polymer films [14–16], polymer derivatives [17–20], and surfactant-capped crystalline nanoparticles [21,22]. Thus, iron(II) triazole complexes serve as spin crossover materials that can be realized in bulk solids and various material systems [23–25].

In addition to the conventional studies focusing on the solid state, spin crossover has also been investigated for monomeric complexes in solutions, [26–32] self-assembly in liquid crystals or gels [25,33–38], and polymer-hybrid systems in gels [39–42]. In solutions, molecularly dissolved iron(II) complexes show spin equilibrium without hysteresis. Metal complexes in gels are more or less solvated by solvent molecules, resulting in a substantial reduction in the cooperativity that requires strong intermolecular interactions. The spin crossover observed for these solutions and gels generally reflects the thermal equilibrium of each complex governed by the Boltzmann distribution, resulting in gradual changes [27–32]. It is widely observed that metal complexes exhibiting abrupt spin crossover in the solid state exhibit a smooth spin equilibrium in solution [43–45], and it remains a challenge to develop molecular design principles to achieve cooperative spin crossover with hysteresis in organic media.

To address this issue, we have developed lipophilic bridging triazole ligands by introducing an alkyl chain containing a flexible ether linkage to disperse one-dimensional triazole complexes as nanowires in organic media [46–53]. Iron(II) complexes bearing 4-dodecyloxypropyl-1,2,4-triazole ligands revealed a low-spin (LS) state in solid or film state and formed organogels when dispersed in organic solvents such as chloroform. Meanwhile, the low-spin (LS) state is destabilized in gels due to the solvation of alkyl chains that increased the Fe-Fe distances, and the gels showed a high-spin (HS) state. To overcome the destabilization of the LS state based on the solvation of the lipid-soluble alkyl chains directly bound to the triazole ligand, we introduced anionic lipids as counter anions of the 1D iron(II) 1,2,4-triazole complexes [54]. This supramolecular approach led to a remarkable stabilization of LS complexes in organic media. It enabled spin conversion, i.e., the spin control via temperature-dependent dynamic self-assembly of linear coordination chains [54]. These results indicate the importance of supramolecular stabilization of LS complexes and self-assembly as valuable strategies for improving spin crossover phenomena in soluble coordination polymer systems.

In this study, we introduced hydrogen bond networks to stabilize the LS state of 1D iron(II) 1,2,4-triazole complexes. We developed new ether-lipophilic triazole ligands containing an amide bondage. These complexes were dispersible in organic media, and we investigated their spin crossover properties in solutions and gels. We found that hydrogen bonding enhances the thermal stability of the low-spin (LS) state in solution. In addition, after the LS-HS transition by heating, the reversed HS-LS transition during the cooling process showed thermal hysteresis originating from the recombination process of hydrogen bonds. The cooperative spin crossover behavior is discussed regarding the structural changes of iron(II) 1,2,4-triazole complexes and their mesoscopic nanostructures formed by self-assembly. These findings provide a simple and valuable means to regulate the self-assembly behavior of iron(II) 1,2,4-triazole complexes and their spin crossover characteristics.

2. Experimental Section

2.1 Materials

Reagents and solvents were obtained from commercial sources. Anhydrous chloroform and methanol were obtained by distillation over $CaCl_2$ and CaH_2, respectively. The product was synthesized according to the previous report (see Supporting Information) [55]. The structures of triazole derivatives and the final ligands were confirmed by thin-layer chromatography, Fourier Transform Infrared Spectroscopy (FT-IR PreStage21, Shimadzu, Kyoto, Japan) and Nuclear Magnetic Resonance (NMR) spectroscopies (DRX600, 600 MHz, Bruker, Billerica, MA, USA), and elemental analysis.

2.2 Measurements

Ultraviolet-visible (UV-vis) spectra were measured on V-550, V-560, or V-570 spectrophotometer (JASCO, Tokyo, Japan). Transmission electron microscopy (TEM) was conducted on a JEM-2010 (JEOL, Tokyo, Japan), operating at 120 kV. Specimens for TEM were prepared by transferring the surface layer of gels or solutions on carbon-coated TEM grids or HOPG [56]. Atomic force microscopy (AFM, contact mode) was carried out with a PicoPlus microscopy (Molecular Imaging, Tempe, AZ, USA) with a cantilever of SI-AF01. Specimens for AFM observations were prepared by using a freshly cleaved, highly oriented pyrolytic graphite (HOPG, ZYA, 10 × 10 mm^2, NT-MDT Co., Tempe, AZ, USA). Differential scanning calorimetry (DSC) was conducted on an SSC-5200H instrument (Seiko Instruments Inc., Chiba, Japan) (heating rate = 1 K min^{-1}). Samples for DSC measurements were placed in an aluminum pan (SSC000E33, Seiko Instruments Inc., Chiba, Japan). Magnetic susceptibility measurements were performed on an MPMS-7XL superconducting quantum interference device (SQUID) magnetometer (Quantum Design, San Diego, CA, USA) in a temperature range of 100–400 K (solid state) and 210–350 K (liquid state). Magnetic data were corrected for diamagnetic contributions from triazole ligands and sample holders. The Pascal constants of the ligands and susceptibilities of the holders, which were measured separately, were used for the correction. The wide-angle X-ray diffraction (WAXD) data were recorded on a powder X-ray diffractometer at BL02B2 in SPring-8 (Hyogo, Japan; operation energy = 8 GeV, stored current = 100 mA, λ = 1 Å). For XRD, samples are placed in a capillary (Markrohrchen aus Glas Nr. 14, 80 mm(long) × 0.5 mm(diameter) × 0.01 mm(thick)), Hilgenberg GmbH, Malsfeld, Germany).

3. Result and Discussion

The lipophilic triazole ligands **1**–**5** (Scheme 1) were synthesized by modifying the literature method [55]. A flexible ether linkage was introduced in **1**–**5**, since it enhances the solubility in organic media and provides the packing of alkyl chains in the supramolecular assemblies [57–61] and coordination polymers [46,48–52]. The iron triazole complexes containing ligands **1**–**5** were prepared by mixing each ligand with $FeCl_2$ in dry methanol at room temperature and were obtained as powders.

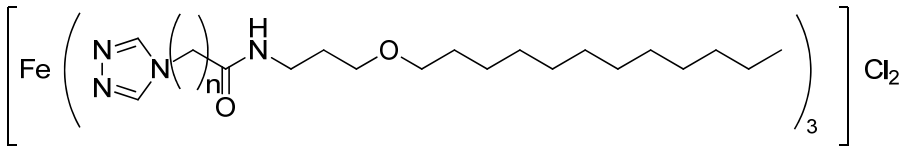

$[Fe(L)_3]Cl_2$

L = 1(n = 1), **2** (n = 2), **3** (n = 3), **4** (n = 4), and **5** (n = 5)

Scheme 1. Chemical structure of $[Fe(\mathbf{L})_3]Cl_2$, (**L** = **1**–**5**).

When $[Fe^{II}(\mathbf{1})_3]Cl_2$ was dissolved in chloroform, a pale purple jelly-like solution was formed at room temperature (concentration, 5 unit mM, Figure 1a). Here, the "unit mM" refers to the concentration per $[Fe(\mathbf{1})_3]^{2+}$ monomeric unit of the coordination polymer. Upon heating, the jelly-like solution turned to a yellow solution above the temperature of ca. 310 K (Figure 1b). It indicates that the LS state is thermally stabilized by possibly polymeric self-assemblies that form the jelly-like solution. In contrast, the complex in the HS state does not retain the jelly-like solution and is dispersed in chloroform. The pale purple jelly-like solution was also formed in the case of $[Fe^{II}(\mathbf{2})_3]Cl_2$. On the other hand, the complex with a more extended spacer methylene unit $[Fe^{II}(\mathbf{3})_3]Cl_2$ formed a colorless, i.e., HS-state jelly-like solution, indicating the absence of LS species. The longer-spacer compounds $[Fe^{II}(\mathbf{4})_3]Cl_2$ and $[Fe^{II}(\mathbf{5})_3]Cl_2$ were dispersed in chloroform without forming jelly-like solutions at 5 unit mM. These results indicate that the solution characteristics depend on the spacer length between the dodecyloxypropyl chain and the triazole ring, and their solution properties and spin state are controlled by the spacer moiety. The spacer-length-dependent properties of the solution are further examined in detail, as discussed later, by FT-IR spectroscopy and wide-angle X-ray diffraction.

Atomic force microscopy (AFM) was performed to investigate the morphology of the coordination structures. Figure 2a shows an AFM image of $[Fe^{II}(\mathbf{1})_3]Cl_2$ transferred on highly oriented pyrolytic graphite (HOPG). Networks of fibrous nanoassemblies with a width of 10–30 nm are abundantly observed. Transmission electron microscopy (TEM) was also conducted to investigate $[Fe^{II}(\mathbf{1})_3]Cl_2$ transferred onto a carbon-coated copper grid (Figure 2b). Fibrous nanostructures with a width of 20–50 nm are abundantly seen. The formation of the fibrous nanostructures are also observed for the other iron triazole complexes $[Fe^{II}(\mathbf{2}–\mathbf{5})_3]Cl_2$ ($[Fe^{II}(\mathbf{2})_3]Cl_2$, 10–30 nm, Figure S1a; $[Fe^{II}(\mathbf{3})_3]Cl_2$, 10–30 nm, Figure S1b; $[Fe^{II}(\mathbf{4})_3]Cl_2$, 10–50 nm, Figure S1c; $[Fe^{II}(\mathbf{5})_3]Cl_2$, 10–50 nm,

Figure S1d). Since the molecular length of ligands **1**–**5** is in the range of 26–32 Å (**1**, 26.5 Å; **2**, 27.1 Å; **3**, 29.0 Å; **4**, 30.0 Å; **5**, 31.5 Å, estimated by Corey–Pauling–Koltun (CPK) model), the widths of fibrous structures are larger than twice the molecular length of ligands. Therefore, they comprise a few strands of linear triazole complexes, as schematically shown in Figure 2c.

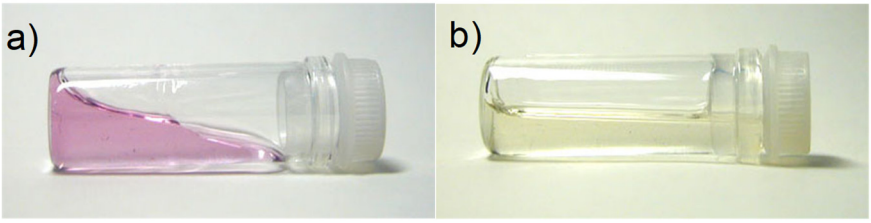

Figure 1. Pictures of $[Fe(\mathbf{1})_3]Cl_2$ in chloroform: (**a**) a pale purple jelly-like phase at 298 K. (**b**) a pale yellow solution at 323 K.

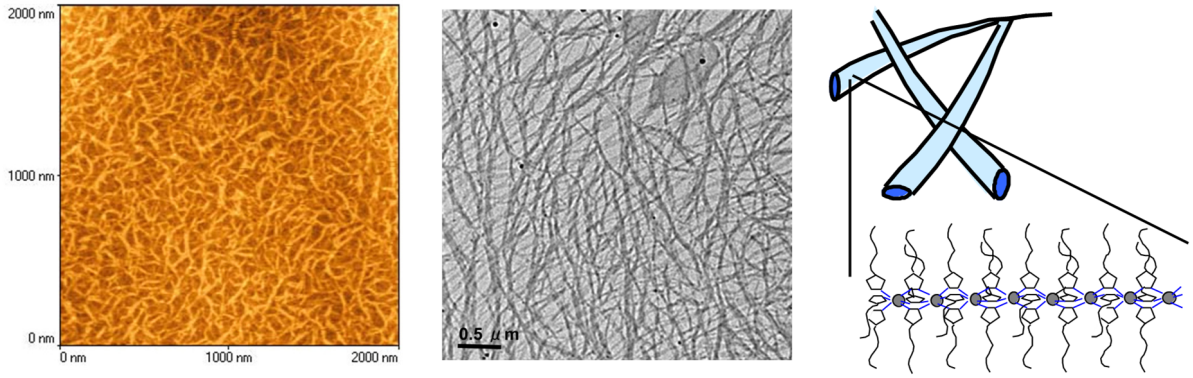

Figure 2. (**a**) AFM image of $[Fe(\mathbf{1})_3]Cl_2$ (5 unit mM) transferred on HOPG. (**b**) TEM image of $[Fe(\mathbf{1})_3]Cl_2$ (5 unit mM) transferred on a carbon-coated TEM grid. (**c**) Schematic illustration of iron triazole complexes in fibrous nanofiber.

Figure 3 compares the temperature dependences of the magnetic susceptibility for $[Fe^{II}(\mathbf{1})_3]Cl_2$ in chloroform and that observed for the powdery $[Fe^{II}(\mathbf{1})_3]Cl_2$. In the solid state, $[Fe^{II}(\mathbf{1})_3]Cl_2$ exhibits a spin crossover upon heating at 340 K, whereas the HS state was maintained during the cooling process to 200 K (Figure 3a). It indicates the spin crossover is irreversible in the solid state. On the other hand, $[Fe^{II}(\mathbf{1})_3]Cl_2$ in chloroform provides reversible spin crossover with thermal hysteresis around room temperature. Spin crossover temperature (T_{sc}) was 301 K ($T_{sc}\uparrow$) and 291 K($T_{sc}\downarrow$, Figure 3b). T_{sc} is the temperature at which the crossover produces a half-fraction of the HS state. Surprisingly, the spin crossover of $[Fe^{II}(\mathbf{1})_3]Cl_2$ in chloroform was accompanied by thermal hysteresis, although the coordination polymer was dispersed as fibrous nanostructures. To confirm the presence of thermal hysteresis, we measured the temperature dependence of UV-vis absorption spectra for $[Fe^{II}(\mathbf{1})_3]Cl_2$ dispersed in chloroform, as shown in Figure 4a. At lower temperatures, a peak is observed around 528 nm, ascribed to the $^1A_1 \rightarrow {}^1T_1$ transition of the LS complex. Upon heating the LS dispersion, the intensity of the $^1A_1 \rightarrow {}^1T_1$ transition decreased, while a new peak appeared around 800 nm. This near-infrared peak is assigned to a *d-d* transition of the HS complex ($^5T_2 \rightarrow {}^5E$). Upon cooling the HS dispersion to 265 K, a reversible spectral change was observed with thermal hysteresis, which is in good agreement with the result of magnetic susceptibility measurement ($[Fe^{II}(\mathbf{1})_3]Cl_2$, $T_{sc}\uparrow$ 301 K, $T_{sc}\downarrow$ 291 K, Figure 4b).

To date, thermal hysteresis of the spin crossover exerted by one-dimensional coordination polymers is observed in bulk or nano-crystalline structures, indicating that the expression of cooperativity requires crystalline order [6–12]. When Fe(II) 1,2,4-triazole complexes are dispersed in organic media as nanofibers, thermal hysteresis is not observed in their spin crossover [46,48,49,51]. Therefore, the thermal hysteresis observed for $[Fe^{II}(\mathbf{1})_3]Cl_2$ in chloroform indicates that the hydrogen bonding enhances the cohesive forces operating among ligand alkyl chains and effectively stabilize the LS complexes.

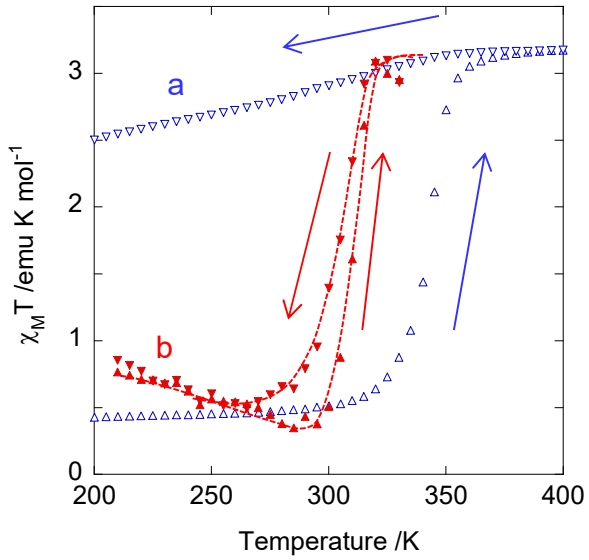

Figure 3. Temperature dependence of magnetic susceptibility $\chi_M T$ of $[Fe(\mathbf{1})_3]Cl_2$ in solid state (blue symbols and arrows) (**a**), and in chloroform (5 unit mM, red symbols and arrows) (**b**). The arrows accompanying the ▲(△) or ▼(▽) symbols represent the heating or cooling processes, respectively. These data suggest reversibly thermal hysteresis in solution, in contrast to irreversible changes observed in the solid state.

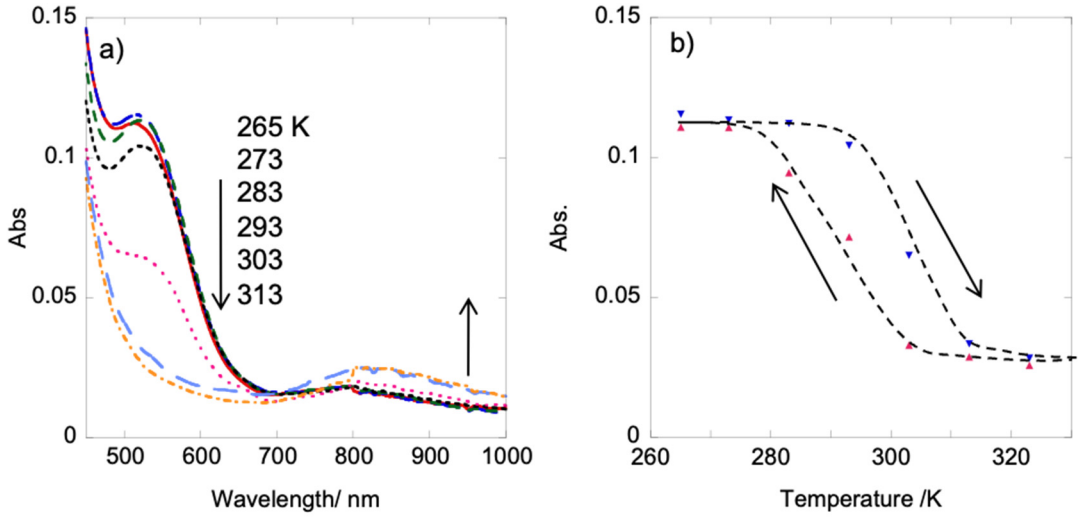

Figure 4. (**a**) Temperature dependence of UV-vis spectra of $[Fe(\mathbf{1})_3]Cl_2$ in chloroform (5 unit mM). The arrows indicate a decrease in the LS-derived absorption band at 528 nm and an increase in the HS-derived band around 800 nm upon heating from 265 K to 313 K. (**b**) Temperature dependence of the absorption intensity (at 540 nm) during the heating and cooling cycles. The arrows accompanying the ▼ or ▲ symbols represent the heating or cooling processes, respectively.

Figure S2 shows temperature dependences of the absorbance at 528 nm (LS species) during the heating and cooling cycles, observed for $[Fe^{II}(\mathbf{L})_3]Cl_2$ (**L** = **2**–**5**). All these complexes showed spin crossover phenomena with weak thermal hysteresis around ambient temperatures. The temperature ranges of spin crossover shifted to lower temperatures for complexes containing more extended spacer unit ($[Fe^{II}(\mathbf{2})_3]Cl_2$, T_{sc}↑ 293 K, T_{sc}↓ 292 K, Figure S2a; $[Fe^{II}(\mathbf{3})_3]Cl_2$, T_{sc}↑ 298 K, T_{sc}↓ 289 K, Figure S2b; $[Fe^{II}(\mathbf{4})_3]Cl_2$, T_{sc}↑ 292 K, T_{sc}↓ 281 K, Figure S2c; $[Fe^{II}(\mathbf{5})_3]Cl_2$, T_{sc}↑ 287 K, T_{sc}↓ 282 K, Figure S2d). Among these complexes, however, we note that the complex $[Fe^{II}(\mathbf{2})_3]Cl_2$ did not show sufficient thermal hysteresis despite those observed for the iron(II) triazole complexes with longer-spacer chains (L = **3**, **4**, and **5**, Figure S2a). The peculiar absence of a distinct thermal hysteresis in $[Fe^{II}(\mathbf{2})_3]Cl_2$, in contrast to the behavior observed for the longer-spacer analogues ($[Fe^{II}(\mathbf{L})_3]Cl_2$, **L** = **3**, **4**, and **5**), is further discussed in terms of molecular packing based on the wide-angle X-ray diffraction analysis (discussed later). Moreover, the observed stabilization of the low-spin (LS) state as the spacer length decreases can be attributed to the closer proximity between the hydrogen-bonding amide moieties and the triazole rings, as described by the FT-IR spectra in the following paragraph. In particular, in chloroform, effective intermolecular hydrogen

bonding between the amido linkages is more likely to occur due to this structural proximity, which can restrict the molecular mobility of the triazole complexes. This suppression of dynamic motion may result in enhanced spin compaction and a preference for the LS state even at relatively higher temperatures.

Fourier transition infrared (FT-IR) spectra of iron triazole complexes, $[Fe^{II}(\mathbf{L})_3]Cl_2$ (**L** = **1**–**5**) in chloroform were measured at varied temperatures to investigate the relevance of hydrogen bonding between amide bonds to the observed thermal hysteresis. Chloroform dispersions of $[Fe^{II}(\mathbf{L})_3]Cl_2$ (**L** = **1**–**5**) were introduced into a thin layer cell made of NaCl (Figure S3). In the course of heating chloroform dispersion of $[Fe^{II}(\mathbf{1})_3]Cl_2$, C=O stretching (ν(C=O)) and N-H vending (δ(N-H)) vibrations were observed at 1680 and 1561 cm^{-1}, respectively (Temperatures at 278 K and 293 K, Figure S3a). These peaks indicate the formation not only of intermolecular hydrogen bonding among amido groups, but also intermolecular hydrogen bonding between amido group and halide anion, and intramolecular hydrogen bonding between amido group and C-H of triazole ligand [62,63]. In addition, a C=N stretching vibration (ν(C=N)) of the triazole unit was seen at 1416 cm^{-1}, characteristic of the LS complex [64]. At 323 K, the peak at 1416 cm^{-1} disappeared and was replaced by a new peak at 1401 cm^{-1}, a typically observed change in IR spectra during the spin crossover of iron(II) 1,2,4-triazole complexes. When the dispersion was cooled to 293 K, the wavenumber of the ν(C=N) band did not change, but further cooling to 278 K shifted it back to 1413 cm^{-1}. The hysteretic change of ν(C=N) band is consistent with those observed in SQUID and UV-vis measurements. On the other hand, the C=O stretching (ν(C=O)) and N-H vending (δ(N-H)) peaks from the amido group were maintained in the temperature range from 278 K to 323 K. This indicates that hydrogen bonds are maintained during the process of spin crossover between LS and HS species in this temperature range, which contributes to stabilizing the coordination polymer structure in chloroform solution. It is also likely that the appearance of hysteresis is due to the recombination of hydrogen bonds during the cooling process.

$[Fe^{II}(\mathbf{2})_3]Cl_2$ and $[Fe^{II}(\mathbf{3})_3]Cl_2$ showed the different temperature-dependence in FT-IR spectra (Figure S3b,c). In the case of $[Fe^{II}(\mathbf{4})_3]Cl_2$ and $[Fe^{II}(\mathbf{5})_3]Cl_2$, not only a gradual change of ν(C=N) band but also the red shift of ν(C=O) on heating was observed ($[Fe^{II}(\mathbf{4})_3]Cl_2$, 1643 cm^{-1} at 278 K, 1651 cm^{-1} at 323 K, Figure S3d,; $[Fe^{II}(\mathbf{5})_3]Cl_2$, 1649 cm^{-1} at 278 K, 1655 cm^{-1} at 323 K, Figure S3e). The reversible shift of ν(C=O) indicates that these intermolecular hydrogen bondings are formed and are not maintained at higher temperatures. Since the shorter spacer methylene length between the alkoxy chain and the triazole ring in $[Fe^{II}(\mathbf{1})_3]Cl_2$ led to the maintenance of hydrogen bonding, whether hydrogen bonding works strongly or not depends on the spacer chain length directly connected to the triazole complex. In amide bonds close to the triazole group, effective hydrogen bonds are formed because of the proximity of the amide groups. Still, as the spacer chain length increases, the distance between the alkyl chains extending radially from the triazole complex increases, and at high temperatures, the intermolecular hydrogen bonds become easily broken due to the increased thermal fluctuations of the alkyl chains. Consequently, in $[Fe^{II}(\mathbf{4})_3]Cl_2$ and $[Fe^{II}(\mathbf{5})_3]Cl_2$, the radially extended alkyl chains become less susceptible to hydrogen bonding, which weakens the intermolecular interactions necessary for jelly-like formation. As a result, these complexes are presumed to be dispersed as solutions rather than forming jelly-like states.

After the dispersions of iron triazole complexes in chloroform were freeze-dried, wide-angle X-ray diffraction was measured for dried powder of $[Fe^{II}(\mathbf{1})_3]Cl_2$ at 223 K and 373 K (Figure 5). $[Fe^{II}(\mathbf{1})_3]Cl_2$ showed the 001, 002, and 003 Bragg peaks, respectively. These diffraction peaks indicate the presence of a lamellar structure with a long period of 41.0 Å. The heating of the powder samples of $[Fe^{II}(\mathbf{1})_3]Cl_2$ increases a lamellar d-spacing to 44.5 Å. The increase in the long spacing is consistent with the melting of long alkyl chains and the changes in the molecular orientation of lipophilic alkyl chains [47,49,51,52]. $[Fe^{II}(\mathbf{L''})_3]Cl_2$ (**L''** = **3**–**5**) also produced a lamellar structure with the increase of d-spacing depending on temperature (Figure S4b–d). It indicates the introduction of the alkyl chains with ether-linkage effectively decouples the alignment of alkyl chains from the radially oriented chains around the iron triazole complex. Previous reports on 4-alkylated triazole complexes form anisotropic, rodlike structures with organic substituents radially attached to the main chains [13,23,33,34,64–68]. In the present system, introducing the ether linkage into the alkyl chain moiety has effectively decoupled the alignment of alkyl chains from linear Fe^{II} tris-triazole main chains, thereby allowing the formation of regular lamellar structures. In addition, it also seems to separate van der Waals interaction among alkyl chains from hydrogen bonding of amido-linkage. In contrast, the complex $[Fe^{II}(\mathbf{2})_3]Cl_2$ exhibited a decrease in d-spacing upon heating (see Figure S4a), suggesting that it adopts a distinct molecular packing mode compared to its analogues with other spacer lengths. This distinctive structural behavior aligns with the spin crossover properties observed in UV-vis spectroscopy, where $[Fe^{II}(\mathbf{2})_3]Cl_2$ did not exhibit a thermal hysteresis profile that diverged from those observed in complexes with longer or shorter spacers. Furthermore, FT-IR analysis revealed that the C=O stretching vibration for $[Fe^{II}(\mathbf{2})_3]Cl_2$ appears at 1651 cm^{-1} (Figure S3b), which is at lower energy compared to $[Fe^{II}(\mathbf{1})_3]Cl_2$ and $[Fe^{II}(\mathbf{3})_3]Cl_2$, and shows negligible thermal dependence. These results suggest that the hydrogen bonding mode in $[Fe^{II}(\mathbf{2})_3]Cl_2$ is less susceptible to thermal fluctuations, indicating the presence of a relatively weak hydrogen-

bonding environment. Given that the distance from the triazole ring to the amide group in $[Fe^{II}(\mathbf{2})_3]Cl_2$ is neither excessively short nor long, it is likely that ether intramolecular hydrogen bonding involving intermolecular hydrogen bonding between the alkyl chains moderately contributes to the observed spin crossover behavior and molecular packing characteristics. These findings highlight the crucial role of spacer length in regulating hydrogen-bonding interactions and spin-state dynamics in lipophilic iron(II) triazole complexes.

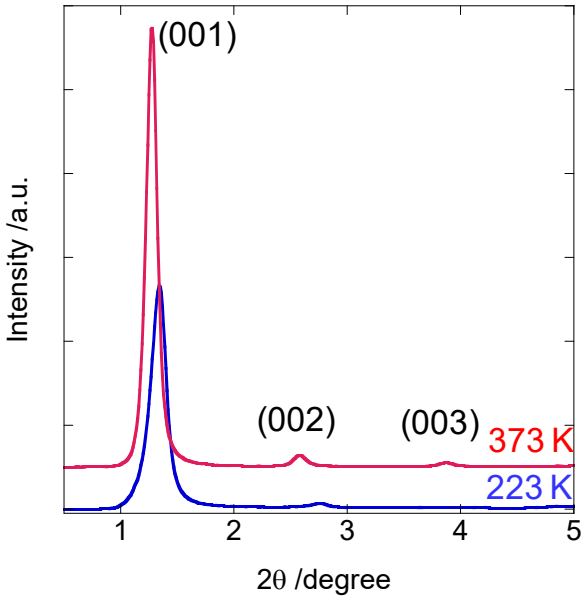

Figure 5. WAXS profiles of freeze-dried samples from $[Fe(\mathbf{1})_3]Cl_2$ in chloroform (5 unit mM) at 223 K and 373 K.

4. Conclusions

In conclusion, we have investigated the spin crossover phenomena of lipophilic iron triazole complex in organic media. Regarding nanofibrous dispersions in organic media, this is the first example of spin crossover with thermal hysteresis. A few works have been reported as lipophilic iron triazole complex in organic media to date. However, there has been no example of spin crossover with thermal hysteresis since the 3D interaction among triazole chain chains is weak in organic media [46,48,49,51,54]. It is to be noted that hydrogen bonding plays a key role in realizing spin crossover phenomena with hysteresis. The spacer length between the alkoxy chain and triazole ring is essential to the effective formation of hydrogen bonding from amide bondings, which is critical in determining the spin crossover characteristics. Introducing lipophilic chain units around coordination polymers is essential to convert solid-state pseudo-one dimensional complexes to flexible, soluble supramolecular nanowires. The effective use of hydrogen bonding contributes to stabilizing the coordination polymers in solution and creates bistable properties in thermally induced dynamic structural changes. These findings will be widely used to create functional, soft, and innovative functional coordination polymers.

Supplementary Materials: Synthetic procedures, Thermal dependence of UV-vis spectra, TEM images, FT-IR spectra, and WAXD pattern can be downloaded at https://media.sciltp.com/articles/others/2506051646541837/MI-777-SI.pdf.

Author Contributions: K.K., N.K.: conceptualization, methodology, writing—original draft preparation, reviewing and editing, TEM imaging, visualization, investigation; Y.J.: data collection, visualization, software; All authors have read and agreed to the published version of the manuscript.

Funding: This work is supported by a Grant-in-Aid for Scientific Research (A) (No. 19205030) from the Japan Society for the Promotion of Science and by JST CREST.

Data Availability Statement: Raw data will be made available upon reasonable request.

Acknowledgments: This work was supported by a Grant-in-Aid for Scientific Research (A) (No. 19205030) from the Japan Society for the Promotion of Science and by JST CREST. We also thank the Japan Synchrotron Radiation Research Institute as part of the Nanotechnology Support Project of the Ministry of Education, Culture, Sports, Science and Technology, for the approval of the synchrotron radiation experiments at SPring-8 (Hyogo, Japan).

Conflicts of Interest: The authors declare no conflict of interest.

References

1. Gütlich, P.; Goodwin, H.A. *Spin Crossover in Transition Metal Compounds I*; Springer: Berlin/Heidelberg, Germany, 2004.
2. Kahn, O.; Kröber, J.; Jay, C. Spin Transition Molecular Materials for displays and data recording. *Adv. Mater.* **1992**, *4*, 718–728.
3. Kahn, O.; Martinez, C.J. Spin-Transition Polymers: From Molecular Materials Toward Memory Devices. *Science* **1998**, *279*, 44–48.
4. Weber, B.; Kaps, E.; Weigand, J.; Carbonera, C.; Letard, J.F.; Achterhold, K.; Parak, F.G. Cooperative Iron(II) spin crossover complexes with N_4O_2 coordination sphere. *Inorg. Chem.* **2008**, *47*, 487–496.
5. Bronisz, R. 1,4-Di(1,2,3-triazol-1-yl)butane as building block for the preparation of the iron(II) spin-crossover 2D coordination polymer. *Inorg. Chem.* **2005**, *44*, 4463–4465.
6. Niel, V.; Martinez-Agudo, J.M.; Munoz, M.C.; Gaspar, A.B.; Real, J.A. Cooperative spin crossover behavior in cyanide-bridged Fe(II)-M(II) bimetallic 3D Hofmann-like networks (M = Ni, Pd, and Pt). *Inorg. Chem.* **2001**, *40*, 3838–3839.
7. Real, J.A.; Gaspar, A.B.; Niel, V.; Muñoz, M.C. Communication between iron(II) building blocks in cooperative spin transition phenomena. *Coord. Chem. Rev.* **2003**, *236*, 121–141.
8. Galet, A.; Munoz, M.C.; Gaspar, A.B.; Real, J.A. Architectural isomerism in the three-dimensional polymeric spin crossover system $[Fe(pmd)_2[Ag(CN)_2]_2]$: Synthesis, structure, magnetic properties, and calorimetric studies. *Inorg. Chem.* **2005**, *44*, 8749–8755.
9. Munoz, M.C.; Gaspar, A.B.; Galet, A.; Real, J.A. Spin-crossover behavior in cyanide-bridged iron(II)-silver(I) bimetallic 2D Hofmann-like metal-organic frameworks. *Inorg. Chem.* **2007**, *46*, 8182–8192.
10. Agusti, G.; Gaspar, A.B.; Munoz, M.C.; Real, J.A. Thermal- and pressure-induced cooperative spin transition in the 2D and 3D coordination polymers $Fe(5\text{-}Br\text{-}pmd)_z[M(CN)_x]_y$ ($M=Ag^I$, Au^I, Ni^{II}, Pd^{II}, Pt^{II}). *Inorg. Chem.* **2007**, *46*, 9646–9654.
11. Agusti, G.; Munoz, M.C.; Gaspar, A.B.; Real, J.A. Spin-crossover behavior in cyanide-bridged iron(II)-gold(I) bimetallic 2D Hofmann-like metal-organic frameworks. *Inorg. Chem.* **2008**, *47*, 2552–2561.
12. Bonhommeau, S.; Molnar, G.; Galet, A.; Zwick, A.; Real, J.A.; McGarvey, J.J.; Bousseksou, A. One shot laser pulse induced reversible spin transition in the spin-crossover complex $[Fe(C_4H_4N_2)Pt(CN)_4]$ at room temperature. *Angew. Chem. Int. Ed. Engl.* **2005**, *44*, 4069–4073.
13. Krober, J.; Codjovi, E.; Kahn, O.; Groliere, F.; Jay, C. A spin transition system with a thermal hysteresis at room temperature. *J. Am. Chem. Soc.* **1993**, *115*, 9810–9811.
14. Nakamoto, A.; Ono, Y.; Kojima, N.; Matsumura, D.; Yokoyama, T.; Liu, X.J.; Moritomo, Y. Spin transition and its photo-induced effect in spin crossover complex film based on $[Fe(II)(trz)_3]$. *Synth. Met.* **2003**, *137*, 1219–1220.
15. Nakamoto, A.; Ono, Y.; Kojima, N.; Matsumura, D.; Yokoyama, T. Spin Crossover Complex Film, $[Fe^{II}(H\text{-}trz)_3]$-Nafion, with a Spin Transition around Room Temperature. *Chem. Lett.* **2003**, *32*, 336–337.
16. Nakamoto, A.; Kojima, N.; XiaoJun, L.; Moritomo, Y.; Nakamura, A. Demonstration of the thermally induced high spin–low spin transition for a transparent spin crossover complex film $[Fe(II)(H\text{-}trz)_3]$-Nafion (trz = triazole). *Polyhedron* **2005**, *24*, 2909–2912.
17. Lee, S.W.; Lee, J.W.; Jeong, S.H.; Park, I.W.; Kim, Y.M.; Jin, J.I. Processable magnetic plastics composites—Spin crossover of PMMA/Fe(II)-complexes composites. *Synth. Met.* **2004**, *142*, 243–249.
18. Schwarzenbacher, G.; Gangl, M.S.; Goriup, M.; Winter, M.; Grunert, M.; Renz, F.; Linert, W.; Saf, R. Preparation and Radical Oligomerization of an Fe(II) Complex without Loss of Spin-Crossover Properties. *Monatsh. Chem.* **2001**, *132*, 519–529.
19. Saf, R.; Schwarzenbacher, G.; Mirtl, C.; Hayn, G.; Hobisch, J.; Gatterer, K. Synthesis of Poly(ethylene oxide)s with 1,2,4-Triazol-4-yl End Groups—Macroligands for Bistable Metal—Polymer Complexes. *Macromol. Rapid Commun.* **2004**, *25*, 911–915.
20. Enriquez-Cabrera, A.; Rapakousiou, A.; Piedrahita Bello, M.; Molnár, G.; Salmon, L.; Bousseksou, A. Spin crossover polymer composites, polymers and related soft materials. *Coord. Chem. Rev.* **2020**, *419*, 213396.
21. Coronado, E.; Galán-Mascarós, J.R.; Monrabal-Capilla, M.; García-Martínez, J.; Pardo-Ibáñez, P. Bistable Spin-Crossover Nanoparticles Showing Magnetic Thermal Hysteresis near Room Temperature. *Adv. Mater.* **2007**, *19*, 1359–1361.
22. Gural'skiy, I.A.; Quintero, C.M.; Molnar, G.; Fritsky, I.O.; Salmon, L.; Bousseksou, A. Synthesis of spin-crossover nano- and micro-objects in homogeneous media. *Chem. Eur. J.* **2012**, *18*, 9946–9954.
23. Gaspar, A.B.; Ksenofontov, V.; Seredyuk, M.; Gütlich, P. Multifunctionality in spin crossover materials. *Coord. Chem. Rev.* **2005**, *249*, 2661–2676.
24. Roubeau, O. Triazole-based one-dimensional spin-crossover coordination polymers. *Chem. Eur. J.* **2012**, *18*, 15230–15244.
25. Gaspar, A.B.; Seredyuk, M. Spin crossover in soft matter. *Coord. Chem. Rev.* **2014**, *268*, 41–58.
26. Koudriavtsev, A.B.; Linert, W. Thermally Induced Spin Crossover in the Liquid State: The Effects of Non-Ideality. *Monatsh. Chem.* **2001**, *132*, 235–243.

27. Toftlund, H. Spin Equilibrium in Solutions. *Monatsh. Chem.* **2001**, *132*, 1269–1277.
28. Turner, J.W.; Schultz, F.A. Intramolecular and Environmental Contributions to Electrode Half-Reaction Entropies of $M(tacn)_2^{3+/2+}$ (M = Fe, Co, Ni, Ru; tacn = 1,4,7-Triazacyclononane) Redox Couples. *Inorg. Chem.* **1998**, *38*, 358–364.
29. Turner, J.W.; Schultz, F.A. Solution characterization of the iron(II) bis(1,4,7-triazacyclononane) spin-equilibrium reaction. *Inorg. Chem.* **2001**, *40*, 5296–5298.
30. Schenker, S.; Stein, P.C.; Wolny, J.A.; Brady, C.; McGarvey, J.J.; Toftlund, H.; Hauser, A. Biphasic behavior of the high-spin-->low-spin relaxation of $[Fe(btpa)](PF_6)_2$ in solution (btpa = *N*,*N*,*N'*,*N'*-tetrakis(2-pyridylmethyl)-6,6′-bis(aminomethyl)-2,2′- bipyridine). *Inorg. Chem.* **2001**, *40*, 134–139.
31. Tsubasa, A.; Otsuka, S.; Maekawa, T.; Takano, R.; Sakurai, S.; Deming, T.J.; Kuroiwa, K. Development of hybrid diblock copolypeptide amphiphile/magnetic metal complexes and their spin crossover with lower-critical-solution-temperature(LCST)-type transition. *Polymer* **2017**, *128*, 347–355.
32. Fujitsuka, M.; Araki, K.; Kodama, T.; Hien, T.T.D.; Sakuragi, M.; Shetty, S.S.; Koyama, Y.; Kuroiwa, K. Supramolecular Control of Spin Equilibrium and Oxidation State in Nanohybrids of Amphiphilic Glycyrrhetinic Acid Derivatives with $[Fe(TACN)_2]^{2+}$. *Chem. Lett.* **2021**, *50*, 1142–1145.
33. Roubeau, O.; Colin, A.; Schmitt, V.; Clerac, R. Thermoreversible gels as magneto-optical switches. *Angew. Chem. Int. Ed. Engl.* **2004**, *43*, 3283–3286.
34. Fujigaya, T.; Jiang, D.L.; Aida, T. Spin-crossover physical gels: A quick thermoreversible response assisted by dynamic self-organization. *Chem. Asian J.* **2007**, *2*, 106–113.
35. Grondin, P.; Roubeau, O.; Castro, M.; Saadaoui, H.; Colin, A.; Clerac, R. Multifunctional gels from polymeric spin-crossover metallo-gelators. *Langmuir* **2010**, *26*, 5184–5195.
36. Echeverría, C.; Rubio, M.; Mitchell, G.R.; López, D. Structure of a spin-crossover Fe(II)-1,2,4-triazole polymer complex gel in toluene. Small angle neutron scattering and viscoelastic studies. *Eur. Polym. J.* **2014**, *53*, 238–245.
37. Sánchez-Ferrer, A.; Bräunlich, I.; Ruokolainen, J.; Bauer, M.; Schepper, R.; Smith, P.; Caseri, W.; Mezzenga, R. Gels, xerogels and films of polynuclear iron(ii)–aminotriazole spin-crossover polymeric complexes. *RSC Adv.* **2014**, *4*, 60842–60852.
38. Gural'skiy, I.A.; Reshetnikov, V.A.; Szebesczyk, A.; Gumienna-Kontecka, E.; Marynin, A.I.; Shylin, S.I.; Ksenofontov, V.; Fritsky, I.O. Chiral spin crossover nanoparticles and gels with switchable circular dichroism. *J. Mater. Chem. C* **2015**, *3*, 4737–4741.
39. Luo, Y.-H.; Dong, H.; Ma, S.-H.; Zeng, F.-L.; Jin, X.-T.; Liu, M. Atmospheric humidity-triggered reversible spin-state switching. *J. Mater. Chem. A* **2023**, *11*, 1232–1238.
40. Luo, Y.H.; Jin, X.T.; Zhang, S.X.; Xue, C.; Liu, M. Dynamic Aggregation Triggering Reversible Spin-State Switching. *ACS Appl. Mater. Interfaces* **2023**, *15*, 48365–48374.
41. Zeng, F.L.; Jin, X.T.; Zhao, J.; Zhang, S.X.; Xue, C.; Luo, Y.H. Construction and screening of spin-crossover-sponge materials based on iron(II)-triazole coordination polymers. *Dalton Trans.* **2024**, *53*, 2333–2340.
42. Luo, Y.-H.; Xue, C.; Zhang, S.-X.; Zhao, J.; Jin, X.-T.; Liu, M. Charge transfer-triggered reversible spin-state switching. *J. Mater. Chem. C* **2024**, *12*, 1693–1700.
43. Real, J.A.; Gaspar, A.B.; Munoz, M.C. Thermal, pressure and light switchable spin-crossover materials. *Dalton Trans.* **2005**, *12*, 2062–2079.
44. Ortega-Villar, N.; Thompson, A.L.; Munoz, M.C.; Ugalde-Saldivar, V.M.; Goeta, A.E.; Moreno-Esparza, R.; Real, J.A. Solid- and solution-state studies of the novel mu-dicyanamide-bridged dinuclear spin-crossover system $[(Fe(bztpen)]_2[\mu\text{-}N(CN)_2](PF_6)_3\cdot nH_2O$. *Chem. Eur. J.* **2005**, *11*, 5721–5734.
45. Bryliakov, K.P.; Duban, E.A.; Talsi, E.P. The Nature of the Spin-State Variation of $[Fe^{II}(BPMEN)(CH_3CN)_2](ClO_4)_2$ in Solution. *Eur. J. Inorg. Chem.* **2004**, *2005*, 72–76.
46. Kimizuka, N.; Shibata, T. Linear transition metal complexes of lipophilic triazoles and their thermochromism in cast films. *Polym. Prepr. Jpn.* **2000**, *49*, 3774.
47. Kuroiwa, K.; Shibata, T.; Takada, A.; Nemoto, N.; Kimizuka, N. Heat-set gel-like networks of lipophilic Co(II) triazole complexes in organic media and their thermochromic structural transitions. *J. Am. Chem. Soc.* **2004**, *126*, 2016–2021.
48. Kuroiwa, K.; Shibata, T.; Sasaki, S.; Ohba, M.; Takahara, A.; Kunitake, T.; Kimizuka, N. Supramolecular control of spin-crossover phenomena in lipophilic Fe(II)-1,2,4-triazole complexes. *J. Polym. Sci. Part A Polym. Chem.* **2006**, *44*, 5192–5202.
49. Kume, S.; Kuroiwa, K.; Kimizuka, N. Photoresponsive molecular wires of Fe^{II} triazole complexes in organic media and light-induced morphological transformations. *Chem. Commun.* **2006**, *23*, 2442–2444.
50. Kuroiwa, K.; Kimizuka, N. Coordination Structure Changes of Linear Cobalt(II) Triazole Complexes Induced by Binding of Long-chained Alcohols: Adaptive Molecular Clefts. *Chem. Lett.* **2008**, *37*, 192–193.
51. Matsukizono, H.; Kuroiwa, K.; Kimizuka, N. Self-assembly-directed Spin Conversion of Iron(II) 1,2,4-Triazole Complexes in Solution and Their Effect on Photorelaxation Processes of Fluorescent Counter Ions. *Chem. Lett.* **2008**, *37*, 446–447.

52. Kuroiwa, K.; Kikuchi, H.; Kimizuka, N. Spin crossover characteristics of nanofibrous Fe(II)-1,2,4-triazole complexes in liquid crystals. *Chem. Commun.* **2010**, *46*, 1229–1231.
53. Kuroiwa, K.; Kimizuka, N. Self-assembly and functionalization of lipophilic metal-triazole complexes in various media. *Polym. J.* **2012**, *45*, 384–390.
54. Matsukizono, H.; Kuroiwa, K.; Kimizuka, N. Lipid-packaged linear iron(II) triazole complexes in solution: Controlled spin conversion via solvophobic self-assembly. *J. Am. Chem. Soc.* **2008**, *130*, 5622–5623.
55. Vos, G.; De Graaff, R.A.G.; Haasnoot, J.G.; Van der Kraan, A.M.; De Vaal, P.; Reedijk, J. Crystal structure at 300 and 105 K, magnetic properties and Moessbauer spectra of bis(triaquatris(4-ethyltriazole-N^1)iron(II)-N^2,$N^{2'}$,$N^{2''}$)iron(II) hexakis(trifluoromethanesulfonate). A linear, trinuclear iron(II) compound, showing a unique high-spin-low-spin transition of the central iron atom. *Inorg. Chem.* **1984**, *23*, 2905–2910.
56. Kimizuka, N.; Shimizu, M.; Fujikawa, S.; Fujimura, K.; Sano, M.; Kunitake, T. AFM Observation of Organogel Nanostructures on Graphite in the Gel-Assisted Transfer Technique. *Chem. Lett.* **1998**, *27*, 967–968.
57. Kimizuka, N.; Kawasaki, T.; Kunitake, T. Self-organization of bilayer membranes from amphiphilic networks of complementary hydrogen bonds. *J. Am. Chem. Soc.* **1993**, *115*, 4387–4388.
58. Kimizuka, N.; Kawasaki, T.; Kunitake, T. Thermal Stability and Specific Dye Binding of a Hydrogen-Bond-Mediated Bilayer Membrane. *Chem. Lett.* **1994**, *23*, 33–36.
59. Kimizuka, N.; Kawasaki, T.; Kunitake, T. Spectral Characteristics and Molecular Orientation of Azobenzene-Containing Hydrogen-Bond-Mediated Bilayer Membranes. *Chem. Lett.* **1994**, *23*, 1399–1402.
60. Kimizuka, N.; Kawasaki, T.; Hirata, K.; Kunitake, T. Tube-like Nanostructures Composed of Networks of Complementary Hydrogen Bonds. *J. Am. Chem. Soc.* **1995**, *117*, 6360–6361.
61. Kimizuka, N.; Kawasaki, T.; Hirata, K.; Kunitake, T. Supramolecular Membranes. Spontaneous Assembly of Aqueous Bilayer Membrane via Formation of Hydrogen Bonded Pairs of Melamine and Cyanuric Acid Derivatives. *J. Am. Chem. Soc.* **1998**, *120*, 4094–4104.
62. Dolenský, B.; Konvalinka, R.; Jakubek, M.; Král, V. Identification of intramolecular hydrogen bonds as the origin of malfunctioning of multitopic receptors. *J. Mol. Struct.* **2013**, *1035*, 124–128.
63. Ostaszewski, R.; Urbańczyk-Lipkowska, Z. Solution and solid-state studies on the molecular conformation of mono- and disubstituted pyridine amidoesters: The role of characteristic C-H…O and N-H…O interactions. *J. Mol. Struct.* **1999**, *474*, 197–206.
64. Armand, F.; Badoux, C.; Bonville, P.; Ruaudel-Teixier, A.; Kahn, O. Langmuir-Blodgett Films of Spin Transition Iron(II) Metalloorganic Polymers. 1. Iron(II) Complexes of Octadecyl-1,2,4-triazole. *Langmuir* **1995**, *11*, 3467–3472.
65. Roubeau, O.; Alcazar Gomez, J.M.; Balskus, E.; Kolnaar, J.J.A.; Haasnoot, J.G.; Reedijk, J. Spin-transition behaviour in chains of Fe^{II} bridged by 4-substituted 1,2,4-triazoles carrying alkyl tails. *New J. Chem.* **2001**, *25*, 144–150.
66. Kroeber, J.; Audiere, J.-P.; Claude, R.; Codjovi, E.; Kahn, O.; Haasnoot, J.G.; Groliere, F.; Jay, C.; Bousseksou, A. Spin Transitions and Thermal Hysteresis in the Molecular-Based Materials $[Fe(Htrz)_2(trz)](BF_4)$ and $[Fe(Htrz)_3](BF_4)_2{\cdot}H_2O$ (Htrz = 1,2,4-4H-triazole; trz = 1,2,4-triazolato). *Chem. Mater.* **1995**, *6*, 1404–1412.
67. Fujigaya, T.; Jiang, D.L.; Aida, T. Switching of spin states triggered by a phase transition: Spin-crossover properties of self-assembled iron(II) complexes with alkyl-tethered triazole ligands. *J. Am. Chem. Soc.* **2003**, *125*, 14690–14691.
68. Fujigaya, T.; Jiang, D.L.; Aida, T. Spin-crossover dendrimers: Generation number-dependent cooperativity for thermal spin transition. *J. Am. Chem. Soc.* **2005**, *127*, 5484–5489.

Article

Modelling the Growth and Aggregation of Gold Nanoparticles Using Liquid-Phase Transmission Electron Microscopy

Thao Ngo, Siying Yu, and Hong Yang *

Department of Chemical and Biomolecular Engineering, University of Illinois Urbana-Champaign, 206 Roger Adams Laboratory, 600 South Mathews Avenue, Urbana, IL 61801, USA
* Correspondence: hy66@illinois.edu
Received: 2 August 2024; Revised: 5 June 2025; Accepted: 8 June 2025; Published: 18 June 2025

Abstract: The ability to synthesize nanoparticles of desired shape, size and composition relies heavily on our understanding on how to finely control various factors influencing the formation, such as the kinetics of growth. Fundamental study on the nucleation and growth of nanoparticles found itself at the forefront with the application of liquid-phase transmission electron microscopy (LTEM) in the investigation of dynamic growth and assembly processes. Since early study using LTEM to observe and quantify the nucleation and growth of single colloidal platinum nanoparticles, several theoretical models have been developed. More complex mode of formation was also revealed based on a hybrid growth process of gold on platinum icosahedral nanoparticles to form core-shell structures. These studies have been carried out by focusing on single or a small number of nanoparticles. Herewith, we present a study on the establishment of an analytical method to quantify the particle formation using in situ LTEM technique. This approach is based on the analysis of median particle size and focused on main events accounted for the formation of nanoparticles at a given time. We found that unlike the cases for single particle analysis, the observed formation rate could not be explained by any single formation mode, such as diffusion- and/or reaction-controlled growth described by the Liftshitz-Slyosov-Wagner theory or formation through coalescence as described by the Smoluchowski aggregative kinetics. A global fit was used to describe the entire formation of nanoparticles in an ensemble.

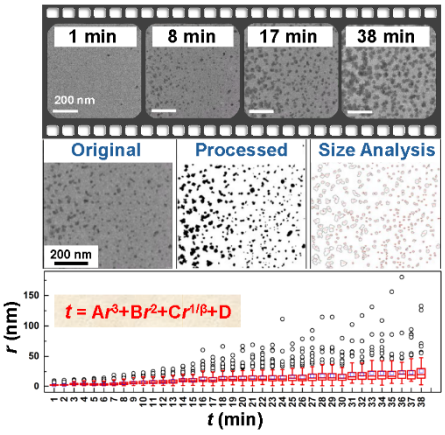

Keywords: LTEM; modelling; nanoparticle; growth; aggregation

1. Introduction

Nanomaterials are important in various fields including catalysis, biomedicine, gas sensing, and magnetic data storage, just to name a few, because of their unique properties, which arise from size- and shape-related properties [1–8]. It is essential that the formation of well-controlled nanoparticles can be quantitatively understood through the analysis of data obtained in reaction media throughout the various stages of formation [9–11]. Transmission electron microscopy (TEM) has been the method of choice for studying the kinetics and formation mechanisms of nanoparticles, such as growth and dissolution of colloidal nanocrystals. Prior to the invention of liquid-phase TEM (LTEM), a commonly used strategy for obtaining information regarding growth is to examine samples taken out from solutions at predetermined time points using TEM imaging [12–14]. This method, however, has the intrinsic uncertainty on whether ex situ data can offer an accurate picture of the formation in solution.

In this regard, LTEM is a powerful tool to investigate the formation of nanoparticles through various dynamic processes, such as growth and attachment in reaction media [15–24]. Noticeably, LTEM has been used to quantify the growth rate of colloidal Pt nanocrystals [25], Pt_3Fe nanorods [16], and core-shell nanostructures [26–28]. LTEM is also instrumental in revealing details of complex growth processes such as hybrid growth and subsequent surface diffusion [28,29], oriented attachment [9,30–33], self-assembly [34,35], and formation of superlattices and supracrystals [36–38]. LTEM studies have not only furthered the development of existing theories, but also

uncovered new growth processes that do not strictly adhere to those classical models of nucleation and growth based largely on precipitation phenomena [39–42].

The majority of LTEM studies on the formation of nanoparticles have so far focused on single or few nanoparticles without giving the much-needed consideration of the dynamics of nanoparticle formation as an ensemble [24,43,44]. While it is extremely useful in understanding the growth [45], the current approach does not entirely encompass the formation of nanoparticles in a solution containing a population of polydisperse nanoparticles at various growing stages, herein referred to as an ensemble, which is the most common case. For an ensemble, coalescence is yet another major factor for the formation of nanoparticles, besides the nucleation and growth from monomers [46,47]. Therefore, there is a clear need to develop methods to describe the formation by taking into consideration of both individual nanoparticle and ensemble in a solution environment.

Previously, it was shown by in situ LTEM the rate of formation of hybrid organic-inorganic perovskite nanoparticles did not follow either diffusion- or reaction-limited growth model as predicted by the Liftshitz-Slyosov-Wagner (LSW) theory [44]. Non-classical growth modes involving aggregation and coalescence were reported to be responsible for the formation of Au nanoparticles in an ensemble [43]. Quantitative analysis on particle size reveals that although the rate of growth follows that explained by the classical LSW theory, particle size distribution follows the model described by Smoluchowski aggregative kinetics [43]. In this study, we present a new method to quantify the formation of the whole formation of Au nanoparticles, including both the growth and ensemble, through mathematical fitting of particle size and size distribution. The data obtained through in situ LTEM are used to analyze the possible contributions of major driving forces for the formation of nanoparticles, that is, diffusion, surface reaction, and particle coalescence. We show that no single formation factor can be used to fit the entire experimental data obtained for an ensemble of Au nanoparticles formed under different conditions in a spatiotemporal analysis. Instead, the formation rate can be in both diffusion- and reaction-controlled regime in the early stages, while the coalescence-controlled regime is too complicated to be interpreted by the classical models.

2. Experimental Section

2.1 In Situ Growth of Au Nanoparticles

The solution mixture for the synthesis was made of 0.1 M tetrachloroauric acid ($HAuCl_4$, Sigma-Alrich (St. Louis, MO, USA), 99.995% trace metal basis) prepared by dissolving its hydrated form in deionized water (DI, H_2O). A droplet of the growth solution was placed in a liquid cell made of two 50 nm thick silicon nitride (SiN) windows supported on Si wafers separated by a 250-nm thick spacer (Figure 1). First, the spacer chip was placed into its slot in the tip of the LTEM holder (Hummingbird Scientific, Lacey, WA, USA), followed by the placement of a 2-μL droplet of 0.1 M $HAuCl_4$. The top chip was then carefully positioned atop the droplet of growth solution. A toothpick was used to gently press the top chip down so that the droplet spread out and to align the SiN windows. Once the windows were aligned, the cell was closed and tested for vacuum leakage using an external vacuum pump. Upon achieving a desirable pressure in the order of 10^{-6} bar, which is an indication of a well-sealed cell, the liquid cell was inserted into a TEM (Hitachi 9500, Hitachi High-Tech., Schaumburg, IL, USA) for study.

Au nanoparticles formed under the electron beam that was also used for the imaging of the growth process inside the liquid cell in TEM. The growth of Au nanoparticles was recorded at a beam current density of 8×10^{-12} A/cm^2 and magnification of ×12,000, corresponding to a constant electron dosage of 0.727 electron per Å^2 per second (e^-/(Å^2·s)). The typical total recording time was 40 min, after which no further changes were observed. The electron beam was kept on the imaging area for the entire duration of in-situ study.

2.2 Image Analysis

Still frames of 1 min apart each were obtained from the recorded in situ video of LTEM study. ImageJ software was used to count and measure the sizes of Au nanoparticles over time. By utilizing the difference in contrast between the nanoparticles and the surrounding solution, outlines of the nanoparticles in each frame were extracted (Figure 2). ImageJ was then used to measure the projected area of the nanoparticle. To comparing the formation rate of these nanoparticles over time with the growth rate predicted by LSW theory, the areas were converted to radius according to the equation, $A = \pi r^2$, where A is the projected area of the particle and r is the calculated radius. Particle overlapping can be an issue when the density of particles is high, especially at the later stage of particle growth. Thus, we only applied the proposed analysis to frames obtained from the very beginning till the time when particle overlapping became significant (i.e., 38 min in this study). Overlapped particles exhibited dark color and were distinguishable from non-overlapping ones in our TEM micrographs, which all had relatively clean backgrounds.

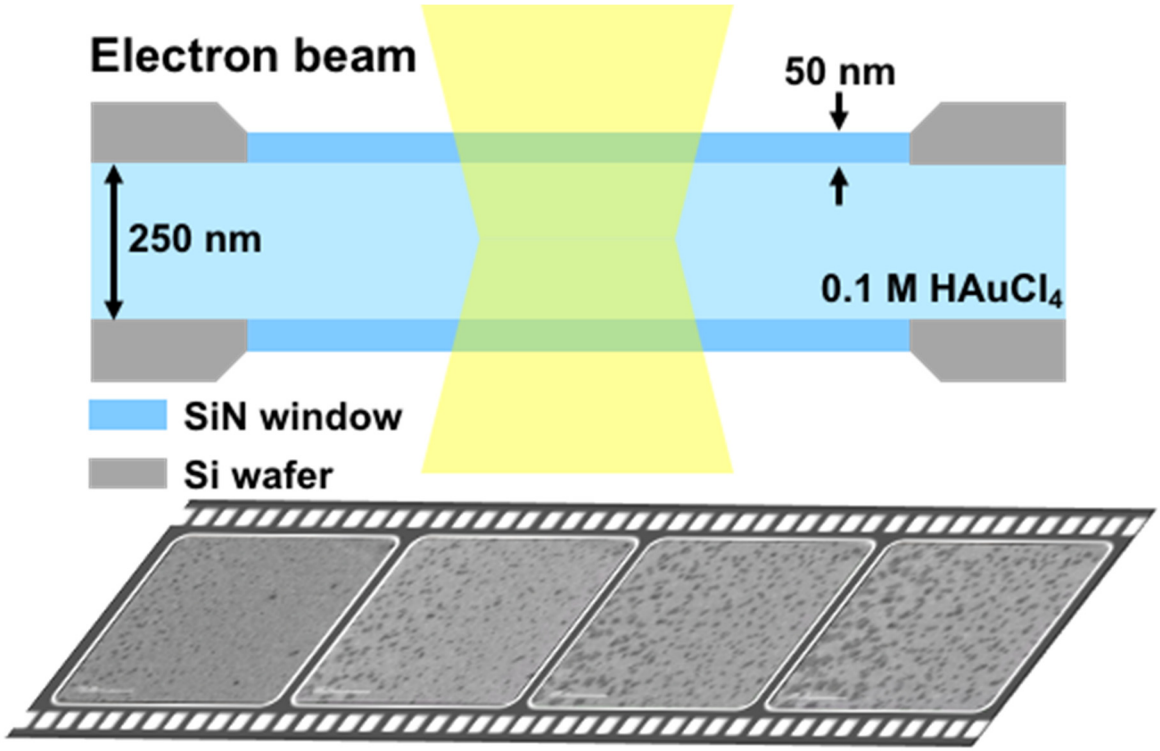

Figure 1. Illustration of the liquid cell for TEM used in this study. The scale bars in the micrographs are 200 nm.

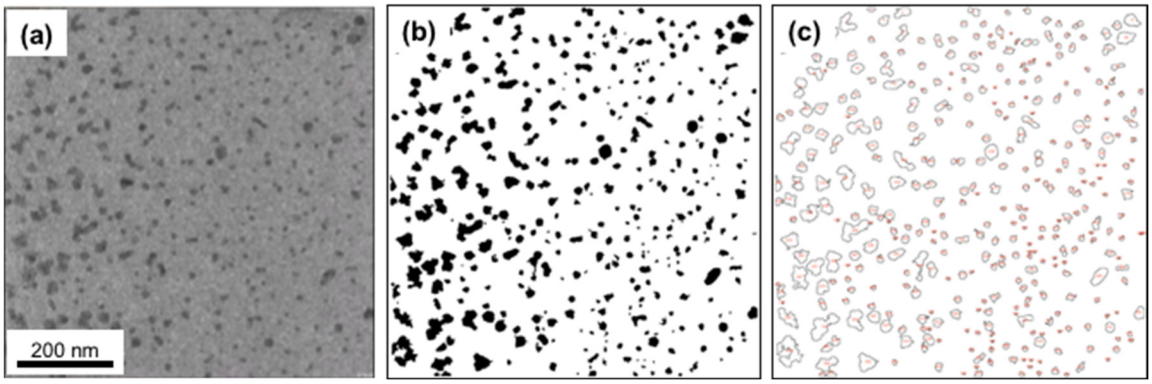

Figure 2. Illustration of the analysis of particle number and size from a LTEM micrograph using ImageJ software. (**a**) Still frame extracted from the LTEM video recorded during the growth, (**b**) processed image based on the contrast, and (**c**) image showing the outlines of the counted nanoparticles.

3. Results and Discussion

Figure 3 shows an ensemble of Au nanoparticles formed over a period of 38 min in an aqueous solution inside a TEM liquid cell at a dose rate of 0.727 $e^{-}/(Å^2 \cdot s)$. This rate of irradiation is significantly lower than the typically imaging condition, i.e., 5~50 $e^{-}/(Å^2 \cdot s)$ [48–50], thus the dendritic growth of Au particles was efficiently suppressed at the onset of the process [28]. Both the number and size of particles grew over time. The nanoparticles forming at the initial stages tend to be spherical in shape but became faceted and irregular in shape over the time of the recording period [51].

In the first 20 min, these nanoparticles grew both by the addition of monomer and later through the interactions among neighboring particles (Figure 4). Two types of particle interactions were observed from 8 to 20 min: the consumption of small particles by large ones (i.e., Ostwald ripening) and the coalescence of nanoparticles of similar sizes. Toward the end of recording, dendritic growth, which appeared to be suppressed to some extent, could however still be observed even though the dose rate was kept at a low level. It is likely the solvated electrons generated by the interaction between the electron beam and the aqueous solution was able to accumulate over time till eventually establishing a steady state, because the experiments were carried out under the static environment [52]. In addition, the last two images recorded at 36 and 38 min were noticeably brighter in

contrast than the others, suggesting a decrease in the thickness of liquid layer (Figure 3). The accumulation of solvated electrons and thinning of liquid thickness likely caused the formation of dendrites.

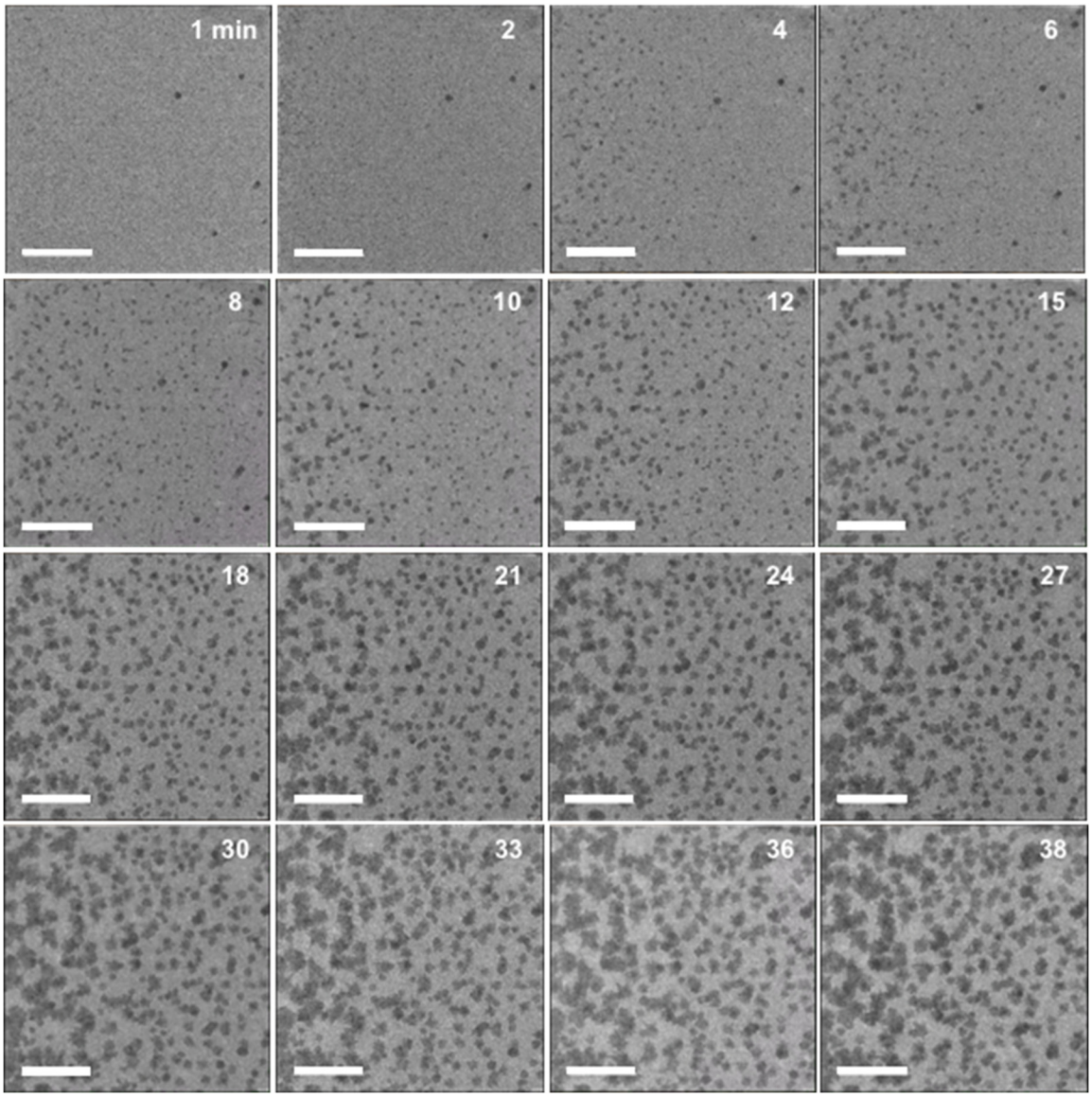

Figure 3. Still images extracted from in situ LTEM video of the formation of an ensemble of Au nanoparticles over the given times in minutes (at the top right of each TEM micrograph). The scale bars are 200 nm.

Figure 5 shows the quantitative analysis of number of nanoparticles formed using ImageJ software. The formation could be divided into three stages, as determined by the rate of change in the number of nanoparticles (n_s) and particle size over time (t), which is the slope of the linear function between n_s and t (Figure 5a). In Stage I, nanoparticles grew rapidly at a rate of ~59 particles/min, apparently via monomer addition, up to about 6 min. During Stage II, the total number of nanoparticles decreased with time at a rate of 23 particles/min. In Stage III, the combination of neighboring particles slowed down, as indicated by a decrease in the rate of change of n_s over t to 6.6 particles/min from 23 particles/min in Stage II. The main mode of formation at this stage was dendritic growth from the existing particles with some combination of particles, judging by the TEM images. No major changes in n_s and particle size were observed after reaction time reached 38 min, as shown in Figure 3.

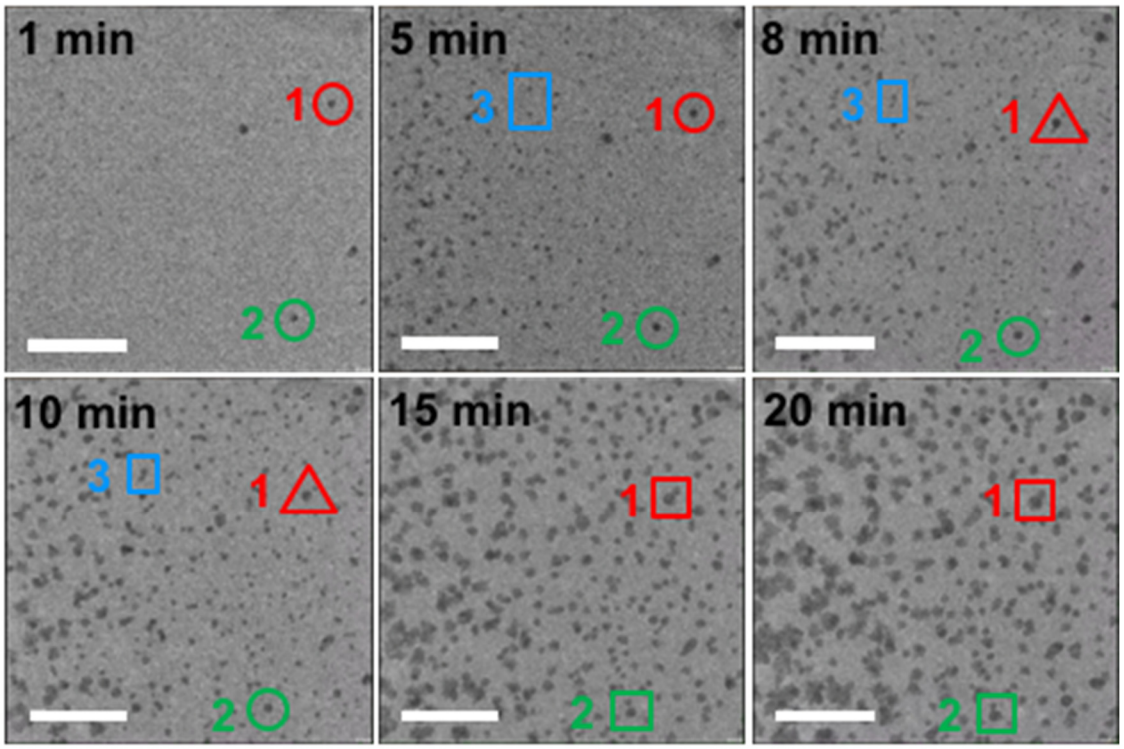

Figure 4. TEM images showing the formation of three Au nanoparticles via monomer addition (circle), coalescence (square), and Ostwald ripening (triangle). Same color is used to follow the same particle. The scale bars are 200 nm.

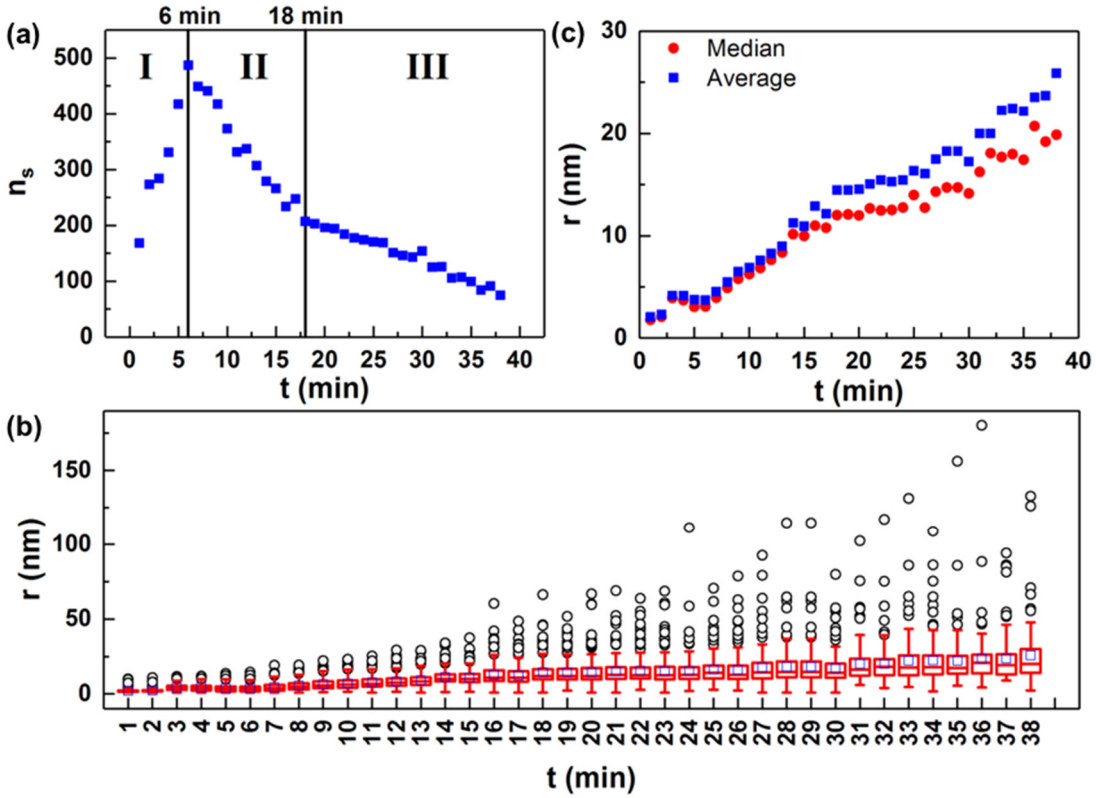

Figure 5. Changes of number and size of particles extracted from in situ LTEM data. (**a**) Number of particles (n_s,) as a function of time (t). (**b**) Particle size (r) over time (t) in the form of a box plot with outliers. The line and blue square inside each box represent the median and average particle size at that time, respectively. The top of the box represents the upper quartile while the bottom of the box represents the lower quartile. The upper and lower whiskers represent particles with sizes that fall outside the middle 50%. (**c**) Median and average particle size as a function of time extracted from (**b**).

One challenge on analyzing ensemble data from the LTEM is the heterogeneity of the nanoparticle formed under rather complex reaction conditions due to the electron beam irradiation of static nature of the cell [53]. Thus, it was important to perform a statistical analysis to determine the data set to be used prior to the fitting of experimental data. Particularly, it is necessary to determine whether to choose the average or median radii for the particle size. As shown in Figure 5b, as time increased, the variation in size increased. Furthermore, the average radii were deviated greatly from the median at some time points (Figure 5c). Our study indicates based on the statistical analysis, median radii could be the representative values to analyze the rate of formation based on majority of the particle population in the ensemble and were used for the data analysis.

Based on the data set obtained through the above statically analysis of median radii, we quantified the formation of nanoparticles by considering main controlling factors, including diffusion, reaction, and particle coalescence both individually and in a global analysis. For the growth, we turned to the classical LSW theory, which considers the nanoparticle growth a solution in two major steps: diffusion of monomers from the bulk solution onto the surface of a seed, and reaction of monomers at the surface [54]. Equation (1) gives the general expression describing the size evolution of a single nanoparticle (a detailed derivation of Equation (1) based on the Fick's first law is presented in the Supporting Information):

$$\frac{dr}{dt} = \frac{2\gamma V_m^2 C_\infty}{RT(1/D + 1/k_d r)} \frac{1/r_b - 1/r}{r} \tag{7}$$

where r is the radius, r_b is the distance from the bulk to the center of the particle, γ is the interfacial energy, V_m is the molar volume, C_∞ is the concentration of a flat particle, R is the gas constant, T is temperature, D is the diffusion coefficient, and k_d is the rate constant. In the case of a diffusion-limited growth that the particle size is controlled by the diffusion of the monomers to the surface Equation (1) is reduced to the following form:

$$\frac{dr}{dt} = \frac{2\gamma D V_m^2 C_\infty}{RT} \frac{(r/r_b - 1)}{r^2} \tag{8}$$

Given that the total mass of the system is conserved, the LSW theory shows that the ratio r/r_b is a constant; Equation (2) can further be simplified to

$$\frac{dr}{dt} = K_D \frac{1}{r^2} \tag{9}$$

Equation (3) can be solved to obtain the time-dependent expression for particle size:

$$r^3 - r_0^3 = K_D t \tag{10}$$

where r_0 is the median radius of the particle at time $t = 0$, and K_D is a coefficient leading t and is given by the following expression:

$$K_D = \frac{8\gamma D V_m^2 C_\infty}{9RT} \tag{11}$$

For the growth of particle controlled by reactions of monomers at a surface of a particle, Equation (1) is reduced to the following form:

$$\frac{dr}{dt} = \frac{2\gamma k_d V_m^2 C_\infty}{RT} \frac{(r/r_b - 1)}{r} \tag{12}$$

Similar to the diffusion-controlled growth, the ratio r/r_b remains constant if the total mass of the system is conserved. Integrating Equation (6) yields the relationship between particle size and time for the case of a reaction-controlled growth:

$$r^2 \approx K_R t \tag{13}$$

The obtained radii of the nanoparticles were fit with the above equation (Figure 6). Neither the diffusion- nor reaction-controlled case derived from LSW theory could fit the experimental data of the relationship between particle size and time over the entire period. For particle formation under this experimental condition, the initial formation was indeed influenced mainly by both the diffusion of monomers and surface reaction, as shown by a reasonable fit using the LSW theory to the experimental data within the first 6 min or so (Figure 6) [45,55].

The deviation from the experimental data based on the LSW theory stems from the formation dominated by modes other than growth, that is, particle coalescence in the ensemble. One approach is to include new terms to the existing fit to account for the formation through both monomer growth and particle coalescence. In another

word, the formation through coalescence can be factored into the fit describing only the growth. We hypothesized effect of coagulation should be included to fit the curve of size evolution over time when particle aggregated [56].

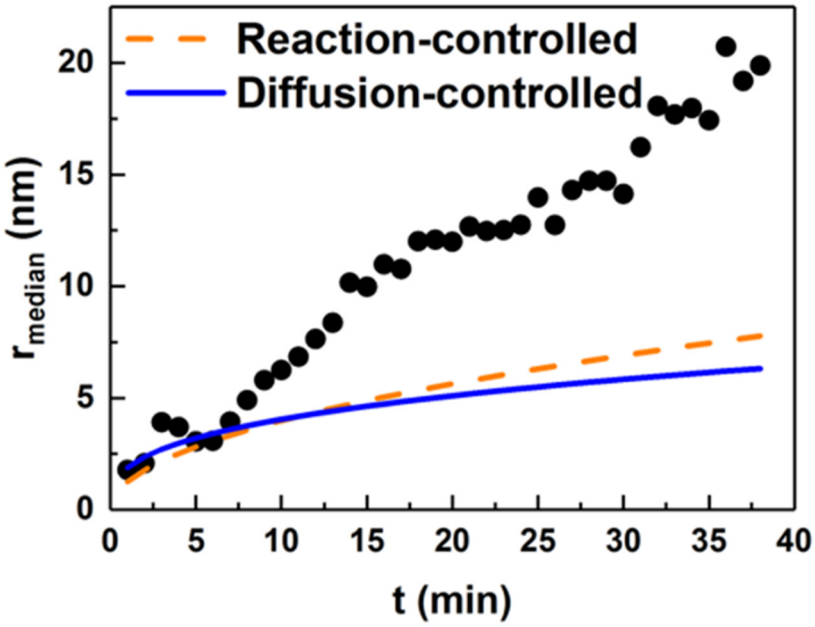

Figure 6. Experimental data and theoretical fits of median particle size as a function of time using expressions describing reaction- and diffusion-controlled growth by LSW theory.

The necessity to incorporate both LSW theory and coagulation kinetics was analyzed based on particle size distribution (PSD) of the samples. As shown in Figure S1, PSD is obtained by normalizing the radii of nanoparticles in each time frame to the respective mean nanoparticle radius at that time. The normalized radii are then normalized to the total integral to gain the frequency. To compare experimental data with existing theories, PSD predicted by LSW theory and Smoluchowski aggregation kinetics were included. The expressions and derivation for theorical PSD can be found in the SI. As can be seen in Figure S1, the PSD extracted from the growth of nanoparticles did not follow those predicted by either LSW or Smoluchowski theories. The experimental PSD is observably more symmetric compared to theoretical PSD curves in general. For the first stage of growth (stage I), the PSD decreased in magnitude and shifted to the left, as indicated by the red arrow. Based on the PSD predicted by the LSW theory and the Smoluchowski coalescence kinetics, the changes in the PSD for the first 6 min reflected a shift from growth via mixed diffusion- and reaction-limited regime toward growth via coalescence. During the second stage of growth (stage II), PSD shifts from right to left with an increase in magnitude, suggesting a shift in the mode of formation. In this study nanoparticles could freely move to coalesce to reduce surface energy because there was no surfactant used. After the movable nanoparticles exhausted, the ensemble reverted to the growing mode via monomer addition. In the last stage of growth (stage III), the PSD determined experimentally showed little change in terms of shift in relative size and magnitude in frequency.

It is worthwhile to note that during the last stage of growth, nanoparticles continued to grow via the formation of dendrites. The formation of dendrites is characteristic of a kinetic-controlled process and highly sensitive to the monomer supersaturation level in the growth solution. Dendrites tend to form under high supersaturation conditions and evaporation time of the aqueous precursor solution. Oversaturation (S) was calculated and plotted against time (t) in Figure S2 using experimental growth rate, based on the relationship between critical radius (r_{cr}) [45]:

$$r_{cr} = \frac{2\gamma V_m}{RT \ln S} \tag{14}$$

Figure S2 shows that oversaturation decreased rapidly over time because of monomer consumption during the growth process. Other factors may include evaporation or thinning of the liquid layer, as evidenced by the change to lighter contrast of the background at the later stages of formation of particles (as shown in the inset of Figure S2) or movement of the liquid within the cell, causing oversaturation to be much higher than expected and subsequent formation of dendrite.

Evolution of an ensemble of nanoparticles was previously examined theoretically using Monte Carlo simulation [45]. The obtained rate from the simulation was much higher than that predicted by the LSW theory,

but similar to the rate obtained experimentally in this study. A solution thus is to include an additional parameter to the two-term expansion of the Gibbs-Thompson equation in the followings:

$$\frac{dr}{dt} = \frac{2K'\gamma V_m^2 C_\infty}{RTr^2(1/D + 1/k_d r)} \tag{15}$$

Equation (9) can be rearranged to

$$\frac{RT}{2DK'\gamma V_m^2 C_\infty} r^2 dr + \frac{RT}{2k_d K'\gamma V_m^2 C_\infty} r dr = dt \tag{16}$$

which can then be integrated to obtain the following equation for data simulation:

$$Ar^3 + Br^2 + C = t \tag{17}$$

where A is equal to $\frac{RT}{2DK'\gamma V_m^2 C_\infty}$, B is equal to $\frac{RT}{2k_d K'\gamma V_m^2 C_\infty}$, and C is a constant. This treatment considers the intermediate regime in which both diffusion and surface reaction contribute to the growth process and the ratio r/r_b is assumed to be a constant, K'.

Particle growth via coalescence has been analyzed using a power law in the Monte Carlo simulation, $r \sim t^\beta$ [57], where β is the coalescence exponent and a function of a parameter α that describes the nature of the movement of nanoparticles. The relationship between β and α is described by the following expression:

$$\beta = \frac{1}{2(\alpha + 1)} \tag{18}$$

Equation (11) offers an approach via which formation of nanoparticles based on coalescence can be considered by measuring the coalescence exponent. To evaluate what a likely value β could be, we analyzed the changes in size of several individual nanoparticles at the late stages, during which coalescence took place and plotted against time (Figure S3). The radii as a function of time of several nanoparticles were fitted using a power law, $r \sim t^\beta$, and the results for β are shown in Figure 7.

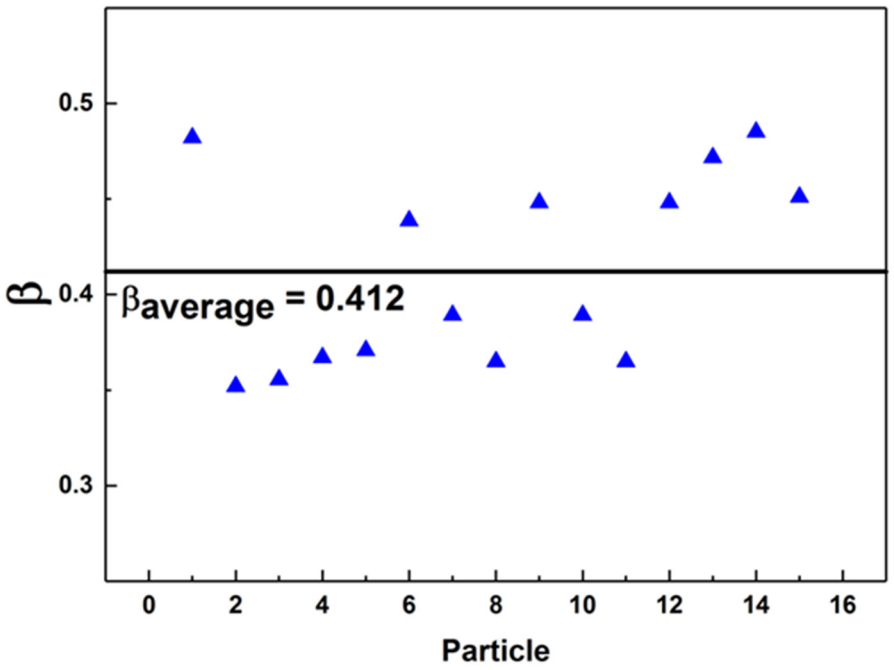

Figure 7. β value obtained from fitting the growth rate of nanoparticles grown via coalescence.

Values for α were typically in the range of $0 < \alpha < 2$, corresponding to β values not to exceed 0.5 [56]. In this study, all of experimentally determined β values met this upper limit. For the analysis, an average value of 0.412 was used for β, corresponding to an α value of 0.214. Thus, to factor in contribution to the particle formation from coalescence, a term corresponding to the particle formation via coalescence in the form of $t \sim r^{1/\beta}$ should be added to Equation (10) to obtain a new form describing the formation of particles in an ensemble in solution through all the stages:

$$t \approx Ar^3 + Br^2 + Cr^{1/\beta} + D \quad (19)$$

We used this new global analysis equation to fit the experimental data for the formation of Au nanoparticles in solution obtained by in situ LTEM (Figure 8). The fitting resulted in the following equation for quantifying the change of particle size over time, $r(t)$:

$$(8.06 \times 10^{-19})r^3 + 0.31r^2 - 0.062r^{2.43} + 1.92 = t \quad (20)$$

where the values of A, B, C and D are 8.06×10^{-19}, 0.31, −0.062, and 1.92, respectively; and β is 0.412. One may use the obtained coefficients and experientials to further examine the various regimes for the particle formation, though the negative value of coefficient C is not understood. For example, in this system the value of A (8.06×10^{-19}) is much smaller than that of B (0.31). This result indicates that under this reaction condition, diffusion is more prominent than surface reaction, because coefficient A is inversely related to the diffusion coefficient, while coefficient B is inversely related to the surface reaction coefficient (k_d).

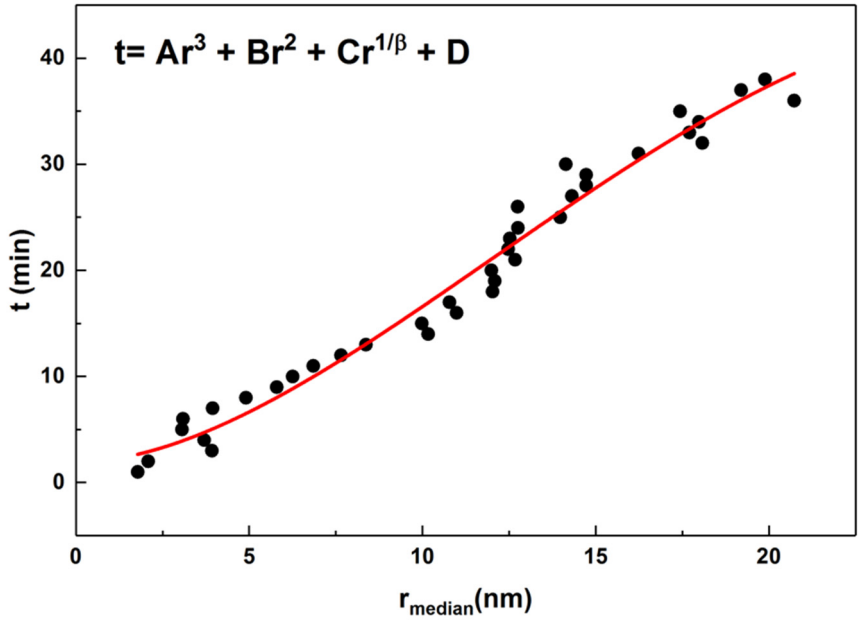

Figure 8. Time (t) as a function of radius (r) and a fit based on Equation (13) aiming at describing the formation of nanoparticles by mixed diffusion- and reaction-controlled growth and particle coalescence (red curve).

4. Conclusions

In this study, the formation of Au nanoparticles was quantitatively analyzed using in situ LTEM. The simulation of the data for the formation was analyzed by considering both LSW theory for nucleation and growth, and coagulation kinetics of an ensemble. No existing treatment could satisfactorily describe the entire formation process observed, and a polynomial expression was developed to fit the diffusion- and reaction-controlled growth and particle coalescence. This approach allows for a description of the complexity in the particle formation for the entire process: the initial monomer addition controlled by both diffusion and surface reaction processes (Stage I); the monomer addition and coalescence (Stage II); and the dendritic formation at the end (Stage III). Using polynomial expression to fit the data could be applicable for simulation of the formation of nanoparticles that go through growth and coagulation in solution, though understanding the insight of the formation is still a challenge.

Supplementary Materials: The following supporting information can be downloaded at: https://media.sciltp.com/articles/others/2506181658399634/MI-439-Supplementary-Materials.pdf, Supplementary notes on derivation of LSW theory and PSD; Figure S1: Particle size distribution (PSD) of the experimental radii compared to those predicted from the LSW theory; Figure S2: Oversaturation (S) as a function of time (t); Figure S3: Analysis of nanoparticles grown via coalescence. Reference [58] is cited in the Supplementary Materials.

Author Contributions: T.N.: Conceptualization, Validation, Methodology, Data Duration, Formal Analysis, Writing-original draft, Writing-review & editing; S.Y.: Writing-review & editing; H.Y.: Conceptualization, Methodology, Writing-review & editing, Supervision, Resources, Investigation, Funding acquisition. All authors have read and agreed to the published version of the manuscript.

Funding: This research was funded by U.S. National Science Foundation (Funding No.: OISE-1515376), and University of Illinois.

Data Availability Statement: Data is available from the corresponding author upon reasonable request.

Acknowledgments: We thank U.S. National Science Foundation (NSF, OISE-1515376) and University of Illinois for support of this research. The electron microscopy study was carried out at Materials Research Laboratory at University of Illinois. T. N. is grateful for a National Science Foundation Graduate Research Fellowship.

Conflicts of Interest: The authors declare no conflict of interest. The funders had no role in the design of the study; in the collection, analyses, or interpretation of data; in the writing of the manuscript; or in the decision to publish the results.

References

1. Lu, J.; Wu, W.; Colombari, F.M.; Jawaid, A.; Seymour, B.; Whisnant, K.; Zhong, X.; Choi, W.; Chalmpes, N.; Lahann, J.; et al. Nano-Achiral Complex Composites for Extreme Polarization Optics. *Nature* **2024**, *630*, 860–865.
2. Boles, M.A.; Ling, D.; Hyeon, T.; Talapin, D.V. The Surface Science of Nanocrystals. *Nat. Mater.* **2016**, *15*, 141–153.
3. Yang, X.; Yang, M.; Pang, B.; Vara, M.; Xia, Y. Gold Nanomaterials at Work in Biomedicine. *Chem. Rev.* **2015**, *115*, 10410–10488.
4. Murphy, C.J.; Vartanian, A.M.; Geiger, F.M.; Hamers, R.J.; Pedersen, J.; Cui, Q.; Haynes, C.L.; Carlson, E.E.; Hernandez, R.; Klaper, R.D.; et al. Biological Responses to Engineered Nanomaterials: Needs for the Next Decade. *ACS Cent. Sci.* **2015**, *1*, 117–123.
5. Wu, J.; Yang, H. Platinum-Based Oxygen Reduction Electrocatalysts. *Acc. Chem. Res.* **2013**, *46*, 1848–1857.
6. Xia, Y.; Yang, P.; Sun, Y.; Wu, Y.; Mayers, B.; Gates, B.; Yin, Y.; Kim, F.; Yan, H. One-Dimensional Nanostructures: Synthesis, Characterization, and Applications. *Adv. Mater.* **2003**, *15*, 353–389.
7. Zhou, L.; Huang, Q.; Xia, Y. Plasmon-Induced Hot Electrons in Nanostructured Materials: Generation, Collection, and Application to Photochemistry. *Chem. Rev.* **2024**, *124*, 8597–8619.
8. Yu, S.; Yang, H. Design Principles for the Synthesis of Platinum–Cobalt Intermetallic Nanoparticles for Electrocatalytic Applications. *Chem. Commun.* **2023**, *59*, 4852–4871.
9. Peng, Z.; You, H.; Yang, H. Composition-Dependent Formation of Platinum Silver Nanowires. *ACS Nano* **2010**, *4*, 1501–1510.
10. Park, J.; Joo, J.; Kwon, S.G.; Jang, Y.; Hyeon, T. Synthesis of Monodisperse Spherical Nanocrystals. *Angew. Chem., Int. Ed.* **2007**, *46*, 4630–4660.
11. Xia, Y.; Xiong, Y.; Lim, B.; Skrabalak, S.E. Shape-Controlled Synthesis of Metal Nanocrystals: Simple Chemistry Meets Complex Physics? *Angew. Chem. Int. Ed.* **2009**, *48*, 60–103.
12. Yin, X.; Shi, M.; Wu, J.; Pan, Y.-T.; Gray, D.L.; Bertke, J.A.; Yang, H. Quantitative Analysis of Different Formation Modes of Pt Nanocrystals Controlled by Ligand Chemistry. *Nano Lett.* **2017**, *17*, 6146–6150.
13. Yu, S.; Zhang, C.; Yang, H. Two-Dimensional Metal Nanostructures: From Theoretical Understanding to Experiment. *Chem. Rev.* **2023**, *123*, 3443–3492.
14. Drake, G.A.; Keating, L.P.; Shim, M. Design Principles of Colloidal Nanorod Heterostructures. *Chem. Rev.* **2023**, *123*, 3761–3789.
15. Grogan, J.M.; Rotkina, L.; Bau, H.H. In-Situ Liquid-Cell Electron Microscopy of Colloid Aggregation and Growth Dynamics. *Phys. Rev. E* **2011**, *83*, 061405.
16. Liao, H.G.; Cui, L.; Whitelam, S.; Zheng, H. Real-Time Imaging of Pt_3Fe Nanorod Growth in Solution. *Science* **2012**, *336*, 1011–1014.
17. Wu, J.; Gao, W.; Yang, H.; Zuo, J.-M. Dissolution Kinetics of Oxidative Etching of Cubic and Icosahedral Platinum Nanoparticles Revealed by in situ Liquid Transmission Electron Microscope. *ACS Nano* **2017**, *11*, 1696–1703.
18. Lyu, Z.; Yao, L.; Chen, W.; Kalutantirige, F.C.; Chen, Q. Electron Microscopy Studies of Soft Nanomaterials. *Chem. Rev.* **2023**, *123*, 4051–4145.
19. Kim, B.H.; Yang, J.; Lee, D.; Choi, B.K.; Hyeon, T.; Park, J. Liquid-Phase Transmission Electron Microscopy for Studying Colloidal Inorganic Nanoparticles. *Adv. Mater.* **2018**, *30*, 1703316.
20. Kim, B.H.; Heo, J.; Kim, S.; Reboul, C.F.; Chun, H.; Kang, D.; Bae, H.; Hyun, H.; Lim, J.; Lee, H.; et al. Critical Differences in 3D Atomic Structure of Individual Ligand-Protected Nanocrystals in Solution. *Science* **2020**, *368*, 60–67.
21. Ngo, T.; Yang, H. Toward Ending the Guessing Game: Study of the Formation of Nanostructures Using In Situ Liquid Transmission Electron Microscopy. *J. Phys. Chem. Lett.* **2015**, *6*, 5051–5061.
22. Hodnik, N.; Dehm, G.; Mayrhofer, K.J.J. Importance and Challenges of Electrochemical in Situ Liquid Cell Electron Microscopy for Energy Conversion Research. *Acc. Chem. Res.* **2016**, *49*, 2015–2022.
23. Ross, F.M. Opportunities and Challenges in Liquid Cell Electron Microscopy. *Science* **2015**, *350*, aaa9886.
24. Peng, X.; Shangguan, J.; Zhang, Q.; Hauwiller, M.; Yu, H.; Nie, Y.; Bustillo, K.C.; Alivisatos, A.P.; Asta, M.; Zheng, H. Unveiling Corrosion Pathways of Sn Nanocrystals through High-Resolution Liquid Cell Electron Microscopy. *Nano Lett.* **2024**, *24*, 1168–1175.

25. Zheng, H.; Smith, R.K.; Jun, Y.W.; Kisielowski, C.; Dahmen, U.; Alivisatos, A.P. Observation of Single Colloidal Platinum Nanocrystal Growth Trajectories. *Science* **2009**, *324*, 1309–1312.
26. Zhang, Q.; Peng, X.; Nie, Y.; Zheng, Q.; Shangguan, J.; Zhu, C.; Bustillo, K.C.; Ercius, P.; Wang, L.; Limmer, D.T.; et al. Defect-Mediated Ripening of Core-Shell Nanostructures. *Nat. Commun.* **2022**, *13*, 2211.
27. Zheng, L.; Zhang, X.; Bustillo, K.C.; Yao, Y.; Zhao, L.; Zhu, M.; Li, W.; Zheng, H. Growth Mechanism of Core–Shell PtNi–Ni Nanoparticles Using in Situ Transmission Electron Microscopy. *Nanoscale* **2018**, *10*, 11281–11286.
28. Wu, J.; Gao, W.; Wen, J.; Miller, D.J.; Lu, P.; Zuo, J.-M.; Yang, H. Growth of Au on Pt Icosahedral Nanoparticles Revealed by Low-Dose In Situ TEM. *Nano Lett.* **2015**, *15*, 2711–2715.
29. Zheng, L.; Zhao, L.; Zhao, S.; Zhang, X.; Bustillo, K.C.; Yao, Y.; Yi, X.; Zhu, M.; Li, W.; Zheng, H. A Unique Pathway of PtNi Nanoparticle Formation Observed with Liquid Cell Transmission Electron Microscopy. *Nanoscale* **2020**, *12*, 1414–1418.
30. Li, D.; Nielsen, M.H.; Lee, J.R.I.; Frandsen, C.; Banfield, J.F.; De Yoreo, J.J. Direction-Specific Interactions Control Crystal Growth by Oriented Attachment. *Science* **2012**, *336*, 1014–1018.
31. Welch, D.A.; Woehl, T.J.; Park, C.; Faller, R.; Evans, J.E.; Browning, N.D. Understanding the Role of Solvation Forces on the Preferential Attachment of Nanoparticles in Liquid. *ACS Nano* **2015**, *10*, 181–187.
32. Wang, Y.; Peng, X.; Abelson, A.; Zhang, B.-K.; Qian, C.; Ercius, P.; Wang, L.-W.; Law, M.; Zheng, H. In Situ TEM Observation of Neck Formation During Oriented Attachment of PbSe Nanocrystals. *Nano Res.* **2019**, *12*, 2549–2553.
33. Zhu, C.; Liang, S.; Song, E.; Zhou, Y.; Wang, W.; Shan, F.; Shi, Y.; Hao, C.; Yin, K.; Zhang, T.; et al. *In-Situ* Liquid Cell Transmission Electron Microscopy Investigation on Oriented Attachment of Gold Nanoparticles. *Nat. Commun.* **2018**, *9*, 421.
34. Luo, B.; Smith, J.W.; Ou, Z.; Chen, Q. Quantifying the Self-Assembly Behavior of Anisotropic Nanoparticles Using Liquid-Phase Transmission Electron Microscopy. *Acc. Chem. Res.* **2017**, *50*, 1125–1133.
35. Kim, A.; Akkunuri, K.; Qian, C.; Yao, L.; Sun, K.; Chen, Z.; Vo, T.; Chen, Q. Direct Imaging of "Patch-Clasping" and Relaxation in Robust and Flexible Nanoparticle Assemblies. *ACS Nano* **2024**, *18*, 939–950.
36. Park, J.; Zheng, H.; Lee, W.C.; Geissler, P.L.; Rabani, E.; Alivisatos, A.P. Direct Observation of Nanoparticle Superlattice Formation by Using Liquid Cell Transmission Electron Microscopy. *ACS Nano* **2012**, *6*, 2078–2085.
37. Ou, Z.; Yao, L.; An, H.; Shen, B.; Chen, Q. Imaging How Thermal Capillary Waves and Anisotropic Interfacial Stiffness Shape Nanoparticle Supracrystals. *Nat. Commun.* **2020**, *11*, 4555.
38. Chen, Q.; Yuk, J.M.; Hauwiller, M.R.; Park, J.; Dae, K.S.; Kim, J.S.; Alivisatos, A.P. Nucleation, Growth, and Superlattice Formation of Nanocrystals Observed in Liquid Cell Transmission Electron Microscopy. *MRS Bull.* **2020**, *45*, 713–726.
39. Son, Y.; Kim, B.H.; Choi, B.K.; Luo, Z.; Kim, J.; Kim, G.-H.; Park, S.-J.; Hyeon, T.; Mehraeen, S.; Park, J. In Situ Liquid Phase TEM of Nanoparticle Formation and Diffusion in a Phase-Separated Medium. *ACS Appl. Mater. Interfaces* **2022**, *14*, 22810–22817.
40. Hong, J.; Bae, J.-H.; Jo, H.; Park, H.-Y.; Lee, S.; Hong, S.J.; Chun, H.; Cho, M.K.; Kim, J.; Kim, J.; et al. Metastable Hexagonal Close-Packed Palladium Hydride in Liquid Cell TEM. *Nature* **2022**, *603*, 631–636.
41. Crook, M.F.; Laube, C.; Moreno-Hernandez, I.A.; Kahnt, A.; Zahn, S.; Ondry, J.C.; Liu, A.; Alivisatos, A.P. Elucidating the Role of Halides and Iron during Radiolysis-Driven Oxidative Etching of Gold Nanocrystals Using Liquid Cell Transmission Electron Microscopy and Pulse Radiolysis. *J. Am. Chem. Soc.* **2021**, *143*, 11703–11713.
42. Hauwiller, M.R.; Ye, X.; Jones, M.R.; Chan, C.M.; Calvin, J.J.; Crook, M.F.; Zheng, H.; Alivisatos, A.P. Tracking the Effects of Ligands on Oxidative Etching of Gold Nanorods in Graphene Liquid Cell Electron Microscopy. *ACS Nano* **2020**, *14*, 10239–10250.
43. Woehl, T.J.; Park, C.; Evans, J.E.; Arslan, I.; Ristenpart, W.D.; Browning, N.D. Direct Observation of Aggregative Nanoparticle Growth: Kinetic Modeling of the Size Distribution and Growth Rate. *Nano Lett.* **2014**, *14*, 373–378.
44. Qin, F.; Wang, Z.; Wang, Z.L. Anomalous Growth and Coalescence Dynamics of Hybrid Perovskite Nanoparticles Observed by Liquid-Cell Transmission Electron Microscopy. *ACS Nano* **2016**, *10*, 9787–9793.
45. Talapin, D.V.; Rogach, A.L.; Haase, M.; Weller, H. Evolution of an Ensemble of Nanoparticles in a Colloidal Solution: Theoretical Study. *J. Mater. Chem. B* **2001**, *105*, 12278–12285.
46. Kang, S.; Kim, J.-H.; Lee, M.; Yu, J.W.; Kim, J.; Kang, D.; Baek, H.; Bae, Y.; Kim, B.H.; Kang, S.; et al. Real-Space Imaging of Nanoparticle Transport and Interaction Dynamics by Graphene Liquid Cell TEM. *Sci. Adv.* **2021**, *7*, eabi5419.
47. Kim, J.; Kang, D.; Kang, S.; Kim, B.H.; Park, J. Coalescence Dynamics of Platinum Group Metal Nanoparticles Revealed by Liquid-Phase Transmission Electron Microscopy. *iScience* **2022**, *25*, 104699.
48. Ma, X.; Lin, F.; Chen, X.; Jin, C. Unveiling Growth Pathways of Multiply Twinned Gold Nanoparticles by In Situ Liquid Cell Transmission Electron Microscopy. *ACS Nano* **2020**, *14*, 9594–9604.
49. Ma, X.; Lin, F.; Chen, X.; Jin, C. Synergy between Structure Characteristics and the Solution Chemistry in a Near/Non-Equilibrium Oxidative Etching of Penta-Twinned Palladium Nanorods. *J. Phys. Chem. C* **2021**, *125*, 4010–4020.

50. Zhang, Y.; Keller, D.; Rossell, M.D.; Erni, R. Formation of Au Nanoparticles in Liquid Cell Transmission Electron Microscopy: From a Systematic Study to Engineered Nanostructures. *Chem. Mater.* **2017**, *29*, 10518–10525.
51. Choi, B.K.; Kim, J.; Luo, Z.; Kim, J.; Kim, J.H.; Hyeon, T.; Mehraeen, S.; Park, S.; Park, J. Shape Transformation Mechanism of Gold Nanoplates. *ACS Nano* **2023**, *17*, 2007–2018.
52. Schneider, N.M.; Norton, M.M.; Mendel, B.J.; Grogan, J.M.; Ross, F.M.; Bau, H.H. Electron–Water Interactions and Implications for Liquid Cell Electron Microscopy. *J. Phys. Chem. C* **2014**, *118*, 22373–22382.
53. Woehl, T.J.; Moser, T.; Evans, J.E.; Ross, F.M. Electron-Beam-Driven Chemical Processes During Liquid Phase Transmission Electron Microscopy. *MRS Bull.* **2020**, *45*, 746–753.
54. Lifshitz, I.M.; Slyozov, V.V. The Kinetics of Precipitation from Supersaturated Solid Solutions. *J. Phys. Chem. Solids* **1961**, *19*, 35–50.
55. Viswanatha, R.; Sapra, S.; Satpati, B.; Satyam, P.V.; Dev, B.N.; Sarma, D.D. Understanding the Quantum Size Effects in ZnO Nanocrystals. *J. Mater. Chem.* **2004**, *14*, 661–668.
56. Sholl, D.S.; Skodje, R.T. Late-Stage Coarsening of Adlayers by Dynamic Cluster Coalescence. *Phys. A* **1996**, *231*, 631–647.
57. Meakin, P. Diffusion-Limited Droplet Coalescence. *Phys. A* **1990**, *165*, 1–18.
58. Viswanatha, R.; Sarma, D. D. Growth of Nanocrystals in Solution. In *Nanomaterials Chemistry: Recent Developments and New Directions*; Rao, C.N.R., Müller, A., Cheetham, A.K., Eds.; Verlag GmbH & Co. KGaA: Weinheim, Germany, 2007; pp. 139–170.

Materials and Interfaces

Perspective

Steady-State Synthesis of Colloidal Metal Nanocrystals

Jianlong He [1,†], Hansong Yu [2,†], and Younan Xia [1,3,*]

[1] School of Chemistry and Biochemistry, Georgia Institute of Technology, Atlanta, GA 30332, USA
[2] School of Materials Science and Engineering, Georgia Institute of Technology, Atlanta, GA 30332, USA
[3] The Wallace H. Coulter Department of Biomedical Engineering, Georgia Institute of Technology and Emory University, Atlanta, GA 30332, USA
* Correspondence: younan.xia@bme.gatech.edu
† These authors contributed equally to this work.
Received: 19 March 2025; Revised: 21 April 2025; Accepted: 25 April 2025; Published: 20 June 2025

Abstract: Despite remarkable progress, colloidal synthesis of metal nanocrystal is still far away from reaching the goal for robust, reproducible, and scalable production. Even with the adoption of seed-mediated growth, the synthesis can still be complicated by issues such as self-nucleation, galvanic replacement, stochastic symmetry reduction, and unwanted compositional variation. All these issues can be addressed by switching to steady-state synthesis characterized by a slow, constant, and tightly controlled reduction rate. Steady-state synthesis can be achieved by adding one reactant dropwise while using the other reactant in large excess, but this method is not suitable for scale-up production in a continuous flow reactor. There is a pressing need to develop alternative methods capable of establishing the steady-state kinetics characteristic of dropwise addition while introducing both reactants by one-shot injection. In this Perspective, we discuss a number of methods that allow for both one-shot injection and steady-state synthesis.

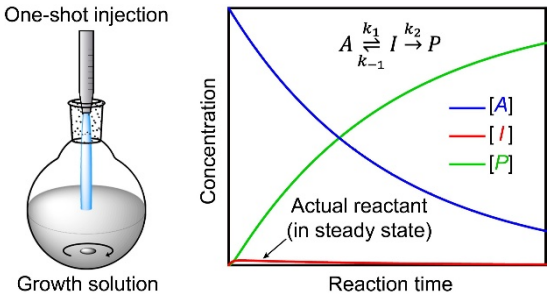

Keywords: metal nanocrystals; colloidal synthesis; steady-state kinetics; one-shot injection; scalable production

1. Introduction

The last two decades have witnessed the development of many methods capable of producing colloidal metal nanocrystals with uniform sizes and diverse shapes [1–4]. These nanocrystals not only provide a well-defined system to investigate the structure-property relationship [5–7], but also offer opportunities for applications in catalysis, plasmonics, electronics, and medicine [8–14]. Owing to their well-defined surface structures, in particular, these nanocrystals are causing a paradigm shift in an array of catalytic applications for energy conversion (as exemplified by fuel cells and water splitting devices), environmental protection, as well as production of chemicals, pharmaceuticals, and agrochemicals [15–20]. As an immediate advantage over the conventional catalysts based upon poorly-defined nanoparticles, these nanocrystals offer a viable platform to optimize their catalytic performance by maximizing the proportion of the most active and/or selective facets on the surface. For example, the area-specific activities of Pt and Pt_3Ni alloy toward oxygen reduction were enhanced by two and nine folds, respectively, by switching from cubic to octahedral nanocrystals to maximize the proportion of {111} facets on the surface [21–23]. In the case of benzene hydrogenation, only cyclohexene was formed on Pt nanocubes encased by {100} facets while both cyclohexane and cyclohexene were produced on Pt cuboctahedral nanocrystals covered by a mix of {111} and {100} facets [7]. These and many other examples demonstrate the promise held by shape control in augmenting the merits of metal nanocrystals for a spectrum of catalytic applications, both existing and emerging.

Despite recent progress, shape-controlled synthesis of metal nanocrystals is yet to reach the ultimate goal for robust, reproducible, and scalable production. Even with the adoption of seed-mediated growth [24], the products can still become out of control due to the involvement of self-nucleation and/or stochastic symmetry reduction. Recent studies suggest that these issues can be addressed by achieving and keeping the reduction kinetics in a steady state characterized by a constant and relatively slow reduction rate [25,26]. In this case, self-nucleation can

be suppressed by slowing down the reduction kinetics and thus maintaining the atom concentration at a level below the threshold for homogeneous nucleation. A constant reduction rate is also advantageous for tightly controlling heterogeneous nucleation and growth. Under steady-state kinetics, for example, the reduction rate can be tuned to different levels, enabling a tight control over the pattern of symmetry reduction.

Owing to its ability to achieve steady-state kinetics, introducing the reactant solution dropwise rather than in one shot has emerged as a powerful tool for a number of synthetic tasks [27,28]. However, it should be noted that dropwise synthesis is not suitable for high-throughput or scale-up production because of the necessity to continuously add the reactant into a reaction system throughout the synthesis and thus the incompatibility with the setting of a continuous flow reactor [29]. There is a pressing need to develop alternative methods capable of achieving the steady-state kinetics characteristic of dropwise addition while introducing the reactant by one-shot injection. Such methods hold the key to the deterministic, reliable, and scalable production of colloidal metal nanocrystals with controllable shapes and related properties.

Building on the principles of chemical kinetics, this perspective examines the feasibility and underlying mechanism to accomplish steady-state synthesis of colloidal metal nanocrystals while the reactants are introduced in one shot. The essence to achieve steady-state kinetics is to keep one of the reactants (e.g., the metal ion) at a stable, relatively low level while the other reactant (e.g., the reductant) is used in large excess so its concentration will stay at the same level during the entire synthesis. Specifically, we discuss the use of consecutive reactions to help maintain the reactant of interest at a stable, relatively low level by balancing the rates for its formation and consumption. Typical examples include (*i*) the use of ascorbic acid (or another weak acid) as a reductant, with its dissociated form (i.e., the actual reductant) existing in an equilibrium with the acid directly added into a synthesis; (*ii*) the use of an insoluble salt, with the metal ions (to be reduced to atoms) existing in an equilibrium with the powder added into a synthesis; (*iii*) the use of an unreactive metal complex, with the metal ions (to be reduced to atoms existing in an equilibrium with the complex directly added into a synthesis; and (*iv*) the use of a controlled-release system, where the metal ion or reductant is slowly released and immediately consumed to keep its concentration in a steady state. It is hoped this perspective can serve as a framework for guiding the future synthesis of colloidal metal nanocrystals under steady-state kinetics by providing both practical strategies and mechanistic rationale for their stable and scalable production.

2. Conventional Synthesis Involving One-Shot Injection

For a colloidal synthesis of metal nanocrystals, the reaction kinetics is governed by the second-order rate law because of the requirement for electron transfer and thus collision between the metal ion (M^{m+}) and reductant molecules [30,31]. As such, the reduction rate is directly proportional to the concentrations of both the metal ion and reductant, and it is expected to decay over time as both reactants are continually consumed. As a common practice, one of the two reactants is often used in large excess relative to the other one, so its concentration remains largely fixed during the synthesis. If the reductant is used in large excess, for example, the reduction kinetics can be approximated to follow the pseudo-first-order rate law with regard to the metal ion [32]:

$$R = -\mathrm{d}[M^{m+}]/\mathrm{d}t = k\cdot[M^{m+}], \tag{21}$$

where k is the rate constant, whose magnitude depends on the coordination ligand binding to the metal ion, the type and concentration of the reductant, as well as the number of active sites on the surface of the growing nanocrystals (or preformed seeds added into the reaction mixture). Upon integration, we obtain:

$$[M^{m+}] = [M^{m+}]_0\cdot e^{-kt}, \tag{22}$$

with $[M^{m+}]_0$ being the initial concentration of the metal ion. The instantaneous reduction rate can be written as:

$$R = k\,[M^{m+}]_0\cdot e^{-kt}. \tag{23}$$

In a conventional synthesis, the metal ion is introduced through one-shot injection. As shown in Figure 1a, its concentration (Equation (2)) and thus the reduction rate (Equation (3)) will both undergo exponential decay as a function of time. For the scenario shown in Figure 1b, it involves a reduction rate constant of $k = 0.5$ min^{-1}. Upon injection in one shot, the concentration of the metal ion rapidly rises to 1 M, followed by an exponential decay. The half-life of this pseudo first-order reaction can be calculated as $t_{1/2} = (\ln 2)/k = 1.4$ min, indicating that half of the added metal ions will be consumed after only 1.4 min into the synthesis. The reaction will be nearly completed by $t = 10$ min as the concentration of the metal ion is approaching zero, transitioning from exponential decay to steady-state kinetics toward the end of the synthesis. Despite the establishment of a steady state toward the end of a synthesis, there is almost no growth for the nanocrystals as all the added metal ions have been consumed.

The nonlinearity of the reduction rate, as well as its strong dependence on the value of k, has a major impact on the shape and size distribution of the resultant nanocrystals and it can also cause variations to the spatial distributions of different elements in a bi- or multi-metallic system [33]. For example, when synthesizing bimetallic alloy nanocrystals from two distinct metal salts using one-shot injection, the composition of the nanocrystals is expected to vary continuously along the growth direction, as determined by the ratio between the instantaneous reduction rates of the metal salts. At the current stage of development, it remains a challenge to control the compositions of nanocrystals comprised of two or more metals. The issues noted above can be addressed by conducting the synthesis under steady-state kinetics, in which both the metal ion and reductant are maintained at constant concentrations throughout the synthesis.

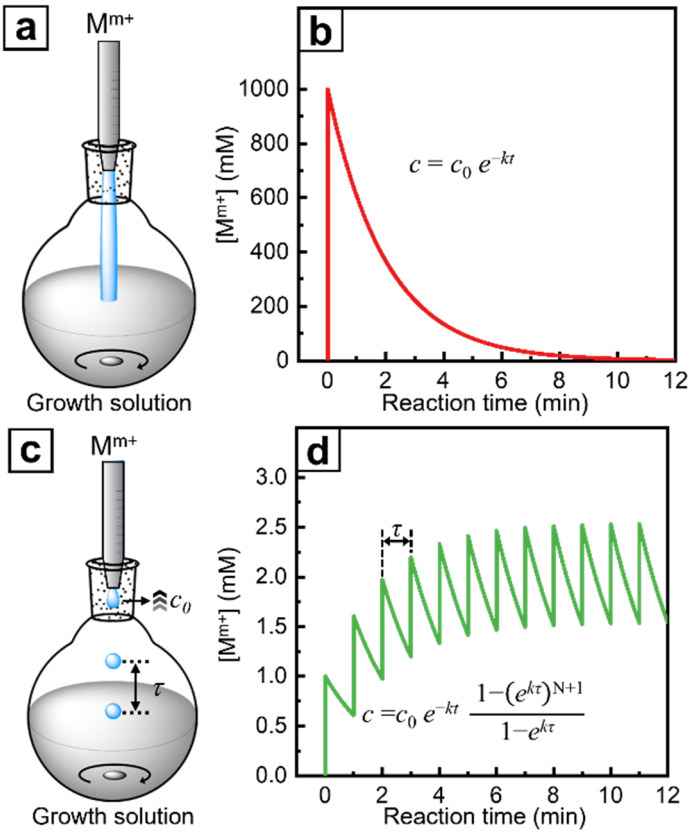

Figure 1. (**a**,**b**) Schematic of a synthesis involving one-shot injection of the metal ion and plot of its concentration as a function of time (c_0 = 1 M and k = 0.5 min^{-1}). (**c**,**d**) Schematic of a synthesis involving dropwise addition of the metal ion and plot of its concentration as a function of time (c_0 = 1 mM, k = 0.5 min^{-1}, and τ = 1 min). Note that the concentrations of the metal ion (the vertical axis), and thus the reduction rates, differ by 2–3 orders of magnitude between these two scenarios. Modified from Ref. [28] with permission.

3. Steady-State Synthesis under Dropwise Addition

One can achieve steady-state kinetics while maintaining growth by switching from one-shot injection to dropwise addition for either the metal ion or the reductant. For example, by adding a solution of the metal ion as regularly-paced droplets into a mixture containing an excess amount of the reductant (Figure 1c), it is practical to maintain the metal ion at a relatively low and stable concentration for the establishment of steady-state kinetics [26]. To simplify the analysis, we assume the solution of the metal ion is added in the form of uniform droplets at a regular pace while neglecting the slight increase in reaction volume when a droplet is introduced. As such, the reduction of the metal ion from individual droplets can be treated as independent events, with the concentration following the same exponential decay as observed in the case of one-shot injection. The addition of the first droplet contributes to a rapid increase in concentration, followed by an exponential decay, as described by Equation (2), until the second droplet arrives. The introduction of each subsequent droplet will induce a similar pattern featuring a sudden increase and then exponential decay in concentration for the metal ion. After six droplets, the concentration of the metal ion in the reaction mixture will enter a steady state. Mathematically, the concentration of the metal ion at time point t can be calculated as the sum of contributions from all the droplets added up to this point [26]:

$$c_t = c_0 \cdot e^{-kt} + c_0 \cdot e^{-k(t-\tau)} + c_0 \cdot e^{-k(t-2\tau)} + \cdots + c_0 \cdot e^{-k(t-N\tau)} = c_0 \cdot e^{-kt}\,(1 - e^{Nk\tau + k\tau})/(1 - e^{k\tau}), \quad (24)$$

where c_0 is the increase in concentration caused by one droplet of the metal ion solution; τ is the interval of time between adjacent droplets; and N (i.e., t/τ) is the total number of elapsed time intervals. According to Equation (4), c_t is determined by c_0, k, and τ, and can be calculated for any combination of c_0 and τ if k is known.

As the concentration of the metal ion continually increases, its rate of reduction also increases proportionally. This eventually leads to a steady state in which the decrease in concentration caused by reduction between two adjacent droplets is fully compensated by the increase in concentration contributed by the addition of one droplet. In the steady state, the concentration of the metal ion and thereby the reduction rate only fluctuates between two close values defined by the upper limit (c_{up}) and lower limit (c_{low}). The condition for establishing such a steady state is:

$$c_0 = c_{up} - c_{up} \cdot e^{-k\tau} = c_{up}\,(1 - e^{-k\tau}). \quad (25)$$

From Equation (5), we have the upper limit as:

$$c_{up} = c_0/(1 - e^{-k\tau}), \quad (26)$$

and the lower limit as:

$$c_{low} = c_{up} \cdot e^{-k\tau} = c_0 \cdot e^{-k\tau}/(1 - e^{-k\tau}). \quad (27)$$

The average concentration (c_{avg}) in the steady state can be calculated as the total area under the decay curve between two adjacent droplets divided by the duration of time (τ):

$$c_{avg} = \int_0^t c_{up} \cdot e^{-kt} \cdot dt/\tau = \{\int_0^t [c_0/(1 - e^{-kt})] \cdot e^{-kt} \cdot dt\}/\tau = c_0/(k \cdot \tau). \quad (28)$$

When the synthesis described in Figure 1a is switched from one-shot injection to dropwise addition, the same amount of metal ion solution is divided into 1000 droplets and added at a regular pace with τ = 1 min. As shown in Figure 1d, the concentration of the metal ion in the reaction mixture is maintained at a much lower but stable level throughout the synthesis. Upon the addition of the first droplet, the concentration reaches a low peak of 1.0 mM, equivalent to 0.1% of the concentration associated with one-shot injection. Upon adding the sixth droplet, a steady state is established, with a maximum concentration (i.e., c_{up}) of 2.5 mM. Using Equation (8), the average concentration in the steady state is calculated to be 2.0 mM, which is 400 times lower than the maximum concentration involved in one-shot synthesis. It is worth noting that dropwise addition stretches over a much longer period of 16.7 h, with 99.2% of the synthesis occurring under steady-state kinetics. In this case, the nanocrystals continually grow into larger sizes under the steady-state kinetics.

In addition to the elimination of self-nucleation and control of the pattern of symmetry reduction, steady-state kinetics holds the key to maneuvering the elemental distribution of bi- or multi-metallic nanocrystals as the spatial distributions of the elements are governed by the instantaneous reduction rates of the metal ions involved. In the steady state, the average reduction rate (R_{avg}) can be expressed as:

$$R_{avg} = k \cdot c_{avg} = c_0/\tau. \quad (29)$$

Significantly, R_{avg} is only dependent on c_0 and τ, not k. As a result, the reactivity of the metal ion becomes irrelevant in determining its reduction rate in the steady state. This unique feature of dropwise addition is instrumental in manipulating the composition of a nanocrystal as it allows for a precise control of the elemental ratio by simply adjusting the concentrations and injection frequencies of the metal ions, regardless of their difference in reactivity. This capability offers immediate advantages. For example, when k increases from 0.5 to 1.0 min^{-1}, the range of variation in reaction rate expands from 0.77–1.27 to 0.58–1.58 mM min^{-1} due to the changes in c_{up} and c_{low}. However, R_{avg} remains at 1.0 mM min^{-1}, implying that the atomic deposition rate stays unaffected despite the increase in reactivity for the metal ion. As such, if the solutions of the two metal ions are prepared with the same concentration and added into the growth solution dropwise at the same frequency, bimetallic nanocrystals with a uniform atomic ratio of 1:1 will be obtained [34].

In a preliminary study, we utilized the dropwise method to successfully synthesize nanocrystals composed of a quaternary alloy [27]. We used four acetylacetonate complexes as the metal ions for Ru, Rh, Pd, and Pt despite their large difference in reactivity. To assist nucleation and control the facets on the alloy nanocrystals, Rh nanocubes were added as the seeds. A mixture of the different complexes was introduced into the reaction system in the form of tiny droplets that contained approximately 2.2 nmol of each metal per droplet. In this way, the reduction rates of the precursors became synchronized after 1 h into the synthesis (Figure 2a), ensuring the formation of quaternary alloy nanocrystals with a homogeneous and well-controlled surface composition (Figure 2b).

In principle, the reductant can also be added dropwise, while the metal ion is supplied in large excess, to achieve steady-state synthesis. Since the metal ion is often more expensive than the reductant, it is more practical to apply dropwise addition to the metal ion rather than the reductant. Despite the ability to create steady-state kinetics, dropwise addition has a set of drawbacks. Firstly, the metal ion must be continuously added into the reaction system, making it impractical to increase the volume of production by switching from a batch to a continuous flow reactor. Secondly, about six droplets must be added before reaching the steady state. During the reduction of these first six droplets, the growth can be forced to take a specific pattern of symmetry reduction because the deposition of atoms from these six droplets on the surface can create high-energy sites to dictate the following pathway for reduction and atom deposition. Thirdly, in the steady state, the concentration of the metal ion still oscillates within a narrow range defined by c_{up} and c_{low}, and both of them are dependent on k, as shown in Equations (6) and (7). In general, one should minimize the value of k in order to reduce the range of fluctuation and thus possible variations to the spatial distributions of elements along the growth direction. Taken together, there is a need to develop one-shot injection methods capable of creating and maintaining steady-state kinetics throughout the synthesis.

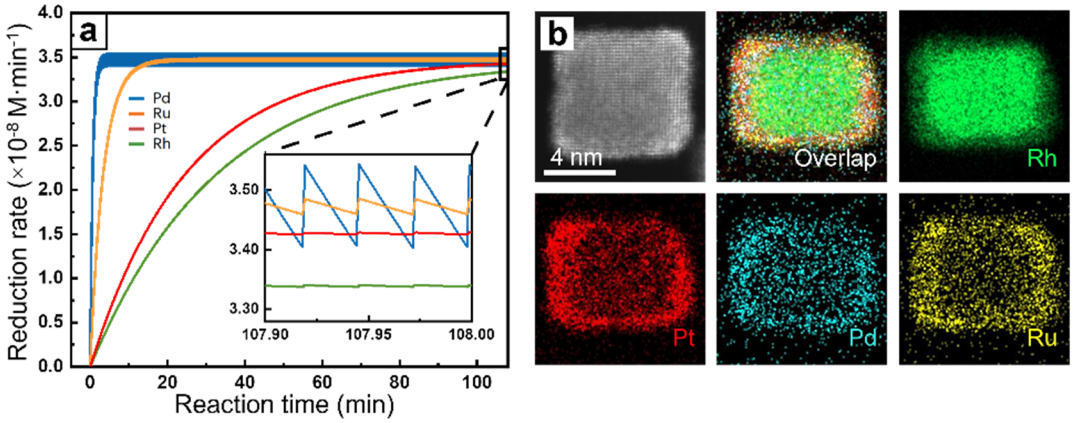

Figure 2. Controlling the composition of quaternary alloy nanocrystals through dropwise addition. (**a**) Simulated reduction rate as a function of the reaction time in the case of dropwise addition. (**b**) Scanning transmission electron microscopy image and energy-dispersive X-ray spectroscopy elemental mapping of an alloy nanocrystal, showing the uniform distributions of Rh, Pt, Pd, and Ru. Modified from Ref. [28] with permission.

4. Steady-State Synthesis under One-Shot Injection

An alternative approach to the dropwise method is to avoid directly adding the metal ion or reductant into a synthesis. Instead, a precursor to the metal ion or reductant is used. During a synthesis, the metal ion or reductant will be formed and consumed through consecutive reactions, naturally resulting in the establishment of a steady-state concentration. As an immediate advantage over dropwise addition, the precursor can be added in one shot into the reaction system at the very beginning of a synthesis, making it practical to conduct the colloidal synthesis in a continuous flow reactor.

4.1. Consecutive Reactions Involving an Equilibrium

Let us consider a situation where the metal ion or reductant exists in an equilibrium with the precursor while it is consumed through an irreversible reaction. For simplicity, we can describe this process using the following equation, with reactant A corresponding to the added precursor and intermediate I corresponding to the actual metal ion or reductant involved in the reduction reaction for the generation of product P:

$$A \underset{k_{-1}}{\overset{k_1}{\rightleftharpoons}} I \overset{k_2}{\rightarrow} P. \tag{30}$$

In this case, we can express the reaction rates as:

$$\frac{d[A]}{dt} = -k_1[A] + k_{-1}[I], \tag{31}$$

$$\frac{d[I]}{dt} = k_1[A] - k_{-1}[I] - k_2[I], \tag{32}$$

$$\frac{d[P]}{dt} = k_2[I]. \tag{33}$$

Under the condition of $k_{-1}+k_2 \gg k_1$, a steady state will be achieved, in which the concentration of intermediate *I* stays at a stable level, with essentially no change over time:

$$\frac{d[I]}{dt} \approx \mathbf{0}. \tag{34}$$

As such, Equation (12) can be rewritten as:

$$\frac{d[I]}{dt} = k_1[A] - k_{-1}[I]_{ss} - k_2[I]_{ss} \approx 0, \tag{35}$$

where $[I]_{ss}$ represents the steady-state concentration of intermediate *I*. From this equation, $[I]_{ss}$ can be derived as:

$$[I]_{ss} = \frac{k_1}{k_{-1}+k_2}[A]. \tag{36}$$

Meanwhile, Equation (11) can be written as:

$$\frac{d[A]}{dt} = -k_1[A] + k_{-1}\frac{k_1}{k_{-1}+k_2}[A] = -\frac{k_1k_2}{k_{-1}+k_2}[A]. \tag{37}$$

Upon integration, we have:

$$[A] = [A]_0 e^{-\frac{k_1k_2}{k_{-1}+k_2}t}. \tag{38}$$

In Figure 3, we plot the concentration profiles of *A*, *I*, and *P* for the case of A_0 = 100 mM, k_2 = 1, $k_1 = 5k_{-1}$, with the ratios of $k_{-1}+k_2$ to k_1 being 100, 50, 20, 10, 5, and 2, respectively. When the ratio of $k_{-1}+k_2$ to k_1 is greater than 20, the intermediate *I* can be kept at a stable, relatively low concentration throughout the synthesis, resulting in steady-state kinetics (Figure 3a–c). When the ratio is below 20, as shown in Figure 3d–f, the concentration of *I* shows a significant increase at the beginning of the synthesis, followed by an exponential decay, like the scenario of a conventional one-shot synthesis.

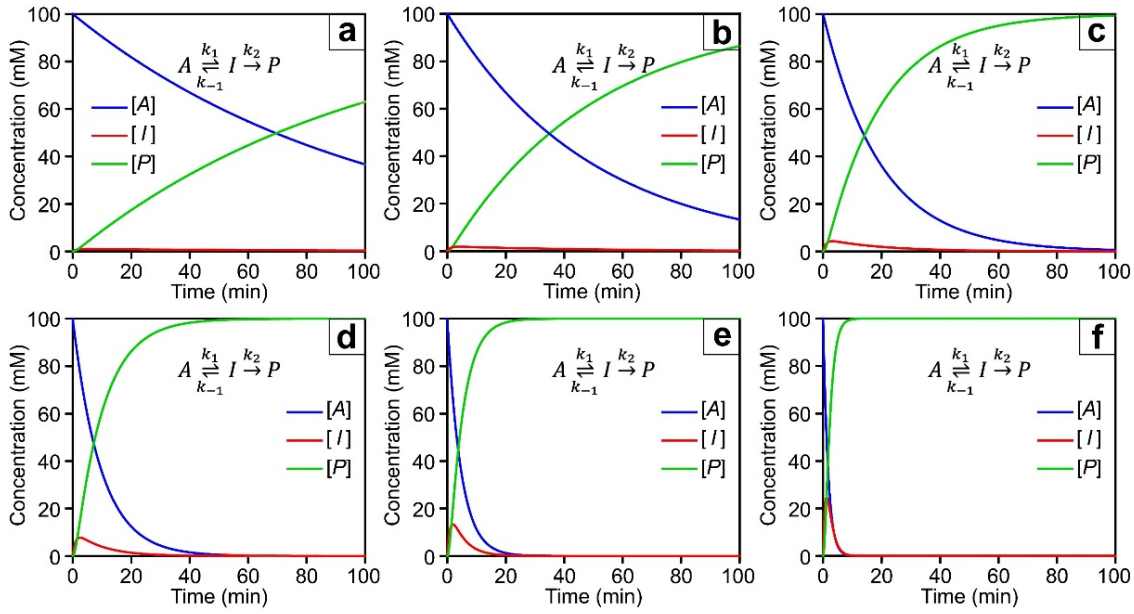

Figure 3. Plots of [*A*] (blue), [*I*] (red), and [*P*] (green) as a function of reaction time in the case of consecutive reactions involving an equilibrium, under the conditions of A_0 = 100 mM, k_2 = 1, $k_1 = 5k_{-1}$, with the ratios of $k_{-1}+k_2$ to k_1 being (**a**) 100, (**b**) 50, (**c**) 20, (**d**) 10, (**e**) 5, and (**f**) 2.

In practice, reactant *A* represents the precursor directly added into the reaction system while *I* pertaining to the actual metal ion or reductant involved in the reduction reaction. In the following sections, we discuss three different approaches that can be explored to achieve steady-state synthesis under one-shot injection by engaging consecutive reactions involving an equilibrium. In these approaches, all the reactants are added in one shot and the establishment of steady-state kinetics can be validated by analyzing the concentration of the metal ion using techniques such as inductively-coupled mass spectrometry (ICP-MS) or UV-vis spectroscopy. As a common

advantage of these approaches, it is feasible to tune the reduction rate in the steady state across a broad range that varies by several orders of magnitude.

4.1.1. Reductant from the Dissociation of a Weak Acid

Carboxylic acids are widely used as reductants in the synthesis of noble-metal nanocrystals [35]. Notable examples include ascorbic acid, citric acid, and formic acid. Upon dissolution in water, the carboxyl group quickly dissociates into carboxylate and proton ions to build an equilibrium:

$$HA \rightleftharpoons A^- + H^+. \tag{39}$$

Typically, A^- would serve as the actual reductant owning to its much stronger reducing power than *HA*. By simply controlling the pH, it is feasible to maintain the concentration of A^- and thus the reduction rate at constant levels if there is still *HA* in the reaction solution. Taking ascorbic acid (H_2Asc) as an example, we can write the consecutive reactions as follows:

$$H_2Asc \underset{k_{-1}}{\overset{k_1}{\rightleftharpoons}} HAsc^- \overset{k_2}{\rightarrow} DHA, \tag{40}$$

where *DHA* represents dehydroascorbic acid. There exists an equilibrium between H_2Asc and $HAsc^-$, while $HAsc^-$ can be subsequently oxidized to *DHA* by reacting with the metal ion. In a synthesis involving the addition of H_2Asc, $HAsc^-$ serves as the actual reductant to react with the metal ion. Regardless of the concentration of H_2Asc (added into a synthesis in one shot) in the reaction mixture, the concentration of $HAsc^-$ is determined by the dissociation constant (K_a) of H_2Asc and the pH: $[HAsc^-] = K_a/[H^+]$. When the metal ion is used in large excess and thus kept at a stable concentration, one can adjust the concentration of $HAsc^-$ to different levels for the creation of steady states with different reduction rates by simply varying the pH.

In practice, one can also vary the reduction rate constant of ascorbic acid by adjusting the pH. As shown in Figure 4, an aqueous solution of ascorbic acid is dominated by three different species, respectively, when the pH is adjusted from 0–14: acid (H_2Asc), ascorbate ($HAsc^-$), and diascorbate (Asc^{2-}) [35]. For all these forms, the reduction mechanism is similar in terms of electron transfer and the oxidized product, with each molecule donating one pair of electrons for the reduction of a metal ion and the formation of dehydroascorbate as the oxidized product. There is a distinct rate constant associated with each of these forms. As documented in literature, the rate constant (i.e., the reducing power) of ascorbic acid increases as the pH is increased [36–38], primarily due to the involvement of different dominant species. As analyzed above, steady-state kinetics can be achieved for both $HAsc^-$ and Asc^{2-}, but not for H_2Asc. In such a synthesis, it is crucial to control the pH of the reaction mixture, while maintaining the metal ion at a constant concentration, to achieve steady-state kinetics. It is worth noting that most of the synthetic protocols reported in the literature might involve steady-state kinetics albeit this concept has never been explicitly discussed.

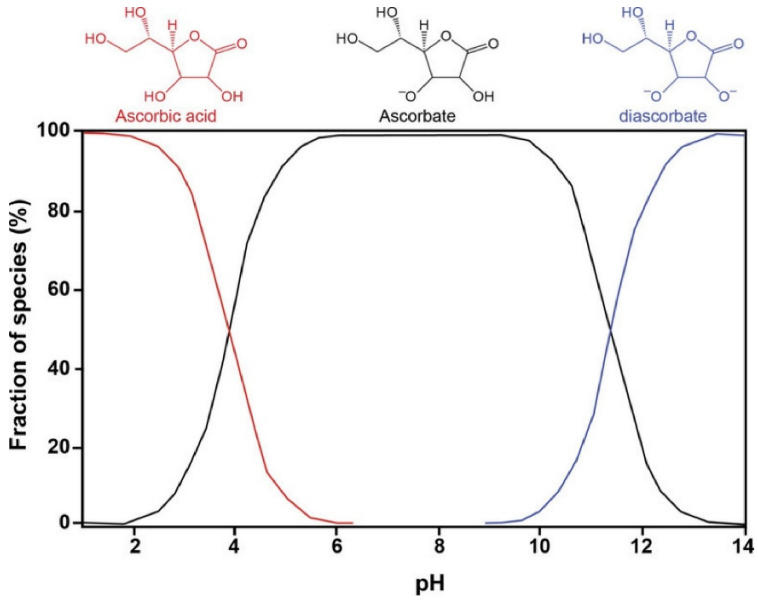

Figure 4. Graph showing the three species derived from ascorbic acid as a function of pH, including H_2Asc at pH below 3, $HAsc^-$ at pH between 6–10, Asc^{2-} at pH above 12. Modified from Ref. [35] with permission.

4.1.2. Metal Ion from the Dissolution of an Insoluble Salt

Insoluble metal salts can also be utilized to achieve steady-state synthesis due to the solubility equilibrium. When the powder of an insoluble salt is added into a reaction solution, it partially dissolves and then dissociates into metal ion and counterion to build an equilibrium:

$$ML_m(s) \rightleftharpoons M^{m+} + mL^{-}. \tag{41}$$

In this case, the consecutive reactions include the dissolution of the powder and the subsequent reduction of the metal ion, as shown below:

$$ML_m(s) \underset{k_{-1}}{\overset{k_1}{\rightleftharpoons}} M^{m+} \overset{k_2}{\rightarrow} M. \tag{42}$$

Regardless of the amount of ML_m powder added into the reaction solution, the concentration of the metal ion is only determined by the solubility product constant (K_{sp}) of ML_m and the concentration of the counterion: $[M^{m+}] = K_{sp}/[L^{-}]^m$. If the reductant is used in large excess relative to the total amount of ML_m, one can adjust the concentration of M^{m+} and thereby attain steady states with different reduction rates by varying the concentration of free L^{-} in the reaction solution. To this end, powders such as $PdCl_2$, $PdBr_2$, AgCl, AgBr, and $AuBr_3$ can all be utilized to achieve steady-state synthesis. In general, to achieve the optimal metal ion concentration in the reaction solution, a metal salt with an intermediate dissolution strength is required. It should be neither too strong to be completely soluble, nor too weak so that it can serve as a source of metal ion and maintain a stable M^{m+} concentration in the solution phase. Again, in reviewing the literature, we felt that this concept might have contributed to the success of some protocols without proper discussion. For example, AgCl and AgBr precipitates were often formed in situ during the successful synthesis of some Ag nanocrystals with controlled shapes. The formation of such precipitates might lead to the establishment of steady-state kinetics and thereby enable a tight control over the nucleation and growth. Of course, it should be pointed out that the shape control might also benefit from other mechanisms due to the accelerated photo-reduction of AgCl and AgBr in the presence of Ag seeds. A revisit to, and a systematic study of, such a synthesis is warranted.

4.1.3. Metal Ion from the Dissociation of an Unreactive Complex

Similar to the dissolution of an insoluble salt, steady-state kinetics can also be achieved using an unreactive complex by leveraging its dissociation equilibrium:

$$(ML_m)^{n+} \rightleftharpoons M^{k+} + mL^{(\frac{k-n}{m})-}. \tag{43}$$

when added into the reaction system in one shot, the complex dissociates into the metal ion (the actual precursor) and ligand, followed by reduction of the metal ion:

$$(ML_m)^{n+} \underset{k_{-1}}{\overset{k_1}{\rightleftharpoons}} M^{k+} \overset{k_2}{\rightarrow} M. \tag{44}$$

In this case, the rate constant k_1 (for the dissociation of the complex) should be considerably smaller than the sum of k_{-1} (for the reverse process of dissociation) and k_2 (for the reduction of the metal ion). By choosing an appropriate ligand, it is feasible to control the rate constants k_1 and k_{-1} to ensure $k_{-1} + k_2 \gg k_1$ and thus achievement of steady-state kinetics. For instance, switching from Cl^{-} to NH_3, a ligand with a much stronger binding to the Pd^{2+} ion, would allow for the achievement of steady-state synthesis [39].

4.2. Consecutive Reactions Involving No Equilibrium

In some cases, it is also possible to have $k_{-1} = 0$. As such, intermediate *I* is directly consumed to generate product *P* without going back to reactant *A*:

$$A \overset{k_1}{\rightarrow} I \overset{k_2}{\rightarrow} P. \tag{45}$$

We can define three reaction rates in terms of *A*, *I*, *P*, respectively, as follows:

$$\frac{d[A]}{dt} = -k_1[A], \tag{46}$$

$$\frac{d[I]}{dt} = k_1[A] - k_2[I], \tag{47}$$

$$\frac{d[P]}{dt} = k_2[I]. \tag{48}$$

Integrating $[A]$, $[I]$, $[P]$ with respect to t leads to:

$$[A] = [A]_0 e^{-k_1 t}, \tag{49}$$

$$[I] = \frac{k_1[A]_0}{k_2 - k_1}(e^{-k_1 t} - e^{-k_2 t}), \tag{50}$$

$$[P] = [A]_0[1 + \frac{1}{k_1 - k_2}(k_2 e^{-k_1 t} - k_1 e^{-k_2 t})], \tag{51}$$

In the case of $k_2 \gg k_1$, the concentration of I can be approximated as:

$$[I] \approx \frac{k_1[A]_0}{k_2}(e^{-k_1 t}) = \frac{k_1}{k_2}[A]. \tag{52}$$

In this case, intermediate I will stay at a stable, relatively low concentration, resulting in the establishment of a steady state (I_{ss}). Figure 5 shows the concentration profiles of A, I, and P calculated for the condition of $A_0 = 100$ mM, $k_2 = 1$, with the ratios of k_2 to k_1 being set to 100, 50, 20, 10, 5, and 2, respectively. If the ratio of k_2 to k_1 is greater than 20, intermediate I will stay at a stable, low concentration throughout the reaction, resulting in steady-state kinetics (Figure 5a–c). In contrast, when the ratio of k_2 to k_1 drops below 20, the concentration of intermediate I will show a surge at the beginning, followed by an exponential decay (Figure 5d–f).

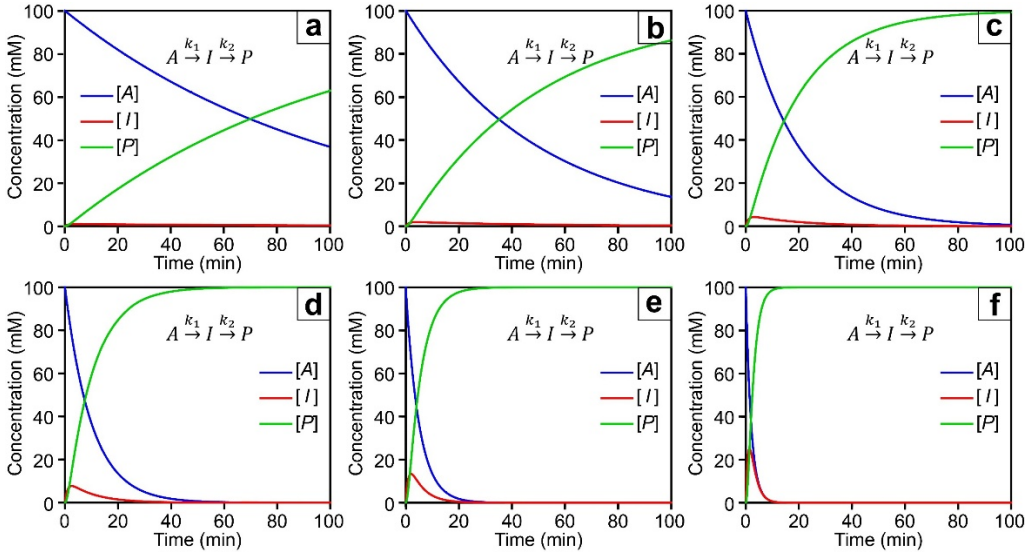

Figure 5. Plots of $[A]$ (blue), $[I]$ (red), and $[P]$ (green) as a function of reaction time in the case of consecutive irreversible reactions, under the conditions of $A_0 = 100$ mM, $k_2 = 1$, and ratios of k_2 to k_1 are (**a**) 100, (**b**) 50, (**c**) 20, (**d**) 10, (**e**) 5, and (**f**) 2, respectively.

Again, there are many good examples of such a synthesis in the literature albeit none of the reports attributed the success to the involvement of steady-state kinetics. Here we choose polyol synthesis as an example to demonstrate the concept. Polyol synthesis has been widely utilized for the production of colloidal noble-metal nanocrystals with controllable shapes [40]. Notable examples include Ag nanowires, nanocubes, and right bipyramids, as well as Au polyhedrons [41–44]. The key feature is the use of a polyol such as ethylene glycol as both the solvent and a precursor to the actual reductant. When heated in air to an elevated temperature, ethylene glycol will be partially oxidized to glycoaldehyde, an intermediate believed to be the reductant responsible for the reduction of metal ion [45]:

$$\text{Ethylene glycol} \xrightarrow{k_1} \text{Glycoaldehyde} \xrightarrow{k_2} \text{Carboxylic acid}. \tag{53}$$

This process involves two consecutive reactions: the slow oxidation of ethylene glycol to glycoaldehyde by the oxygen from air and the subsequent fast oxidation of the glycoaldehyde by the metal ion. Under the condition of $k_2 \gg k_1$, glycoaldehyde is expected to exist at a stable, relatively low concentration throughout the synthesis. Although it was not explicitly discussed in the literature, the steady-state kinetics seems to be responsible for the control of both nucleation and growth and thereby the twin structure and shape taken by the nanocrystals. Taking

the synthesis of Ag nanowire as a sample, $AgNO_3$ can be directly added in one shot into ethylene glycol held at an elevated temperature for the nucleation of decahedral seeds, followed by their growth into penta-twinned Ag nanowires [46–48]. In this process, the Ag^+ ions from $AgNO_3$ can be reduced slowly even at a relatively high concentration for the generation of penta-twinned seeds while preventing self-nucleation and unwanted growth.

4.3. Controlled Release of the Reactant from Polymer Beads

In nanomedicine, drugs are often encapsulated in carriers such as polymer beads to achieve zero-order release, by which the drug molecules come out at a constant rate to minimize the fluctuation in plasma concentration while maintaining the plasma drug level in the therapeutic window throughout a treatment, giving the highest therapeutic efficacy [49]. This concept can also be borrowed to achieve steady-state synthesis by pre-loading the metal ion or reductant in polymer beads. As shown in Figure 6, the pre-loaded metal ions undergo a controlled release process from polymer beads into the reaction mixture, followed by reduction into metal atoms. In this process, the slow release of metal ions corresponds to a small release rate constant (k_1), which can be made smaller than the reduction rate constant (k_2), leading to the establishment of steady-state kinetics. In principle, different polymers, such as poly(lactic-co-glycolic acid) of varying compositions can be used to help control the release profile, thereby controlling the magnitude of k_1 [50]. Altogether, it is feasible to maintain the concentration of the metal ion in the reaction mixture at a small and stable by optimizing the release rate constant and/or the reduction rate constant for the establishment of steady states with different rates.

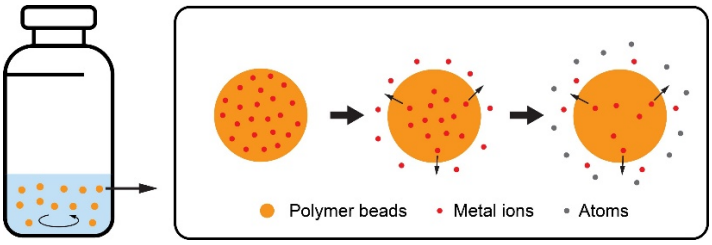

Figure 6. Schematic illustration showing the controlled release of metal ions from polymer beads during a steady-state synthesis of colloidal metal nanocrystals.

5. Concluding Remarks

Achieving robust, reproducible, and scalable production of colloidal metal nanocrystals calls for new methods capable of establishing and maintaining steady-state kinetics in the setting of one-shot injection and continuous flow reactor. The essence is to keep one of the reactants at a stable, relatively low level while the other reactant is used in large excess so the reduction rate will stay at the same level during the entire synthesis. A number of methods are discussed in this Perspective. In the first method, we can leverage the dissociation equilibrium of a weak acid to help maintain the actual reductant at a constant level throughout a synthesis. A notable example is ascorbic acid, whose conjugated bases have much stronger reducing powers than that of the acid. By leveraging the dissociation equilibrium and varying the pH of the reaction solution, we can control the base (the actual reductant) and its concentration at different levels until all the added acid has been consumed. In the second method, we can use an insoluble salt to ensure that the metal ion (the actual precursor) in reaction solution will stay at a constant level controlled by temperature and the concentration of free counterion until all the solid is consumed. In the third method, we can borrow the concept of controlled release from drug delivery by loading the metal ion or reductant in polymer beads. Under zero-order release, the metal ion or reductant in the reaction mixture can be maintained at a low and constant level because it will be immediately consumed as soon as it has been released from the beads. When the other reactant is used in excess, all these methods can be used to achieve steady-state synthesis. In principle, the knowledge gained from the monometallic system can be readily extended to bi- and even multi-metallic systems.

Steady-state synthesis offers immediate advantages over the conventional synthesis that involves reduction rates in an exponential decay. For example, by controlling the reduction rate in the steady state, self-nucleation can be eliminated in the presence of seeds while controlling the pattern of growth, moving toward a reliable, reproducible, and precise synthesis of colloidal nanocrystals. At the moment, steady-state synthesis is mainly achieved through the dropwise addition of the metal salt solution, but this method is not suitable for scale-up production in a continuous flow reactor because of the necessity to continuously add the precursor solution during a synthesis. The methods discussed in this Perspective are capable of achieving steady-state kinetics under one-shot injection, making it practical to directly translate the synthetic method from a batch to a continuous flow

reactor. To our knowledge, all these methods are yet to be explored. They hold the key to the deterministic, reliable, and scalable production of colloidal metal nanocrystals with well-controlled properties.

Author Contributions: Y.X. conceived the concept; J.H. and H.Y. prepared the manuscript and Y.X. revised the writing. All authors have read and agreed to the published version of the manuscript.

Funding: This work was supported in part by research grants from the NSF (CHE-2105602, CBET-2219546, and DMR 2333595), as well as startup funds from the Georgia Institute of Technology.

Data Availability Statement: Not applicable.

Conflicts of Interest: The authors declare no conflict of interest.

References

1. Sun, S.; Murray, C.B.; Weller, D.; Folks, L.; Moser, A. Monodisperse FePt Nanoparticles and Ferromagnetic FePt Nanocrystal Superlattices. *Science* **2000**, *287*, 1989–1992.
2. Jin, R.; Cao, Y.; Mirkin, C.A.; Kelly, K.L.; Schatz, G.C.; Zheng, J.G. Photoinduced Conversion of Silver Nanospheres to Nanoprisms. *Science* **2001**, *294*, 1901–1903.
3. Xia, Y.; Xiong, Y.; Lim, B.; Skrabalak, S.E. Shape-Controlled Synthesis of Metal Nanocrystals: Simple Chemistry Meets Complex Physics? *Angew. Chem. Int. Ed.* **2009**, *48*, 60–103.
4. Nguyen, Q.N.; Wang, C.; Shang, Y.; Janssen, A.; Xia, Y. Colloidal Synthesis of Metal Nanocrystals: From Asymmetrical Growth to Symmetry Breaking. *Chem. Rev.* **2023**, *123*, 3693–3760.
5. Quan, Z.; Wang, Y.; Fang, J. High-Index Faceted Noble Metal Nanocrystals. *Acc. Chem. Res.* **2013**, *46*, 191–202.
6. Sherry, L.J.; Chang, S.-H.; Schatz, G.C.; Van Duyne, R.P.; Wiley, B.J.; Xia, Y. Localized Surface Plasmon Resonance Spectroscopy of Single Silver Nanocubes. *Nano Lett.* **2005**, *5*, 2034–2038.
7. Bratlie, K.M.; Lee, H.; Komvopoulos, K.; Yang, P.; Somorjai, G.A. Platinum Nanoparticle Shape Effects on Benzene Hydrogenation Selectivity. *Nano Lett.* **2007**, *7*, 3097–3101.
8. Guo, S.; Zhang, S.; Sun, S. Tuning Nanoparticle Catalysis for the Oxygen Reduction Reaction. *Angew. Chem. Int. Ed.* **2013**, *52*, 8526–8544.
9. Shi, Y.; Lyu, Z.; Zhao, M.; Chen, R.; Nguyen, Q.N.; Xia, Y. Noble-Metal Nanocrystals with Controlled Shapes for Catalytic and Electrocatalytic Applications. *Chem. Rev.* **2021**, *121*, 649–735.
10. Rathmell, A.R.; Bergin, S.M.; Hua, Y.; Li, Z.; Wiley, B.J. The Growth Mechanism of Copper Nanowires and Their Properties in Flexible, Transparent Conducting Films. *Adv. Mater.* **2010**, *22*, 3558–3563.
11. Li, M.; Zhao, Z.; Cheng, T.; Fortunelli, A.; Chen, C.-Y.; Yu, R.; Zhang, Q.; Gu, L.; Merinov, B.V.; Lin, Z.; et al. Ultrafine Jagged Platinum Nanowires Enable Ultrahigh Mass Activity for the Oxygen Reduction Reaction. *Science* **2016**, *354*, 1414–1419.
12. Burda, C.; Chen, X.; Narayanan, R.; El-Sayed, M.A. Chemistry and Properties of Nanocrystals of Different Shapes. *Chem. Rev.* **2005**, *105*, 1025–1102.
13. Jones, M.R.; Osberg, K.D.; Macfarlane, R.J.; Langille, M.R.; Mirkin, C.A. Templated Techniques for the Synthesis and Assembly of Plasmonic Nanostructures. *Chem. Rev.* **2011**, *111*, 3736–3827.
14. Wang, Y.; Black, K.C.L.; Luehmann, H.; Li, W.; Zhang, Y.; Cai, X.; Wan, D.; Liu, S.-Y.; Li, M.; Kim, P.; et al. Comparison Study of Gold Nanohexapods, Nanorods, and Nanocages for Photothermal Cancer Treatment. *ACS Nano* **2013**, *7*, 2068–2077.
15. Linic, S.; Christopher, P.; Ingram, D.B. Plasmonic-Metal Nanostructures for Efficient Conversion of Solar to Chemical Energy. *Nat. Mater.* **2011**, *10*, 911–921.
16. Lee, I.; Delbecq, F.; Morales, R.; Albiter, M.A.; Zaera, F. Tuning Selectivity in Catalysis by Controlling Particle Shape. *Nat. Mater.* **2009**, *8*, 132–138.
17. Reske, R.; Mistry, H.; Behafarid, F.; Roldan Cuenya, B.; Strasser, P. Particle Size Effects in the Catalytic Electroreduction of CO_2 on Cu Nanoparticles. *J. Am. Chem. Soc.* **2014**, *136*, 6978–6986.
18. Singh, A.R.; Rohr, B.A.; Schwalbe, J.A.; Cargnello, M.; Chan, K.; Jaramillo, T.F.; Chorkendorff, I.; Nørskov, J.K. Electrochemical Ammonia Synthesis—The Selectivity Challenge. *ACS Catal.* **2017**, *7*, 706–709.
19. Kang, Y.; Li, M.; Cai, Y.; Cargnello, M.; Diaz, R.E.; Gordon, T.R.; Wieder, N.L.; Adzic, R.R.; Gorte, R.J.; Stach, E.A.; et al. Heterogeneous Catalysts Need Not Be so "Heterogeneous": Monodisperse Pt Nanocrystals by Combining Shape-Controlled Synthesis and Purification by Colloidal Recrystallization. *J. Am. Chem. Soc.* **2013**, *135*, 2741–2747.
20. Kline, T.R.; Paxton, W.F.; Mallouk, T.E.; Sen, A. Catalytic Nanomotors: Remote-Controlled Autonomous Movement of Striped Metallic Nanorods. *Angew. Chem. Int. Ed.* **2005**, *44*, 744–746.

21. Choi, S.-I.; Xie, S.; Shao, M.; Odell, J.H.; Lu, N.; Peng, H.-C.; Protsailo, L.; Guerrero, S.; Park, J.; Xia, X.; et al. Synthesis and Characterization of 9 nm Pt–Ni Octahedra with a Record High Activity of 3.3 A/mg$_{Pt}$ for the Oxygen Reduction Reaction. *Nano Lett.* **2013**, *13*, 3420–3425.
22. Zhang, J.; Yang, H.; Fang, J.; Zou, S. Synthesis and Oxygen Reduction Activity of Shape-Controlled Pt_3Ni Nanopolyhedra. *Nano Lett.* **2010**, *10*, 638–644.
23. Xie, M.; Shen, M.; Chen, R.; Xia, Y. Development of Highly-Active Catalysts toward Oxygen Reduction by Controlling the Shape and Composition of Pt–Ni Nanocrystals. *ACS Appl. Mater. Interfaces* **2023**, *15*, 49146–49153.
24. Xia, Y.; Gilroy, K.D.; Peng, H.-C.; Xia, X. Seed-Mediated Growth of Colloidal Metal Nanocrystals. *Angew. Chem. Int. Ed.* **2017**, *56*, 60–95.
25. Zhang, H.; Li, W.; Jin, M.; Zeng, J.; Yu, T.; Yang, D.; Xia, Y. Controlling the Morphology of Rhodium Nanocrystals by Manipulating the Growth Kinetics with a Syringe Pump. *Nano Lett.* **2011**, *11*, 898–903.
26. Peng, H.-C.; Park, J.; Zhang, L.; Xia, Y. Toward a Quantitative Understanding of Symmetry Reduction Involved in the Seed-Mediated Growth of Pd Nanocrystals. *J. Am. Chem. Soc.* **2015**, *137*, 6643–6652.
27. Wang, C.; Huang, Z.; Ding, Y.; Xie, M.; Chi, M.; Xia, Y. Facet-Controlled Synthesis of Platinum-Group-Metal Quaternary Alloys: The Case of Nanocubes and {100} Facets. *J. Am. Chem. Soc.* **2023**, *145*, 2553–2560.
28. Wang, C.; He, J.; Xia, Y. Controlling the Composition and Elemental Distribution of Bi- and Multi-Metallic Nanocrystals via Dropwise Addition. *Nat. Synth.* **2024**, *3*, 1076–1082.
29. Niu, G.; Ruditskiy, A.; Vara, M.; Xia, Y. Toward Continuous and Scalable Production of Colloidal Nanocrystals by Switching from Batch to Droplet Reactors. *Chem. Soc. Rev.* **2015**, *44*, 5806–5820.
30. Zhou, M.; Wang, H.; Vara, M.; Hood, Z.D.; Luo, M.; Yang, T.-H.; Bao, S.; Chi, M.; Xiao, P.; Zhang, Y.; et al. Quantitative Analysis of the Reduction Kinetics Responsible for the One-Pot Synthesis of Pd–Pt Bimetallic Nanocrystals with Different Structures. *J. Am. Chem. Soc.* **2016**, *138*, 12263–12270.
31. Luty-Błocho, M.; Pacławski, K.; Wojnicki, M.; Fitzner, K. The Kinetics of Redox Reaction of Gold(III) Chloride Complex Ions with L-Ascorbic Acid. *Inorg. Chim. Acta* **2013**, *395*, 189–196.
32. Corbett, J.F. Pseudo First-Order Kinetics. *J. Chem. Educ.* **1972**, *49*, 663.
33. Yang, T.-H.; Gilroy, K.D.; Xia, Y. Reduction Rate as a Quantitative Knob for Achieving Deterministic Synthesis of Colloidal Metal Nanocrystals. *Chem. Sci.* **2017**, *8*, 6730–6749.
34. Smith, J.H.; Luo, Q.; Millheim, S.L.; Millstone, J.E. Decoupling Intrinsic Metal Ion Reduction Rates from Structural Outcomes in Multimetallic Nanoparticles. *J. Am. Chem. Soc.* **2024**, *146*, 34822–34832.
35. Rodrigues, T.S.; Zhao, M.; Yang, T.-H.; Gilroy, K.D.; da Silva, A.G.M.; Camargo, P.H.C.; Xia, Y. Synthesis of Colloidal Metal Nanocrystals: A Comprehensive Review on the Reductants. *Chem. Eur. J.* **2018**, *24*, 16944–16963.
36. Zhang, H.; Lu, Y.; Liu, H.; Fang, J. Controllable Synthesis of Three-Dimensional Branched Gold Nanocrystals Assisted by Cationic Surfactant Poly(Diallyldimethylammonium) Chloride in Acidic Aqueous Solution. *RSC Adv.* **2014**, *4*, 36757–36764.
37. Lee, H.; Habas, S.E.; Somorjai, G.A.; Yang, P. Localized Pd Overgrowth on Cubic Pt Nanocrystals for Enhanced Electrocatalytic Oxidation of Formic Acid. *J. Am. Chem. Soc.* **2008**, *130*, 5406–5407.
38. Wilkins, P.C.; Johnson, M.D.; Holder, A.A.; Crans, D.C. Reduction of Vanadium(V) by L-Ascorbic Acid at Low and Neutral pH: Kinetic, Mechanistic, and Spectroscopic Characterization. *Inorg. Chem.* **2006**, *45*, 1471–1479.
39. Yu, H.; He, J.; Li, K.K.; Huang, Q.; Ding, Y.; Xia, Y. Synthesis of Ag@Pd Nanocubes and Pd-Based Nanoframes via One-Shot Injection of a Halide-Free Precursor for Continuous Production in a Flow Reactor. *Chem. Eur. J.* **2025**, *31*, e202500201.
40. Fiévet, F.; Ammar-Merah, S.; Brayner, R.; Chau, F.; Giraud, M.; Mammeri, F.; Peron, J.; Piquemal, J.-Y.; Sicard, L.; Viau, G. The Polyol Process: A Unique Method for Easy Access to Metal Nanoparticles with Tailored Sizes, Shapes and Compositions. *Chem. Soc. Rev.* **2018**, *47*, 5187–5233.
41. Sun, Y.; Xia, Y. Shape-Controlled Synthesis of gold and silver nanoparticles. *Science* **2002**, *298*, 2176–2179.
42. Zhang, D.; Chen, Y.; Huang, Y.-S.; Huang, Q.; Kwan Li, K.; Xia, Y. Robust, Reproducible, and Scalable Synthesis of Silver Nanocubes. *Chem. Eur. J.* **2024**, *30*, e202400833.
43. Wiley, B.J.; Xiong, Y.; Li, Z.-Y.; Yin, Y.; Xia, Y. Right Bipyramids of Silver: A New Shape Derived from Single Twinned Seeds. *Nano Lett.* **2006**, *6*, 765–768.
44. Wiley, B.J.; Sun, Y.; Xia, Y. Synthesis of Silver Nanostructures with Controlled Shapes and Properties. *Acc. Chem. Res.* **2007**, *40*, 1067–1076.
45. Skrabalak, S.E.; Wiley, B.J.; Kim, M.; Formo, E.V.; Xia, Y. On the Polyol Synthesis of Silver Nanostructures: Glycolaldehyde as a Reducing Agent. *Nano Lett.* **2008**, *8*, 2077–2081.
46. Sun, Y.; Gates, B.; Mayers, B.; Xia, Y. Crystalline Silver Nanowires by Soft Solution Processing. *Nano Lett.* **2002**, *2*, 165–168.

47. Sun, Y.; Mayers, B.; Herricks, T.; Xia, Y. Polyol Synthesis of Uniform Silver Nanowires: A Plausible Growth Mechanism and the Supporting Evidence. *Nano Lett.* **2003**, *3*, 955–960.
48. Korte, K.E.; Skrabalak, S.E.; Xia, Y. Rapid Synthesis of Silver Nanowires through a CuCl- or $CuCl_2$-Mediated Polyol Process. *J. Mater. Chem.* **2008**, *18*, 437–441.
49. Chan, J.M.; Zhang, L.; Yuet, K.P.; Liao, G.; Rhee, J.-W.; Langer, R.; Farokhzad, O.C. PLGA–Lecithin–PEG Core–Shell Nanoparticles for Controlled Drug Delivery. *Biomaterials* **2009**, *30*, 1627–1634.
50. Fredenberg, S.; Wahlgren, M.; Reslow, M.; Axelsson, A. The Mechanisms of Drug Release in Poly(Lactic-Co-Glycolic Acid)-Based Drug Delivery Systems—A Review. *Int. J. Pharm.* **2011**, *415*, 34–52.

Article

Carbon Monoxide-Assisted Synthesis of Nickel Cobalt Phosphide Nanorods for the Hydrogen Evolution Reaction

Sarah York [1], Zachary R. Mansley [2,3], Feng Wang [1], Yimei Zhu [3], and Jingyi Chen [1,*]

[1] Department of Chemistry and Biochemistry, University of Arkansas, Fayetteville, AR 72701, USA
[2] Interdisciplinary Science Department, Brookhaven National Laboratory, Upton, NY 11973, USA
[3] Condensed Matter Physics and Materials Science Department, Brookhaven National Laboratory, Upton, NY 11973, USA
* Correspondence: chenj@uark.edu

Received: 23 April 2025; Revised: 7 June 2025; Accepted: 11 June 2025; Published: 20 June 2025

Abstract: The development of efficient and cost-effective catalysts for hydrogen evolution reaction (HER) is crucial for the advancement of electrochemical water splitting technology. Here, we report a novel synthetic method for the preparation of single-crystalline NiCoP nanorods with tunable aspect ratios using a carbon monoxide (CO)-assisted, trioctylphosphine (TOP)-mediated approach. The introduction of CO gas at different temperatures allows for the control of the nanorod growth, resulting in various aspect ratios while maintaining a hexagonal crystal structure and a composition of 1:1 Ni/Co as NiCoP. Our results demonstrate that the NiCoP nanorods with higher aspect ratios exhibit improved HER activity and stability, with the highest aspect ratio nanorods showing the lowest overpotential and Tafel slope in both acidic and alkaline media. This study highlights the importance of controlling the size and morphology of bimetallic phosphide nanoparticles to optimize their catalytic activity for HER, providing new insights into the design and optimization of nanostructured catalysts for electrochemical water splitting applications.

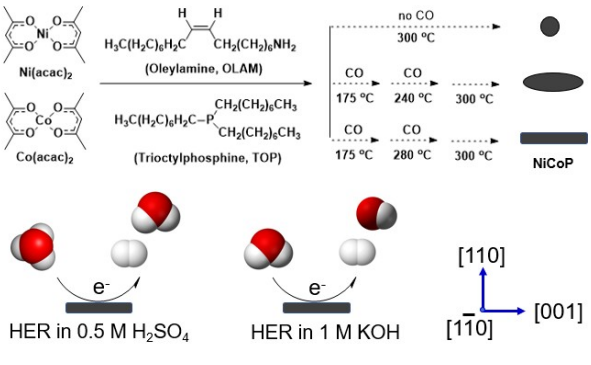

Keywords: CO; NiCoP; nanorods; DFT; HER

1. Introduction

Transition metal phosphides have emerged as a promising class of catalysts in various industrial applications, including water splitting for hydrogen production [1–5], biomass hydrogenation or hydrodeoxygenation [6], as well as energy conversion and storage [7,8]. Their exceptional properties and abundance make them attractive alternatives to precious metals in these applications, allowing for lower costs. Notably, transition metal phosphides have been extensively explored for the hydrogen evolution reaction (HER) since the seminal work of one of the nickel phosphides (Ni_2P) as an alternative to Pt for HER reported by Schaak and Lewis in 2013 [9]. Studies have demonstrated the importance of controlling the size and morphology of nickel phosphide nanoparticles to optimize their catalytic activity for HER [5]. For example, one-dimensional (1D) nanostructures, such as nanorods and nanowires, have been demonstrated to exhibit enhanced HER activity [10–13]. Theoretical calculations have shown that the nickel bridge sites on the surface of the long side of the 1D nanostructures, which grow along the [001] direction of the hexagonal Ni_2P, exhibit lower Tafel slopes for HER compared to the (001) facet [10]. Other studies have provided evidence that 1D Ni_2P can expose a Ni_3P_2 surface, generated during HER, as active sites, or offer the possibility of tuning the surface roughness to enhance HER [11].

On the other hand, adding a secondary metal to create bimetallic phosphides has resulted in significantly improved catalytic activity, often surpassing that of their monometallic counterparts [14,15]. The enhanced performance is thought to stem from synergistic electronic and structural modifications that alter the characteristics of the active sites. $Ni_xCo_yP_z$ is one of the most active catalysts, as predicted by theoretical calculations and confirmed by the experimental results [14,15]. A composition study of $Ni_{2-x}Co_xP$ ($0 \leq x \leq 2$) nanocrystals for HER

showed that these electrocatalysts exhibited enhanced activity, with NiCoP showing particularly promising performance and excellent long-term stability [16]. Building on these findings, this work focuses on the synthesis of the NiCoP nanorods using a CO-assisted, trioctylphosphine (TOP)-mediated method, and investigates the effects of aspect ratios on the HER electrocatalytic activity.

The TOP-mediated synthesis is a solution-based method of metal phosphides involving TOP as the phosphorus source. Back in the early 2000s, TOP and trioctylphosphine oxide (TOPO) were used for the synthesis of iron phosphides nanorods and nanowires by Liu and coworkers [17]. The method was generalized to several mono-metal phosphide nanorods including MnP, Co_2P, FeP, and Ni_2P by Hyeon and coworkers [18]. Some of the progress was later summarized by Brock and coworkers for the synthesis of MnP, FeP, and Fe_2P with their magnetic and catalytic applications [19]. Recently, Zhang and coworkers used Co_2P nanorods as seeds to grow Co_2P/MP_x (M = Fe, Ni, Mn, and Cu) core/shell nanorods, which were then loaded them onto a support for further annealing to form $CoMP_x$ nanorods [20]. However, it remains challenging to synthesize single-crystalline bimetallic phosphide nanorods using this method.

In this work, we report a TOP-mediated method assisted by the in-situ generated CO for the synthesis of single-crystalline NiCoP nanorods with different aspect ratios. The method introduces in-situ generated CO into our previously-established synthesis for nickel phosphides [21], in which the equimolar metal precursors are thermally decomposed in the presence of oleylamine (OLAM) and TOP, resulting in the synthesis of single-crystalline NiCoP nanorods. Depending on the stage of CO introduced to the reaction, the aspect ratio could be tuned from 1:3 to 1:16 while maintaining hexagonal crystal structure the same as that of Ni_2P and a composition of 1:1 Ni/Co as NiCoP. The crystallinity and growth direction of the resulting NiCoP were characterized by high resolution transmission electron microscopy (HRTEM) and energy dispersive X-ray spectroscopy (EDS). The NiCoP nanorods are single-crystalline in nature and growing preferentially along the [001] direction. The role of CO in the synthesis was investigated by monitoring the kinetics of the formation and disappearance of metal-TOP complex. The electrocatalytic activities and stabilities of these nanostructures for HER were compared, revealing a positive correlation between aspect ratio and electrocatalytic performance.

2. Experimental Methods

2.1. Chemicals and Materials

Nickel(II) acetylacetonate ($Ni(acac)_2$, 96%) and cobalt(II) acetylacetonate ($Co(acac)_2$, 99%) were purchased from Acros Organics, Geel, Belgium. 1-octadecene (ODE, 90%) was purchased from Alfa Aesar, Lancashire, United Kingdom. Oleylamine (OLAM, 70%) and methoxy-polyethylene glycol acetic acid (PEG-COOH, M.W. = 5000) were purchased from Sigma-Aldrich, St. Louis, MO, USA. Trioctylphosphine (TOP, 90%) was purchased from Thermo Scientific, Waltham, MA, USA. Toluene was purchased from Macron Fine Chemicals, Radnor, PA, USA. Ethanol (200 proof) was purchased from Koptec, King of Prussia, PA, USA. Sulfuric acid (95–98%, ACS) and potassium hydroxide (KOH) pellets were purchased from J.T. Baker, Radnor, PA, USA. Formic acid (≥88.0%, ACS) was purchased from VWR BDH Chemicals, Radnor, PA, USA. Hexane and chloroform were purchased from EMD Millipore, Burlington, MA, USA. Ultrapure water (18.2 MΩ) was obtained from a Milli-Q Integral system (Rahway, NJ, USA). The chemicals were used directly as purchased, unless further specified.

2.2. Synthesis of NiCoP Nanorods

The NiCoP nanorods were synthesized using thermal decomposition of Ni and Co precursors simultaneously in the presence of TOP, OLAM, and CO. Typically, $Ni(acac)_2$ (25.7 mg, 0.1 mmol) and $Co(acac)_2$ (25.7 mg, 0.1 mmol) were added to a 3-neck round-bottom flask, followed by adding 4 mL of ODE and 1 mL of OLAM. The reaction flask was equipped with a magnetic stirring bar, a condenser, and a Schlenk line under Ar protection. The reaction mixture was degassed for 10 min under Ar. Prior to heating, 1 mL of TOP was injected into the reaction mixture under magnetic stirring. The reaction mixture was heated to 300 °C and held at this temperature for 20 min. In order to form nanorods, CO was introduced to the reaction mixture during the heating process twice, using a balloon. Briefly, CO was generated by mixing 10 mL of sulfuric acid and 10 mL of formic acid in a single neck round-bottom flask equipped with a balloon via a syringe and a needle. After the formed CO inflated the balloon, the balloon was transferred to the reaction flask and left there for 10 s. During this process, the CO-filled balloon was introduced to the reaction mixture with a noticeable smog that was observed. Details regarding CO generation and introduction are provided in the Supporting Information (Figure S1). For nanorods with a low aspect ratio, CO was introduced at 175 and 240 °C, respectively. For the nanorods with a high aspect ratio, CO was introduced at 175 and 280 °C, respectively. In this two-step CO addition process, CO

was generated via one reaction for 10 min prior to the first injection. Each CO introduction delivered 3.2 ± 0.32 mL under approximate ideal gas conditions.

2.3. Synthesis of CoNiP Spherical Nanoparticles (Nanospheres)

The nanospheres were synthesized using the same method, except that no CO was introduced to the mixture during the reaction.

2.4. UV-Vis Measurement

The UV-vis spectra were acquired by diluting 10 μL of solution at different temperatures or time points from the reaction of interest in 2 mL of ODE at 60 °C in a quartz cuvette. Warmed ODE at 60 °C was used as a blank. In a typical reaction, 100 μL aliquots were taken out by a 1 mL syringe equipped with a long needle from the reaction at each temperature or time point into 1-dram glass vials. From these aliquots, a 10 μL quantity was taken out by a 50 μL glass syringe for dilution in 2 mL of warmed ODE prior to the UV-vis measurement.

2.5. Characterization

The transmission electron microscope (TEM) images were taken using a TEM (JEOL JEM-1011, Tokyo Japan) with an acceleration voltage of 100 kV. Each TEM sample was prepared by drop-casting 5–10 μL of diluted nanoparticle suspension on a 200-mesh carbon-formvar coated copper grid. Powder X-ray diffraction (XRD) patterns were recorded using a diffractometer (Rigaku XtaLAB Synergy-S, Tokyo, Japan) with a Cu K_α radiation source. A sample pellet of 100 μg was dried using a N_2 stream before it was loaded on a nylon loop for XRD measurement. Elemental concentrations of the samples were measured using inductively coupled plasma mass spectrometry (ICP-MS, Thermo Scientific iCAP Q, Waltham, MA, USA). The samples were digested using nitric acid and diluted in 2 vol.% nitric acid as a matrix into the concentration range of 1–100 ppb. High-resolution TEM (HRTEM) images were collected using a JEOL ARM200CF (Tokyo, Japan) operated at 200 kV equipped with dual CEOS GmbH C_s correctors and a Gatan K3 IS detector for image collection. Scanning transmission electron microscopy—annular dark-field (STEM-ADF) images and energy dispersive spectroscopy (EDS) maps were collected using a FEI Talos S/TEM (Waltham, MA, USA) operated at 200 kV with a Super-X EDS system. Annular dark-field (ADF) images were collected with an inner acceptance angle of approximately 30–35 mrad.

2.6. Electrochemical Measurements

All electrochemical measurements were performed in a 3-electrode cell setup using a potentiostat (Biologic SP-150, Seyssinet-Pariset, France). A glassy carbon (GC) rotating disk electrode (0.2 cm^2) was used as the working electrode. Prior to preparation of catalyst inks, the nanoparticle samples were transferred into an ethanol suspension via a ligand exchange process where 2 mL of each sample in toluene was stirred with 2.5 mg of PEG-COOH dissolved in 5 mL of chloroform for 6 h, followed by purification with hexane, ethanol, water, and subsequently resuspended in ethanol. The catalyst ink was prepared by mixing 500 μL of ~2 mg/mL nanoparticle suspension in ethanol with 50 μL of a 0.04 wt.% Nafion solution and drop-casted onto the GC electrode with a catalyst loading of 50 μg/cm^2.

The electrochemical measurements were performed in both acidic and basic media with the working electrode rotated at a rate of 2400 rpm controlled by an electrode rotator (Pine Research, Durham, NC, USA). For the measurement in acidic medium, 0.5 M H_2SO_4 was used as an electrolyte, while a Ag/AgCl, double junction electrode (Pine Research, Durham, NC, USA) was used as the reference electrode, and a graphite rod seated inside a fritted glass tube (Pine Research, Durham, NC, USA) was used as the counter electrode. The potential conversion followed: $\mathrm{E\ (vs.\ RHE)} = \mathrm{E\ (vs.\ Ag/AgCl)} + (0.0591 \times \mathrm{pH}) + \mathrm{E^o(Ag/AgCl)}$, where pH is 1 and $\mathrm{E^o(Ag/AgCl)}$ is 0.199 V. For the measurements in alkaline medium, 1 M KOH was used as the electrolyte, while a Hg/HgO electrode (CHI) was used as the reference electrode, and a home-customized Pt foil or Pt wire (~4.7 cm^2) seated inside a fritted glass tube (Pine Research) was used as the counter electrode. The potential conversion followed: $\mathrm{E\ (vs.\ RHE)} = \mathrm{E\ (vs.\ Hg/HgO)} + (0.0591 \times \mathrm{pH}) + \mathrm{E^o(Hg/HgO)}$, where pH is 14 and $\mathrm{E^o(Hg/HgO)}$ is 0.98 V. Nitrogen was used to purge the electrolyte solution for 5 min prior to the electrochemical measurements. Linear sweep voltammetry (LSV) was carried out at a scan rate of 10 mV/s from 0 to −0.5 V vs. RHE. An 85% iR correction was applied to all scans. The stability tests were performed at 10 mA/cm^2 for 2 h.

3. Results and Discussion

The synthesis of NiCoP at a stoichiometric ratio of 1:1:1 was carried out in the presence of OLAM at elevated temperature using $Ni(acac)_2$ and $Co(acac)_2$ at an equimolar ratio as metal precursors, and TOP as the phosphorus source. During the reaction, CO gas, which was generated by the decomposition of formic acid by sulfuric acid [22], was introduced via a balloon, syringe and needle at different temperatures for 10 s. Figure 1A illustrates the reaction scheme of the synthesis. Depending on how the CO was added during the reaction, three distinct morphologies of NiCoP nanostructures were formed: the spherical nanoparticles or nanospheres (NSs), the nanorods with low aspect ratio (LAR NRs), and the nanorods with high aspect ratio (HAR NRs). TEM images reveal that the NSs have an average size of 17.9 ± 2.3 nm (Figure 1B), while the LAR NRs exhibit lengths of 53.3 ± 7.8 nm and widths of 16.8 ± 2.6 nm, resulting in an aspect ratio of 3.2 (Figure 1C). In contrast, the HAR NRs display lengths of 50.4 ± 5.2 nm and widths of 6.7 ± 0.9 nm, yielding an aspect ratio of 7.5 (Figure 1D). XRD analysis indicates that all of these nanostructures exhibit a set of the peaks at 41.02, 44.94, 47.62, ~55 (specifically, 54.48, 54.79 and 55.38), 75.48, and 80.94 degrees of 2θ, which can be indexed to the XRD pattern of NiCoP (COD1008056) [23–25]. The ICP-MS results, listed in Table S1, confirm that the composition of the nanostructures is approximately 1:1:1.

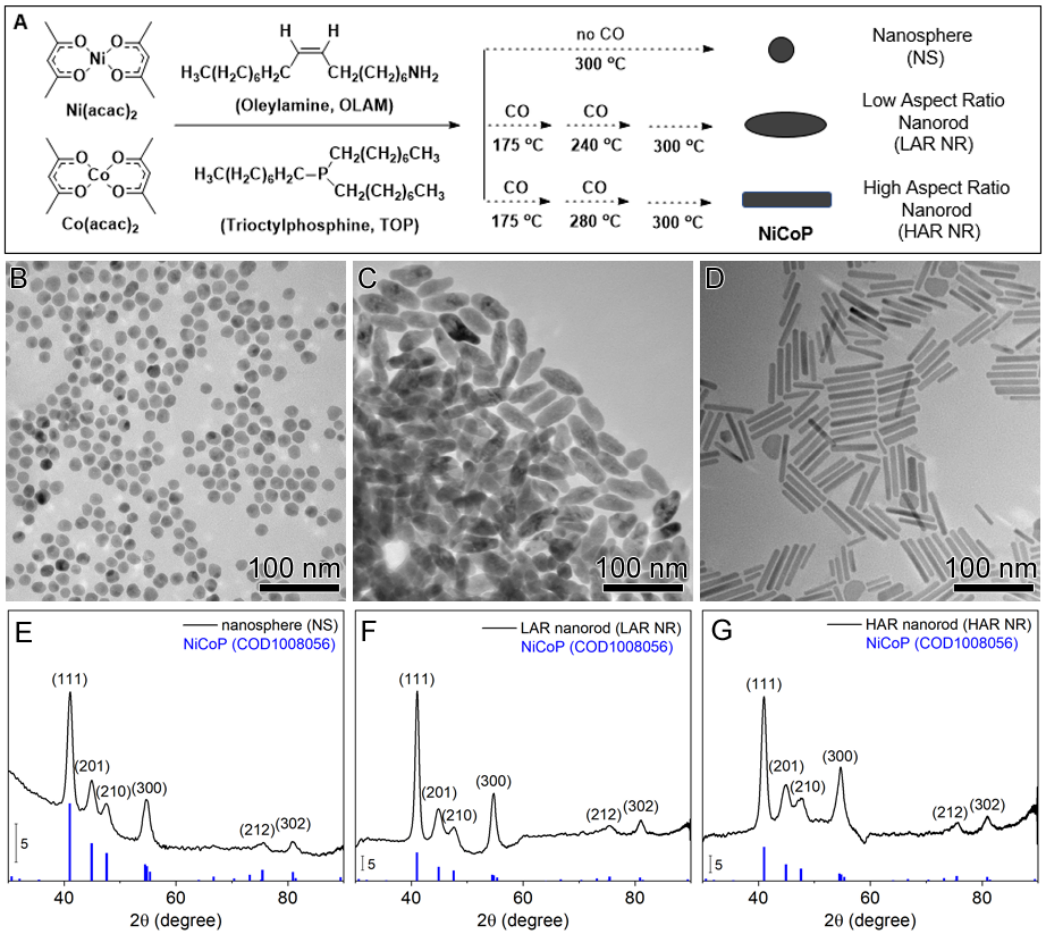

Figure 1. (**A**) Schematic illustrating the synthesis of NiCoP nanostructures. (**B**–**D**) TEM images of the NiCoP nanostructures: (**B**) nanospheres (NSs) with an average size of 17.9 ± 2.3 nm; (**C**) low-aspect-ratio nanorods (LAR NRs) with a length of 53.3 ± 7.8 nm and a width of 16.8 ± 2.6 nm, resulting in an aspect ratio of 3.2; (**D**) high-aspect-ratio nanorods (HAR NRs) with a length of 50.4 ± 5.2 nm and a width of 6.7 ± 0.9 nm, resulting in an aspect ratio of 7.5. (**E**,**F**) XRD patterns of the corresponding samples in (**B**–**D**): (**E**) NS; (**F**) LAR NR; and (**G**) HAR NR, which can be indexed to the XRD pattern of the crystal structure of NiCoP labeled in blue.

In the absence of CO gas, the reaction yielded spherical NiCoP nanoparticles. To further elucidate their structure, HRTEM and EDS mapping were employed. The results reveal a mixture of single-crystalline and polycrystalline nanoparticles. A representative single-crystalline nanoparticle, shown in Figure 2A, exhibits lattice spacings corresponding to the $(0\bar{2}1)_{NiCoP}$ and $(1\bar{2}\bar{1})_{NiCoP}$ crystallographic planes, viewed from the [412] zone axis of hexagonal NiCoP similar to hexagonal Ni_2P. In contrast, Figure 2B illustrates a polycrystalline nanoparticle

with distinct grain boundaries within the particle. Notably, EDS maps (Figure 2D–F) demonstrate that Ni, Co, and P are uniformly distributed throughout each particle, irrespective of their crystallinity, indicating no elemental segregation.

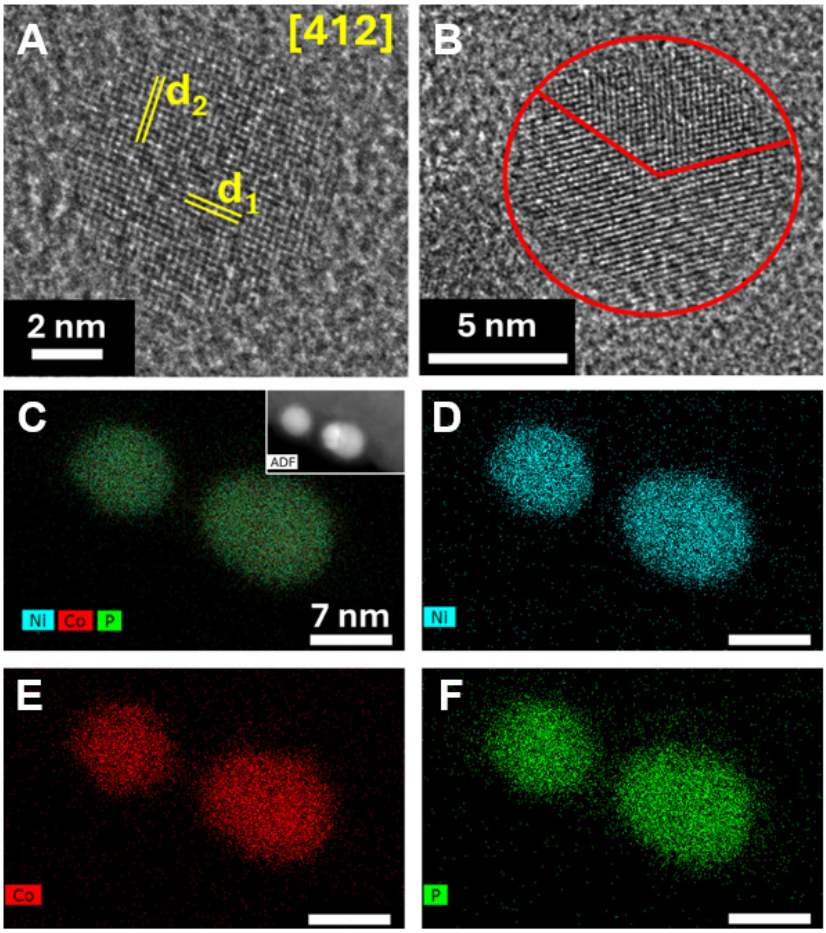

Figure 2. HRTEM and EDS mapping of NiCoP NS: (**A**) HRTEM image of the nanoparticle with lattice spacings marked with $d_1 = (0\bar{2}1)_{\mathrm{NiCoP}}$ and $d_2 = (1\bar{2}\bar{1})_{\mathrm{NiCoP}}$. (**B**) HRTEM image of a polycrystalline nanoparticle with the grain boundary and particle outlined in red. (**C**–**F**) EDS mapping of Ni, Co, and P in two nanoparticles, with an ADF image inset in (**C**). Simplified scale bars of 7 nm are used in (**D**–**F**) for data visibility.

Upon addition of CO gas at 175 and 240 °C, the reaction resulted in nanorods with low aspect ratio. HRTEM analysis of a representative LAR NR, shown in Figure 3A, reveals that it is single-crystalline in nature. The crystallographic orientation of the LAR NR is characterized by a lateral direction along the [110] axis and a longitudinal direction along the [001] axis. It is implied that the reaction conditions promote the growth of the NiCoP nanostructures along the [001] direction, leading to the formation of nanorods. These observations are consistent with previous studies on the growth of mono-metal phosphide Ni_2P nanorods, which also exhibit growth along the [001] direction of the hexagonal Ni_2P crystal structure [26,27]. Furthermore, the EDS mapping (Figure 3B–E) indicates a uniform distribution of Ni, Co, and P throughout individual particles, with no apparent elemental segregation. Based on these results, the addition of CO facilitates the formation of single-crystalline seeds that lead to elongation of the nanoparticles into nanorods.

The introduction of CO gas at 175 and 280 °C led to the formation of nanorods with high aspect ratio. Similarly, HRTEM analysis of a representative HAR NR (Figure 4A) confirms its single-crystalline nature, with growth occurring along the [001] direction and a lateral direction along the [110] axis, analogous to that of the LAR NR. It is noted that the [112] direction is not aligned with the long axis of the rod, likely due to out-of-plane rotation as the rod is in a cluster instead of lying flat on the TEM grid as in Figure 3A. While most HAR NRs exhibit a uniform distribution of Ni, Co, and P throughout the particle, occasional deviations are observed, where excess Co is present at specific locations (indicated by arrows), coinciding with the absence of Ni, suggesting segregation. P is consistently present throughout normal and Co-rich regions. Compared to LAR NRs, the second addition of CO gas at a higher temperature allows the thinner rods to form while both LAR NRs and HAR NRs have similar length. The temperature of second CO gas addition affects the growth of the NRs in the lateral direction.

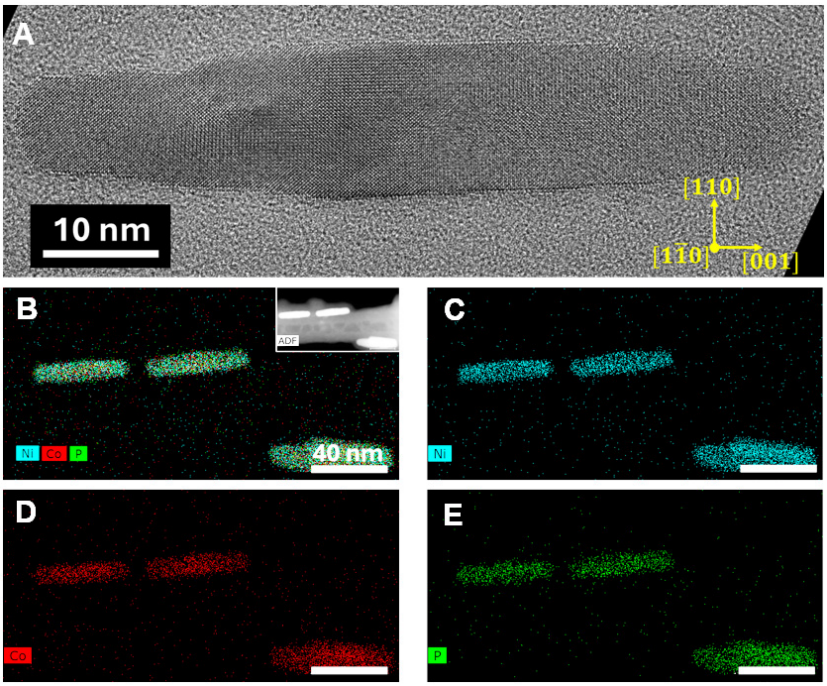

Figure 3. HRTEM and EDS mapping of NiCoP LAR NR: (**A**) HRTEM image of a thick rod with orientation indicated. (**B**–**E**) EDS mapping of Ni, Co, and P in three rods, with an ADF image inset in (**B**). Simplified scale bars of 40 nm are used in (**C**–**E**) for data visibility.

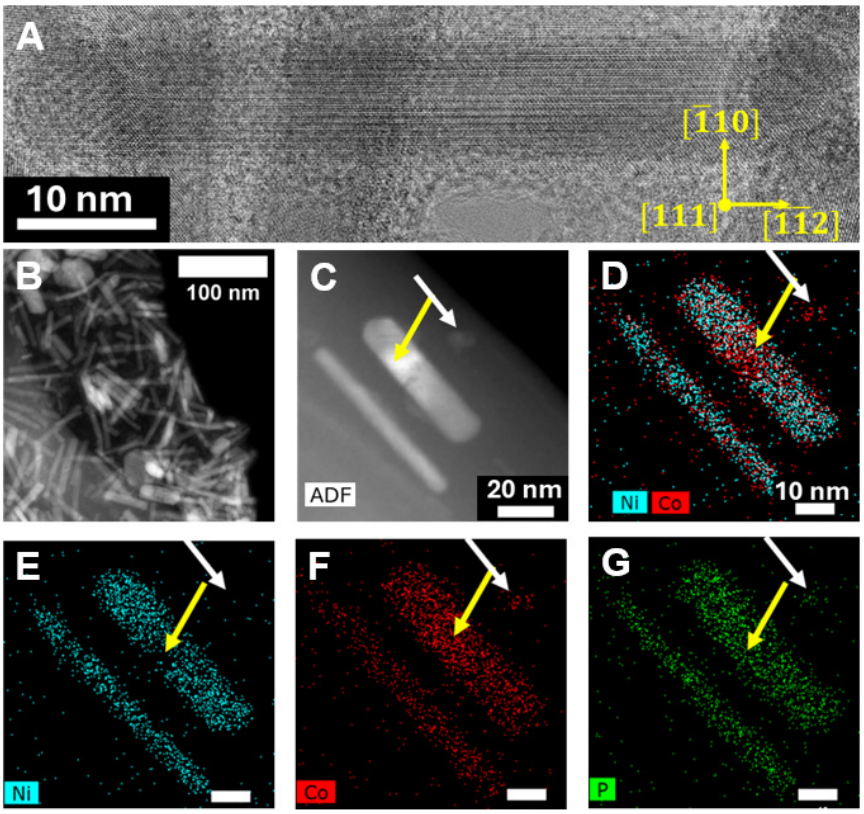

Figure 4. HRTEM and EDS mapping of NiCoP HAR NR: (**A**) HRTEM image of a thin rod with orientation indicated (**B**) Lower magnification ADF image of thin rod morphology. (**C**) ADF image and (**D**–**G**) EDS mapping of two rods with arrows indicating areas of Co segregation/Ni depletion. P was excluded from the composite map in (**D**) to highlight the Ni/Co segregation. Simplified scale bars of 10 nm are used in (**E**–**G**) for data visibility.

Since CO plays an important role in the synthesis to promote the growth of NiCoP nanorods, we carried out additional experiments using various CO addition conditions to explore their effects on the nanorod formation. We determined whether two CO additions are necessary. For comparison, we performed a single addition of CO

gas at the three different temperatures previously chosen: 175, 240, and 280 °C while keeping all other conditions the same as the reaction without CO addition. The results are shown in Figure 5. The TEM images display the size and shape of the nanoparticles. Upon CO addition at 175 °C, the size of the nanoparticles has a length of 51.0 ± 6.0 nm and a width of 29.6 ± 3.8 nm, resulting in an aspect ratio of 1.7, whereas both CO additions at 240 and 280 °C resulted in spherical particles with similar average sizes of 9.0 ± 1.5 nm and 11.9 ± 1.3 nm, respectively. The XRD patterns of these three samples indicate that they match well with the hexagonal NiCoP, the same as those of LAR NR and HAR NR. Based on these results, we found that the addition of CO at 175 °C is important for the formation of elongated particles. The additional CO gas that was introduced to the reaction allowed for the reduction of the lateral dimension of the nanorods, resulting in the increase of the aspect ratio of the rods.

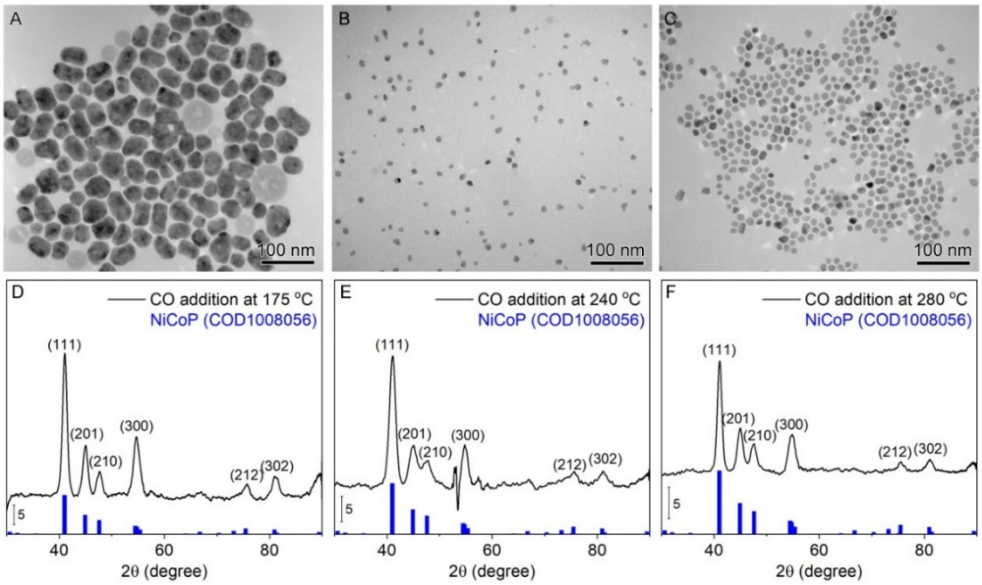

Figure 5. TEM images (**A**–**C**) and XRD patterns (**D**–**F**) of products obtained from reactions with a single CO addition at 175 °C (**A**,**D**), 240 °C (**B**,**E**), and 280 °C (**C**,**F**).

To further investigate the effects of CO on the reaction kinetics, we carried out UV-vis measurements on the aliquots taken out from the reactions for NS, LAR NR, and HAR NR at various stages. The resulting UV-vis spectra of the aliquots for each reaction are presented in Figure 6. According to our previous study, the peak at 313 nm can be attributed to electronic transition of Ni(0)-TOP complex [21]. However, we could not find the spectral signature for Co(0)-TOP which is expected to exhibit a peak at 378 nm based on our theoretical prediction (Figure S1). Although Co precursor is present, the Ni(0)-TOP complex is expected to form initially due to the lower redox potential of Ni^{2+} to Ni(0) compared to that of Co^{2+} to Co(0). In the absence of CO gas, the peak intensity at 313 nm increases gradually with the rising temperature, reaching its maximum at 280 °C, and then decreases and disappears after being held at 300 °C for 5 min (Figure 6A). Based on the TEM results, the reaction forms a mixture of single-crystalline and polycrystalline spherical nanoparticles with no anisotropic growth.

In the presence of CO gas, CO can play multiple roles in the reaction, including acting as a chelating ligand to coordinate with the metal center, a reducing agent to reduce the metal cation, and a capping ligand that adsorbs onto the particle surface. In particular, CO has been introduced as reducing agent in the shape and composition-control of platinum alloy nanocrystals by Yang and co-workers [28,29]. In our case, the first CO addition at 175 °C facilitates the reduction of metal precursors, as evident from the jump in the intensity of the peak at 313 nm for LAR NR (Figure 6B) and HAR NR (Figure 6C) compared to that of NS. The TEM study also supports that the first CO addition also facilitates the formation of single crystals which serves as the seeds for the growth of metal phosphide nanorods. Since the nucleation of the reactions occurs at around 220 °C, the second addition of CO at a higher temperature can act as a reducing agent to reduce the metal precursors, as well as a capping agent to guide the nanocrystal growth. The addition of CO at a higher temperature suppresses the lateral growth of the nanorod, thereby increasing the aspect ratio of the nanorods.

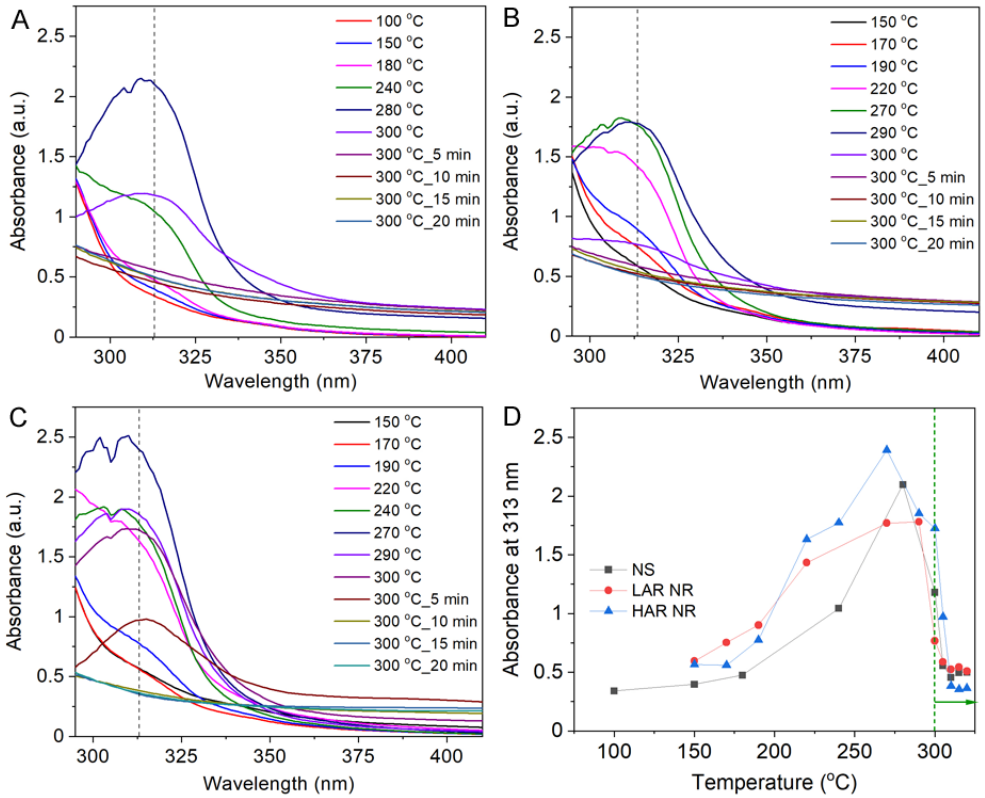

Figure 6. UV-vis spectra of reaction aliquots taken at various stages during the synthesis of NS (**A**), LAR NR (**B**), and HAR NR (**C**). (**D**) Plots of absorbance at 313 nm as a function of temperature for each reaction, with data points beyond 300 °C corresponding to reactions held at 300 °C for extended periods (5, 10, 15, and 20 min), as indicated by the green arrow pointing from the dashed green line.

We also investigated the effects of the reaction time on the nanorod growth. We extended the reaction time at 300 °C from 20 min to 60 min, while keeping the other reaction conditions constant for each set of reactions. Extending reaction time increases the aspect ratios of nanorods, as shown in Figure 7A–C. For a single CO addition at 175 °C, the nanorods grew to a length of 64.4 ± 12.8 nm and a width of 33.0 ± 4.7 nm, with an aspect of 2.0 after 60 min of reaction, compared to 1.7 after 20 min of reaction. For dual CO additions at 175 and 240 °C, the nanorods resulted in a length of 58.3 ± 7.6 nm and a width of 16.1 ± 2.2 nm, with an aspect ratio of 3.6 after 60 min of reaction, versus 3.2 after 20 min of reaction. For dual CO additions at 175 and 280 °C, the reaction yielded a mixture of thinner nanorods (99.0 ± 20.8 nm in length and 6.6 ± 1.2 nm) width with an aspect ratio of 15 and thicker nanorods (78.5 ± 7.3 nm in length and 16.2 ± 2.7 nm) width with an aspect ratio of 4.8 after 60 min of reaction. The comparison of dimensional information for different reaction conditions is listed in Table S2. The XRD patterns in Figure 7D–F, confirm that all the nanorods are composed of hexagonal NiCoP.

We conducted a comparative study of the HER activities of 1D nanostructures in both acidic and alkaline media. The LSV experiments were performed at a scan rate of 10 mV/s in 0.5 M H_2SO_4 and 1 M KOH, respectively. In the acidic medium (0.5 M H_2SO_4), we observed that the HER overpotential at a current density of 10 mA/cm^2 decreased with increasing aspect ratio of the nanostructures. Specifically, the HAR rods exhibited the lowest overpotential of 187 mV, while the LAR rods and NS particles showed similar overpotentials of 237 and 264 mV, respectively, as illustrated in Figure 8A. Further analysis of the LSV data using Tafel plots revealed that the Tafel slopes for the HAR rods, LAR rods, and NS particles were 56, 66, and 88 mV/dec, for their overpotential ranges of 125–182 mV, 169–236 mV, and 175–262 mV, respectively (Figure 8B). These values suggest that the HER mechanism on the HAR rods proceeds via a Volmer-Heyrovsky pathway, whereas the LAR rods and NS particles follow a Volmer mechanism. The result is based on the general consideration that Tafel slop can provide insights into the reaction mechanism of HER on the catalyst surface with the theoretical values for the Volmer step, the Heyrovsky step, and the Tafel step in the HER to be 120, 40, and 30 mV/dec [30,31]. In contrast, when the same catalysts were tested in an alkaline medium (1 M KOH), the HER overpotential at 10 mA/cm^2 increased compared to the acidic condition, in agreement with the findings for other catalysts such as noble metals due to water as the proton source in the HER under the alkaline conditions [32,33]. Notably, the HAR rods still exhibited the lowest overpotential of 412 mV, while the LAR rods and NS particles showed higher overpotentials of

approximately 500 mV, as shown in Figure 8C. Tafel analysis in the alkaline medium yielded slopes of 101, 142, and 146 mV/dec in the potential ranges of 306–460 mV, 342–495 mV, and 348–500 mV for the HAR rods, LAR rods, and NS particles, respectively (Figure 8D). These values indicate that the HER mechanism on the HAR rods also proceeds via a Volmer-Heyrovsky pathway, whereas the LAR rods and NS particles follow a Volmer mechanism. Based on these results, we conclude that the 1D nanostructures enhance the catalytic activity for HER by promoting the Heyrovsky mechanism and optimizing the hydrogen binding energy, which is associated with a more efficient hydrogen evolution process.

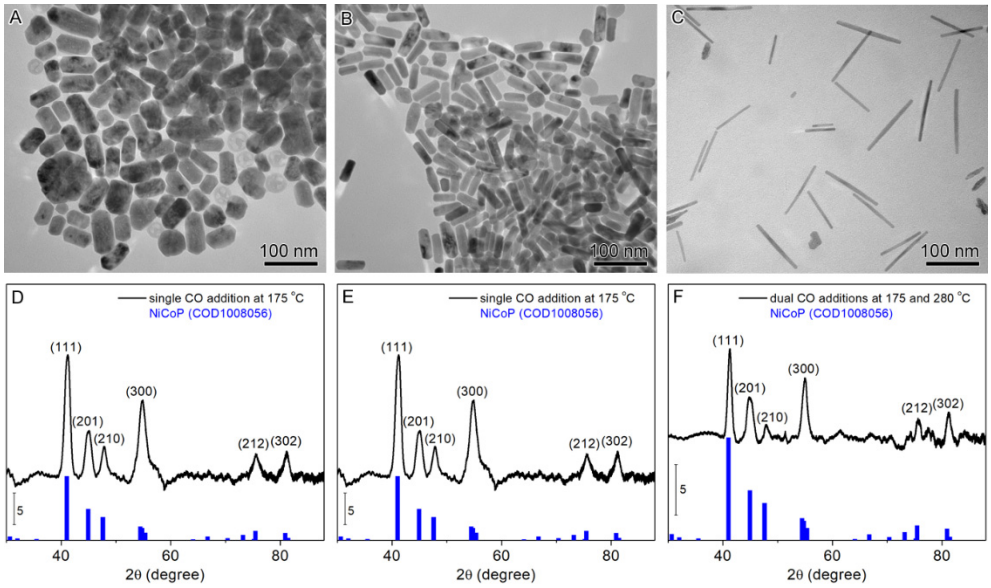

Figure 7. TEM images (**A**–**C**) and XRD patterns (**D**–**F**) of products obtained from reactions with a single CO addition at 175 °C (**A**,**D**), dual CO additions at 175 and 240 °C (**B**,**E**), and dual CO additions at 175 and 280 °C (**C**,**F**).

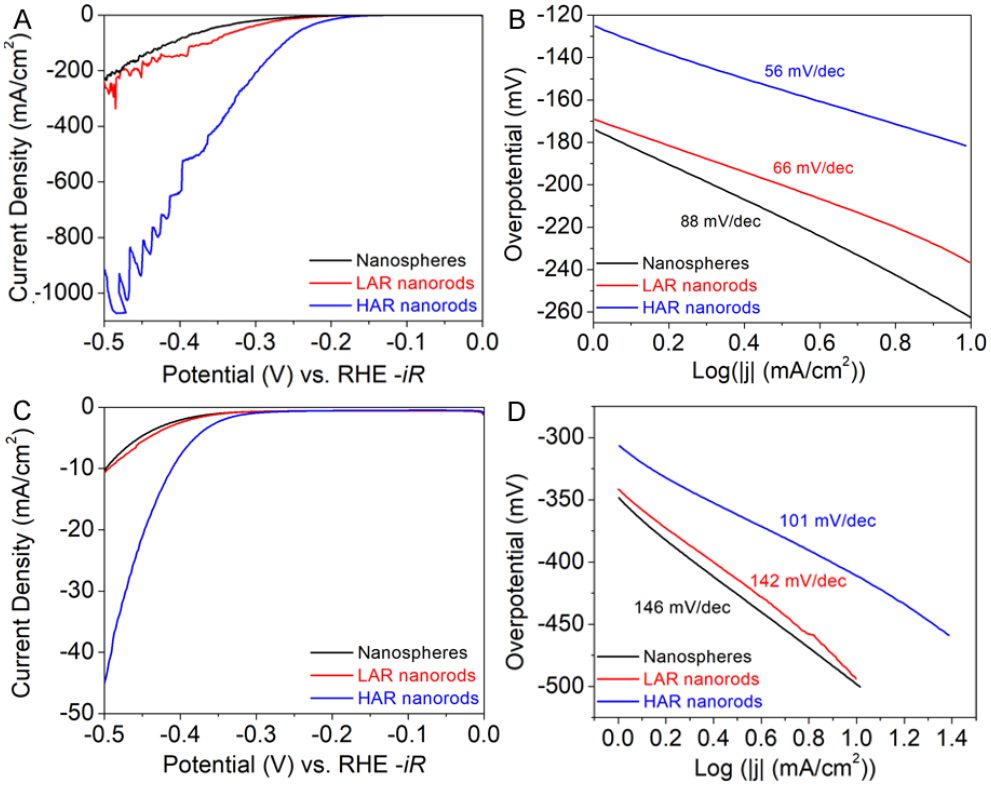

Figure 8. HER evaluation on NS, LAR NR, and HAR NR under acidic and alkaline media: (**A**,**B**) LSVs at a scan rate of 10 mV/s in 0.5 M H_2SO_4 and their Tafel plots; and (**C**,**D**) LSVs at a scan rate of 10 mV/s in 1 M KOH and their Tafel plots. The current density is normalized by the geometric surface area (0.2 cm^2) of the GC rotating disk electrode. The oscillation in the LSVs at high negative potentials (>−0.3 V vs. RHE) is due to the bubble formation on the catalyst surface.

The electrochemically active surface area (ECSA) of each catalyst was evaluated using the double layer capacitance (C_{dl}) method, a widely accepted technique for determining the ECSA of electrocatalysts [34–36]. This method measures the capacitance of the double layer formed at the electrode-electrolyte interface, which is assumed to be directly proportional to the ECSA. To determine the ECSA, cyclic voltammetry (CV) was performed on each catalyst in the non-Faradaic region (±50 mV of open circuit potential, OCP), where no redox reactions occur, with their scan rate varying from 1 to 250 mV/s. The C_{dl} was calculated from the slope of the linear relationship between the current obtained at OCP and scan rate. The ECSA was then calculated using the equation: ECSA = C_{dl}/C_s, where C_s is the specific capacitance of the material. The values of C_s used in this study were 0.035 cm^2 for acidic conditions and 0.040 cm^2 for basic conditions, which are typical values reported in the literature [36]. The results show that HAR NR has a significantly higher ECSA than LAR NR and NS under acidic conditions, indicating that it has a more extensive surface area available for electrochemical reactions (Figure S3 and Table S3). This is likely due to the unique morphology of HAR NR, which may provide more active sites for HER. In contrast, under basic conditions, the ECSA of HAR NR is only slightly higher than those of LAR NR and NS, suggesting that the surface area advantage of HAR NR is less pronounced in this environment (Figure S4 and Table S4). The LSVs normalized by the ECSA of each catalyst were plotted in Figure S5.

We further investigate the stability of NS, LAR NR, and HAR NR for HER under acidic and alkaline conditions using chronopotentiometry (CP). The CP experiments were conducted at a constant current density of 10 mA/cm^2. Figure 9A illustrates the potential changes as a function of time in 0.5 M H_2SO_4, revealing distinct stability profiles for each material. Notably, the overpotential increases at rates of −10.0 mV/h and −12.9 mV/h for HAR NR and LAR NR, respectively. In contrast, NS exhibits a decrease in overpotential at a rate of 0.4 mV/h, suggesting that its surface may undergo reconstruction to facilitate HER. To further assess activity after the stability test, we performed LSV before and after the CP experiments, with the results presented in Figure S6. The LSV data indicate a slight decrease in HAR NR activity, negligible change in LAR NR activity, and an increase in NS activity. Under alkaline conditions, HAR NR demonstrates superior stability compared to NS and LAR NR, with overpotential increases of −3.8 mV/h, −7.0 mV/h, and −20.9 mV/h for HAR NR, NS, and LAR NR, respectively (Figure 9B). Notably, the CP experiments induce a significant enhancement in the catalytic activity of all three materials, as evidenced by a substantial decrease in overpotential at 10 mA/cm^2. Specifically, the overpotentials decrease from 421 mV to 180 mV for HAR NR, and from 500 mV to 280 mV for both LAR NR and NS (Figure S7). The enhancement of HER activity can be attributed to the structural evolution of the phosphide catalysts to their corresponding hydroxide phases under the alkaline conditions [37,38]. The aspect ratio of the nanostructures plays a crucial role in determining the HER activity and stability, with higher aspect ratios leading to improved performance. These findings have important implications for the design and optimization of nanostructured catalysts for electrochemical water splitting applications.

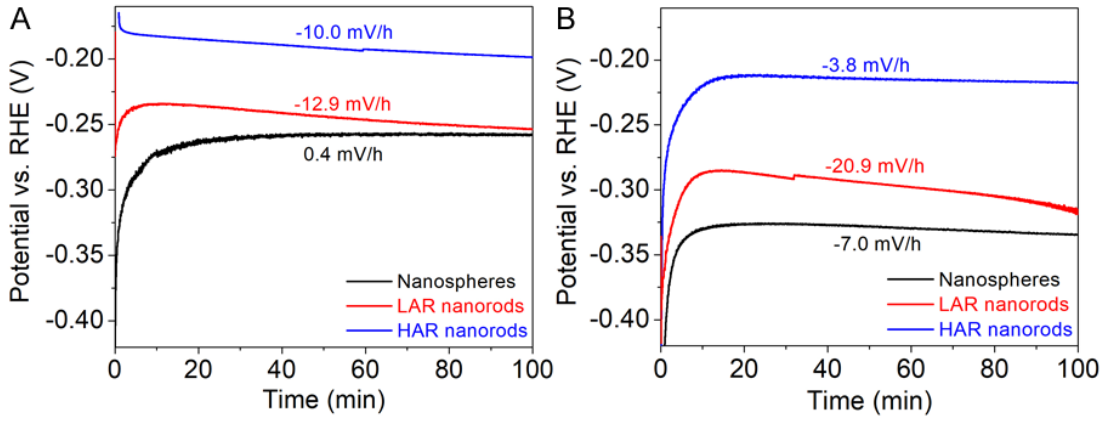

Figure 9. Chronopotentiometry (CP) evaluation on NS, LAR NR, and HAR NR by recording the potential changes while holding the current density at 10 mA/cm^2 under acidic and alkaline media: (**A**) in 0.5 M H_2SO_4; and (**B**) in 1 M KOH.

4. Conclusions

We have successfully synthesized single-crystalline NiCoP nanorods with tunable aspect ratios using a CO-assisted, TOP-mediated approach. The introduction of CO gas at different temperatures allows for the control of the nanorod growth, resulting in various aspect ratios while maintaining a hexagonal crystal structure and a composition of 1:1 Ni/Co as NiCoP. The electrocatalytic activities of these nanostructures for the HER were investigated, revealing a positive correlation between aspect ratio and electrocatalytic performance. Our results

demonstrate that the NiCoP nanorods with higher aspect ratios exhibit improved HER activity and stability, with the highest aspect ratio nanorods showing the lowest overpotential and Tafel slope. Our results are in line with previous studies on the Ni_2P 1D nanostructures, which have shown that the Ni bridge sites on the surface of the long side of these nanostructures, oriented along the [001] direction of the hexagonal Ni_2P crystal structure, exhibit enhanced HER activity compared to the (001) facet [10]. The enhanced performance is thought to stem from synergistic electronic and structural modifications that alter the characteristics of the active sites. The study highlights the importance of controlling the size and morphology of bimetallic phosphide nanoparticles to optimize their catalytic activity for HER. The findings have significant implications for the design and optimization of nanostructured catalysts for electrochemical water splitting applications, which is crucial for the development of sustainable energy systems.

Supplementary Materials: The following supporting information can be downloaded at: https://media.sciltp.com/articles/others/2506201608320087/MI-1091-SI-proofreading.pdf, CO generation setup and experimental details, ICP-MS results, DFT calculation of the UV-vis spectrum of Co(0)-TOP_4 complex, ECSA measurement, LSVs normalized by ECSA, LSVs before and after CP measurements. References [39–42] are cited in the Supplementary Materials.

Author Contributions: J.C.: conceptualization, supervision, writing; S.Y.: methodology, data curation; Z.R.M. and Y.Z.: HRTEM and STEM-EDS data curation and interpretation; F.W.: theoretical calculation of UV-vis spectrum. All authors have read and agreed to the published version of the manuscript.

Funding: This research was funded by the U.S. National Science Foundation (NSF), award number CHE-2304999.

Data Availability Statement: Not applicable.

Acknowledgments: J.C. and S.Y. acknowledge support from the U.S. National Science Foundation (NSF) under award number CHE-2304999. HRTEM were carried out at Brookhaven National Laboratory (BNL) sponsored by the U.S. DOE Basic Energy Sciences (BES) and by the Materials Sciences and Engineering Division under Contract No. DE-SC0012704. STEM-EDS data was collected at the Center for Functional Nanomaterials (CFN), which is a U.S. Department of Energy Office of Science User Facility, at Brookhaven National Laboratory under Contract No. DE-SC0012704.

Conflicts of Interest: The authors declare no conflict of interest.

References

1. Shi, Y.; Zhang, B. Recent Advances in Transition Metal Phosphide Nanomaterials: Synthesis and Applications in Hydrogen Evolution Reaction. *Chem. Soc. Rev.* **2016**, *45*, 1529–1541.
2. Pei, Y.; Cheng, Y.; Chen, J.; Smith, W.; Dong, P.; Ajayan, P.M.; Ye, M.; Shen, J. Recent Developments of Transition Metal Phosphides as Catalysts in the Energy Conversion Field. *J. Mater. Chem. A* **2018**, *6*, 23220–23243.
3. Wu, W.; Luo, S.; Huang, Y.; He, H.; Shen, P.K.; Zhu, J. Recent Advances in Transition Metal Phosphide-Based Heterostructure Electrocatalysts for the Oxygen Evolution Reaction. *Mater. Chem. Front.* **2024**, *8*, 1064–1083.
4. Li, Y.; Xin, T.; Cao, Z.; Zheng, W.; He, P.; Yoon Suk Lee, L. Optimized Transition Metal Phosphides for Direct Seawater Electrolysis: Current Trends. *ChemSusChem* **2024**, *17*, e202301926.
5. Ray, A.; Sultana, S.; Paramanik, L.; Parida, K.M. Recent Advances in Phase, Size, and Morphology-Oriented Nanostructured Nickel Phosphide for Overall Water Splitting. *J. Mater. Chem. A* **2020**, *8*, 19196–19245.
6. Lu, X.; Yan, K.; Yu, Z.; Wang, J.; Liu, R.; Zhang, R.; Qiao, Y.; Xiong, J. Transition Metal Phosphides: Synthesis Nanoarchitectonics, Catalytic Properties, and Biomass Conversion Applications. *ChemSusChem* **2024**, *17*, e202301687.
7. Sun, M.; Liu, H.; Qu, J.; Li, J. Earth-Rich Transition Metal Phosphide for Energy Conversion and Storage. *Adv. Energy Mater.* **2016**, *6*, 1600087.
8. Li, G.; Feng, Y.; Yang, Y.; Wu, X.; Song, X.; Tan, L. Recent Advances in Transition Metal Phosphide Materials: Synthesis and Applications in Supercapacitors. *Nano Mater. Sci.* **2024**, *6*, 174–192.
9. Popczun, E.J.; McKone, J.R.; Read, C.G.; Biacchi, A.J.; Wiltrout, A.M.; Lewis, N.S.; Schaak, R.E. Nanostructured Nickel Phosphide as an Electrocatalyst for the Hydrogen Evolution Reaction. *J. Am. Chem. Soc.* **2013**, *135*, 9267–9270.
10. Hansen, M.H.; Stern, L.-A.; Feng, L.; Rossmeisl, J.; Hu, X. Widely Available Active Sites on Ni2p for Electrochemical Hydrogen Evolution—Insights from First Principles Calculations. *Phys. Chem. Chem. Phys.* **2015**, *17*, 10823–10829.
11. Chung, Y.-H.; Gupta, K.; Jang, J.-H.; Park, H.S.; Jang, I.; Jang, J.H.; Lee, Y.-K.; Lee, S.-C.; Yoo, S.J. Rationalization of Electrocatalysis of Nickel Phosphide Nanowires for Efficient Hydrogen Production. *Nano Energy* **2016**, *26*, 496–503.
12. Xiao, J.; Lv, Q.; Zhang, Y.; Zhang, Z.; Wang, S. One-Step Synthesis of Nickel Phosphide Nanowire Array Supported on Nickel Foam with Enhanced Electrocatalytic Water Splitting Performance. *RSC Adv.* **2016**, *6*, 107859–107864.
13. Wang, Y.; Liu, L.; Zhang, X.; Yan, F.; Zhu, C.; Chen, Y. Self-Supported Tripod-Like Nickel Phosphide Nanowire Arrays for Hydrogen Evolution. *J. Mater. Chem. A* **2019**, *7*, 22412–22419.

14. Kibsgaard, J.; Tsai, C.; Chan, K.; Benck, J.D.; Nørskov, J.K.; Abild-Pedersen, F.; Jaramillo, T.F. Designing an Improved Transition Metal Phosphide Catalyst for Hydrogen Evolution Using Experimental and Theoretical Trends. *Energy Environ. Sci.* **2015**, *8*, 3022–3029.
15. Downes, C.A.; Van Allsburg, K.M.; Tacey, S.A.; Unocic, K.A.; Baddour, F.G.; Ruddy, D.A.; LiBretto, N.J.; O'Connor, M.M.; Farberow, C.A.; Schaidle, J.A.; et al. Controlled Synthesis of Transition Metal Phosphide Nanoparticles to Establish Composition-Dependent Trends in Electrocatalytic Activity. *Chem. Mater.* **2022**, *34*, 6255–6267.
16. Liu, J.; Wang, Z.; David, J.; Llorca, J.; Li, J.; Yu, X.; Shavel, A.; Arbiol, J.; Meyns, M.; Cabot, A. Colloidal Ni2−Xcoxp Nanocrystals for the Hydrogen Evolution Reaction. *J. Mater. Chem. A* **2018**, *6*, 11453–11462.
17. Qian, C.; Kim, F.; Ma, L.; Tsui, F.; Yang, P.; Liu, J. Solution-Phase Synthesis of Single-Crystalline Iron Phosphide Nanorods/Nanowires. *J. Am. Chem. Soc.* **2004**, *126*, 1195–1198.
18. Park, J.; Koo, B.; Yoon, K.Y.; Hwang, Y.; Kang, M.; Park, J.-G.; Hyeon, T. Generalized Synthesis of Metal Phosphide Nanorods Via Thermal Decomposition of Continuously Delivered Metal−Phosphine Complexes Using a Syringe Pump. *J. Am. Chem. Soc.* **2005**, *127*, 8433–8440.
19. Brock, S.L.; Senevirathne, K. Recent Developments in Synthetic Approaches to Transition Metal Phosphide Nanoparticles for Magnetic and Catalytic Applications. *J. Solid State Chem.* **2008**, *181*, 1552–1559.
20. Zhang, Y.; Li, N.; Zhang, Z.; Li, S.; Cui, M.; Ma, L.; Zhou, H.; Su, D.; Zhang, S. Programmable Synthesis of Multimetallic Phosphide Nanorods Mediated by Core/Shell Structure Formation and Conversion. *J. Am. Chem. Soc.* **2020**, *142*, 8490–8497.
21. Thompson, D.; Hoffman, A.S.; Mansley, Z.R.; York, S.; Wang, F.; Zhu, Y.; Bare, S.R.; Chen, J. Synthesis of Amorphous and Various Phase-Pure Nanoparticles of Nickel Phosphide with Uniform Sizes via a Trioctylphosphine-Mediated Pathway. *Inorg. Chem.* **2024**, *63*, 18981–18991.
22. DeRight, R.E. The Decomposition of Formic Acid by Sulfuric Acid. *J. Am. Chem. Soc.* **1933**, *55*, 4761–4764.
23. Crystallography Open Database: Information Card for Entry 1008056. Available online: https://www.crystallography.net/cod/1008056.html (access on 11 April 2025).
24. Sénateur, J.; Rouault, A.; L'Héritier, P.; Krumbügel-Nylund, M.A.; Fruchart, R.; Fruchart, D.; Convert, P.; Roudaut, E. La Selectivite Des Substitutions Dans Les Phases Mm'p Etude De L'ordre Par Diffraction Neutronique Dans Nicop. *Mater. Res. Bull.* **1973**, *8*, 229–238.
25. American Mineralogist Crystal Structure Database: Conip. Available online: https://rruff.geo.arizona.edu/AMS/result.php?key=_database_code_amcsd+0015998&viewing=html (access on 11 April 2025).
26. Chen, Y.; She, H.; Luo, X.; Yue, G.-H.; Peng, D.-L. Solution-Phase Synthesis of Nickel Phosphide Single-Crystalline Nanowires. *J. Cryst. Growth* **2009**, *311*, 1229–1233.
27. She, H.; Chen, Y.; Luo, X.; Yue, G.-H.; Peng, D.-L. Preparation of Anisotropic Transition Metal Phosphide Nanocrystals: The Case of Nickel Phosphide Nanoplatelets, Nanorods, and Nanowires. *J. Nanosci. Nanotechnol.* **2010**, *10*, 5175–5182.
28. Wu, J.; Gross, A.; Yang, H. Shape and Composition-Controlled Platinum Alloy Nanocrystals Using Carbon Monoxide as Reducing Agent. *Nano Lett.* **2011**, *11*, 798–802.
29. You, H.; Yang, S.; Ding, B.; Yang, H. Synthesis of Colloidal Metal and Metal Alloy Nanoparticles for Electrochemical Energy Applications. *Chem. Soc. Rev.* **2013**, *42*, 2880–2904.
30. Zhao, G.; Rui, K.; Dou, S.X.; Sun, W. Heterostructures for Electrochemical Hydrogen Evolution Reaction: A Review. *Adv. Funct. Mater.* **2018**, *28*, 1803291.
31. Lasia, A. Mechanism and Kinetics of the Hydrogen Evolution Reaction. *Int. J. Hydrog. Energy* **2019**, *44*, 19484–19518.
32. Strmcnik, D.; Lopes, P.P.; Genorio, B.; Stamenkovic, V.R.; Markovic, N.M. Design Principles for Hydrogen Evolution Reaction Catalyst Materials. *Nano Energy* **2016**, *29*, 29–36.
33. Shinagawa, T.; Garcia-Esparza, A.T.; Takanabe, K. Insight on Tafel Slopes from a Microkinetic Analysis of Aqueous Electrocatalysis for Energy Conversion. *Sci. Rep.* **2015**, *5*, 13801.
34. Trasatti, S.; Petrii, O. Real Surface Area Measurements in Electrochemistry. *J. Electroanal. Chem.* **1992**, *327*, 353–376.
35. Morales, D.M.; Risch, M. Seven Steps to Reliable Cyclic Voltammetry Measurements for the Determination of Double Layer Capacitance. *J. Phys. Energy* **2021**, *3*, 034013.
36. McCrory, C.C.L.; Jung, S.; Ferrer, I.M.; Chatman, S.M.; Peters, J.C.; Jaramillo, T.F. Benchmarking Hydrogen Evolving Reaction and Oxygen Evolving Reaction Electrocatalysts for Solar Water Splitting Devices. *J. Am. Chem. Soc.* **2015**, *137*, 4347–4357.
37. Manso, R.H.; Hong, J.; Wang, W.; Acharya, P.; Hoffman, A.S.; Tong, X.; Wang, F.; Greenlee, L.F.; Zhu, Y.; Bare, S.R.; et al. Revealing Structural Evolution of Nickel Phosphide-Iron Oxide Core–Shell Nanocatalysts in Alkaline Medium for the Oxygen Evolution Reaction. *Chem. Mater.* **2024**, *36*, 6440–6453.
38. Zhang, Y.; Gao, L.; Hensen, E.J.M.; Hofmann, J.P. Evaluating the Stability of Co_2P Electrocatalysts in the Hydrogen Evolution Reaction for Both Acidic and Alkaline Electrolytes. *ACS Energy Lett.* **2018**, *3*, 1360–1365.
39. Neese, F.; Wennmohs, F.; Becker, U.; Riplinger, C. The ORCA Quantum Chemistry Program Package. *J. Chem. Phys.* **2020**, *152*, 224108.

40. Becke, A.D. A New Mixing of Hartree-Fock and Local Density-Functional Theories. *J. Chem. Phys.* **1993**, *98*, 1372–1377.
41. Weigend, F.; Ahlrichs, R. Balanced Basis Sets of Split Valence, Triple Zeta Valence and Quadruple Zeta Valence Quality for H to Rn: Design and Assessment of Accuracy. *Phys. Chem. Chem. Phys.* **2005**, *7*, 3297–3305.
42. Helmich-Paris, B.; de Souza, B.; Neese, F.; Izsák, R. An Improved Chain of Spheres for Exchange Algorithm. *J. Chem. Phys.* **2021**, *155*, 104109.

Article

An Anisotropic Hydrogel with Simple Preparation and Well-Defined Structure as a New Platform for Flexible Sensors with Directional Strain and Force Sensing

Yitong Xie [1,2], Shuxu Wang [1,*], Yunlei Zhang [1], Hayato Kanai [1], Kuniyo Yamada [1], Toshie Wakamatsu [1], Yuko Hamada [1], Sei Obuse [1], Daihui Zhang [2], Fuxiang Chu [2], and Yasuhiro Ishida [1,*]

[1] RIKEN Center for Emergent Matter Science, 2-1 Hirosawa, Wako, Saitama 351-0198, Japan
[2] Institute of Chemical Industry of Forest Products, Chinese Academy of Forestry (CAF), No 16, Suojin Wucun, Nanjing 210042, China
* Correspondence: shuxu.wang@riken.jp (S.W.); y-ishida@riken.jp (Y.I.)
Received: 10 April 2025; Revised: 16 June 2025; Accepted: 18 June 2025; Published: 25 June 2025

Abstract: As a platform to construct the next-generation flexible strain and force sensors, anisotropic hydrogels have recently attracted considerable attention, with an expectation that they would visualize the anisotropic motion of biological systems in a direction-specific manner. To date, a number of anisotropic hydrogels have been developed with an intensive pursuit to improve their practical performance, so that their composition, preparation, and structure have become increasingly complex over the years. In fact, most of these anisotropic hydrogels are prepared from many components including naturally occurring materials, using multiple steps that often require skillful control of kinetic events. Therefore, although some of them show good performances, their complicated and unclear structures make it difficult to elucidate the relationship between structure and properties. As an approach complementary to such trend, here we report a very simple anisotropic hydrogel that would provide a versatile platform for flexible sensors with directional sensing capability. This hydrogel was simply prepared by one-pot reaction from two components, i.e., by magnetic orientation of titanate nanosheet (TiNS) in water and subsequent in-situ formation of a polyacrylamide network. In the resulting hydrogel (TiNS-gel), TiNS platelets were arranged in a lamellar structure with highly oriented, periodic, and homogeneous state. Due to such structure, TiNS-gel exhibited remarkable anisotropy in tensile modulus, nanostructural transformability, and ionic conductivity. Furthermore, TiNS-gel changed its electrical resistance upon tensile deformation, demonstrating its potential utility as a flexible strain and force sensor. TiNS-gel, characterized by easy synthesis, simple composition, well-defined structure, and various anisotropic properties will serve as a useful platform for developing flexible devices with direction-selective strain and force sensing capabilities.

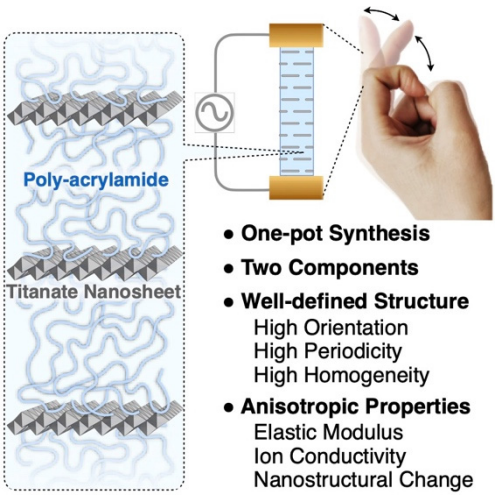

Keywords: anisotropic hydrogels; nanosheets; magnetic alignment; strain sensing; force sensing; flexible electronics; wearable devices

1. Introduction

Hydrogels, a class of soft and flexible polymer networks that retain abundant water, have attracted considerable attention as attractive materials for constructing advanced devices [1–3]. Their inherent flexibility, tunable physical properties, and biocompatibility make hydrogels promising platforms for wearable electronics, soft robotics, and bio-integrated systems [4,5]. In fact, some hydrogels can conform to complex shapes, respond to external stimuli, and provide mechanical or electrical feedback, suggesting their potential use in flexible and

wearable devices. Compared to other soft elastomers, an additional advantage of hydrogels is their similarity to biological tissue [6,7], which allows for seamless integration with human skin or other soft interfaces, leading to various applications such as motion monitoring, pressure sensing, and dynamic force detection [8–10].

Traditionally, hydrogels with isotropic structures have been used for such flexible sensors [11,12], while recently, hydrogels with anisotropic structures and properties [13–20] have attracted considerable attention due to their potential to visualize anisotropic motion of biological systems in a direction-specific manner. For this aim, various anisotropic hydrogels have been developed in these years [21–37]. Some of them exhibit excellent sensing ability, such as high sensitivity [25,28], rapid sensing [24], repeatability [26,31,34], and strain–signal linearity [34]. Remarkable progress has also been made in mechanical properties, including enhanced modulus [23], stretchability [24,25], fracture strength [23,29] and fracture energy [33]. Additional functions have also been realized, including moisture-electric generation [21], self-healing [22,23], swelling resistance [26,30], photo responsiveness [35], and magnetothermal conversion [36]. Further advanced applications have also been pursued, including action signal prediction and classification driven by machine learning [27], and in vivo intraspinal neural recordings [31].

However, most of them have been designed with a focus on practical performance only, so that their preparations, compositions, and structures have become increasingly complex over the years. In fact, most of these anisotropic hydrogels are composed of three or more components, including biomass-derived materials (white wood [21–23], cellulose nanofiber [24], chitosan [24], sodium alginate [25,26], etc.) that tend to have different properties depending on their origin. In addition, these components are assembled through many steps that often require the skillful control of kinetic events (delignification [21–23], infiltration [21–23,27], spinning [24], pre-stretching [25–32], post metal chelation [25–30,32], salt out [33], directional ice growth [33,34], etc.). Consequently, the resulting hydrogels tend to have complex and ambiguous internal structures, whose structural anisotropy and uniformity are not always quantitatively evaluated. There may also be a potential risk in the quality control of such hydrogel samples, since their properties tend to depend on the purities of the plant-derived components and the skill of operators etc. Under such circumstances, even though some of them show good performance, their complicated and unclear structures make it difficult to elucidate the relationship between structures and properties.

To address this situation, here we report a very simple anisotropic hydrogel that can provide a versatile platform for the construction of flexible sensors with directional sensing ability. This hydrogel was obtained in a one-pot reaction from two components, i.e., by magnetic orientation of titanate nanosheets (TiNS) [38,39] in water and subsequent in-situ formation of a polyacrylamide network [13,40–44]. TiNS is a sort of monolayer single crystal of TiO_6 octahedra with a ultrathin (0.75-nm thickness) and ultrawide (several-μm width) shape, and is magnetically orientable due to its anisotropic diamagnetic susceptibility [45,46]. The resulting gel (TiNS-gel) exhibited remarkable anisotropy in tensile modulus and ionic conductivity. As a mechanism of tensile anisotropy, the nanostructure of TiNS-gel was found to drastically change specifically in response to the stretching of the gel perpendicular to TiNS platelets. Furthermore, TiNS-gel changed its electrical resistance upon tensile deformation, demonstrating its potential utility as a flexible strain and force sensor. Given the clear relationship between its structure and properties, TiNS-gel is a useful platform for developing flexible devices with direction-selective strain and force sensing capabilities.

2. Materials and Methods

2.1. General

For deionization of aqueous dispersions of TiNS, a CF16RXII centrifuge equipped with a T15A41 rotor (Hitachi Koki, Tokyo, Japan) was used. For magnetic alignment of TiNS, a JMTD-10T100 superconducting magnet (Japan Superconductor Technology, Inc. (JASTEC), Kobe, Japan) with a bore of 100 mm was employed. Photoinduced radical polymerization was initiated with an OPM2-502H high-pressure mercury arc lamp (500 W) (USHIO, Tokyo, Japan). Small angle X-ray scattering (SAXS) measurements were conducted using a NANOPIX 3.5 m system equipped with a HyPix-6000 detector (Rigaku, Tokyo, Japan). Polarized optical microscopy (POM) images were taken using an Eclipse LV100POL optical polarizing microscope (Nikon, Tokyo, Japan). Mechanical tensile tests were performed using an ARES-G2 RW rheometer with a normal force sensor (TA Instruments, New Castle, DE, USA). Electrical resistance measurements were performed using a Keithley 2450 source meter (Tektronix, Beaverton, OR, USA).

Acrylamide (AAm) and *N*,*N*'-methylenebis(acrylamide) (BMAAm) were purchased from Tokyo Chemical Industry (TCI), Tokyo, Japan. Tetramethylammonium hydroxide (TMAOH; 15% water solution) and 2,2-diethoxyacetophenone (DEAP) were purchased from FUJIFILM Wako Pure Chemical, Osaka, Japan. The

commercially purchased regents were used without purification. An aqueous dispersion of TiNS was synthesized according to the literature [38,39]. Deionized water was obtained from a Millipore Milli-Q integral water purification system (Merk Millipore, Burlington, MA, USA).

2.2. Preparation of TiNS-Gel

TiNS-gel was prepared by the procedure we reported previously [13,42]. Briefly, an aqueous dispersion of TiNS was deionized by repeating the cycle of centrifugation of TiNS dispersion, collection of TiNS sediment, and redispersion of TiNS sediment with deionized water 12 times [41]. The deionized aqueous dispersion of TiNS (0.6, 0.8, or 1.0 wt%) was mixed with TMAOH (0.3 mM), AAm (6.0 wt%), MBAAm (0.06 wt%), and DEAP (0.08 wt%) and then filled into a glass cell with 2 mm-thick. The cell was placed in the bore of a superconducting magnet with applying a 10 T magnetic field applied in the in-plane direction of the glass-sandwiched cell for 2.5 h. The cell was then irradiated with a mercury arc light for 2.5 h to afford a film of TiNS-gel. For each of the following experiments, the film was trimmed into rectangular strips of appropriate lengths and widths (e.g., 12 mm × 3 mm) so that the alignment of TiNS platelets became perpendicular and parallel to the sides of the rectangle (Figure S1).

2.3. SAXS Analysis

A strip of TiNS-gel was irradiated with an X-ray beam (CuKα, wavelength = 1.5418 Å) in the direction perpendicular to the film plane with the sample–detector distance of 1400 mm to collect a 2D scattering image, where the scattering vector q and the position of the incident X-ray beam were calibrated using the scattering image of silver behenate as a standard sample. The 2D scattering image was converted into the corresponding intensity–q plot and intensity–azimuthal angle plot using Fit2D software version 18 (http://www.esrf.eu/computing/scientific/FIT2D/ (accessed on 1 July 2023)). For the intensity–azimuthal angle plot, the scattering intensity was integrated along the Debye-Scherrer ring with the q range of 0.1~1.0 nm^{-1}. For the SAXS measurement under tensile deformation of the gel, the relationship between the TiNS aligned direction and the stretched direction is shown in Figure 3.

2.4. Tensile Test

A strip of TiNS-gel was attached at its ends of the long axis with the sample stage and with the normal force sensor of a mechanical tester. With increasing the gap between the sample stage and the normal force sensor at a speed of 0.1 mm min^{-1}, the stress of the gel strip was recorded. The relationship between the alignment of TiNS platelets and the stretched direction is shown in the corresponding figures.

2.5. Evaluation of Strain/Force Sensing Ability

A strip of TiNS-gel was attached at its ends of the longer axis with copper wires, which connected to a source meter. The gel's ends were also attached to the sample stage and the normal force sensor of a mechanical tester. Upon increasing the gap between the sample stage and the normal force sensor at a speed of 0.1 mm min^{-1}, the electrical resistance and the stress of the gel strip were measured simultaneously. Alternatively, the gel strip connected to the source meter as above was pasted along the index finger with covering the second knuckle. Upon changing the bending angle of the knuckle among 0°, 45°, and 90°, the electrical resistance of the gel strip was measured. The resistance change ($\Delta R/R_0$) is defined as follows:

$$\Delta R/R_0 = (R - R_0)/R_0 \quad (1)$$

where R_0 and R were the initial resistance and resistance after sample stretching, respectively. The gauge factor (GF) and force sensitivity (FS), which are the indicators of the sensitivity of strain/force sensors, were calculated as follows:

$$GF = (\Delta R/R_0)/\Delta\varepsilon \quad (2)$$

$$FS = (\Delta R/R_0)/\Delta F \quad (3)$$

where $\Delta\varepsilon$ is the change in applied strain, while ΔF is the change in applied force.

3. Results and Discussion

3.1. Synthesis and Characterization of TiNS-Gel

Using the magnetic-alignment method as we have reported [13,42], films of TiNS-gel were synthesized (Figure 1a), where TiNS concentration was systematically changed (0.6, 0.8 and 1.0 wt%). 2D small-angle X-ray scattering (SAXS) measurements revealed a highly anisotropic and ordered arrangement of TiNS platelets in the gel. For example, TiNS-gel with [TiNS] = 0.8 wt% exhibited scattering specifically along the longitudinal direction as an array of regularly separated spots (Figure 1(bi)). Accordingly, the intensity–azimuthal angle plot obtained from the 2D scattering image showed two sharp peaks at 90° and 270° (Figure 1(bii)), indicating the alignment of TiNS platelets perpendicular to the magnetic field with an excellent order parameter of >0.95. In addition, the intensity–*q* plot obtained from the 2D scattering image showed a series of peaks corresponding to a layered structure of TiNS platelets with a uniform plane-to-plane distance of 35 nm (Figure 1(biii)). Such a large plane-to-plane distance, no less than 45 times larger than that of the thickness of a TiNS platelet, indicates the presence of strong electrostatic repulsion between them. Although the observation area of SAXS was limited by the size of the X-ray beam, polarized optical microscopy (POM) revealed that such a highly ordered arrangement of TiNS platelets was homogeneously present over a several centimeter size scale in the gel (Figure 1c). Overall, the combination of SAXS and POM analysis revealed the excellent structural anisotropy of TiNS-gel in a direct, quantitative, and global manner. This is in sharp contrast to the alignment evaluation of conventional anisotropic hydrogel sensors, which are usually based on the SEM images of gels after drying [21,24–29,31,33–36].

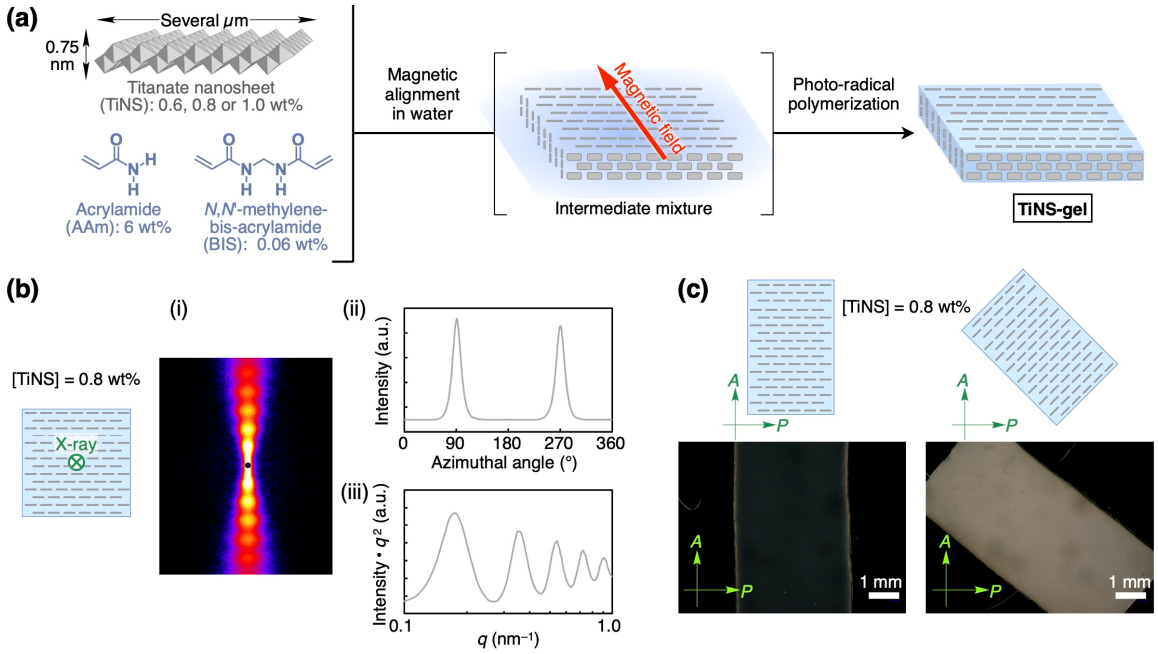

Figure 1. (**a**) Schematic illustration of the synthesis of TiNS-gel. (**b**) SAXS profiles of TiNS-gel: (**i**) 2D scattering pattern, (**ii**) intensity–azimuthal angle plot, and (**iii**) intensity–*q* plot. (**c**) POM images under crossed Nicols conditions of TiNS-gel with directing the alignment of TiNS platelets at angles of 0° (**left**) and 45° (**right**) relative to the polarizer. *P* and *A* denote the polarizer and analyzer, respectively.

Compared with other alignment methods such as shear-induced alignment and electric alignment, one attractive feature of magnetic alignment is its applicability to the alignment of thick samples due to the highly penetrative nature of magnetic fields. Another attractiveness of magnetic alignment is its high reproducibility. Indeed, multiple samples of TiNS-gel could be synthesized with good reproducibility, in terms of macroscopic homogeneity and microscopic anisotropy as confirmed by POM and SAXS (Figure S2). Although a drawback of the present method is that a 10 T magnetic field, which is not easily accessible in general, is indispensable for the alignment of diamagnetic TiNS, this problem would be addressed by using a ferromagnetic nanosheet $Ti_{0.8}Co_{0.2}O_2$ [47] in place of TiNS.

3.2. Mechanical Properties of TiNS-Gel

In our previous reports, the mechanical properties of TiNS-gel was investigated only in the compression of cubic samples for ease of operation [13,42]. Meanwhile, such compression is not very similar to the deformation that sensor films of flexible electronic devices undergo during their use. In addition, composite hydrogels such as TiNS-gel often exhibit quite different mechanical properties between compression and tensile deformation. Therefore, in the present work, we performed new tensile tests of TiNS-gel with stretching perpendicular and parallel to the alignment of TiNS platelets (Figure 2a). Regardless of the TiNS concentration, the modulus when stretched parallel to TiNS ($E_{//}$) was much higher than that when stretched perpendicular to TiNS ($E_{\perp}$) (Figure 2(ai–iii)). The anisotropic factor ($E_{//}/E_{\perp}$) was estimated to be 40~70, which manifests that TiNS-gel exhibits prominent mechanical anisotropy not only in compression as we reported previously [13,42] but also in tension. Also, the anisotropy factor of ~70 is at the top level among reported anisotropic hydrogels [19]. Reflecting on such direction-dependent hardness, the fracture strain ($^{max}\varepsilon$) was also direction dependent. Thus, TiNS-gel with [TiNS] = 1.0 wt% was stretchable up to 6.5 times in the direction perpendicular to TiNS ($^{max}\varepsilon_{\perp}$ = 550%) but was broken at 1.5 times upon parallel tensile ($^{max}\varepsilon_{//}$ = 47%).

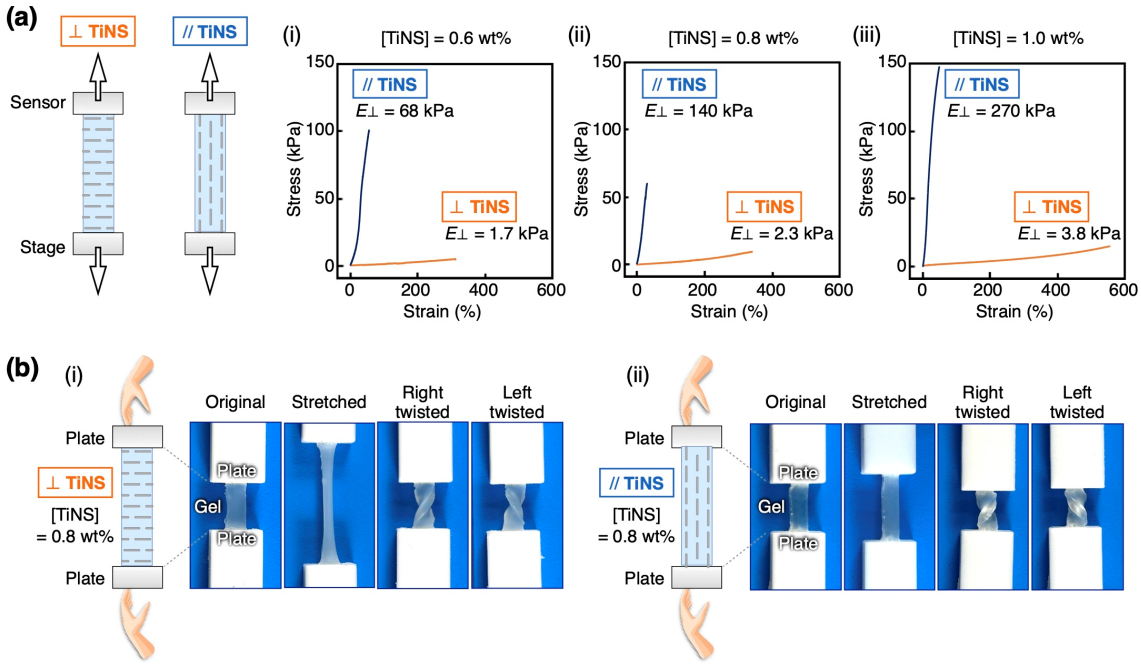

Figure 2. (**a**) Strain–stress curves of TiNS-gel upon tensile deformation along parallel (navy) and vertical (orange) to the alignment of TiNS platelets with TiNS concentrations of (**i**) 0.6, (**ii**) 0.8, and (**iii**) 1.0 wt%. (**b**) Optical images upon tensile and twist deformation of rectangular strips of TiNS-gel with TiNS platelets aligned (**i**) vertical and (**ii**) parallel to the longer axis of the rectangular shape.

In addition to the above uniaxial tensile test, a manual stretching and twisting of TiNS-gel could visualize its toughness and elasticity sufficient for application as strain/force sensors. Therefore, TiNS-gel was trimmed into rectangular strips with TiNS platelets aligned perpendicular (Figure 2(bi)) and parallel (Figure 2(bii)) to the long axis of the rectangle. The strips could be repeatedly stretched and twisted within the strain ranges blow their fracture points without notable crack formation and plastic deformation.

3.3. Mechanism for Tensile Anisotropy of TiNS-Gel though Nanostructure Change

To clarify the mechanism of the tensile anisotropy from the nanostructural viewpoints, TiNS-gel ([TiNS] = 0.8 wt%) was subjected to 2D SAXS measurement upon stretching perpendicular (Figure 3a) and parallel (Figure 3b) to the alignment of TiNS platelets. As described in the previous section, TiNS-gel before stretching exhibited a scattering pattern corresponding to the unidirectional orientation of TiNS platelets with a uniform plane-to-plane distance of 35 nm (Figure 3(ai–iii), original). However, when TiNS-gel was stretched in the direction perpendicular to TiNS platelet up to 25% strain, the scattering pattern changed to a more rounded shape with a shift toward the central region (Figure 3(ai), stretched), resulting in the broadening of the peaks in the intensity–azimuthal angle plot (Figure 3(aii), stretched) together with the broadening and smaller-q shift of the peaks in the intensity–q plot (Figure 3(aiii), stretched). Such changes indicate the orientational randomization of TiNS platelets [5] as well as the

increase and divergence of their plane-to-plane distance. Meanwhile, when the tensile force was released, the scattering profile became essentially similar to the original state (Figure 3(ai–iii), released), indicating the recovery of the original nanostructure. On the other hand, upon stretching parallel to TiNS platelets, the orientational order of TiNS platelets was hardly changed, while their plane-to-plane distance became narrower (Figure 3(bi–iii), stretched) [5]. When the tensile force was released, the plane-to-plane distance returned toward the original one (Figure 3(ai–iii), released). When the concentration of TiNS in the gel was varied between 0.6 and 1.0 wt%, essentially identical changes in the SAXS profiles upon tensile deformation were observed (Figures S3 and S4).

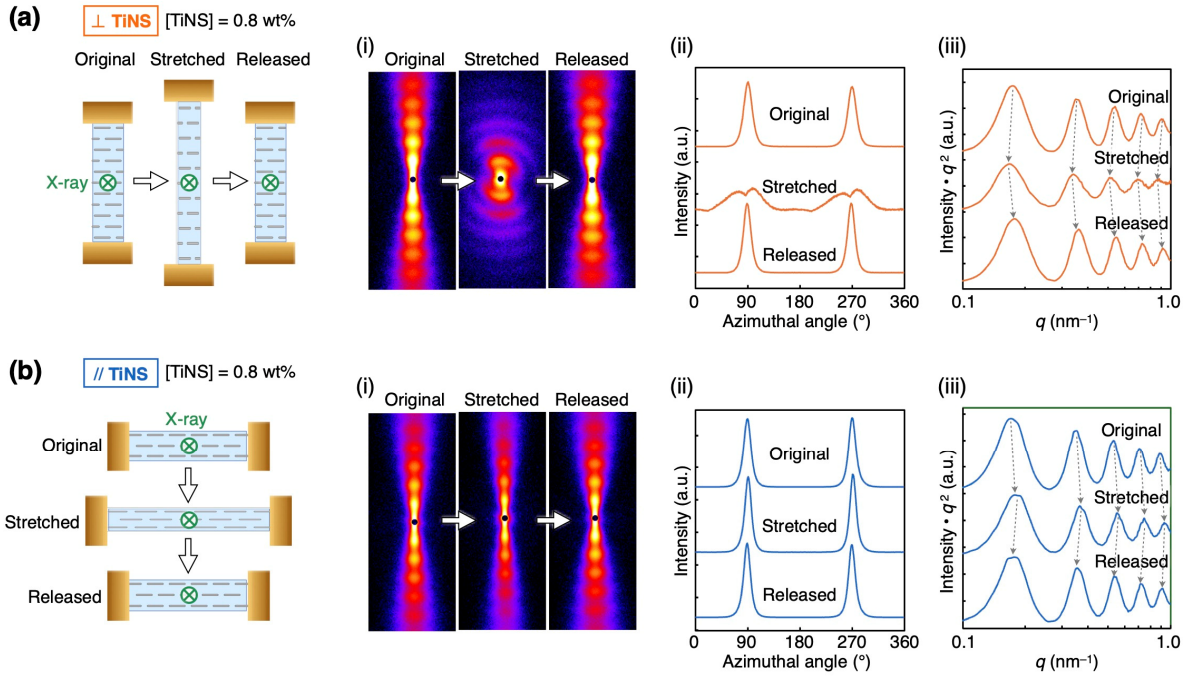

Figure 3. (**a**,**b**) Changes in the SAXS profiles of TiNS-gel ([TiNS] = 0.8 wt%) upon tensile deformation up to 25% strain along parallel (**a**) and vertical (**b**) to the alignment of TiNS platelets. Measurements were taken before deformation (original), after deformation (stretched), and then after releasing the force (released): (**i**) 2D SAXS images, (**ii**) intensity–azimuthal angle plots, and (**iii**) intensity–*q* plots.

Based on the nanostructural changes that occur upon tensile direction, as clarified above, the mechanism of the tensile anisotropy of TiNS-gel (Figure 2a) can be elucidated as follows. Upon parallel stretching (Figure 3b), the intrinsic hardness of TiNS platelets, the anchoring of polymer chains on TiNS platelets and the electrostatic repulsion between TiNS platelets are likely to cooperate to restrict the deformation of the gel, so that $E_{//}$ becomes high. In contrast, upon perpendicular stretching (Figure 3a), TiNS platelets are expected to buckle to lose their intrinsic hardness and polymer-anchoring ability, and to move away from each other to reduce the electrostatic repulsion, so that $E_{\perp}$ becomes small.

The nanostructural changes described above imply that TiNS-gel has a certain durability upon tensile deformation. The original nanostructure was recovered when the tensile force was released, regardless of the direction (Figure 3). A more serious issue regarding long-term durability is the evaporation of water, a general problem with all hydrogels, not just TiNS-gel. When a film of TiNS-gel (10 mm × 10 mm × 2 mm) was placed in open air (25 °C, 50% RH) for 6 h, the film contracted preferentially in the direction perpendicular to the TiNS platelets due to water evaporation (Figure S5(ai)), and its weight decreased to 54% (Figure S5(aii)). The film contracted preferentially in the direction perpendicular to the TiNS platelets (Figure S5(ai)). During this drying process, the alignment of the TiNS platelets remained intact (Figure S5(bi)), while the periodic distance of the layered TiNS platelet structure decreased (Figure S5(bii)), consistent with the contraction of the entire film.

3.4. Ion Conductivity of TiNS-Gel

In our previous studies on TiNS-gel, its mechanical [13,42], actuation [40,43], and optical [41,44] properties have been extensively studied, while its electrical properties have never been explored. In the present work, we begin with evaluating the anisotropy in ion conductivity of TiNS-gel. At an alternating current (AC) mode, the resistance of TiNS-gel ([TiNS] = 0.8 wt%) was measured in the direction perpendicular and parallel to the alignment of TiNS platelets (Figure 4a). Over a frequency range of 0.1~10^5 Hz, the resistance in the perpendicular

direction was one-order higher than that of the parallel direction (Figure 4(ai)). Furthermore, the phase difference also differs between the perpendicular and parallel measurements (Figure 4(aii)). These observations indicate that the ion migration parallel to TiNS platelets is smoother than the perpendicular one and that the capacitance parallel to TiNS platelets is larger than the perpendicular one.

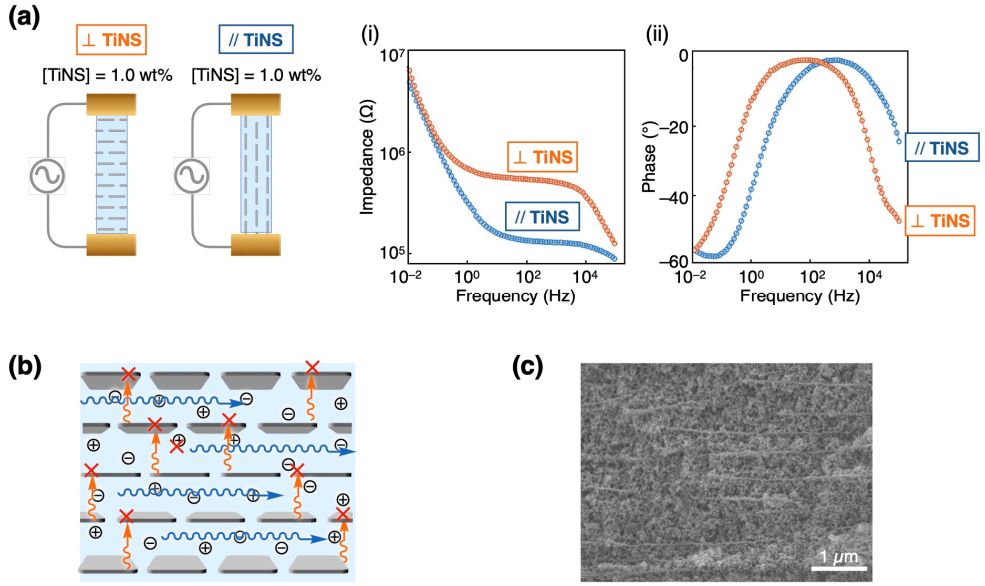

Figure 4. (**a**) Impedance–frequency (**i**) and phase–frequency (**ii**) curves of TiNS-gel measured along the direction parallel (navy) and vertical (orange) to TiNS. (**b**) Schematic illustration of ion transport in the anisotropic hydrogel. (**c**) Cross-sectional SEM image of the anisotropic hydrogel after fixation of the gel network and subsequent removal of water.

Such anisotropic resistance of TiNS-gel is attributable to the blocking of ion-migration by unidirectionally aligned TiNS platelets (Figure 4b,c). As depicted in the SAXS measurements (Figure 1b), TiNS platelets in TiNS-gel form a layered structure with a plane-to-plane distance of 35 nm. Given this structure, the ion-migration pathway is ensured in the direction parallel to TiNS platelets over a long range, while in the vertical direction, the pathway is intersected by TiNS platelets at each of the layer period. Although there exists a certain gap between neighboring TiNS platelets in same layer that would allow ions to migrate, the ratio of such gap relative to the whole area is negligibly small, as visualized by the scanning electron microscopy (SEM) cross-sectional image of the gel (Figure 4c), which was taken after fixation of the gel network by in-situ silica condensation and subsequent removal of water from the gel.

3.5. Resistance Change of TiNS-Gel upon Tensile Deformation

To evaluate the potential utility of TiNS-gel as a flexible strain sensor, we then investigated how TiNS-gel changes its electrical properties in response to the tensile deformation along perpendicular (Figure 5a) and parallel (Figure 5b) to the alignment of TiNS platelets, with resistance measured in the stretched direction. Upon perpendicular stretching of TiNS-gel ([TiNS] = 1.0 wt%) up to ~200% strain, the resistance change ($\Delta R/R_0$) raised to ~800% (Figure 5(ai)), demonstrating its sufficient sensitivity over a wide strain range. The resistance increased nonlinearly with strain, so that the gauge factor ($GF_\perp$) changed from 1.8 (0~50% strain) to 3.5 (60~110% strain) to 5.7 (120~160% strain). These *GF* values suggest that the sensitivity of the current system is moderate compared to other reported sensing systems based on anisotropic hydrogels [21–38]. This is probably because not only the macroscopic deformation of TiNS-gel but also the nanostructural change that occur upon perpendicular stretching, as clarified by our in-situ SAXS measurements (Figure 3a), contributed to the increase in resistance. The same tendency was observed regardless of the TiNS concentration in TiNS-gel (Figures S6 and S7).

Considering that the intrinsic ion conductivity of TiNS-gel is anisotropic (Figure 4) and that the nanostructure change of TiNS-gel occurs specifically depending on the tensile direction (Figure 3), the resistance change upon perpendicular stretching was expected to be different from that upon parallel stretching, which is favorable for directional strain sensing. However, the relationship between resistance change and tensile strain in parallel stretching differed only slightly from that in perpendicular stretching. The gauge factor of the parallel stretching ($GF_{//}$) at 0~25% strain was 2.0 (Figure 5(bi)), which was only 1.1 times higher than that of the perpendicular

stretching at the similar strain range ($GF_{\perp}$ = 1.8 at 0~50% strain; Figure 5(ai)). This unexpected result is likely because the anisotropy of resistance change is determined by the delicate balance of various anisotropic parameters. These parameters include not only ion conductivity and nanostructure change, but also macroscopic shape change, etc. [48,49]. Indeed, we confirmed that TiNS-gel exhibits a highly anisotropic Poisson's ratio upon stretching (Figure S8), which should also affect the anisotropy of resistance change. These anisotropic parameters do not always cooperate, but rather, they may compete to cancel their effects. In any case, to realize more directional strain sensing, further optimization is necessary, including the size of nanosheets, concentration, and components, as well as doping the gel with electron-conductive components. It should also be noted that, even for the latest flexible sensors based on anisotropic hydrogels, the anisotropy factors in *GF* are either undetermined [21,23–26,31,35] or moderate, ranging from 1.1 to 2.4 [22,27–30,32–34,36].

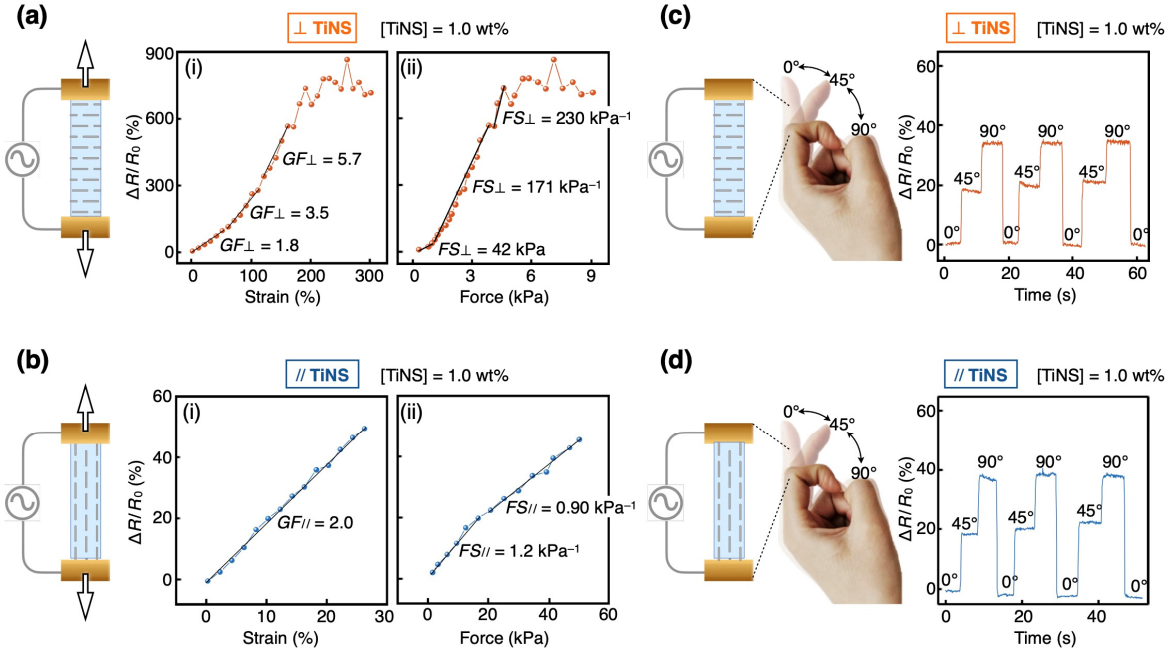

Figure 5. (**a**,**b**) Relative resistance change ($\Delta R/R_0$) of TiNS-gel ([TiNS] =1.0 wt%) upon tensile deformation along parallel (**a**) and vertical (**b**) to the alignment of TiNS platelets: plots of (**i**) $\Delta R/R_0$ versus strain and (**ii**) $\Delta R/R_0$ versus force. (**c**,**d**)(Application of TiNS-gel ([TiNS] =1.0 wt%) as a strain/force sensors for monitoring the bending motion of a finger, with directing the alignment of TiNS platelets vertical (**c**) and parallel (**d**) to the finger.

Meanwhile, current TiNS-gel already seems to have a great potential as a direction-selective force sensor. Indeed, the resistance change–force plots (Figure 5(aii,bii)) reveal a critical difference in the force sensitivity (*FS*) between the perpendicular and parallel stretching, where *FS* of perpendicular stretching (Figure 5(aii); $FS_{\perp}$ = 42~230 kPa^{-1}) was about two orders higher than that of $TiNS_{//}$-gel (Figure 5(bii); $FS_{//}$ = 0.9~1.2 kPa^{-1}). Such pronounced directional dependence of *FS* ($FS_{\perp} >> FS_{//}$; Figure 5a,b) is attributable to the direction dependency of tensile elastic modulus ($E_{\perp} << E_{//}$; Figure 2a); because TiNS-gel is about 70 times easier to stretch in the perpendicular direction than in the parallel direction, and because the resistance in the stretched direction generally increases with increasing tensile strain, forces applied in the direction perpendicular to TiNS platelets are more sensitively reflected in the resistance change. These observations suggest that when TiNS-gel receives tensile forces in many directions, it would respond specifically to forces perpendicular to TiNS platelets.

Finally, as a preliminary attempt to assess the practical utility as flexible wearable sensors, we used TiNS-gel to monitor the binding motion of a finger. Thus, TiNS-gel ([TiNS] = 1.0 wt%) was trimmed into a rectangular strip (12 mm × 3 mm) with the long axis of the rectangle perpendicular or parallel to the alignment of TiNS platelets (Figure S1), so that the gel strip was preferentially stretched along its long axis. The gel strip was pasted along the index finger with covering the second knuckle, and its resistance change ($\Delta R/R_0$) was monitored when the bending angle of the knuckle was changed among 0°, 45°, and 90° (Figure 5c,d). As a result, the bending and stretching motion of the finger could be monitored in real time with satisfactory sensitivity and low noise level over multiple cycles (Figure 5c,d).

4. Conclusions

We report an ultimately simple anisotropic hydrogel, which can be synthesized in a one-pot reaction from only two components. Despite its simple synthesis, our hydrogel possesses near-perfectly aligned structure and exhibits remarkable anisotropy in tensile modulus, nanostructural transformability, and ion conductivity, as well as strain/forces responsiveness in its electrical resistance. These observations suggest that our hydrogel will serve as a useful platform for the development of flexible devices with directional strain/force sensing capabilities. The clear structure–function relationship, which is a characteristic of our hydrogel compared with other anisotropic hydrogels developed for sensing applications, would provide new insight into anisotropy-driven mechanisms in soft sensing materials. Furthermore, this work would also contribute to theoretical elucidation of how nanoscopic structural orientation governs macroscopic sensing behavior, since the simple, well-defined, and near-perfectly anisotropic structure of this hydrogel is beneficial for theoretical modeling. Possible interesting challenges based on this hydrogel include the optimization of compositions to realize directional strain sensing, the introduction of electrically conductive components to improve sensitivity, and the introduction of photo-functional components for strain and force sensing by color change.

Supplementary Materials: The following supporting information can be downloaded at: https://media.sciltp.com/articles/others/2506251057370684/MI_882_SM-FC.pdf. Figure S1: Schematic illustration of the trimming of TiNS-gel into two types of rectangular strips; Figure S2: Reproducibility of TiNS-gel synthesis at 0.8 wt% was confirmed by SAXS and POM characterization of two additional batches; Figure S3: SAXS reveals anisotropic structural changes in TiNS-gel (0.6 wt%) under tensile strain along parallel and vertical directions; Figure S4: SAXS reveals anisotropic structural changes in TiNS-gel (1.0 wt%) under tensile strain along parallel and vertical directions; Figure S5: TiNS-gel (0.8 wt%) shows dimensional and structural changes during drying; Figure S6: Relationship between $\Delta R/R_0$ and applied tensile strain and force of TiNS-gel at [TiNS] = 0.6 wt%; Figure S7: Relationship between $\Delta R/R_0$ and applied tensile strain and force of TiNS-gel at [TiNS] = 0.8 wt%. Figure S8: TiNS-gel (0.8 wt%) exhibits different Poisson ratios depending on the tensile direction.

Author Contributions: Y.X., S.W. and Y.I. conceived the project. Y.X and S.W. designed and performed all experiments. Y.Z. conducted the tensile measurements. K.Y., T.W., Y.H. and S.O. helped the preparation of TiNS-gel samples. H.K. conducted a part of SAXS measurements. Y.X, S.W, D.Z., F.C. and Y.I. analyzed the data and wrote the manuscript with the input of all other authors. All authors have read and agreed to the published version of the manuscript.

Funding: This work was supported by JST CREST Grant Number JPMJCR22B1.

Data Availability Statement: The data supporting this article have been included as part of the Supplementary Materials. Further data is available upon reasonable request from the authors.

Acknowledgments: We thank J. Liu (RIKEN) for SAXS measurements. Y. Xie acknowledges the Chinese Scholarship Council scholarship (No. 202303270021). S.W. acknowledges the Junior Research Associate (JRA) Program from RIKEN and JSPS for a Young Scientist Fellowship.

Conflicts of Interest: There are no conflict of interest to declare.

References

1. Zhang, Z.; Yang, J.; Wang, H.; Wang, C.; Gu, Y.; Xu, Y.; Lee, S.; Yokota, T.; Haick, H.; Someya, T.; et al. A 10-micrometer-thick nanomesh-reinforced gas-permeable hydrogel skin sensor for long-term electrophysiological monitoring. *Sci. Adv.* **2024**, *10*, eadj5389.
2. Li, Y.; Liu, C.; Zou, H.; Che, L.; Sun, P.; Yan, J.; Liu, W.; Xu, Z.; Yang, W.; Dong, L.; et al. Integrated wearable smart sensor system for real-time multi-parameter respiration health monitoring. *Cell Rep. Phys. Sci.* **2023**, *4*, 101191.
3. Xia, S.; Zhang, Q.; Song, S.; Duan, L.; Gao, G., Bioinspired dynamic cross-linking hydrogel sensors with skin-like strain and pressure sensing behaviors. *Chem. Mater.* **2019**, *31*, 9522–9531.
4. Gong, J., Double-network hudrogels with extremely high mechanical strength. *Adv. Mater.* **2003**, *15*, 1155–1158.
5. Wang, X.; Li, Z.; Wang, S.; Sano, K.; Sun, Z.; Shao, Z.; Takeishi, A.; Matsubara, S.; Okumura, D.; Sakai, N; et al. Mechanical nonreciprocity in a uniform composite material. *Science* **2023**, *380*, 192–198.
6. Hu, L.; Chee, P.L.; Sugiarto, S.; Yu, Y.; Shi, C.; Yan, R.; Yao, Z.; Shi, X.; Zhi, J.; Kai, D.; et al. Hydrogel-based flexible electronics. *Adv. Mater.* **2023**, *35*, e2205326.
7. Gao, Q.; Sun, F.; Li, Y.; Li, L.; Liu, M.; Wang, S.; Wang, Y.; Li, T.; Liu, L.; Feng, S.; et al. Biological tissue-inspired ultrasoft, ultrathin, and mechanically enhanced microfiber composite hydrogel for flexible bioelectronics. *Nanomicro Lett.* **2023**, *15*, 139.
8. Bai, M.; Chen, Y.; Zhu, L.; Li, Y.; Ma, T.; Li, Y.; Qin, M.; Wang, W.; Cao, Y.; Xue, B., Bioinspired adaptive lipid-integrated bilayer coating for enhancing dynamic water retention in hydrogel-based flexible sensors. *Nat. Commun.* **2024**, *15*, 10569.
9. Park, B.; Shin, J.H.; Ok, J.; Park, S.; Jung, W.; Jeong, C.; Choy, S.; Jo, Y.J.; Kim, T.-i., Cuticular pad–inspired selective frequency damper for nearly dynamic noise–free bioelectronics. *Science* **2022**, *376*, 624–629.
10. Zhao, Z.; Liu, J.; Wu, M.; Yao, X.; Wang, H.; Liu, X.; He, Z.; Song, X., A soft, adhesive self-healing naked-eye

strain/stress visualization patch. *Adv. Mater.* **2024**, *36*, e2307582.
11. Li, W.; Zheng, S.; Zou, X.; Ren, Y.; Liu, Z.; Peng, W.; Wang, X.; Liu, D.; Shen, Z.; Hu, Y.; et al. Tough hydrogels with isotropic and unprecedented crack propagation resistance. *Adv. Funct. Mater.* **2022**, *32*, 2207348.
12. Xie, Y.; Shi, X.; Gao, S.; Lai, C.; Lu, C.; Huang, Y.; Zhang, D.; Nie, S.; Xu, F.; Chu, F., Biomimicking natural wood to fabricate isotropically super-strong, tough, and transparent hydrogels for strain sensor and triboelectric nanogenerator applications. *J. Mater. Chem. A* **2024**, *12*, 5124–5132.
13. Liu, M.; Ishida, Y.; Ebina, Y.; Sasaki, T.; Hikima, T.; Takata, M.; Aida, T., An anisotropic hydrogel with electrostatic repulsion between cofacially aligned nanosheets. *Nature* **2015**, *517*, 68–72.
14. Mredha, M.T.I.; Guo, Y.Z.; Nonoyama, T.; Nakajima, T.; Kurokawa, T.; Gong, J.P., A facile method to fabricate anisotropic hydrogels with perfectly aligned hierarchical fibrous structures. *Adv. Mater.* **2018**, *30*, 1704937.
15. Hiratani, T.; Kose, O.; Hamad, W.Y.; MacLachlan, M.J. Stable and sensitive stimuli-responsive anisotropic hydrogels for sensing ionic strength and pressure. *Materals Horiz.* **2018**, *5*, 1076–1081.
16. Zhu, Q.L.; Du, C.; Dai, Y.; Daab, M.; Matejdes, M.; Breu, J.; Hong, W.; Zheng, Q.; Wu, Z.L. Light-steered locomotion of muscle-like hydrogel by self-coordinated shape change and friction modulation. *Nat. Commun.* **2020**, *11*, 5166.
17. Liang, X.; Chen, G.; Lin, S.; Zhang, J.; Wang, L.; Zhang, P.; Wang, Z.; Wang, Z.; Lan, Y.; Ge, Q.; et al. Anisotropically fatigue-resistant hydrogels. *Adv. Mater.* **2021**, *33*, e2102011.
18. Xue, P.; Bisoyi, H.K.; Chen, Y.; Zeng, H.; Yang, J.; Yang, X.; Lv, P.; Zhang, X.; Priimagi, A.; Wang, L.; et al. Near-infrared light-driven shape-morphing of programmable anisotropic hydrogels enabled by MXene nanosheets. *Angew. Chem. Int. Eddition* **2021**, *60*, 3390–3396.
19. Sano, K.; Ishida, Y.; Aida, T., Synthesis of anisotropic hydrogels and their applications. *Angew. Chem. Int. Ed.* **2018**, *57*, 2532–2543.
20. Uchida, N.; Ishida, Y., Macroscopically oriented polymeric soft materials: Synthesis and functions. **2019**, *51*, 709–719.
21. Xiong, J.; Wu, W.; Hu, Y.; Guo, Z.; Wang, S., An anisotropic conductive hydrogel for strain sensing and breath detection. *Appl. Mater. Today* **2023**, *34*, 101909.
22. Zhang, Y.; Fu, Z.; Wu, T.; Ren, B.; Chen, J.; Xie, F.; Leng, W.; Shi, J.; Lu, Y., Skin-inspired ultra-tough, self-healing anisotropic wood-based electronic skin for multidimensional sensing. *Chem. Eng. J.* **2024**, *496*, 154000.
23. Teng, Y.; Zhang, Z.; Cui, Y.; Su, Z.; Godwin, M.; Chung, T.; Zhou, Y.; Leontowich, A.F.G.; Islam, M.S.; Tam, K.C.; et al. High-sensitivity and flexible motion sensing enabled by robust, self-healing wood-based anisotropic hydrogel composites. *Small* **2025**, *21*, 2500944.
24. Geng, L.; Liu, W.; Fan, B.; Wu, J.; Shi, S.; Huang, A.; Hu, J.; Peng, X., Anisotropic double-network hydrogels integrated superior performance of strength, toughness and conductivity for flexible multi-functional sensors. *Chem. Eng. J.* **2023**, *462*, 142226.
25. Chen, L.; Chang, X.; Chen, J.; Zhu, Y., Ultrastretchable, antifreezing, and high-performance strain sensor based on a muscle-inspired anisotropic conductive hydrogel for human motion monitoring and wireless transmission. *ACS Appl. Mater. Interfaces* **2022**, *14*, 43833–43843.
26. Zhang, Y.; Jing, X.; Zou, J.; Feng, P.; Wang, G.; Zeng, J.; Lin, L.; Liu, Y.; Mi, H.; Nie, S., Mechanically robust and anti-swelling anisotropic conductive hydrogel with fluorescence for multifunctional sensing, *Adv. Funct. Mater.* **2024**, *34*, 2410698.
27. Hang, C.; Guo, Z.; Li, K.; Yao, J.; Shi, H.; Ge, R.; Liang, J.; Quan, F.; Zhang, K.; Tian, X.; et al. Anisotropic hydrogel sensors with muscle-like structures based on high-absorbent alginate fibers. *Carbohydr. Polym.* **2025**, *349*, 123015.
28. Wang, W.; Deng, X.; Luo, C., Anisotropic hydrogels with high-sensitivity and self-adhesion for wearable sensors. *J. Mater. Chem. C* **2023**, *11*, 196–203.
29. Lin, H.; Wang, R.; Xu, S.; Li, X.; Song, S., Tendon-inspired anisotropic hydrogels with excellent mechanical properties for strain sensors. *Langmuir* **2023**, *39*, 6069–6077.
30. Ghosh, A.; Pandit, S.; Kumar, S.; Pradhan, D.; Das, R.K., Human muscle inspired anisotropic and dynamic metal ion-coordinated mechanically robust, stretchable and swelling- resistant hydrogels for underwater motion sensing and flexible supercapacitor application. *ACS Appl. Mater. Interfaces* **2024**, *16*, 62743–62761.
31. Huang, S.; Xiao, R.; Lin, S.; Wu, Z.; Lin, C.; Jang, G.; Hong, E.; Gupta, S.; Lu, F.; Chen, B.; et al. Anisotropic hydrogel microelectrodes for intraspinal neural recordings in vivo. *Nat. Commun.* **2025**, *16*, 1127.
32. Lin, H.; Yuan, W.; Zhang, W.; Dai, R.; Zhang, T.; Li, Y.; Ma, S.; Song, S., Strong and tough anisotropic short-chain chitosan-based hydrogels with optimized sensing properties for flexible strain sensors. *Carbohydr. Polym.* **2025**, *348*, 122781.
33. Fu, X.; Tong, H.; Zhang, X.; Zhang, K.; Douadji, L.; Kang, S.; Luo, J.; Pan, Z.; Lu, W., Anisotropic hydrogels with multiscale hierarchy based on ionic conductivity for flexible sensors. *ACS Appl. Polym. Mater.* **2023**, *5*, 9876–9887.
34. Chen, S.; Guo, B.; Yu, J.; Yan, Z.; Liu, R.; Yu, C.; Zhaoa, Z.; Zhang, H.; Yao, F.; Li, J., A polypyrrole-dopamine/poly(vinyl alcohol) anisotropic hydrogel for strain sensor and bioelectrodes. *Chem. Eng. J.* **2024**, *486*, 150182.

35. Shang, M.; Ma, S.; Ma, J.; Guo, L.; Liu, C.; Xu, X., Somatosensory actuators based on light-responsive anisotropic hydrogel for storage encryption of information systems. *Chem. Eng. J.* **2024**, *496*, 153895.
36. Zhanga, X.; Langb, B.; Yu, W.; Jia, L.; Zhu, F.; Xue, Y.; Wu, X.; Qin, Y.; Chen, W.; Wang, Y.; et al. Magnetically induced anisotropic conductive hydrogels for multidimensional strain sensing and magnetothermal physiotherapy. *Chem. Eng. J.* **2023**, *474*, 145832.
37. Chen, Z.; Wang, H.; Cao, Y.; Chen, Y.; Akkus, O.; Liu, H.; Cao, C., Bio-inspired anisotropic hydrogels and their applications in soft actuators and robots. *Matter* **2023**, *6*, 3803–3837.
38. Sasaki, T.; Watanabe, M.; Hashizume, H.; Yamada, H.; Nakazawa, H. Macromolecule-like aspects for a colloidal suspension of an exfoliated titanate. Pairwise association of nanosheets and dynamic reassembling process initiated from it. *J. Am. Chem. Soc.* **1996**, *118*, 8329–8335.
39. Tanaka, T.; Ebina, Y.; Takada, K.; Kurashima, K.; Sasaki, T., Oversized titania nanosheet crystallites derived from flux-grown layered titanate single crystals. *Chem. Mater.* **2003**, *15*, 3564–3568.
40. Kim, Y.S.; Liu, M.; Ishida, Y.; Ebina, Y.; Osada, M.; Sasaki, T.; Hikima, T.; Takata, M.; Aida, T., Thermoresponsive actuation enabled by permittivity switching in an electrostatically anisotropic hydrogel. *Nat. Mater.* **2015**, *14*, 1002–1007.
41. Sano, K.; Kim, Y.S.; Ishida, Y.; Ebina, Y.; Sasaki, T.; Hikima, H.; Aida, T. Photonic water dynamically responsive to external stimuli. *Nat. Commun.* **2016**, *7*, 12559.
42. Sano, K.; Arazoe, Y.; Ishida, Y.; Ebina, Y.; Osada, M.; Sasaki, T.; Hikima, T.; Aida, T., Extra-large mechanical anisotropy of a hydrogel with maximized electrostatic repulsion. *Angew. Chem. Int. Ed.* **2018**, *57*, 12508–12513.
43. Sun, Z.; Yamauchi, Y.; Araoka, F.; Kim, Y.S.; Bergueiro,J.; Ishida, Y.; Ebina, Y.; Sasaki, T.; Hikima, T.; Aida, T., An Anisotropic hydrogel actuator enabling earthworm-like directed peristaltic crawling. *Angew. Chem. Int. Ed.* **2018**, *57*, 15772–15776.
44. Zhan, Y.; Ogawa, D.; Sano, K.; Wang, X.; Araoka, F.; Sakai, N.; Sasaki, T.; Ishida, Y., Reconfigurable photonic crystal reversibly exhibiting single and double structural colors. *Angew. Chem. Int. Ed.* **2023**, *62*, e202311451.
45. Gabriel, J.-C. P.; Camerel, F.; Lemaire, B.J.; Desvaux, H.; Davidson, P.; Batail, P. Swollen liquid-crystalline lamellar phase based on extended solid-like sheets. *Nature* **2001**, *413*, 504–508.
46. Hu, H.; Gopinadhan, M.; Osuji, C.O., Directed self-assembly of block copolymers: A tutorial review of strategies for enabling nanotechnology with soft matter. *Soft Matter* **2014**, *10*, 3867–3889.
47. Osada, M.; Ebina, Y.; Fukuda, K.; Ono, K.; Takada, K.; Yamaura, K.; Takayama-Muromachi, E.; Sasaki, T., Ferromagnetism in two-dimensional $Ti_{0.8}Co_{0.2}O_2$ nanosheets. *Phys. Rev. B* **2006**, *73*, 153301.
48. Qu, M.; Xie, Z.; Liu, S.; Zhang, J.; Peng, S.; Li, Z.; Lin, C.; Nilsson, F., Electric resistance of elastic strain sensors—Fundamental mechanisms and experimental validation. *Nanomaterials* **2023**, *13*, 1813.
49. Vázquez-Torres, N.A.; Benítez-Martínez, J.A.; Vélez-Cordero, J.R.; Sánchez-Arévalo, F.M., Experimental and numerical characterization of a flexible strain sensor based on polydimethylsiloxane polymeric network and MWCNT's. *J. Polym. Res.* **2024**, *31*, 211.

Article

Photochemical Bubble Generation from Polymer Films: Dependence on Molecular Structure and Application for Ultrasound Imaging

Pranaya P. Ghate [1], Christopher Gatpandan [2], Mohammed N. Almtiri [3], Yahya J. Almuallem [3], Rabih O. Al-Kaysi [3], and Christopher J. Bardeen [4,*]

[1] Department of Chemical and Environmental Engineering, University of California, Riverside, CA 92521, USA
[2] School of Medicine Center for Simulated Patient Care (CSPC), University of California, Riverside, CA 92521, USA
[3] College of Science and Health Professions-3124, King Saud bin Abdulaziz University for Health Sciences, and King Abdullah International Medical Research Center (Nanomedicine), Ministry of National Guard Health Affairs, Riyadh 11426, Kingdom of Saudi Arabia
[4] Department of Chemistry, University of California, Riverside, CA 92521, USA
* Correspondence: christopher.bardeen@ucr.edu

Received: 30 May 2025; Revised: 18 June 2025; Accepted: 20 June 2025; Published: 27 June 2025

Abstract: Photochemical generation of N_2 gas by aromatic azide derivatives dissolved in transparent polymers provides a way to generate bubbles without direct heating. In this work, it is shown that molecules 2-azidoanthracene ($2N_3$-AN), 2-(azidomethyl)anthracene ($2N_3$-CH_2-AN), 1-azidopyrene (N_3-PY), and 1-(azidomethyl)pyrene (N_3-CH_2-PY) are all capable of generating stable surface layers of N_2 bubble after exposure to 365 nm light. Bubble formation is modeled as a multistep kinetic process that involves molecular photolysis, gas transport through the polymer, and bubble nucleation in water. Direct conjugation of the azide substituent to the aromatic core leads to more rapid photolysis and facile bubble formation, but even azides with relatively slow reaction rates can generate dense bubble layers if high light intensities are used. Rapid transport of the photogenerated N_2 gas through the polymer appears to be general, with poly(methyl methacrylate), polystyrene and polycarbonate all supporting robust bubble growth. The photoinduced bubble layer was shown to significantly enhance the visibility of a coated glass pipette when imaged by an ultrasound instrument. The ability to prepare polymer coatings that undergo photochemical gas evolution provides a new functionality that may be useful in medical imaging applications.

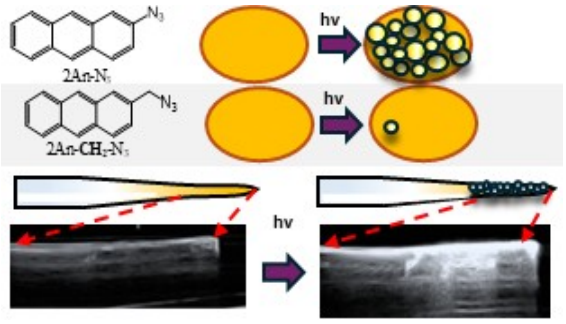

Keywords: polymers; azide; bubble generation; ultrasound imaging; photolysis

1. Introduction

Stimuli-responsive polymer materials have potential applications in a wide variety of areas, including actuation, sensing, and drug delivery [1–3]. The stimulus can take many forms, including changes in temperature, pH, or humidity. Light is a particularly attractive stimulus because it does not require physical contact with the material or changing the chemical environment. The response can also take many forms and usually involves a change in physical properties like size, optical transmission, or surface morphology. In particular, the initiation of a phase change can have dramatic effects. For example, the generation of a gas from a liquid or solid leads to bubble formation that dramatically modifies material properties like fluid drag [4,5], light transmission [6,7], acoustic wave propagation [8–12], force transmission [13], and heat transport [14]. Photogenerated bubbles are often transient, however, because they are composed of vaporized liquid, usually water [15–19]. Such bubbles are unstable due to recondensation of the vapor after the heat source is removed [20]. Azide photolysis in crystals [21] and polymer hosts [22] provides a photochemical route to stable bubbles composed of N_2 gas. In the polymer system, the N_2 gas rapidly migrates to the surface and nucleates into a dense layer of bubbles that can survive for days under water. These bubbles could be patterned across the surface by controlling the spatial distribution of the photolysis light, and

they adhered to the polymer film with sufficient strength to modify its buoyancy. For example, exposure to 365 nm light could induce a submerged polymethyl(methacrylate) (PMMA) film to float to the water surface.

The experimental demonstration of photochemical bubble evolution validated the general concept but left open some questions and challenges. The first question concerns whether the photochemical bubble strategy can be generalized to other azide derivatives and polymer systems. To address this question, we must gain a better understanding of how bubble evolution depends on parameters like photochemical reaction rate, light intensity, and polymer matrix. The second question is whether there exists a practical application for this phenomenon. While buoyancy changes are good for demonstration purposes, it would be more compelling to identify an existing technology and show how it could directly benefit from the ability to generate stable bubble layers after exposure to light.

In this paper, we extend our earlier studies on bubble formation by 2-azidoanthracene ($2N_3$-AN) dissolved in PMMA to new azide derivatives 2-(azidomethyl)anthracene ($2N_3$-CH_2-AN), 1-azidopyrene (N_3-PY), and 1-(azidomethyl)pyrene (N_3-CH_2-PY) as well as additional polymer systems. We examine the dependence of the azide photodecomposition rate on azide structure in both dilute liquid solution and in solid polymers. We find that direct conjugation of the azide substituent to the aromatic core leads to more rapid photolysis and more facile bubble formation, but even azides with relatively slow reaction rates can generate dense bubble layers if high light intensities are used. Bubble formation can be modeled as a multistep process whose overall rate depends on sequential steps, including molecular photolysis, gas transport through the polymer, and bubble nucleation in water. Rapid transport of the photogenerated N_2 gas through the polymer appears to be a general phenomenon, and other transparent polymers including polystyrene and polycarbonate also support robust bubble growth. Lastly, we demonstrate that a photogenerated bubble layer can dramatically enhance contrast in ultrasound imaging, suggesting that this phenomenon could be useful for medical imaging. The ability to prepare polymer coatings that are photochemically active provides a way to create new types of in situ functionality for devices that operate in challenging environments, like underwater or in biological media.

2. Experimental

2.1. Sample Preparation

The synthesis and characterization of $2N_3$-AN has been reported previously [22,23]. The synthesis and characterization of $2N_3$-CH_2-AN, N_3-PY, and N_3-CH_2-PY are described in the Supplementary Information. To make polymer films, the azides were dissolved in HPLC-grade chloroform (Fisher Scientific, USA) under low-light conditions and mixed with a solution of poly(methyl methacrylate) (PMMA, Sigma-Aldrich, USA, average molecular weight ~120,000) in $CHCl_3$. Polystyrene from Sigma-Aldrich (average Mw 280,000) and polycarbonate resin from Acros Organics, USA (average MW 45000) were also used to make films.

Bubble nucleation from the polymer–water interface is strongly influenced by the underlying surface topography. Microscale roughness has previously been shown to facilitate heterogeneous gas nucleation into bubbles by lowering the free energy barrier for phase separation [22,24,25]. To ensure reproducible bubble growth conditions across all samples, polymer films were cast on top of silica-blasted glass slides with a measured RMS roughness of 22 ± 4 μm. This roughened glass acted as a template to ensure uniform roughness for all polymer films. The azide/polymer solution was deposited onto the rough glass surface inside a 1 in. diameter glass cylinder to limit spreading and ensure consistent film diameter and thickness. After enough chloroform had evaporated to make the mixture highly viscous, the glass cylinder was removed, and the films were kept over countertop to dry overnight. After drying, the films were peeled off the roughened glass template to create free-standing polymer samples. The film thicknesses were measured to be 150 ± 25 μm using a Mitutoyo 543–793–10 ID-S112TX Digimatic Indicator (Japan).

2.2. Microscopy

To image bubble formation, the azide/PMMA film was suspended in a water-filled Petri dish with the textured side facing down. The sample was imaged using a stereo microscope model IX50-S8F2 (Olympus Optical Co. Ltd, Japan) with a 4.5× objective and exposed to light from a AloneFire SV-13 UV flashlight (USA) at 365 nm. The light intensity was attenuated with glass neutral density filters (ThorLabs USA) and measured using an Ophir Vega power meter (USA). The light irradiation area was 4.91 cm^2, and a 0.015 cm^2 area was imaged using an AmScope MU1000 digital camera (USA). To calculate bubble volume per unit area, frames were extracted from videos at specific time points. Two-dimensional images were analyzed to measure bubble diameters *d* using the Microsoft Paint application(Paint Windows 11.2503.381.0) to document pixel counts, which were

converted to microns. Individual bubble volumes were calculated with the formula $V = \frac{1}{6}\pi d^3$ and summed up, then divided by the imaged area to obtain the areal volume of N_2 gas.

2.3. Spectroscopy

Spectroscopic measurements were carried out using a quartz cell with a path length of 1 cm. The steady state UV-vis absorption was measured using a Varian CARY-60 spectrometer (Agilent Technologies, USA). To monitor the reaction's progress, the azide samples' absorption spectra were collected at 1-s intervals while exposed to 365 nm light from an AloneFire SV-13 UV light source (China). The 365 nm light intensity was controlled by translating the sample with respect to the diverging beam. The reaction rates for all molecules were determined using global fitting [26] implemented using Origin software (OriginLab, USA, academic version 2017). This analysis utilized a single exponential rate time constant to simultaneously fit the time dependent changes for at least 50 wavelengths across the absorption spectrum.

2.4. Ultrasound Measurement

A 2 mm diameter glass pipette was dipped into the azide/PMMA solution and allowed to dry in air. The coated pipette was suspended in a clear acrylic jar filled with water. Ultrasound imaging was performed using a TE7 Max/Diagnostic Ultrasound System (Shenzhen Mindray Bio-Medical Electronics Co., Ltd, Shenzhen, China) with a L14-6s linear array transducer and scanned in B mode. Aquasonic 100 Ultrasound Gel was applied to the interface of the probe and jar to improve acoustic coupling.

3. Results and Discussion

The four molecules shown in Scheme 1 were synthesized using standard methods as detailed in the Supplementary Information (Supplementary Figures S1–S14). The effect of the azide group on the molecular excited states depends on how it is attached to the aromatic core. Figure 1a compares the absorption spectra of unsubstituted anthracene with that of $2N_3$-AN and $2N_3$-CH_2-AN, while Figure 1b makes the same comparison for the pyrene azides. For both anthracene and pyrene cores, direct attachment of the N_3 group resulted in a large redshift (~25 nm) and reshaping of the absorption spectrum. However, if a methylene group was inserted between the N_3 and the aromatic core, then the original core absorption was largely preserved, albeit with a roughly 10 nm redshift in the case of N_3-CH_2-PY. For both $2N_3$-AN and N_3-PY, direct attachment of the N_3 to the conjugated ring likely creates new charge-transfer character the excited state due to the electron-withdrawing azide group. Similar effects have been observed for other aromatic azides [23,27,28].

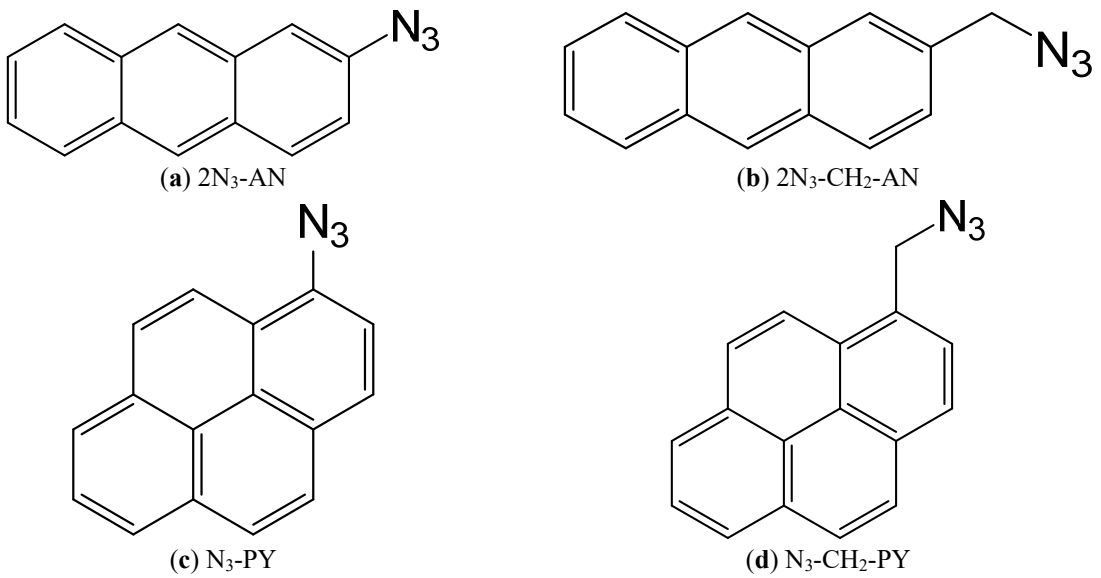

(**a**) $2N_3$-AN (**b**) $2N_3$-CH_2-AN

(**c**) N_3-PY (**d**) N_3-CH_2-PY

Scheme 1. The molecular structure of four molecules studied in this paper (**a**) 2-azidoanthracene $2N_3$-AN, (**b**) 2-(azidomethyl)anthracene $2N_3$-CH_2-AN, (**c**) 1-azidopyrene N_3-PY, and (**d**) 1-(azidomethyl)pyrene N_3-CH_2-PY.

All the azide derivatives in Scheme 1 undergo photoinduced decomposition to the corresponding nitrene when exposed to ultraviolet (UV) light. Subsequent reactions can lead to formation of nitro groups and other products [22,29,30], but those are not the focus of this paper. The pronounced absorption changes provide a

convenient way to monitor the disappearance of the parent azide. Figure 2 shows a series of UV-Vis spectra taken during photolysis of N_3-PY and $2N_3$-CH_2-AN in $CHCl_3$ solution. Both samples show a well-defined spectral evolution with clear isosbestic points, indicating a single-step transformation to a photoproduct that absorbs across the visible region. Visually, the samples turn from light yellow to brown under light exposure. The other derivatives exhibited similar spectral changes (Supplementary Figure S15). Table 1 provides the measured reaction rates for 365 nm excitation for all four azides in $CHCl_3$. Since these sample had a relatively low absorbance at 365 nm, we can make the assumption that the intensity variation across the sample is negligible. Under the assumption of constant 365 nm light intensity, dividing the observed reaction rate by the absorption coefficient allows us to estimate relative quantum yields for the azide photolysis. These yields are also given in Table 1, with the highest relative yield (N_3-PY) normalized to 1.0. It is apparent that direct conjugation of the N_3 group to the aromatic core results in a noticeable enhancement in the photolysis quantum yield, especially for pyrene.

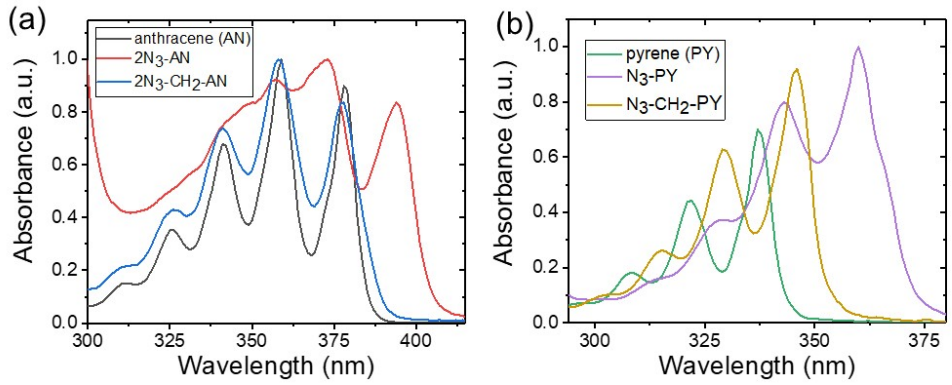

Figure 1. (**a**) Absorption spectra of anthracene AN (black), 2-azidoanthracene $2N_3$-AN (red) and 2-(azidomethyl)anthracene $2N_3$-CH_2-AN (blue). (**b**) Absorption spectra of pyrene PY (green), 1-azidopyrene N_3-PY (purple) and 1-(azidomethyl)pyrene N_3-CH_2-PY (yellow). For both pyrene and anthracene, direct conjugation of the N_3 group leads to a red-shift of the absorption peak.

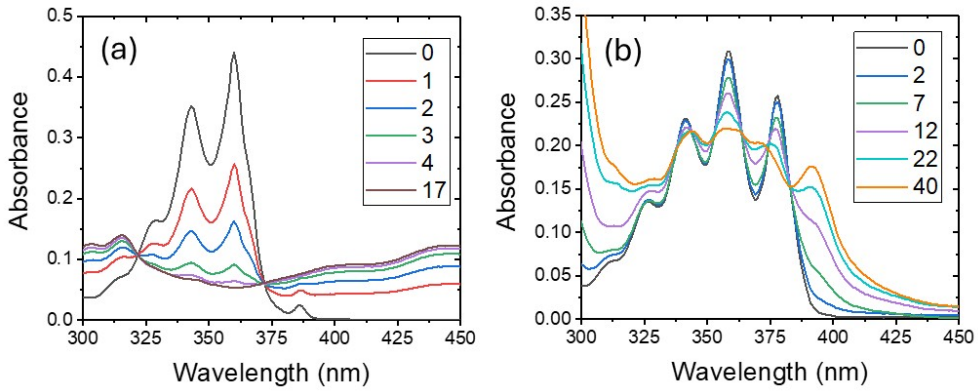

Figure 2. Absorption spectra of (**a**) N_3-PY and (**b**) $2N_3$-CH_2-AN during irradiation with 365 nm (5 mW/cm^2) recorded in chloroform solution. The different color curves show the spectral changes at the time points given in the legend (units of s).

Table 1. Measured reaction rates and relative quantum yields for 365 nm excitation in dilute $CHCl_3$ solution. Also given are the reaction rates for highly absorbing PMMA films.

Molecule	Rate (s^{-1}) in Solution	Normalized Relative Quantum Yield	Rate (s^{-1}) in Film
$2N_3$-AN	0.142	0.9	0.143
$2N_3$-CH_2-AN	0.068	0.6	0.002
N_3-PY	0.648	1	0.111
N_3-CH_2-PY	0.035	0.02	0.005

We were unable to find a systematic study in the literature of how azide connectivity affects its photoreactivity. Although it was originally proposed that the N_2 dissociation proceeds thermally through a

vibrationally hot ground state [31], most researchers now believe that it proceeds along a dissociative excited state [32,33]. In either case, dissociation would be expected to be more efficient when the N_3 is directly bound to the core. The intervening CH_2 group would inhibit both electronic coupling and vibrational energy transfer, although the flexibility of the linker may allow the N_3 group to have a closer approach to the core that partially compensates for the extra distance. The results in Table 1 are at least qualitatively consistent with this reasoning. The important conclusion from the solution data is that the set of molecules in Scheme 1 provides a way to vary azide reactivity and see whether it affects bubble formation.

In concentrated azide/PMMA films, the photolysis reaction showed changes in the absorption spectrum similar to those observed in solution, but in some cases without clear isosbestic points. Figure 3 shows the absorption spectra at various points during the photolysis of N_3-PY and $2N_3$-CH_2-AN in PMMA. Unfortunately, these films were too optically dense to make the assumption of constant intensity, which prevented estimation of relative quantum yields. However, there was an even greater variation in the reaction rates in PMMA than in solution, probably due to absorption shifts and the more rigid polymer environment.

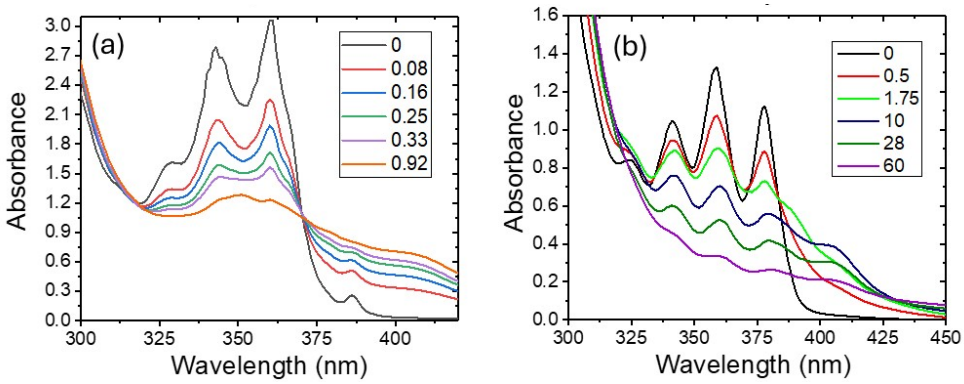

Figure 3. Absorption spectra of (**a**) N_3-PY and (**b**) $2N_3$-CH_2-AN during irradiation with 365 nm (9 mW/cm^2) recorded in solid PMMA films with starting concentrations of 0.1 M. The different color curves show the spectral changes at the time points given in the legend (units of min). The much slower decay in the PMMA films is due to the much higher starting absorption values.

We expected the different photochemical reaction rates to impact the bubble formation rate for the azide/PMMA films. To investigate this, we measured the time-dependent volume of bubbles $\bar{V}_{bub}(t)$ produced at the surface by using microscopy analysis. Representative images of bubble formation are shown in Figure 4a–e for the azides in PMMA under 365 nm illumination at 10 mW/cm^2, along with plots of the growth of the total areal volume of the bubbles, $\bar{V}_{bub}$. As in our previous paper, the $\bar{V}_{bub}(t)$ curves could be fit to an exponential of the form $\bar{V}_{bub}(t) = \bar{V}_{\infty}(1 - e^{-k_{bub}t})$. Surprisingly, we found that the k_{bub} rates for the different azides were within 30% of each other (Table 2). But as the intensity was lowered, the bubble forming ability of the different films diverged, until at 0.180 mW/cm^2 the $2N_3$-CH_2-AN and N_3-CH_2-PY films barely showed any bubble formation at all (Figure 4f–j). At this intensity, the growth for $2N_3$-AN and N_3-PY films showed clear induction periods, with the first bubbles only appearing after 60 s of irradiation. These low intensity $\bar{V}_{bub}(t)$ curves could not be fit using the simple exponential growth function.

Table 2. Total areal volume of the bubbles, $\bar{V}_{bub}$ and bubble growth rate constant k_{bub} for all azide molecules at 10 mW/cm^2 and 365 nm irradiation for 0.1 M azide concentration in PMMA films.

Molecule	$\bar{V}_{bub}$ (μm)	k_{bub} (s^{-1})
$2N_3$-AN	85.92	5.13×10^{-3}
$2N_3$-CH_2-AN	47.25	4.65×10^{-3}
N_3-PY	60.01	6.65×10^{-3}
N_3-CH_2-PY	49.40	5.11×10^{-3}

Bubble formation involves several intermediate steps, including N_2 production, diffusion to the polymer-water interface, and finally bubble nucleation, so it is not obvious that this process can be described by a single first-order kinetic process. To analyze the bubble growth dynamics as a multi-step process, we used the kinetic model outlined in Figure 5. The assumption that all processes, including N_2 transport to the surface and bubble nucleation, obey first-order rate laws is clearly a simplification. In particular, bubble nucleation only starts after a threshold density of N_2 molecules has been achieved [34], and a first-order kinetic model will not be able to capture

this behavior. Nevertheless, this model allows us to understand some qualitative features of the data. The coupled rate equations are

$$\frac{\partial C_{azide}}{\partial t} = -k_{photo} C_{azide} \tag{1a}$$

$$\frac{\partial C_{\mathrm{N2}}^{in}}{\partial t} = -k_{esc} C_{\mathrm{N2}}^{in} + k_{photo} C_{azide} \tag{1b}$$

$$\frac{\partial C_{\mathrm{N2}}^{out}}{\partial t} = -k_{bub} C_{\mathrm{N2}}^{out} + k_{esc} C_{\mathrm{N2}}^{in} \tag{1c}$$

$$\frac{\partial \bar{V}_{bub}}{\partial t} = (k_{bub} - k_{diff}) C_{\mathrm{N2}}^{out} \tag{1d}$$

C_{azide}, C_{N2}^{in}, C_{N2}^{out}, and V_{bub} are the azide concentration, the concentration of N_2 inside the polymer, the N_2 concentration outside the polymer near the surface, and the areal bubble volume, respectively. The rate of photolysis is k_{photo}, the rate of N_2 escape from inside the polymer interior is k_{esc}, the rate of N_2 diffusion into the bulk water is k_{diff}, and the rate of N_2 incorporation into a bubble is k_{bub}. Note that k_{photo} depends on light intensity and the molecule used, while the other rate constants should not vary. These equations can be solved analytically with the initial conditions $C_{\mathrm{N2}}^{in}(0) = C_{\mathrm{N2}}^{out}(0) = V_{bub}(0) = 0$. The solution is a rather long expression for the time dependent volume of N_2 contained in the bubbles:

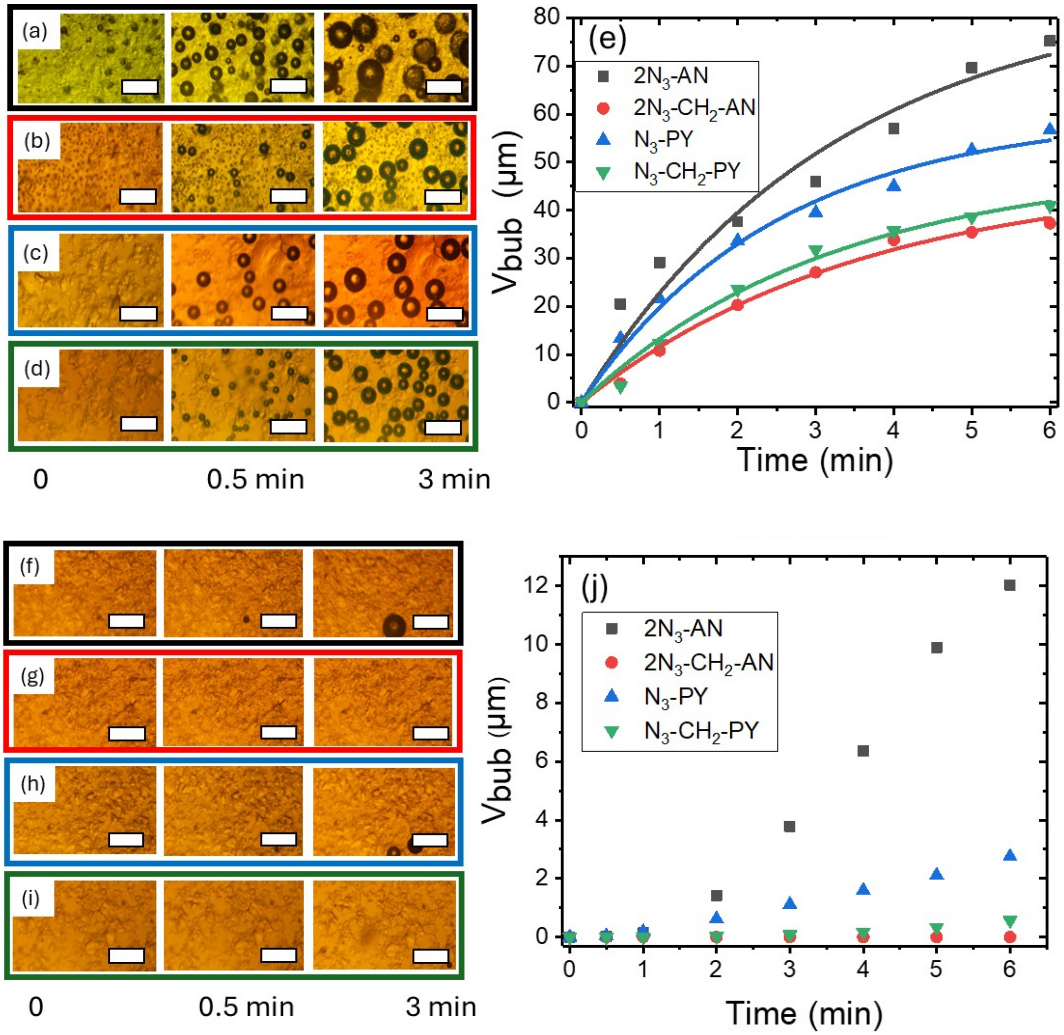

Figure 4. Images of bubble growth on PMMA surfaces with 0.1 M azide doping. Top: Films irradiated at 365 nm (10 mW/cm^2) doped with (**a**) 2N$_3$-AN, (**b**)2N$_3$-CH$_2$-AN, (**c**) N$_3$-PY (**d**) N$_3$-CH$_2$-PY. (**e**) The areal volume of bubbles $\bar{V}_{bub}(t)$ plotted versus time for the four azides. Bottom: Films irradiated at 365 nm (0.1 mW/cm^2) doped with (**f**) 2N$_3$-AN, (**g**)2N$_3$-CH$_2$-AN, (**h**) N$_3$-PY (**i**) N$_3$-CH$_2$-PY. (**j**) The areal volume of bubbles $\bar{V}_{bub}(t)$ plotted versus time for the four azides. Scale bars: 500 μm.

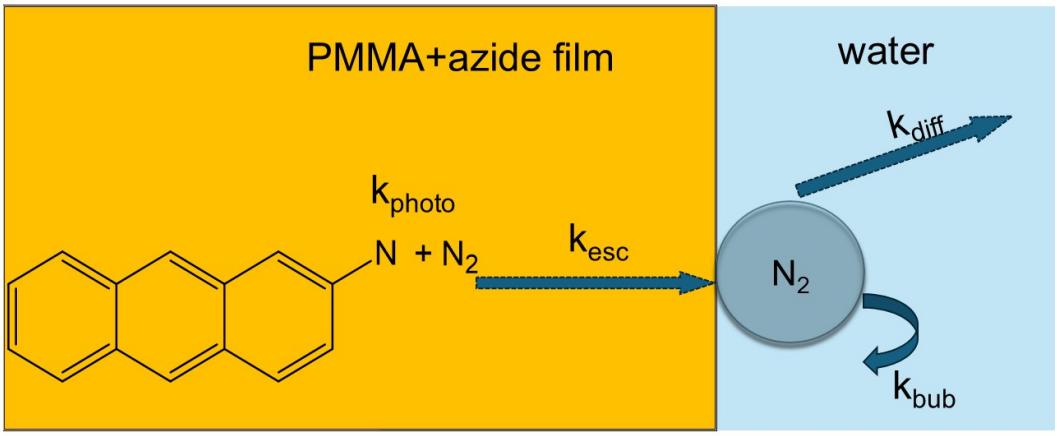

Figure 5. Schematic illustration of the kinetic processes and rates used for modeling the time-dependent growth of N_2 bubbles on the surface of the PMMA film.

$$\bar{V}_{bub}(t) = \frac{k_{bub}k_{esc}k_{photo}C_{azide}(0)}{k_{esc}-k_{photo}}\left(\frac{e^{-k_{esc}t}}{k_{esc}(k_{bub}-k_{diff}-k_{esc})} - \frac{e^{-k_{photo}t}}{k_{photo}(k_{bub}-k_{diff}-k_{photo})} - \frac{(k_{esc}-k_{photo})e^{-(k_{bub}-k_{diff})t}}{(k_{esc}-k_{photo})(k_{bub}-k_{diff}-k_{esc})(k_{bub}-k_{diff}-k_{photo})} + C\right) \quad (2)$$

$$C = \frac{k_{esc}-k_{photo}}{(k_{bub}-k_{diff})(k_{bub}-k_{diff}-k_{esc})(k_{bub}-k_{diff}-k_{photo})} + \frac{1}{k_{photo}(k_{bub}-k_{diff}-k_{photo})} - \frac{1}{k_{esc}(k_{bub}-k_{diff}-k_{esc})}$$

Equation (2) can be used to simulate the experimental $\bar{V}_{bub}(t)$ for $2N_3$-AN under different light intensities. The simulated curves are overlaid with experimental data in Figure 6, and the kinetic parameters used to simulate the growth curves are summarized in Table 3. At high intensities, a large k_{photo} value means that the photolysis is not rate-limiting and the bubble growth is determined by the transport and nucleation rates. This is the situation for all the azides when I = 10 mW/cm^2 and explains why they exhibit similar $\bar{V}_{bub}(t)$ curves at this intensity. As k_{photo} decreases, the photolysis rate eventually becomes the rate limiting step for bubble growth on the polymer surface. It is in this low intensity regime that differences in photolysis rates become reflected in the observed bubble growth rates, as observed in Figure 4j.

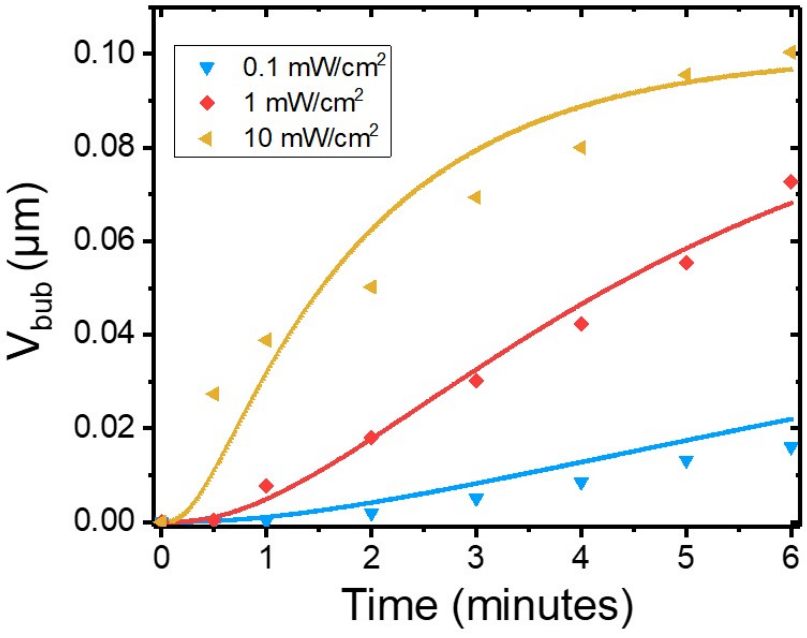

Figure 6. Experimental $\bar{V}_{bub}(t)$ curves measured for different 365 nm intensities for the 0.1 M $2N_3$-AN/PMMA film (points) overlaid with fits (solid lines) using Equation (2) of the text and the parameters in Table 3.

Table 3. Kinetic parameters used to simulate the bubble growth curves in Figure 6 using Equation (2) in the text. The different values for k_{photo} correspond to the three different light intensities given in Figure 6.

Kinetic Parameter	Fit Values
Initial azide concentration	$C_{N2(0)}$ = 0.1 M
Rate of azide photolysis	k_{photo} = 0.01, 0.1, 1 s^{-1}
Rate of N_2 escape	k_{esc} = 0.010 s^{-1}
Rate of bubble growth	k_{bub} = 93 × 10^{-3} s^{-1}
Rate of N_2 diffusion	k_{diff}= 10 × 10^{-11} s^{-1}

The important takeaway is that high light intensity can compensate for a low molecular reaction rate. At high intensities, all derivatives produced a dense layer of bubbles within a few minutes because the N_2 transport is rate-limiting and is similar for all azides. At lower intensities, however, the photolysis becomes rate-limiting, and the behavior of the different azides diverges. Under low-light conditions, $2N_3$-AN will still form a dense bubble layer while $2N_3$-CH_2-AN will generate almost no bubbles at all. While this multistep kinetic model captures the overall dynamics of N_2 bubble growth, it does not explicitly incorporate physical parameters like solvent hydrodynamics [35], bubble coalescence [36] and local gas depletion [37] that also influence bubble growth dynamics. These processes can be highly nonlinear and would be expected to cause the observed dynamics to deviate from first-order (linear) kinetics. Thus, the model presented here cannot be regarded as a first-principles description of the bubble formation, but rather as a framework for comparing kinetic trends across azide derivatives and light intensities.

In addition to the molecular photolysis rate, the multiple kinetic steps in our reaction scheme suggest that the polymer matrix should also play a key role in $\bar{V}_{bub}(t)$ by modifying k_{esc}. However, it does not appear that k_{esc} changes significantly in other polymer systems. We confirmed that azide photolysis could generate bubbles in other polymers besides PMMA. Rapid bubble growth was also observed for 0.1 M $2N_3$-AN in both polystyrene and polycarbonate. At high intensities (10 mW/cm^2) the growth rates and bubble volumes were within a factor of 2 of that in PMMA (Supplementary Figure S16, Supplementary Table S1), show that this strategy can be generalized to a variety of azide/polymer systems.

Sun et al. previously showed that nanoparticles doped with azides could generate N_2 bubbles via a photothermal mechanism. These bubbles could modulate ultrasound contrast in liquids [38,39]. We wanted to determine whether a surface layer of bubbles could generate useful contrast for an object imaged by a medical ultrasound device. PMMA is a biocompatible plastic that is extensively used in medical devices and implants [40]. The use of gas bubbles is now recognized as a safe and effective method to enhance contrast for biomedical ultrasound measurements [41–43]. In most ultrasound applications, the microbubbles are prepared ex situ as a particle containing gas enclosed in a shell composed of lipids, proteins, or polymer. The particle suspension is then injected into the biological medium or the organ to be imaged. Azide photolysis provides a method to generate N_2 bubbles in situ on surfaces, providing a way to generate bubbles on a specific object. Because it is a challenge to use ultrasound to image surgical instruments inside biological media [44], surface bubble generation could provide a complementary ultrasound imaging capability.

To mimic a surgical instrument, a glass pipette with a 2 mm diameter was coated with a layer of $2N_3$-AN doped PMMA with a thickness of ~100 μm. When irradiated under water by an external 365 nm light source, the pipette tip rapidly developed a dense layer of bubbles, as shown in Figure 7a,c. This layer of bubbles increased the contrast when the pipette was imaged using a commercial ultrasound machine, as shown in Figure 7b,d. Using image analysis (Supplementary Figure S17), we found a 6× increase in image brightness after light exposure. This enhancement arises due to the large acoustic index mismatch at the liquid-gas interface [45], which is substantially larger than that of a liquid-solid interface. Moreover, the images in Figure 7 show that this effect leads to good visualization of the object sides, as well as the top surface. This proof-of-principle experiment demonstrates that light can be used to create a high density of bubbles that provides a useful contrast enhancement for medical ultrasound imaging.

One concern about using azide coatings in a biomedical setting is exposure to possibly toxic chemicals. Previously, we hypothesized that production of free N_2 inside the polymer creates an internal pressure that forces the N_2 molecules toward the surface [22]. This flow is several orders of magnitude larger than what would be expected based on random diffusion under equilibrium conditions [46,47]. If this is the case, then adding a second polymer layer to encapsulate the azide layer should still permit N_2 gas transport to the surface while alleviating concerns about possible toxicity of the azide component. To test this idea, we deposited a second layer of undoped PMMA on top of a layer doped with 0.1 M $2N_3$-AN. Exposure of this bilayer sample to 365 nm light resulted in growth of a bubble layer with a slightly slower rate than that observed for the monolayer $2N_3$-AN system

(Supplementary Figure S18). The ability of the photogenerated N_2 to flow through a neat PMMA capping layer shows that it is possible to avoid direct contact between the azide layer and the surrounding medium while still generating a layer of surface bubbles.

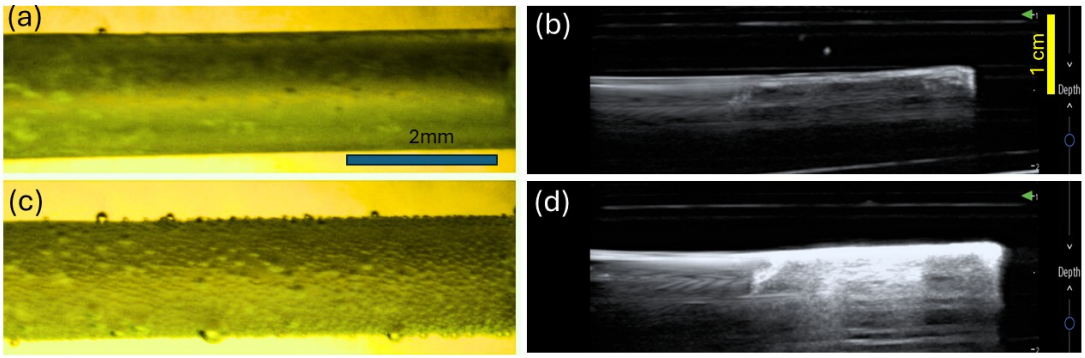

Figure 7. Photochemically generated bubbles enhance contrast in ultrasound imaging. A glass pipette tip is coated with a 0.1 M $2N_3$-AN/PMMA film. (**a**) Optical and (**b**) ultrasound images before 365 nm irradiation. (**c**) Optical and (**d**) ultrasound images after irradiation, showing bubbles and enhanced ultrasound contrast.

4. Conclusions

The results in this paper demonstrate that the phenomenon of photochemical bubble generation can be extended to a variety of aromatic azide derivatives and biocompatible transparent polymers. While insertion of a methyl group between the aromatic absorber and reactive N_2 moiety decreased the photolysis rate, a multi-step first-order kinetic model was developed to show how lower molecular photolysis rates could be compensated for by higher light intensities. The bubble layer created by light exposure could significantly increase the contrast in a medical ultrasound imaging set-up. We also showed that the N_2 produced in the doped PMMA layer could be rapidly transported through a PMMA capping layer for surface bubble formation, so direct contact between the azide layer and the aqueous surroundings can be avoided. Taken together, the results here show that photochemical gas generation by solid polymer films is a general phenomenon that can be understood quantitatively and applied to ultrasound imaging. It is possible that future optimization of these photoactive polymer systems could lead to applications in medicine and other fields.

Supplementary Materials: The following supporting information can be downloaded at: https://media.sciltp.com/articles/others/2506271013537077/MI-983-Supplementary-Materials-v1.pdf, Synthesis of compounds, UV Vis spectra, Bubble generation video on Polystyrene film, ultrasound imaging set-up. References [48–54] are cited in the Supplementary Materials.

Author Contributions: P.G. and C.B.: conceptualization, methodology, software, data curation, writing—original draft preparation, visualization, investigation; C.G.: Ultrasound imaging; Y.A. and M.A.: synthesis; R.K.: synthesis, writing—reviewing and editing. All authors have read and agreed to the published version of the manuscript".

Funding: This work was supported by ONR under grant/contract N00014-24-1-2358 (C.J.B). The views expressed are those of the author and do not reflect the official policy or position of the Department of Defense or the U.S. Government. This work was also supported by the King Abdullah International Medical Research Center (KSAU-HS/KAIMRC) through grant NRC21R25003 (R.O.K.).

Data Availability Statement: Raw data will be made available upon reasonable request.

Conflicts of Interest: The authors declare no conflict of interest.

References

1. Hoffman, A.S. Stimuli-Responsive Polymers: Biomedical Applications and Challenges for Clinical Translation. *Adv. Drug Deliv. Rev.* **2013**, *65*, 10–16. https://doi.org/10.1016/j.addr.2012.11.004.
2. Wei, M.; Gao, Y.; Li, X.; Serpe, M.J. Stimuli-Responsive Polymers and Their Applications. *Polym. Chem.* **2017**, *8*, 127–143. https://doi.org/10.1039/C6PY01585A.
3. Zhao, Y.; Hua, M.; Yan, Y.; Wu, S.; Alsaid, Y.; He, X. Stimuli-Responsive Polymers for Soft Robotics. *Annu. Rev. Control Robot. Auton. Syst.* **2022**, *5*, 515–545. https://doi.org/10.1146/annurev-control-042920-014327.
4. McCormick, M.E.; Bhattacharyya, R. Drag Reduction of a Submersible Hull by Electrolysis. *Nav. Eng. J.* **1973**, *85*, 11–16. https://doi.org/10.1111/j.1559-3584.1973.tb04788.x.
5. Murai, Y. Frictional Drag Reduction by Bubble Injection. *Exp. Fluids* **2014**, *55*, 1773. https://doi.org/10.1007/s00348-014-1773-x.

6. Kim, H.; Chang, J.H. Increased Light Penetration Due to Ultrasound-Induced Air Bubbles in Optical Scattering Media. *Sci. Rep.* **2017**, *7*, 16105. https://doi.org/10.1038/s41598-017-16444-9.
7. Bhanawat, A.; Zhu, K.; Pilon, L. How Do Bubbles Affect Light Absorption in Photoelectrodes for Solar Water Splitting? *Sustain. Energy Fuels* **2022**, *6*, 910–924. https://doi.org/10.1039/D1SE01730F.
8. Domenico, S.N. Acoustic Wave Propagation in Air-bubble Curtains in Water—Part I: History and Theory. *Geophysics* **1982**, *47*, 345–353. https://doi.org/10.1190/1.1441340.
9. Leroy, V.; Strybulevych, A.; Lanoy, M.; Lemoult, F.; Tourin, A.; Page, J.H. Superabsorption of Acoustic Waves with Bubble Metascreens. *Phys. Rev. B* **2015**, *91*, 020301. https://doi.org/10.1103/PhysRevB.91.020301.
10. Sharma, G.S.; Skvortsov, A.; MacGillivray, I.; Kessissoglou, N. Sound Scattering by a Bubble Metasurface. *Phys. Rev. B* **2020**, *102*, 214308. https://doi.org/10.1103/PhysRevB.102.214308.
11. Huang, Z.; Zhao, S.; Su, M.; Yang, Q.; Li, Z.; Cai, Z.; Zhao, H.; Hu, X.; Zhou, H.; Li, F.; et al. Bioinspired Patterned Bubbles for Broad and Low-Frequency Acoustic Blocking. *ACS Appl. Mater. Interfaces* **2020**, *12*, 1757–1764. https://doi.org/10.1021/acsami.9b15683.
12. Gong, X.-T.; Zhou, H.-T.; Zhang, S.-C.; Wang, Y.-F.; Wang, Y.-S. Tunable Sound Transmission through Water–Air Interface by Membrane-Sealed Bubble Metasurface. *Appl. Phys. Lett.* **2023**, *123*, 231703. https://doi.org/10.1063/5.0171461.
13. Goyal, R.; Athanassiadis, A.G.; Ma, Z.; Fischer, P. Amplification of Acoustic Forces Using Microbubble Arrays Enables Manipulation of Centimeter-Scale Objects. *Phys. Rev. Lett.* **2022**, *128*, 254502. https://doi.org/10.1103/PhysRevLett.128.254502.
14. Liang, X.; Kumar, V.; Ahmadi, F.; Zhu, Y. Manipulation of Droplets and Bubbles for Thermal Applications. *Droplet* **2022**, *1*, 80–91. https://doi.org/10.1002/dro2.21.
15. Metwally, K.; Mensah, S.; Baffou, G. Fluence Threshold for Photothermal Bubble Generation Using Plasmonic Nanoparticles. *J. Phys. Chem. C* **2015**, *119*, 28586–28596. https://doi.org/10.1021/acs.jpcc.5b09903.
16. Baffou, G.; Polleux, J.; Rigneault, H.; Monneret, S. Super-Heating and Micro-Bubble Generation around Plasmonic Nanoparticles under Cw Illumination. *J. Phys. Chem. C* **2014**, *118*, 4890–4898. https://doi.org/10.1021/jp411519k.
17. Li, J.; Zhao, F.; Deng, Y.; Liu, D.; Chen, C.-H.; Shih, W.-C. Photothermal Generation of Programmable Microbubble Array on Nanoporous Gold Disks. *Opt. Express* **2018**, *26*, 16893. https://doi.org/10.1364/OE.26.016893.
18. Ohannesian, N.; Li, J.; Misbah, I.; Zhao, F.; Shih, W.-C. Directed Concentrating of Micro-/Nanoparticles via Near-Infrared Laser Generated Plasmonic Microbubbles. *ACS Omega* **2020**, *5*, 32481–32489. https://doi.org/10.1021/acsomega.0c04610.
19. Hu, M.; Wang, F.; Chen, L.; Huo, P.; Li, Y.; Gu, X.; Chong, K.L.; Deng, D. Near-Infrared-Laser-Navigated Dancing Bubble within Water via a Thermally Conductive Interface. *Nat. Commun.* **2022**, *13*, 5749. https://doi.org/10.1038/s41467-022-33424-4.
20. Prosperetti, A. Vapor Bubbles. *Annu. Rev. Fluid Mech.* **2017**, *49*, 221–248. https://doi.org/10.1146/annurev-fluid-010816-060221.
21. Shields, D.J.; Karothu, D.P.; Sambath, K.; Ranaweera, R.A.A.U.; Schramm, S.; Duncan, A.; Duncan, B.; Krause, J.A.; Gudmundsdottir, A.D.; Naumov, P. Cracking under Internal Pressure: Photodynamic Behavior of Vinyl Azide Crystals through N_2 Release. *J. Am. Chem. Soc.* **2020**, *142*, 18565–18575. https://doi.org/10.1021/jacs.0c07830.
22. Ghate, P.P.; Hanson, K.M.; Lam, K.; Al-Kaysi, R.O.; Bardeen, C.J. Generating Stable Nitrogen Bubble Layers on Poly(Methyl Methacrylate) Films by Photolysis of 2-Azidoanthracene. *Langmuir* **2024**, *40*, 4054–4062. https://doi.org/10.1021/acs.langmuir.3c02869.
23. Biswas, B.; Venkateswarulu, M.; Gaur, P.; Sharma, Y.; Sinha, S.; Ghosh, S. Triggered Emission for Rapid Detection of Hydrogen Sulfide Chaperoned by Large Stokes Shift. *J. Photochem. Photobiol. A Chem.* **2019**, *371*, 264–270. https://doi.org/10.1016/j.jphotochem.2018.11.011.
24. Pinchasik, B.-E.; Schönfeld, F.; Kappl, M.; Butt, H.-J. Bubbles Nucleating on Superhydrophobic Micropillar Arrays under Flow. *Soft Matter* **2019**, *15*, 8175–8183. https://doi.org/10.1039/C9SM01224A.
25. Deng, X.; Shan, Y.; Meng, X.; Yu, Z.; Lu, X.; Ma, Y.; Zhao, J.; Qiu, D.; Zhang, X.; Liu, Y.; et al. Direct Measuring of Single–Heterogeneous Bubble Nucleation Mediated by Surface Topology. *Proc. Natl. Acad. Sci. USA* **2022**, *119*, e2205827119. https://doi.org/10.1073/pnas.2205827119.
26. Beechem, J.M.; Ameloot, M.; Brand, L. Global and Target Analysis of Complex Decay Phenomena. *Instrum. Sci. Technol.* **1985**, *14*, 379–402. https://doi.org/10.1080/10739148508543585.
27. Reiser, A.; Bowes, G.; Horne, R.J. Photolysis of Aromatic Azides. Part 1—Electronic Spectra of Aromatic Nitrenes and Their Parent Azides. *Trans. Faraday Soc.* **1966**, *62*, 3162–3169. https://doi.org/10.1039/TF9666203162.
28. Alvarado, R.; Grivet, J.-P.; Igier, C.; Barcelo, J.; Rigaudy, J. Spectroscopic Studies of Azides and Nitrenes Derived from Anthracene. *J. Chem. Soc., Faraday Trans.* **1977**, *73*, 844. https://doi.org/10.1039/f29777300844.
29. Wentrup, C. Nitrenes, Carbenes, Diradicals, and Ylides. Interconversions of Reactive Intermediates. *Acc. Chem. Res.* **2011**, *44*, 393–404. https://doi.org/10.1021/ar700198z.

30. Sankaranarayanan, J.; Rajam, S.; Hadad, C.M.; Gudmundsdottir, A.D. The Ability of Triplet Nitrenes to Abstract Hydrogen Atoms. *J Phys. Org. Chem.* **2010**, *23*, 370–375. https://doi.org/10.1002/poc.1654.
31. Reiser, A.; Marley, R. Photolysis of Aromatic Azides. Part 3—Quantum Yield and Mechanism. *Trans. Faraday Soc.* **1968**, *64*, 1806–1815. https://doi.org/10.1039/TF9686401806.
32. Gritsan, N.P.; Pritchina, E.A. The Mechanism of Photolysis of Aromatic Azides. *Russ. Chem. Rev.* **1992**, *61*, 500–516. https://doi.org/10.1070/RC1992v061n05ABEH000959.
33. Soto, J.; Otero, J.C. Conservation of El-Sayed's Rules in the Photolysis of Phenyl Azide: Two Independent Decomposition Doorways for Alternate Direct Formation of Triplet and Singlet Phenylnitrene. *J. Phys. Chem. A* **2019**, *123*, 9053–9060. https://doi.org/10.1021/acs.jpca.9b06915.
34. Rubin, M.B.; Noyes, R.M. Thresholds for Nucleation of Bubbles of Nitrogen in Various Solvents. *J. Phys. Chem.* **1992**, *96*, 993–1000. https://doi.org/10.1021/j100181a082.
35. Maloth, R.K.N.; Khayat, R.E.; DeGroot, C.T. Bubble Growth in Supersaturated Liquids. *Fluids* **2022**, *7*, 365. https://doi.org/10.3390/fluids7120365.
36. Huber, C.; Su, Y.; Nguyen, C.T.; Parmigiani, A.; Gonnermann, H.M.; Dufek, J. A New Bubble Dynamics Model to Study Bubble Growth, Deformation, and Coalescence. *JGR Solid Earth* **2014**, *119*, 216–239. https://doi.org/10.1002/2013JB010419.
37. Moreno Soto, Á.; Prosperetti, A.; Lohse, D.; Van Der Meer, D. Gas Depletion through Single Gas Bubble Diffusive Growth and Its Effect on Subsequent Bubbles. *J. Fluid Mech.* **2017**, *831*, 474–490. https://doi.org/10.1017/jfm.2017.623.
38. Sun, I.-C.; Emelianov, S. Gas-Generating Nanoparticles for Contrast-Enhanced Ultrasound Imaging. *Nanoscale* **2019**, *11*, 16235–16240. https://doi.org/10.1039/C9NR04471J.
39. Sun, I.-C.; Dumani, D.S.; Emelianov, S.Y. Applications of the Photocatalytic and Photoacoustic Properties of Gold Nanorods in Contrast-Enhanced Ultrasound and Photoacoustic Imaging. *ACS Nano* **2024**, *18*, 3575–3582. https://doi.org/10.1021/acsnano.3c11223.
40. Frazer, R.Q.; Byron, R.T.; Osborne, P.B.; West, K.P. PMMA: An Essential Material in Medicine and Dentistry. *J. Long Term Eff. Med. Implant.* **2005**, *15*, 629–639. https://doi.org/10.1615/JLongTermEffMedImplants.v15.i6.60.
41. Blomley, M.J.K. Science, Medicine, and the Future: Microbubble Contrast Agents: A New Era in Ultrasound. *BMJ* **2001**, *322*, 1222–1225. https://doi.org/10.1136/bmj.322.7296.1222.
42. Lee, H.; Kim, H.; Han, H.; Lee, M.; Lee, S.; Yoo, H.; Chang, J.H.; Kim, H. Microbubbles Used for Contrast Enhanced Ultrasound and Theragnosis: A Review of Principles to Applications. *Biomed. Eng. Lett.* **2017**, *7*, 59–69. https://doi.org/10.1007/s13534-017-0016-5.
43. Ferrara, K.; Pollard, R.; Borden, M. Ultrasound Microbubble Contrast Agents: Fundamentals and Application t o Gene and Drug Delivery. *Annu. Rev. Biomed. Eng.* **2007**, *9*, 415–447. https://doi.org/10.1146/annurev.bioeng.8.061505.095852.
44. Huang, J.; Triedman, J.K.; Vasilyev, N.V.; Suematsu, Y.; Cleveland, R.O.; Dupont, P.E. Imaging Artifacts of Medical Instruments in Ultrasound-Guided Interventions. *J. Ultrasound Med.* **2007**, *26*, 1303–1322. https://doi.org/10.7863/jum.2007.26.10.1303.
45. Godin, O.A. Sound Transmission through Water–Air Interfaces: New Insights into an Old Problem. *Contemp. Phys.* **2008**, *49*, 105–123. https://doi.org/10.1080/00107510802090415.
46. Patel, V.M.; Patel, C.K.; Patel, K.C.; Patel, R.D. Diffusion of Gases in Poly(Methyl Methacrylate). *Makromol. Chem.* **1972**, *158*, 65–79. https://doi.org/10.1002/macp.1972.021580107.
47. Haraya, K.; Hwang, S.-T. Permeation of Oxygen, Argon and Nitrogen through Polymer Membranes. *J. Membr. Sci.* **1992**, *71*, 13–27. https://doi.org/10.1016/0376-7388(92)85002-Z.
48. Kung, Y.-C.; Hsiao, S.-H. Fluorescent and Electrochromic Polyamides with Pyrenylamine Chromophore. *J. Mater. Chem.* **2010**, *20*, 5481.
49. Bräse, S., Banert, K., Eds.; *Organic Azides: Syntheses and Applications*; John Wiley: Chichester, UK, 2010.
50. Morales-Espinoza, E.G.; Lijanova, I.V.; Morales-Saavedra, O.G.; Torres-Zuñiga, V.; Hernandez-Ortega, S.; Martínez-García, M. Synthesis of Porphyrin-Dendrimers with a Pyrene in the Periphery and Their Cubic Nonlinear Optical Properties. *Molecules* **2011**, *16*, 6950–6968.
51. Ingale, S.A.; Seela, F. A Ratiometric Fluorescent On–Off Zn^{2+} Chemosensor Based on a Tripropargylamine Pyrene Azide Click Adduct. *J. Org. Chem.* **2012**, *77*, 9352–9356.
52. Jiang, J.; Lima, O.V.; Pei, Y.; Jiang, Z.; Chen, Z.; Yu, C.; Wang, J.; Zeng, X.C.; Forsythe, E.; Tan, L. Self-Assembled Nanolayers of Conjugated Silane with Π−π Interlocking. *ACS Nano* **2010**, *4*, 3773–3780.
53. Okita, T.; Muto, K.; Yamaguchi, J. Decarbonylative Methylation of Aromatic Esters by a Nickel Catalyst. *Org. Lett.* **2018**, *20*, 3132–3135.
54. Arjunan, P.; Berlin, K.D. An improved synthesis of 2-anthraldehyde. *Org. Prep. Proced. Int.* **1981**, *13*, 368–371.